CHEMICAL AND NANOMATERIAL-BASED INJECTABLE DYE PLATFORMS

EXPANDING THE POSSIBILITIES OF TRANSLATIONAL MOLECULAR IMAGING

Nicholas David Calvert

A Thesis Submitted in Partial Fulfillment
of the Requirements for the Degree of

Doctorate in Philosophy in Chemistry

Department of Chemistry and Biomolecular Sciences

Faculty of Science

University of Ottawa

Supervisor: Adam J. Shuhendler, PhD

Examining Board: Christopher N. Boddy, PhD, Chemistry and Biomolecular Sciences
Eva Hemmer, PhD, Chemistry and Biomolecular Sciences
Jaclyn Brusso, PhD, Chemistry and Biomolecular Sciences

External Examiner: David Wilson, MD, PhD, Radiology and Biomedical Imaging, University of California, San Francisco

Abstract

The continual growth of an aging population has led to a greater incidence of disease and a greater dependence on medical imaging for diagnoses, resulting in a growing clinical need for molecular imaging (MI). MI uses chemical tools to probe or interact with biomarkers of disease and aberrant cellular processes, an area of radiology that has been growing rapidly. MI allows for earlier diagnosis of disease since it identifies changes in biomolecular hallmarks prior to anatomical changes, such as tumors. Commonly used imaging modalities like magnetic resonance imaging (MRI) and intravascular optical coherence tomography (IV-OCT), as well as emerging imaging modalities like magnetic particle imaging (MPI), are in need of chemical innovations to provide MI agents for indications or patient populations that are not currently served but that would significantly benefit from them: kidney disease patients who cannot receive contrast-enhanced MRI, in-stent restenosis and atherosclerosis stratification in IV-OCT, and improvements in cell tracking for cell therapies with MPI.

This thesis describes the use of chemical, nanomaterial, and biochemical techniques to develop, characterize, and evaluate new MI chemical solutions for challenges that exist within these imaging modalities *in vivo*. We have identified and characterized a class of organic radical contrast agent known as verdazyl as a new, metal-free MRI contrast agent that qualitatively and quantitatively evaluates kidney function for a patient population that often cannot receive MRI contrast agents due to safety concerns. We have created a new Au nanostructure that both scatters near-infrared II light and binds molecular markers of inflammation, providing MI to IV-OCT. Finally, we have examined the effect of surface chemistry modulation on anionic superparamagnetic iron oxide nanoparticles towards more biomimetic, zwitterionic groups for improving cell uptake for cell tracking purposes. The chemical probes presented in this thesis

will be fundamental to pursuing both pre-clinical and clinical solutions to problems in the field of MI.

Dedication

To Gen, Rose, and Dave.

Acknowledgements

The completion of this degree would have been impossible without the help, support, and guidance of a number of people. I probably won't get to mention everyone in an effort to keep this section brief, but you know who you are. To my supervisor Dr. Adam Shuhendler, it's been a pleasure spending the last 4 and some odd years in this lab. I have always appreciated your trust and faith in me as a scientist, allowing me the freedom to try things my own way. You have always allowed me to be myself and let my own voice and personality shine through in my work. Your willingness and openness to try any crazy idea to help a project succeed, as well as not being afraid to rely on others for help or advice are qualities I have admired and will continue to carry. I will remember and cherish our many "spirited debates".

To my committee members, thank you for taking the time from your busy schedules to help me throughout the completion of the degree and for taking the time to examine this thesis. Especially to Dr. Boddy, thank you for all of the advice you have given me over the years, both personally and scientifically.

To my lab mates in the Shuhendler lab, both past and present, thank you for all the support and friendship. It's been a great team to be a part of over the years and made coming into the office a lot more fun. I have to give special mention to Alexia who I have unintentionally managed to follow from lab to lab for the last 11 or 12 academic years. We have and will continue to make a great team.

To Mike, Andrè, and Eric (no particular order), I don't think any of us would have survived this degree without each other. From fishing trips, conferences, Airbnb wrestling matches, weekends at the lab, and time spent on the floor in the office, we have really formed a

brotherhood (to steal a line from Gates' thesis). These are friendships and memories I will cherish for a lifetime.

To my parents Rose and Dave, and really to my entire family, thank you for all the love and support over the last decade of school, it would not have been possible without your support. Finally, to my now wife Gen, thank you for all the love, support, and patience through my career as a student since we met 10 years ago. Your continual belief in both me and my goals has been a major driving force in what I have accomplished throughout this degree, and that has meant the world to me.

Table of Contents

List of Figures

List of Symbols, Nomenclature, and Abbreviations

ε*= T_1 Relaxation Rate Enhancement
%ID/g - Percent Injected Dose per Gram Bodyweight
2D - Two-Dimensional
3D - Three-Dimensional
AA - Abdominal Aorta
Ac_2O - Acetic Anhydride
AcN - Acetonitrile
ACR - Albumin-to-Creatinine Ratio
AKI - Acute Kidney Injury
ANOVA - Analysis of Variance
AUC - Area Under the Curve
AuNP - Gold Nanoparticle
$AuNP_{500}$ - 500 nm Diameter Gold Nanoparticles
$AuNP_9$ - 9 nm Diameter Gold Nanoparticles
$AuSC@(13FS)_2$ - Gold Superclusters Twice Coated with a 1 to 3 Ratio of Fucose-Functionalized Myrj52 to Organosulfate-Functionalized Myrj52
AuSC@(Myrj52) - Gold Superclusters Coated with Myrj52
$AuSC@(Myrj52)_2$ - Gold Superclusters Twice Coated with Myrj52
BuOH - Butanol
CAD - Coronary Artery Disease
CKD - Chronic Kidney Disease
CPMG - Car-Purcell-Meiboom-Gill Sequence
CT – Computed Tomography
CVD - Cardiovascular Disease
Cys - L-Cysteine
DCE - Dynamic Contrast Enhanced
DCM - Dichloromethane
DLS - Dynamic Light Scattering
DMF - Dimethylformamide
DMI - Deuterium Metabolic Imaging
DMPO - 5,5-dimethylpyrroline-N-oxide
DOTA - Dodecane Tetraacetic Acid
DTPA - Diethylenetriaminepentaacetic Acid
EDC - 1-ethyl-3-(3-dimethylaminopropyl)carbodiimide
EDL - Electric Double Layer
eGFR - Estimated Glomerular Filtration Rate
EI - Electron Impact
EpiCGS - Epithelial Cell Growth Supplement
EpiMEM - Epithelial Cell Media
EPR - Electron Paramagnetic Resonance
ESI - Electrospray Ionization
Et_3N - Triethylamine
EtOAc - Ethyl Acetate
EtOH - Ethanol

F - Fucose-Functionalized Myrj52
FA - Folic Acid
FAN - Folic Acid Nephropathy
FBS - Fetal Bovine Serum
FCC - Flash Column Chromatography
FDA - Food and Drug Administration
FDG - [^{18}F]-2-deoxy-2-fluoroglucose
FDTD - Finite-Difference Time Domain
Fe@Cys - Superparamagnetic Iron Oxide Nanoparticle Coated with L-Cysteine
Fe@HCys - Superparamagnetic Iron Oxide Nanoparticle Coated with D,L-Homocysteine
Fe@PMAO - Superparamagnetic Iron Oxide Nanoparticle Coated with poly(maleic anhydride-alt-1-octadecene
Fe@PSB - Superparamagnetic Iron Oxide Nanoparticle Coated with Pyridinium Sulfobetaine
Fe@SB - Superparamagnetic Iron Oxide Nanoparticle Coated with Sulfobetaine
FIB - Gallium Focused-Ion Beam
FID - Free Induction Decay
FOV - Field of View
FWHM - Full Width at Half Maximum
G - Galactose-Functionalized Myrj52
GBCA - Gadolinium-Based Contrast Agent
GFR - Glomerular Filtration Rate
GLUT - Glucose Transporter
GPH - Global Plasmon Hybridization
GSH - Reduced Glutathione
H460 - Large-Cell Lung Cancer Cells
HCys - D,L-Homocysteine
HepG2 - Human Hepatocellular Carcinoma Cells
HIM - Helium Ion Microscopy
HPLC -High Performance Liquid Chromatography
HRMS - High Resolution Mass Spectrometry
hRPT - Human Renal Proximal Tubule Cells
HSA - Human Serum Albumin
HSQC - Heteronuclear Single Quantum Coherence
i.v. - Intravascular
ICP-MS - Inductively Coupled Plasma Mass Spectrometry
ICP-OES - Inductively Coupled Plasma Optical Emission Spectroscopy
IPA - Isopropyl Alcohol
IQR - Interquartile Range
IUC - Intraparticle Unit Cell
IV-OCT - Intravascular Optical Coherence Tomography
IVUS - Intravascular Ultrasound
LPS – Lipopolysaccharide
LSPR - Localized Surface Plasmon Resonance
MAG3 - Mercaptoacetyltriglycine
MALDI - Matrix-Asssisted Laser Desorption/Ionization
MDA-MB-231 - Triple Negative Human Breast Cancer Cells

MeOH - Methanol
MES - 2-(N-morpholino)ethanesulfonic acid
MI - Molecular Imaging
Mn - Manganese
MOPS - 3-(N-morpholino)propanesulfonic acid
MPI - Magnetic Particle Imaging
MRI - Magnetic Resonance Imaging
MRP - Medullary and Renal Pelvis Region
MRSI - Magnetic Resonance Spectroscopic Imaging
MSC - Mesenchymal Stem Cell
MVB - Multivesicular Body
M_W – Molecular Weight
Myrj52 - Polyethylene Oxide (40) Stearate
NaOAc - Sodium Acetate
NIR – Near Infrared
NMR - Nuclear Magnetic Resonance
NP - Nanoparticle
NPC - 4-nitrophenol chloroformate
NSF - Nephrogenic Systemic Fibrosis
OCT - Optical Coherence Tomography
ORCA - Organic Radical Contrast Agent
P/S - Penicillin/Streptomycin
PAS - Periodic Acid-Schiff Stain
PBS - Phosphate-Buffered Saline (pH 7.4)
Pd/C - Palladium on Carbon
PEG - Polyethylene Glycol
PET – Positron Emitted Tomography
PMAO - poly(maleic anhydride-alt-1-octadecene
PPB - Perl's Prussian Blue
PSB - Pyridinium Sulfobetaine
PSGL-1 - P-selectin Glycoprotein Ligand 1
r_1 - Molar T_1 Relaxivity
R_1 - T_1 Relaxation Rate
r_2 - Molar T_2 Relaxivity
R_2 - T_2 Relaxation Rate
RARE - Rapid Imaging with Refocused Echoes
RAW 264.7 - Mouse Bone Marrow Macrophage
RDTC - Renal Decay Time Constant (k)
RF - Radiofrequency
ROI - Region of Interest
ROSE - Reflection or Scattering Event
RPMI - RPMI-1640 Media
RT - Room Temperature
S - Organosulfate-Functionalized Myrj52
SB - Sulfobetaine
SCr - Serum Creatinine

SEM - Scanning Electron Microscopy
SGLT2 - Sodium-Glucose Co-Transporter 2
SLeX - Sialyl Lewis-X
SPECT - Single Photon Emission Computed Tomography
SPION - Superparamagnetic Iron Oxide Nanoparticle
T_1 – Spin-Lattice Relaxation
T_{1e} - Electronic Relaxation Time
T_2 – Spin-Spin Relaxation
TE_{eff} - Effective Echo Time
TEM - Transmission Electron Microscopy
TEMPO - 2,2,6,6-tetramethylpiperidine 1-oxyl
TEOS - Tetraethyl Orthosilicate
TR - Repetition Time
US - Ultrasound
UUO - Unilateral Ureter Obstruction
VCAM-1 – Vascular Cell Adhesion Molecule 1
X - Xanthine
XO - Xanthine Oxidase

Chapter 1: Introduction

1.1. Medical Diagnostic Imaging

Prior to 1895, medical practitioners had no method of visualizing what was happening inside of the body of a patient.[1,2] It was at this time that Wilhelm Conrad Roentgen invented X-ray imaging and provided the world with the first picture of the inside of a live human body, a feat for which he was awarded a Nobel prize in 1901.[3,4] The invention of X-ray imaging is widely considered the catalyst for modern medical imaging and the field of radiology. In the following century, the field of medical imaging has grown exponentially. There are now four classifications of medical imaging that are used daily in clinical diagnostics, including radiography, magnetic resonance imaging (MRI), nuclear medicine, optical imaging, and ultrasound (US). Within each of these categories exists multiple different imaging instruments, modalities, and techniques[5], as well as emerging diagnostic imaging modalities that reside within their own category, such as intravascular optical coherence tomography (IV-OCT) and magnetic particle imaging (MPI).[6] The World Health Organization has estimated that there are 3.6 billion diagnostic medical examinations globally,[7] with the most frequently used modalities including PET-computed tomography (PET-CT) and MRI; these two techniques account for over 50 million scans in North America each year.[8,9]

Medical imaging is critical to early, accurate patient diagnoses leading to earlier and more effective treatment for more positive patient outcomes.[10] In addition to providing non-invasive ways to visualize internal structure and function of tissues, each unique imaging modality also allows physicians to monitor patient responses to medical treatment, as well as the progression or regression of underlying diseases.[11,12] Another emerging use for medical imaging in both clinical and pre-clinical settings is in the drug development process. This provides a

means for monitoring uptake, clearance, and response to investigational new drugs before they are approved for patient use.[13,14]

1.1.1. MRI

The core principles of MRI are very similar to those of proton nuclear magnetic resonance imaging (NMR). MRI uses a strong magnetic field to align proton nuclei prior to the application of strong radiofrequency (RF) pulses at the Larmor frequency of the proton, forcing a 90° flip of the proton magnetization vector.[15] Following the pulse, the proton relaxes through two mechanisms simultaneously, each emitting their own radiofrequency signals: free induction decay signal associated with spin-spin (T_2) relaxation and spin-lattice (T_1) relaxation.[16] The Fourier transformation of both T_1 and T_2 signals is used to convert these time domain signals which, in conjunction with magnetic gradient encodings, produces spatial data.[17] T_1 signal is derived from the time it takes the proton to reach 63% of the original net magnetization, derived from the M_z component of the Bloch equation, while T_2 is acquired from the resulting free induction decay signal. The overwhelming majority of the MRI signal is from the up to 60% water the human body contains,[18] meaning the MRI image generated is of the change in water relaxation rates (Figure 1.1). Different tissue components will have different chemical environments that water resides in, as well as different concentrations of water, creating a differential contrast when imaging different areas of the body that is affected by T_1- or T_2-weighted imaging.[19] For example, T_1-weighted MRI images of the brain will show high contrast with white matter and low contrast for grey matter at the same relaxation timepoint, while the grey matter becomes much more visible using T_2-weighted imaging.[20] This evaluation of endogenous water with no introduction of exogenous agent is referred to as non-contrast.

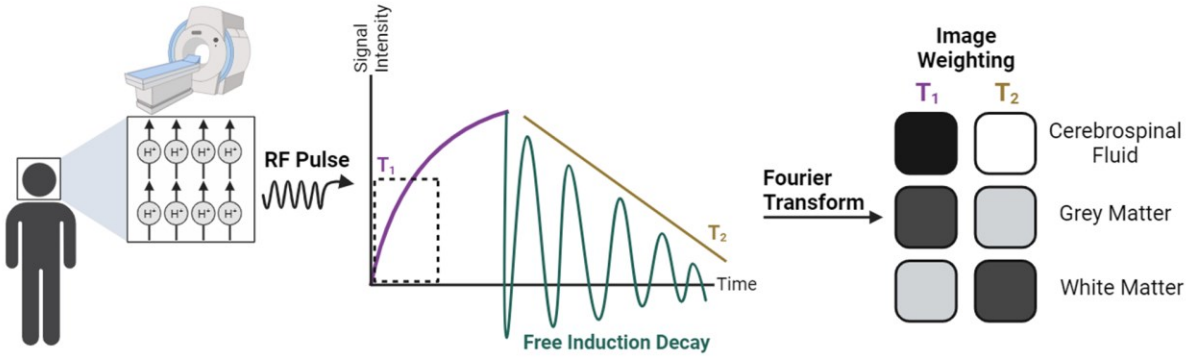

Figure 1.1 Schematic of T_1 or T_2 weighted MRI images in the brain derived from different components of the proton relaxation signal. Illustrated images in the figure were acquired using the same relaxation time following radiofrequency (RF) pulse.

Contrast MRI is more commonly used in the clinic and involves the intravenous injection of a chelated-metal contrast agent, most commonly gadolinium (Gd). The coordinated gadolinium ion contains unpaired electrons that make it strongly paramagnetic and will enhance the relaxation rate of nearby water protons. This modulates both T_1 and T_2 relaxation times through either inner-sphere (water coordination to Gd) or outer-sphere (micro magnetic environment of electrons interfering with water protons) effects.[21] Coordinated Gd exists in a +3-oxidation state and will bind water molecules, enhancing T_1 through primarily inner sphere effects.[22] Specifically with Gd, this greatly shortens T_1 relaxation and generates strong MRI contrast. Gd contrast enhancement with MRI is particularly effective at identifying many diseases or dysfunctions, particularly cancer. Tumors often have aberrant vasculature, which leads to a significant amount of Gd pooling, creating strong contrast in tumors that is not visible in non-contrast MRI (Figure 1.2).[23]

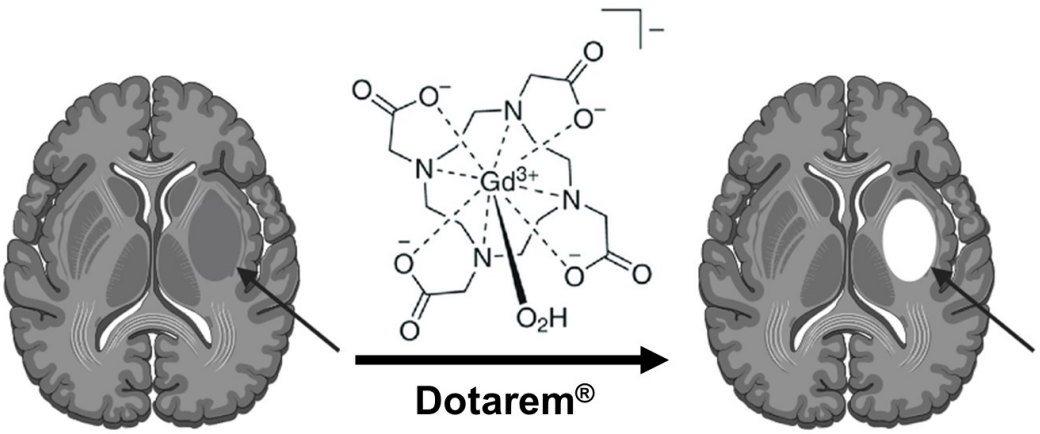

Figure 1.2 MRI scan of a malignant brain tumor before and after injection with the Gd-based contrast agent, Dotarem®. The poorly visible tumor becomes highly visible after Dotarem® contrast injection. The black arrow in the image denotes the location of the tumor both before and after contrast enhancement.

Early Gd contrast agents comprised linear chelates (Figure 1.3), where the Gd ion was not fully surrounded by a chelating molecule, and were highly susceptible to Gd dissociation, leading to high levels of Gd deposition in tissues.[24] With the primary route of clearance through the kidney, reduction in kidney filtration could allow Gd deposition leading to the incurable, fatal disease nephrogenic systemic fibrosis (NSF).[25] Only macrocyclic Gd agents (GBCAs) are used now, most commonly dodecane tetraacetic acid (DOTA, Figure 1.3). No new cases of NSF have been diagnosed since 2009, and in most cases GBCAs are considered safe.[26] However, GBCAs are still contraindicated in several significantly sized patient populations, including patients with acute kidney injury (AKI), late-stage chronic kidney disease (CKD), pregnancies, and allergies, leaving these patients without access to a critical diagnostic imaging modality.[27]

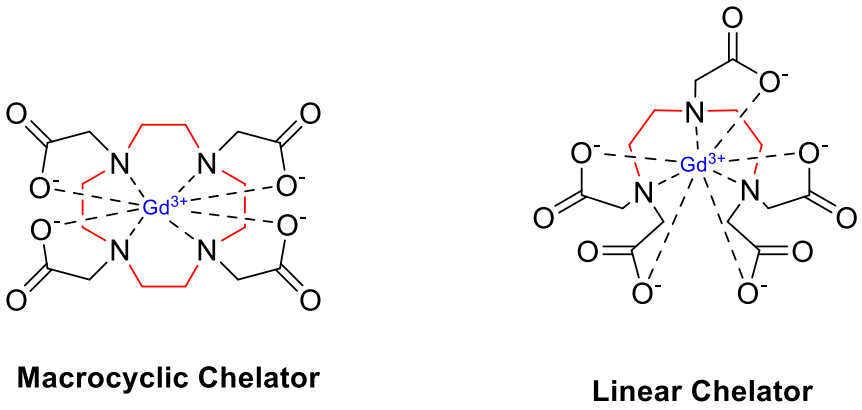

Figure 1.3 A chemical structure comparison between linear and macrocyclic Gd-based contrast agents. Structures of gadoterate (macrocyclic chelator) and gadopentetate (linear chelator). Gd^{3+} ion is shown in blue, while the portion of the molecule that surrounds the ion is shown in red.

1.1.2. IV-OCT

IV-OCT is an optical imaging modality used for imaging the interior of veins and arteries. IV-OCT has been growing in its clinical usage given its superior resolution to its predecessor technology, intravascular ultrasound (IVUS).[28] IV-OCT uses interferometry from a rotating, broadband, near-infrared II (NIR-II, spectral range 800 nm – 1400 nm) light source of central wavelength 1350 nm.[29] This rotating light source is attached to an imaging catheter with a NIR-II detector and is advanced through the vasculature towards the heart. The NIR-II light will backscatter off tissue and red blood cells creating a speckled, contrast image based on the distance the backscattered light has travelled in comparison to an internal reference mirror within the imaging system.[30] Prior to imaging, blood is flushed using saline or iodinated agents to avoid imaging artifacts generated by the heme in whole blood and to ensure the only backscatter signal acquired is from the surround vascular tissue.[31] The signal acquisition during catheter pullback generates both two-dimensional (2D) and three-dimensional (3D) images of the vasculature (Figure 1.4).

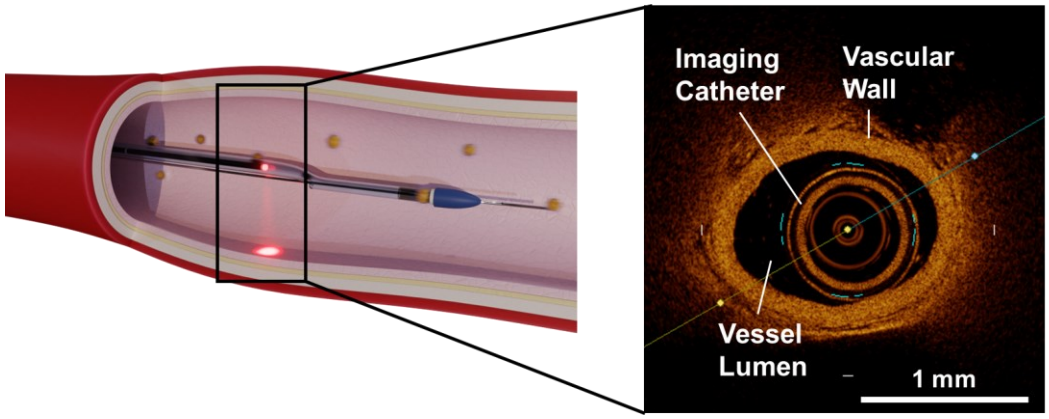

Figure 1.4 Schematic of the IV-OCT imaging catheter within vasculature and the resulting image from the scan. The left panel shows an illustration of an artery that has been catheterized with an IV-OCT catheter, showing the NIR-II light source as the red laser interacting with the arterial wall. The right panel shows the resulting IV-OCT image with labelled components.

In addition to identifying changes in vasculature diameter, IV-OCT is excellent at identifying structural abnormalities within the vasculature. This includes atherosclerotic plaques, fibrosis, thromboses, and stent dysfunctions.[32] All of these are due to how these compositionally different tissues and structures will differentially backscatter the IV-OCT light source compared to regular, healthy tissue. However, IV-OCT is limited to identifying anatomical changes and hallmarks, limiting its usage to later stage disease where medical intervention is less effective. IV-OCT also does not currently have any associated contrast agent, aside from the flush solution that is required for adequate image quality.[33] While this does not provide a contrast component, it is a necessary agent for providing quality imaging data and is delivered through a port built into the IV-OCT catheter, making application of potential future contrast agents simplified.

1.1.3. MPI

MPI is a new imaging modality, first conceived of in 2001, with the first system being constructed in 2005. MPI applies a gradient magnetic field over a region of interest (ROI) to saturate nearby SPIONs.[34] A field free region, where net magnetization is effectively zero, is then raster scanned over the ROI and detects the signals produce by the magnetically saturated SPIONs as they undergo magnetic relaxation.[35] Due to the gradient strength magnetic field applied to the SPIONs, their relaxation within the field free region happens nonlinearly and generates a unique signal. This makes the MPI signal almost entirely specific, as there are no inherent superparamagnetic species within the human body (Figure 1.5). MPI is often coupled to MRI or CT to provide an anatomical image onto which the MPI signal can be overlaid.

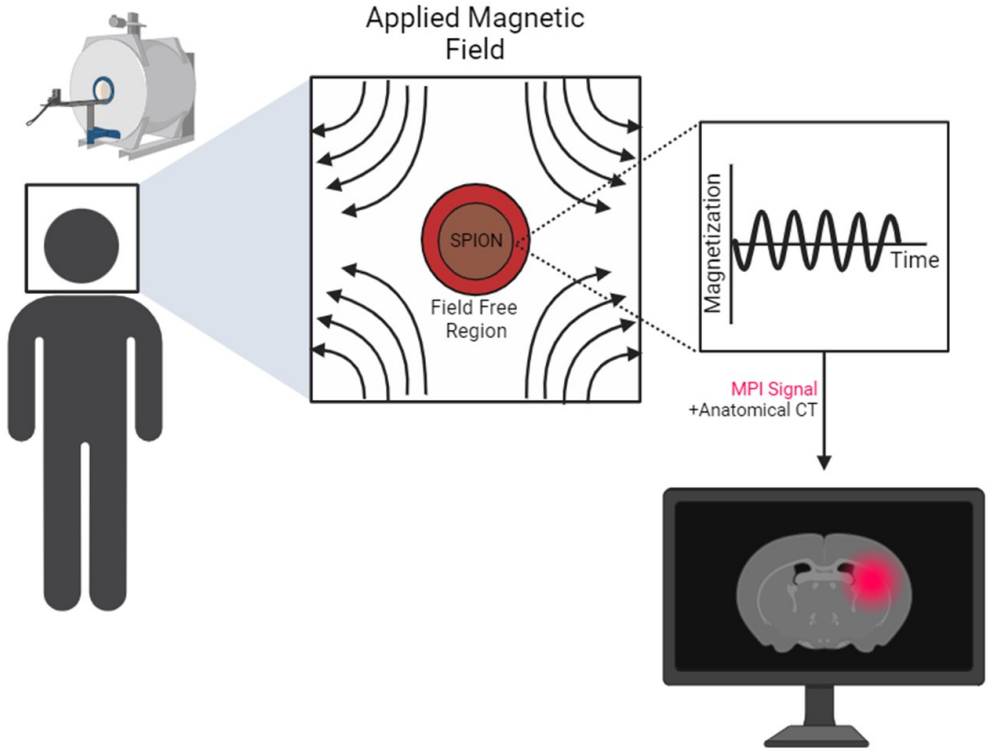

Figure 1.5 Schematic of MPI scan acquisition and the resulting image. An illustration of how SPIONs injected into a patient will be scanned, produce signal, and ultimately produce an image using MPI.

While MPI has yet to achieve clinical translation, the first commercial MPI scanners have become available from Bruker and Magnetic Insight. There has been a significant amount of research into potential uses for clinical MPI, with the most obvious and effective indications being for real-time cardiac imaging, cancer, cell tracking, and functional brain imaging.[36] Since MPI is a nanoparticle (NP) based modality, it can achieve excellent signal in tumors due to the enhanced permeability and retention effect that occurs between circulating NPs and aberrant tumor vasculature.[37]

One of the current limitations of MPI is the lack of surface chemistry diversity of SPIONs used for contrast. Almost all the commercially available SPIONs are stabilized using anionic functional groups at the NP surface. Anionic surface coatings allow for high aqueous dispersibility[38] but preclude high levels of intracellular uptake and can be cytotoxic.[39] This significantly hinders the practicality of what could be the most effective use of MPI: cell labelling and tracking for cell therapies.

1.2. Molecular Imaging

Molecular imaging (MI) is a field of medical imaging that gained traction in the mid-1990s and was pioneered by the numerous works of Dr. Sanjiv Gambhir. MI is the intersection of molecular biology and diagnostic medical imaging. The core focus of medical imaging is the use of chemical tools to interact or probe different biomarkers or cellular processes, allowing both structural and functional imaging of disease markers or aberrant processes.[40,41] MI is inherently dependent on chemical contrast agents and probes to provide molecular information about disease, making probe development a challenging, but critical part of the field.[42]

Disease biomarkers are often present very early into the onset of disease making MI an excellent diagnostic imaging tool for identifying disease prior to the occurrence of macroscopic

anatomical changes have occurred. MI can image specific dysfunctional cellular processes with high spatial resolution, sensitivity, and specificity.[43] This differentiates MI from the traditional imaging modalities discussed in Chapter 1.1. Though some of these modalities may use or require contrast agents, all are broadly focused on identifying macroscopic disease hallmarks like tumors or atherosclerotic plaques that only develop in the later stages of disease.

The clinical example of the diagnostic power of MI is the PET-CT contrast agent [^{18}F]-2-deoxy-2-fluoroglucose (FDG, Figure 1.6). Like dietary-derived D-glucose, the intracellular transport of FDG is facilitated primarily by GLUT1 and GLUT3 and is phosphorylated at the 6' position to prevent cellular export.[44] The radiofluorination of the 2' hydroxyl inhibits further glycolytic or pentose-phosphate pathway shuttling by preventing enzymatic activity with glucose-6-phosphate isomerase,[45] while retaining intracellular transport. The inability to undergo further metabolism, high cellular expression of surface GLUT transporters, and aberrant regulation of hexokinase in cancer cells allows FDG to be highly concentrated by intracellular trapping.[46] This generates a strong, sustained FDG signal during PET-CT that is highly specific to cancerous cells. FDG struggles with identifying diseases in the brain and heart due to the high level of glucose utilization in the healthy cells of these organs.[47,48] Arguably, FDG remains the only MI chemical tool with significant clinical use, with over 2 million scans performed yearly in North America.[49] While MI tools within other imaging modalities remain a very popular area of research, few of these tools have even been evaluated for first-in-human studies, let alone full clinical translation.

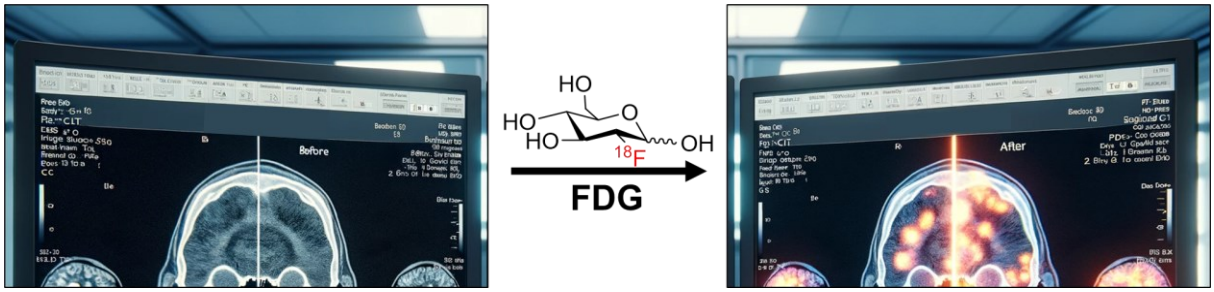

Figure 1.6 Schematic a PET-CT scan before and after [^{18}F]-2-deoxy-2-fluoroglucose (FDG) contrast enhancement. An illustration of a PET-CT scan before (left) and after (right) injection of FDG. The tracer has high uptake in the aberrant metabolic activity of cancer cells that is not observed prior to contrast.

1.2.1 MRI Molecular Imaging

Neither contrast nor non-contrast MRI provide MI indications in its current clinical usage. The high (>1 mm) spatial resolution and ubiquity of use associated with MRI has led to a significant amount of research into providing a MI component for MRI.[50] One of the earliest examples was the technique magnetic resonance spectroscopic imaging (MRSI). In MRSI, the MRI is tuned to proton(s) of a metabolically active molecule (i.e. anomeric proton of D-glucose or the α protons of some amino acids) rather than those of water.[51] MRSI acquires NMR spectra over an ROI, often guided by MRI. The intensity of known metabolite peaks of interest is then used to create an intensity map over the anatomical MRI image.[52] An example of the potential diagnostic power of MRSI was demonstrated in work by Horská *et al*. in 2010.[53] The authors were able to use MRSI to characterize several brain diseases by both appearance with contrast MRI and resulting metabolite intensities. Specifically, they were able to differentiate anatomically similar astrocytoma and glioblastoma multiforme tumors based on the acquired metabolite profile in comparison to healthy brain tissue; an overall reduction in N-acetyl aspartate in both tumors compared to healthy tissue, but differentiation of astrocytoma versus

glioblastoma multiforme based on the increase in myoinositol that occurs in astrocytoma and the very elevated lactate peak in glioblastoma multiforme.

Unfortunately, MRSI is hindered by technical challenges, such as poor sensitivity in detecting low abundance molecules (<5 μM) and occlusion of proton-signals-of-interest by high water background in the spectra or nearby molecules with protons of a similar chemical shift.[54] Deuterium metabolic imaging (DMI) is identical in principle to MRSI but applies a radiofrequency pulse at the Larmor frequency of deuterium (~1/5th the frequency of a proton), allowing the spectroscopic detection of ^{2}H-labelled compounds.[55] The low natural abundance of deuterium (~0.016%) creates significantly less background proton interference from water and other unlabeled molecules in comparison to MRSI.[56] One of the most notable DMI demonstrations was reported in 2018 by de Feyter *et al*., where [6,6'-$^{2}H_2$]-glucose or [$^{2}H_3$]-acetate was infused in both rat and human subjects with glioblastoma to determine uptake of the labelled probes, as well as identification of their downstream metabolic products.[57] de Feyter and coworkers were able to detect glioblastomas sensitively and specifically in human patients through the increase in DMI signal of deuterated lactate that was derived from Warburg-type metabolism of [6,6'-$^{2}H_2$]-glucose. The tumor also showed a reduced deuterated glutamine and glutamate produced by [$^{2}H_3$]-acetate metabolism in comparison to healthy tissue, of the resulting (Figure 1.7). Both features are known metabolic hallmarks of glioblastomas.[58] While an excellent demonstration of the potential diagnostic power of DMI, the authors noted that greater than 10% of the labelled probes were exchanged with ^{1}H from the water pool or lost through other metabolic pathways when tested in humans. Other DMI investigations have also focused on Warburg effect related metabolites, specifically on [6,6'-$^{2}H_2$]-glucose or [3,3-$^{2}H_2$]-lactate.[59–61] More recent work by Zhang *et al*. and Hendriks *et al*. utilized a [6,6'-$^{2}H_2$]-fructose probe instead

of glucose to reduce healthy cell uptake, but still experienced de-labeling through downstream metabolism and hydrolysis.[62,63] Other multinuclear MRI methods exist with similar degrees of limited success, such as ^{13}C MRI and fluorine-MRI.[64,65]

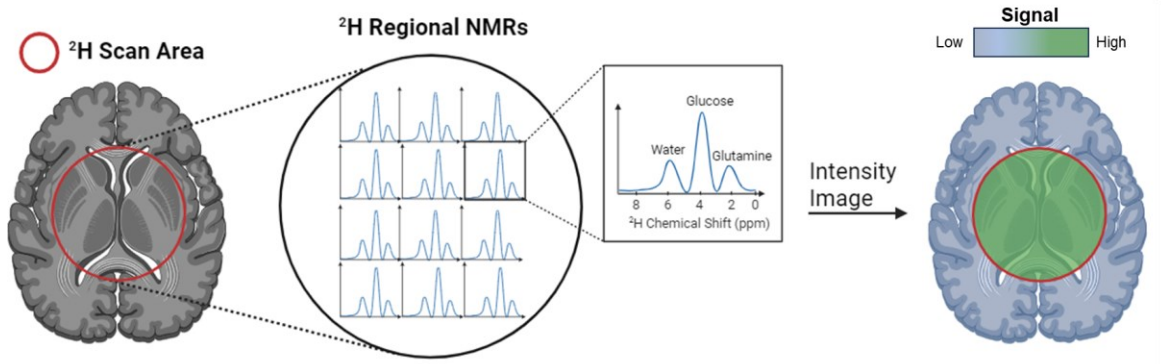

Figure 1.7 Schematic of a DMI scan generating 2H NMR over a region of interest and producing an intensity-scaled image. Illustration of a DMI scan showing the ^{2}H probe ROI and resulting ^{2}H NMR spectra within the ROI. A magnification of this spectra shows the relevant peaks of interest, followed by the generation of an intensity map of these labelled metabolites within the ROI.

Functionalized Gd probes for MRI-MI have achieved little success due to the high hydrophilicity of DOTA-coordinated Gd and similar chelators necessary for maintaining coordination of MRI-active metals.[66,67] Several strategies have been employed to overcome this, central to linking the chelated Gd to either a metal- or polymer-based NP.[68,69] Coordinated Gd functionalization of biomimetic molecules such as proteins or lipids has been demonstrated previously.[70,71] Coordinated Gd functionalized antibodies have successfully facilitated MRI-MI, but high concentrations of labelled antibodies are required to achieve significant contrast enhancement, limiting this technique.[72] The use of GdNPs functionalized with targeting moieties has also been evaluated,[73] but these NPs are often cytotoxic and preclude their potential clinical use.[74]

Alternatives to these NMR-based and Gd-based approaches to MRI-MI have included the use of other paramagnetic metals, such as manganese (Mn), but suffers from similar issues as Gd-based agents (chelation requirements and potential toxicity from manganosis).[75] SPIONs can also generate MRI contrast but create a "negative" signal on MRI (darkening) that can be difficult to differentiate from natural signal variability within the body observed by MRI .[76] A growing class of molecules with MRI-MI potential are organic radical contrast agents (ORCAs). These use primarily outer-sphere effects between the ORCA radical electron and surrounding water to create MRI contrast, but without the need for chelators or metals.[77] ORCAs can be tailored chemically to facilitate cell uptake, but have been highly dependent on nitroxyl radicals, which are quickly quenched by high redox reactive biological environments.[78] The nitroxyl radical has a much lower relaxivity than Gd, creating much lower contrast enhancement in equivalent doses in MRI.[79]

1.2.2 IV-OCT Molecular Imaging

As was introduced in Chapter 1.1.2, IV-OCT remains limited to providing only anatomical information.[80] While there are no clinical or pre-clinical contrast agent for IV-OCT that can provide for MI, there is substantial interest in an IV-OCT technique that could provide molecular information about disease. This would empower IV-OCT to identify hallmarks of vascular disease prior to the major anatomical changes they cause, especially in cardiovascular disease (CVD) and stent restenosis (the growth of tissue around a placed stent causing vessel narrow).[81] This would allow for more meaningful intervention prior to major atherosclerotic plaque formation or stent failure, leading to more positive patient outcomes. Molecular dyes that interact with light in the NIR-II range have been synthesized, but few have been evaluated for biomedical applications.[82,83] An impactful example of NIR-II dye MI was published in 2015 by

Antaris *et al*, who developed a NIR-II fluorescent dye (CH1055, excitation 728 nm, emission 1020 nm) that was coupled to a squamous cell carcinoma-specific affibody.[84] The affibody-coupled NIR-II dye showed highly specific binding to *ex vivo* squamous cell carcinomas in mice with optical imaging. At the time of writing this introduction, however, there have been no examples of NIR-II dyes with or without MI payloads for IV-OCT applications.

Most of the IV-OCT MI efforts have been mediated through plasmonic NP-based platforms. Plasmonic NPs are made of metal or metal-like materials with negative real permittivity, most commonly Au, Ag, Pt, Pd, Cu, and Ti.[85] Excitation by electromagnetic waves (in these specific cases, an incident light source of appropriate wavelength), causes displacement of an electron within the metal atom, leaving a positively charged hole. Recombination of the electron-hole pair occurs in the form of oscillation, producing an electron cloud that will further interact with the light source, referred to as localized surface plasmon resonance (LSPR).[86] The frequency of LSPR oscillation will determine the wavelength of light that will interact with the NP, in the form of photon absorption (followed by relaxation through phonon vibrations or photoluminescence) or photon scattering.[87] The LSPR of a NP can be tuned by modifying the shape, size, and/or surface stabilizing molecule (capping agent), making these materials ideal for purpose-engineered optical probes.[88] In IV-OCT, these NPs would need to be tuned to interact with the IV-OCT light source to provide contrast enhancement (Figure 1.8).

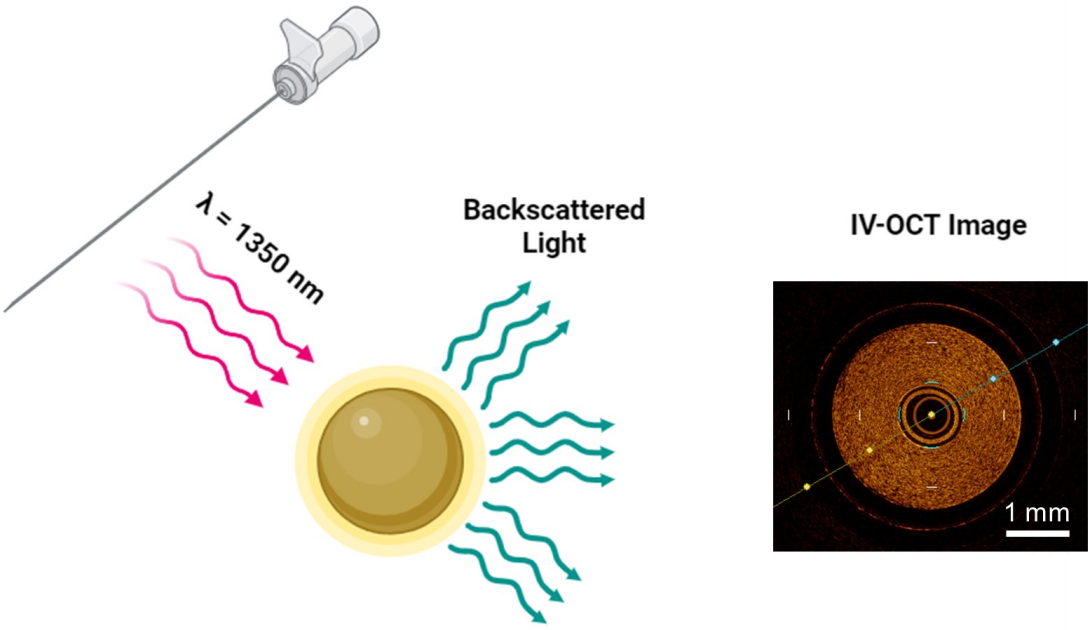

Figure 1.8 Schematic of a NIR-II tuned nanoparticle backscattering IV-OCT incident light and producing IV-OCT signal enhancement. Illustration of IV-OCT NIR-II light interacting with a nanoparticle and the resulting backscattered photons, generating an IV-OCT contrast enhanced image.

The IV-OCT MI literature is primarily synthesis and evaluation of NPs that are composed of bioactive metals like Cu and Ag.[89,90] These metal NPs are chosen as they can easily reach LSPRs >1000 nm with common synthetic techniques but are suboptimal for biomedical usage as they are known to be commonly cytotoxic. While there have been several reported synthesized NPs that have been shown to facilitate IV-OCT contrast through scattering or absorption of the IV-OCT light source, none have facilitated MI or have been evaluated *in vivo*.[91] Gold nanoparticles (AuNPs) have well-reported biocompatibility, but discreet, spherical AuNPs cannot reach the NIR-II wavelengths. Other Au non-spherical nanostructures (i.e. rods) can reach these wavelengths but do not clear the body as effectively as their spherical counterparts.[92] While many of these NPs have shown IV-OCT contrast, few have shown the key MI property of targeting. Work by Muñoz-Ortiz *et al.* in 2021 used Au nanoshells functionalized with anti-

intracellular adhesion molecule 1 for *ex vivo* IV-OCT of infarcted hearts dissected from Sprague-Dawley rats.[93] These nanoshells did show binding to intracellular adhesion molecule 1 that was in high expression following infarct and showed greater total signal. However, this was not a true *in vivo* application, and it was difficult to discern between healthy and infarcted signal even with contrast binding. An optimal approach to IV-OCT MI would be through a combination of NP engineering and surface functionalization for targeting moieties for molecules of interest that generates a clear signal that can be differentiated from the surrounding IV-OCT healthy tissue signal.

1.2.3 MPI Molecular Imaging

MPI relies on the uptake or binding of SPIONs by cells either *in vivo* or *ex vivo*, agnostic of metabolic processes or cell type given the use of primarily anionic surface coatings. As was discussed in Chapter 1.2.3, many of the current SPIONs utilize carboxylic acid-displaying surface coatings to achieve high levels of aqueous dispersibility and interact with the positively charged cell surface, including the previously Food and Drug Administration (FDA)-approved SPION ferumoxytol coated with carboxymethyl dextran.[94] These anionic SPION have been used as blood pool tracers for imaging similar indications as GBCAs in MRI: vascular abnormalities in tumors, angiography, and brain perfusion.[95]

In addition to these indications, the most promising use of MPI is for cellular tracking (Figure 1.9), which involves the *ex vivo* labelling of cells with SPIONs prior to its administration into the body for therapeutic use.[96] Cell tracking and cell therapies will be discussed in greater detail in Chapter 1.5, but considering the differences in both receptor and transporter types and expression within different therapeutically relevant cell types,[97] MPIs reliance on anionic surface

functionalized SPIONs will limit its potential. Not all cells will facilitate intracellular uptake through the same mechanisms or in the same magnitude.

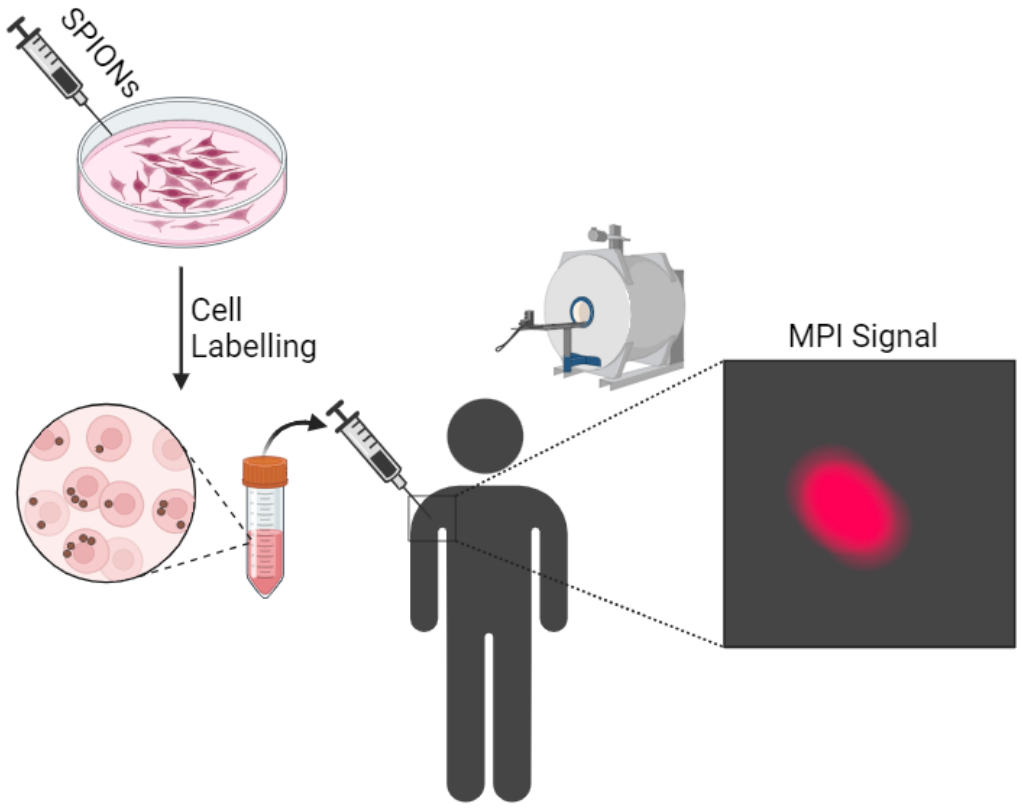

Figure 1.9 Schematic of the MPI cell labelling workflow and the resulting MPI signal of SPION labelled cells. Workflow of clinical MPI beginning from cell labelling with SPIONs, administration to the patient, and subsequent MPI scan to follow the labelled cells.

Despite a lack of variety of surface chemistry available for SPIONs applied to MPI, the majority of the current MPI literature is focused on use indications and optimization in NP syntheses to produce SPIONs that improve MPI contrast.[34,98,99] Recently published work by Gao *et al*. in 2023 is one of the first demonstrations of MI with MPI.[100] Gao and coworkers functionalized a pseudo-SPION with maleimide to facilitate conjugation to the thiol of a cysteine residue for their vascular cell adhesion molecule 1 (VCAM-1) targeting peptide (sequence

VHPKQHRGGSK(Cy7)GC)). VCAM-1 is a known marker with increased expression in epithelial cells during vascular inflammation.[101] In an *in vivo* mouse model, Gao and coworkers used *intravenous* injection of lipopolysaccharide (LPS) to stimulate systemic inflammation and upregulate VCAM-1 expression in the lungs. The authors were able to identify the binding of these VCAM-1 targeting SPIONs to VCAM-1 within the lungs, with a direct correlation between the LPS dosage and the degree of MPI signal facilitated by binding. This work is a strong example of the clinical power of MPI with an MI component.

1.3. Diagnostic Imaging in Kidney Disease

CKD and AKI are current global health burdens that continue to grow in number yearly, with almost 1 billion people worldwide affected by CKD[102] and nearly 1 in 400 North Americans yearly will be on dialysis, with 3% eventually requiring a kidney transplant. The clinical gold standard for identifying kidney dysfunction is through a combination of measurement of proteinuria (albumin-to-creatinine (ACR) > 30 mg/g for >3 months) and/or estimated glomerular filtration rate (eGFR) (< 60 ml/min/1.73 m^2 for >3 months).[103] These values are derived from patient population data pools and do not account for alternative methods of endogenous creatinine production, leading to eGFR variations of up to 30% from the true value.[104] eGFR provides no spatial or anatomical information about kidney disease, which becomes critical in cases of adaptive glomerular hyperfiltration where the true eGFR value will be masked.[105] Additionally, clear cell renal carcinoma, the seventh most common cancer diagnosis in males,[106] is difficult to identify early with current clinical imaging approaches.[107]

1.3.1. Imaging Approaches to Kidney Disease

Dynamic clinical imaging techniques exist that evaluate the rate of clearance of a contrast agent through the kidney as a measurement of kidney function. Clinically used single photon

emission computed tomography (SPECT) agents ^{99m}Tc-diethylenetriaminepentaacetic acid (DTPA) and ^{99m}Tc-mercaptoazyltriglycerine (MAG3) are cleared by renal tubule secretions and can evaluate renal plasma flow.[108,109] Clearance of these tracers are corrected for body surface area and correlate well with creatinine based GFR measurements, but suffer from inaccuracies associated with background subtraction required, or measurement of percent injected dose, as well as renal depth estimation derived from population nomograms from patient height and weight to correct for signal attenuation.[110] More importantly, neither of these techniques provide high-level spatial resolution, even with the CT component.

Dynamic contrast enhanced (DCE) MRI has been a particularly interesting tool for evaluating kidney function. It provides high spatial resolution and can utilize GBCAs for the DCE component to measure renal function by GBCA clearance.[111] However, the majority of the kidney dysfunction population that would benefit by DCE-MRI are precluded from contrast MRI with GBCAs, including patients with an eGFR < 30 mL/min/1.73 m^2, who are on dialysis, or have had a kidney transplant.[112,113] This is due to the potential for GBCAs to lead to Gd deposition, especially in kidneys with reduced filtration function, leading to NSF. In fact, recent work by Le Fur *et al.* in 2023 showed that Gd concentrations of up to 100 mM can remain invisible when deposited within the kidney due to differences in intra-compartmental water exchange.[114] This study highlighted the clinical need for alternatives to metal-based MRI contrast agents, given the level of uncertainty associated with potential Gd deposition from GBCAs.

1.3.2. ORCAs: a Potential Solution for Kidney Disease MI with MRI

ORCAs are one potential solution to providing a Gd-free MRI contrast agent. As discussed in Chapter 1.2.1, these compounds rely on a radical electron, often through the nitroxyl

radical to produce MRI contrast, with the major drawback being the susceptibility of the nitroxyl group to biological redox chemistry that would quench this contrast, such as the reaction between TEMPO and ascorbic acid (Vitamin C, Figure 1.10).[115] One of the earliest and most influential works on ORCA DCE-MRI was done by Rajca *et al.*, where authors used a nitroxyl radical flanked by cyclohexanes to reduce redox interactions. This ORCA was coupled to a polyethylene glycol (PEG) polymer to produce water-soluble dendrimers with a nitroxyl-based ORCA payload.[116] This agent was injected *intravenously* into healthy mice and monitored by DCE-MRI. The authors saw high levels of contrast generated within the kidneys following injection, which slowly returned to baseline over 90 min and began to accumulate in the bladder. No other contrast enhancement was observed in other tissues, confirming that this ORCA was localized to the urinary tract. More recent work by Nguyen *et al*. in 2020 utilized a similar nitroxyl-based ORCA within a brush-arm star polymer nanostructure and were able to show preferential tumor uptake of the construct, one of the first examples of MRI-MI with an ORCA.[117]

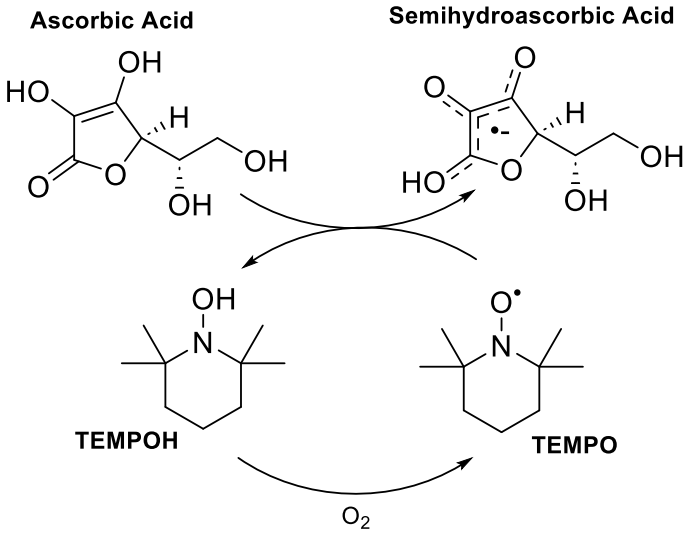

Figure 1.10 Redox reaction between TEMPO and ascorbic acid that leads to in vivo loss of the nitroxyl radical. The catalytic cycle of TEMPO being reduced by endogenous ascorbic acid to TEMPOH, leading to a loss of the radical electron.

ORCAs are attractive agents for MRI-MI given their high degree of chemical functionalization; the contrast generating portion of the ORCA comprises significantly less mass of the compound than the coordinated Gd groups of GBCAs. This high degree of chemical versatility, as well as avoiding the issues of toxicity and reduction of intracellular uptake of GBCAs, ORCAs can provide a chemically organic approach to MRI-MI. This is a potential solution to an MRI-MI method for determining early kidney dysfunction through both DCE-MRI methods and through binding to known markers of kidney disease prior to major changes in eGFR and kidney function. As well, this could prove to be a reliable MRI-MI method for identifying clear cell renal carcinoma prior to significant tumor growth, through designing targeting moieties for molecular markers of this cancer to an ORCA. Finally, new, non-nitroxyl based radical groups need to be evaluated to overcome the issue of ORCA radical loss through biological redox chemistry, beyond the point of adding bulkier chemical groups to flank the nitroxyl radical.

1.4. Diagnostic Imaging in Cardiovascular Disease

CVD remains the highest cause of death worldwide with nearly 20 million deaths globally per year.[118] CVD broadly classifies several diseases involving the heart and/or blood vessels, including heart failure, arrythmia, and valvular disease. The most abundant of all, however, is coronary artery disease (CAD), classified as the reduction in blood flow to the heart. This is caused by the formation and growth of atherosclerotic plaques within the arteries in the heart, formed by the process of atherosclerosis.[119] Atherosclerosis starts with arterial inflammation of epithelial cells which can be caused by several factors, but ultimately triggers the migration and formation of macrophages to the inflammation site.[120] As these macrophages consume low density lipoproteins, they form into foam cells and streak the walls of the arteries.

These streaks progress into atherosclerotic plaques formed of lipids, cellular debris, and calcium, all covered by a fibrous cap of smooth muscle cells. Inflammation or weakening of the fibrous cap, referred to as an unstable plaque, can rupture and lead to thrombosis, arterial occlusion, and ultimately heart attack.[121]

1.4.1. Imaging Approaches to CAD

Primary diagnosis of CAD relies on both imaging (contrast CT) and non-imaging (electrocardiogram and biomarker blood testing) components.[122] However, neither CT nor MRI can stratify atherosclerotic plaque stability as reliably as IV-OCT. Given the high calcium and lipid components, the composition of atherosclerotic plaques are easy to differentiate from healthy epithelial tissue with IV-OCT.[123] Also given the location of the imaging catheter within the artery and proximity to these atherosclerotic plaques, IV-OCT has been primarily helpful for assessing fibrous cap thickness to stratify plaque vulnerability.[124] However, cap thickness is not the only indicator of plaque stability. Plaque compositional heterogeneity, inflammation, and subcellular processes play a significant role in cap stability, and even a thick fibrous cap can still rupture.[125,126]

IV-OCT can measure intra-arterial diameters and is an excellent tool for identifying and assisting in stent placement within the artery. IV-OCT is also used for stenting follow-up procedures to check for stent failure, defects, or a pathology known as in-stent restenosis, which involves the growth of new epithelial tissue occluding the stent and causing re-narrowing of the artery.[127] In-stent restenosis is difficult to identify prior to major tissue growth over the stent, especially in cases of drug-eluting stents, where this cellular growth can happen very rapidly.[128]

1.4.2. Potential Solutions for IV-OCT MI

Since IV-OCT can only provide anatomical information and does not have any contrast agent, let alone one that can provide MI, it leaves a major diagnostic need in identifying vulnerable plaques and in-stent restenosis. An MI contrast agent that could interact with the IV-OCT light source to indicate a binding event, while also being able to bind to cellular markers involved in arterial inflammation, vulnerable plaque formation, or in-stent restenosis would provide valuable diagnostic insight into CAD (Figure 1.11). As was discussed in Chapter 1.2.2, most of the IV-OCT literature has been centered on developing nanomaterials that can generate IV-OCT contrast in *ex vivo* settings, rather than showing contrast enhancement in regions facilitated by biomolecular binding. One of the issues, other than contrast agent availability, that hinders IV-OCT MI is that there remains to be a consensus on biomarkers that are indicative of early in-stent restenosis or plaque vulnerability.[129] Efforts towards an IV-OCT MI agent would allow IV-OCT for diagnostic use in 7 million additional patients to those already being scanned, with indications in stratifying CAD and in-stent restenosis earlier and more confidently.[130]

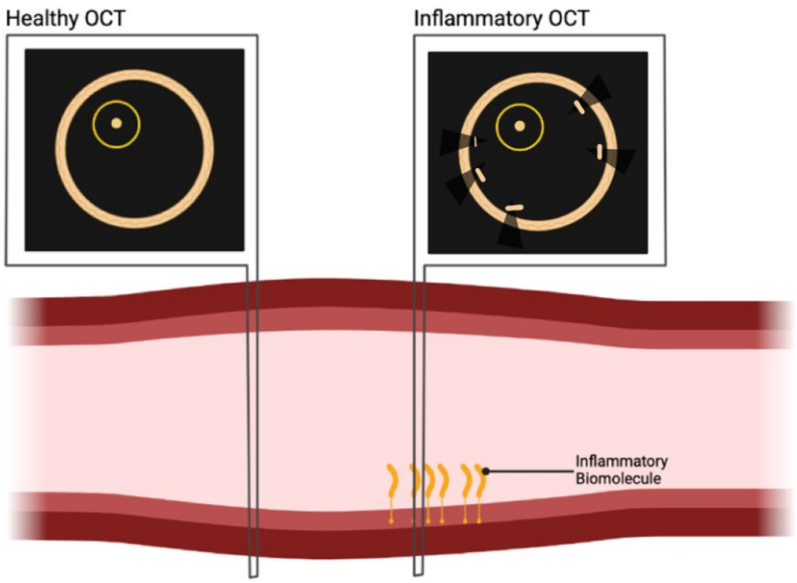

Figure 1.11 Schematic of the IV-OCT scan before and after the injection of an inflammation targeting nanoparticle that can backscatter the IV-OCT NIR-II light source. Illustration of an artery with and without biomarkers of inflammation, and the resulting IV-OCT scan using an inflammatory-targeting IV-OCT NP that scatters the NIR-II light source once bound to the target.

1.5. Diagnostic Imaging for Cell Tracking in Cell Therapies

Cell therapies have been a growing area in both research interest and clinical development due to its potential to treat many currently untreatable diseases and complex injuries.[131] There are over 400 active cell therapy clinical trials, but less than 10 FDA approved products.[132,133] Cell therapy involves the administration of autologous or xenologous cells into a patient to achieve a therapeutic outcome. Some of the most common and powerful examples include the use of immune cells to target cancers, or stem cells (hematopoietic or mesenchymal most commonly) to stimulate regeneration and growth.[134–136] After administration, these cells are expected to travel to their therapeutic destination within the body and deliver their medicine payload. However, given the *in vivo* environment these cells will encounter during their journey

from administration to therapeutic site, several factors will contribute to an insignificant therapeutic effect; most commonly large-scale cell death or failure to reach the destination.[137,138]

1.5.1. Imaging Approaches to Cellular Therapies

In response to the difficulties in monitoring cells administered for cell therapies, there has been a significant amount of research in the field of cell tracking. As was introduced in Chapter 1.2.3, cell tracking involves the often *ex vivo* but possible *in vivo* labelling of cells with agents that can be identified using medical imaging. Cell tracking has the potential to monitor both where cells have travelled, as well as their viability status.[139] This information is critical for monitoring cell therapies to ensure treatment efficiency and efficacy.

PET-CT was one of the first imaging modalities to be used for cell tracking, given the excellent cellular uptake afforded to FDG as was discussed in Chapter 1.2, allowing efficient labelling of many cells. However, the ~2 h half-life associated with the ^{18}F labelled glucose precludes this technique from monitoring cells for long periods of time.[140] MRI was another method evaluated for cellular tracking. As was discussed in chapter 1.2.1, the labelling efficacy in cells using chelated agents is often poor, but paramagnetic NPs have seen some success in cell labelling. A successful example of this was demonstrated by Faucher and coworkers with dual-labelled Gd_2O_3-rhodamine NPs coated with PEG to prevent Gd deposition, and which could label cells with up to 3 pg Gd/cell.[141] Labelled F98 (glioblastoma multiforme) cell injections into Nod-Scid mice were able to be followed by MRI for up to 21 days. However, while no toxicity was observed in this study, long term retention of Gd ions poses a risk of toxicity. Similar MRI imaging with SPION labelling is possible, but as was discussed in Chapter 1.2.1, creates a negative contrast on MRI that is difficult to identify. MPI can produce bright, “positive” contrast

with SPION-labelled cells. In addition to this, the high spatial resolution and sensitivity for only labelled cells makes MPI an ideal technique for cell tracking.

1.5.2. Potential MI Solutions for Cell Tracking

A thorough evaluation of new SPION surface chemistry is critical for furthering the use of MPI for cell tracking, rather than continuing to rely on the anionic, often carboxylic acid-coated particles that are primarily used now. This type of surface chemistry does not allow for the optimal labelling of all cell types equally and will primarily rely on endocytosis for uptake.[142] Surface chemistry is a critical parameter for optimal cell uptake and preventing rapid SPION degradation.[143] Zwitterionic molecules are an attractive potential surface molecule functionalizing SPIONs, as they possess surface charges to optimize dispersibility, but are overall net neutral and highly biomimetic. Endogenous biomolecules that are zwitterionic include many amino acids, proteins, and lipids (Figure 1.12).[144] These molecules have excellent antifouling properties[145] and have alternate modes of intracellular transport, given their usage in cellular metabolism.[146] There have been some studies using zwitterionic SPIONs for MRI based cell tracking, but this has not been translated to MPI.[147,148] A greater research focus on SPION surface chemistry instead of SPION synthesis will be a critical factor to bringing MPI towards becoming a mainstay clinical imaging modality.

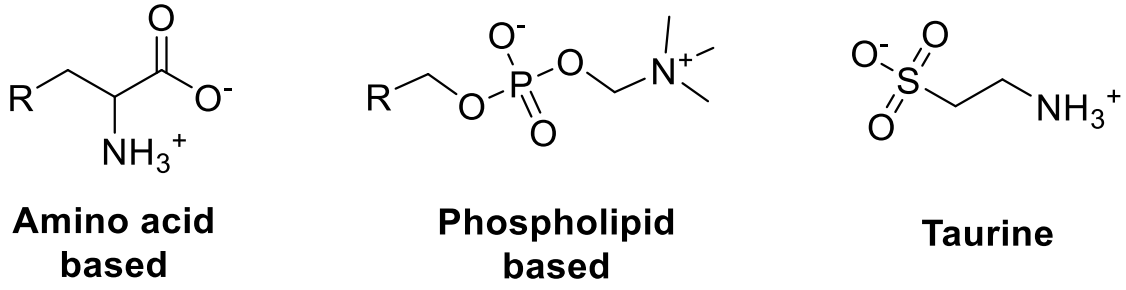

Figure 1.12 Examples of endogenous classes of zwitterionic molecules. Examples of different classes of zwitterionic molecules that are endogenous to human cells.

1.6. Thesis Overview and Goals

The focus of this thesis will be on designing, synthesizing, characterizing, and evaluating new MI probes as a method of addressing some of the shortcomings within these three discussed imaging modalities: MRI, IV-OCT, and MPI. For MRI imaging of kidney, this thesis will discuss the synthesis, characterization, and evaluation of an organic molecule class known as verdazyls as a new approach to ORCA that can be used to both spatially and quantitatively monitor kidney function in mice with induced kidney disease (Chapter 2). For IV-OCT, this thesis will discuss a novel method for producing controlled assemblies of AuNPs into Au superstructures which can reach LSPR interactivity in the NIR-II. This will also look at the surface functionalization of these superstructures with new chemical ligands for targeting inflammatory molecules that are upregulated in heart disease, and how the binding of these targeted superstructures can generate MI with IV-OCT (Chapter 3). Finally, this thesis will look at the direct comparison of MPI NPs that have been surface functionalized with anionic groups, as well as zwitterionic groups with permanent or pKa-based charges, and their uptake within different cell types, as a new MI approach to cell labelling for cell tracking using MPI (Chapter 4).

These successful new MI tools outlined in this thesis act in most cases as platform technologies for future MI tools to expand upon. All the MI agents in this thesis have been fully characterized and evaluated in both cellular and small animal models and span a wide range of multidisciplinary work. Future work will continue to innovate upon these MI building blocks to find new disease use-cases or indications to expand the field of MI.

1.7. Objectives

The overall goal of this thesis is to synthesize, characterize, and evaluate new MI probes for each of MRI, MPI, and IV-OCT. Specific objectives set out to meet this overall goal were:

1. Identify a new class of ORCA known as verdazyls, characterize its inherent MRI contrast properties, evaluate its biodistribution in animal models following injection, and finally to use it to evaluate kidney function both quantitatively and qualitatively with DCE-MRI mapping (Chapter 2).
2. Create new chemical methods for generating a new type of Au nanostructure that can generate NIR-II LSPR while maintaining a spherical shape. Then, to test the IV-OCT contrast generating properties of this Au structure, and chemically modify the surface with targeting groups to inflammatory markers without sacrificing its IV-OCT contrast properties. Finally, to demonstrate the ability to bind inflammatory markers and generate contrast *in vivo* to stratify arterial inflammation in an animal model. The overall objective is to create a new, spherical IV-OCT MI contrast agent from Au and demonstrate *in vivo* IV-OCT MI (Chapter 3).
3. Functionalize anionic SPIONs with different zwitterionic functional group that bear hard or soft zwitterionic charges. Then characterize how these surface chemistries change the physicochemical and magnetic properties of these SPIONs, including their compatibility with cell labelling across cell types and *in vitro* and *in vivo* MPI (Chapter 4).

1.8. References

(1) Bercovich, E.; Javitt, M. C. Medical Imaging: From Roentgen to the Digital Revolution, and Beyond. *Rambam Maimonides Med J* **2018**, *9* (4), e0034. https://doi.org/10.5041/RMMJ.10355.

(2) McMillan, N. C. Developments in Imaging an Historical Review. *http://dx.doi.org/10.1177/003693309904400610* **1999**, *44* (6), 180–185. https://doi.org/10.1177/003693309904400610.

(3) Riesz, P. B.; Riesz, P. B. The Life of Wilhelm Conrad Roentgen. *https://doi.org/10.2214/ajr.165.6.7484601* **2013**, *165* (6), 1533–1537. https://doi.org/10.2214/AJR.165.6.7484601.

(4) Ritter, F.; Boskamp, T.; Homeyer, A.; Laue, H.; Schwier, M.; Link, F.; Peitgen, H. O. Medical Image Analysis. *IEEE Pulse* **2011**, *2* (6), 60–70. https://doi.org/10.1109/MPUL.2011.942929.

(5) Hussain, S.; Mubeen, I.; Ullah, N.; Shah, S. S. U. D.; Khan, B. A.; Zahoor, M.; Ullah, R.; Khan, F. A.; Sultan, M. A. Modern Diagnostic Imaging Technique Applications and Risk Factors in the Medical Field: A Review. *Biomed Res Int* **2022**, *2022*. https://doi.org/10.1155/2022/5164970.

(6) MacRitchie, N.; Frleta-Gilchrist, M.; Sugiyama, A.; Lawton, T.; McInnes, I. B.; Maffia, P. Molecular Imaging of Inflammation - Current and Emerging Technologies for Diagnosis and Treatment. *Pharmacol Ther* **2020**, *211*, 107550. https://doi.org/10.1016/J.PHARMTHERA.2020.107550.

(7) *To X-ray or not to X-ray?* https://www.who.int/news-room/feature-stories/detail/to-x-ray-or-not-to-x-ray- (accessed 2024-01-12).

(8) *PET exam usage rate United States 2020 | Statista*. https://www.statista.com/statistics/962337/pet-examinations-in-united-states-rate-per-one-thousand/ (accessed 2024-01-12).

(9) *MRI units density by country 2019 | Statista*. https://www.statista.com/statistics/282401/density-of-magnetic-resonance-imaging-units-by-country/ (accessed 2024-01-12).

(10) Reviewer, P.; Reviewer, S. The Patient Experience in Medical Imaging: A Qualitative Systematic Review (Protocol). *JBI Libr Syst Rev* **2010**, *8* (Supplement), 1–15. https://doi.org/10.11124/JBISRIR-2010-853.

(11) European Society of Radiology (ESR). Medical Imaging in Personalised Medicine: A White Paper of the Research Committee of the European Society of Radiology (ESR). *Insights Imaging* **2015**, *6* (2), 141. https://doi.org/10.1007/S13244-015-0394-0.

(12) Smith-Bindman, R.; Kwan, M. L.; Marlow, E. C.; Theis, M. K.; Bolch, W.; Cheng, S. Y.; Bowles, E. J. A.; Duncan, J. R.; Greenlee, R. T.; Kushi, L. H.; Pole, J. D.; Rahm, A. K.; Stout, N. K.; Weinmann, S.; Miglioretti, D. L. Trends in Use of Medical Imaging in US Health Care Systems and in Ontario, Canada, 2000-2016. *JAMA* **2019**, *322* (9), 843–856. https://doi.org/10.1001/JAMA.2019.11456.

(13) Lindner, J. R.; Link, J. Molecular Imaging in Drug Discovery and Development. *Circ Cardiovasc Imaging* **2018**, *11* (2). https://doi.org/10.1161/CIRCIMAGING.117.005355.

(14) Wang, Y. X.; Deng, M. Medical Imaging in New Drug Clinical Development. *J Thorac Dis* **2010**, *2* (4), 245. https://doi.org/10.3978/J.ISSN.2072-1439.2010.11.10.

(15) Grover, V. P. B.; Tognarelli, J. M.; Crossey, M. M. E.; Cox, I. J.; Taylor-Robinson, S. D.; McPhail, M. J. W. Magnetic Resonance Imaging: Principles and Techniques: Lessons for

Clinicians. *J Clin Exp Hepatol* **2015**, *5* (3), 246. https://doi.org/10.1016/J.JCEH.2015.08.001.

(16) Berger, A. How Does It Work?: Magnetic Resonance Imaging. *BMJ : British Medical Journal* **2002**, *324* (7328), 35. https://doi.org/10.1136/BMJ.324.7328.35.

(17) Kose, K. Physical and Technical Aspects of Human Magnetic Resonance Imaging: Present Status and 50 Years Historical Review. *Adv Phys X* **2021**, *6* (1). https://doi.org/10.1080/23746149.2021.1885310.

(18) Duren, D. L.; Sherwood, R. J.; Czerwinski, S. A.; Lee, M.; Choh, A. C.; Siervogel, R. M.; Chumlea, W. C. Body Composition Methods: Comparisons and Interpretation. *Journal of diabetes science and technology (Online)* **2008**, *2* (6), 1139. https://doi.org/10.1177/193229680800200623.

(19) Rampton, J. W.; Young, P. M.; Fidler, J. L.; Hartman, R. P.; Herfkens, R. J. Putting the Fat and Water Protons to Work for You: A Demonstration through Clinical Cases of How Fat-Water Separation Techniques Can Benefit Your Body MRI Practice. *American Journal of Roentgenology* **2013**, *201* (6), 1303–1308. https://doi.org/10.2214/AJR.13.10606.

(20) Kawahara, D.; Nagata, Y. T1-Weighted and T2-Weighted MRI Image Synthesis with Convolutional Generative Adversarial Networks. *Reports of Practical Oncology and Radiotherapy* **2021**, *26* (1), 35. https://doi.org/10.5603/RPOR.A2021.0005.

(21) De Leõn-Rodríguez, L. M.; Martins, A. F.; Pinho, M. C.; Rofsky, N. M.; Sherry, A. D. Basic MR Relaxation Mechanisms and Contrast Agent Design. *Journal of Magnetic Resonance Imaging* **2015**, *42* (3), 545–565. https://doi.org/10.1002/JMRI.24787.

(22) Iyad, N.; S.Ahmad, M.; Alkhatib, S. G.; Hjouj, M. Gadolinium Contrast Agents-Challenges and Opportunities of a Multidisciplinary Approach: Literature Review. *Eur J Radiol Open* **2023**, *11*, 100503. https://doi.org/10.1016/J.EJRO.2023.100503.

(23) Kiviniemi, A.; Gardberg, M.; Ek, P.; Frantzén, J.; Bobacka, J.; Minn, H. Gadolinium Retention in Gliomas and Adjacent Normal Brain Tissue: Association with Tumor Contrast Enhancement and Linear/Macrocyclic Agents. *Neuroradiology* **2019**, *61* (5), 535–544. https://doi.org/10.1007/S00234-019-02172-6.

(24) Malikova, H. Nephrogenic Systemic Fibrosis: The End of the Story? *Quant Imaging Med Surg* **2019**, *9* (8), 1470. https://doi.org/10.21037/QIMS.2019.07.11.

(25) Prince, M. R.; Zhang, H. L.; Roditi, G. H.; Leiner, T.; Kucharczyk, W. Risk Factors for NSF: A Literature Review. *Journal of Magnetic Resonance Imaging* **2009**, *30* (6), 1298–1308. https://doi.org/10.1002/JMRI.21973.

(26) Prince, M. R.; Zhang, H. L.; Prowda, J. C.; Grossman, M. E.; Silvers, D. N. Nephrogenic Systemic Fibrosis and Its Impact on Abdominal Imaging. **2009**, *29* (6), 1565–1574. https://doi.org/10.1148/RG.296095517.

(27) Woolen, S. A.; Shankar, P. R.; Gagnier, J. J.; MacEachern, M. P.; Singer, L.; Davenport, M. S. Risk of Nephrogenic Systemic Fibrosis in Patients With Stage 4 or 5 Chronic Kidney Disease Receiving a Group II Gadolinium-Based Contrast Agent: A Systematic Review and Meta-Analysis. *JAMA Intern Med* **2020**, *180* (2), 223–230. https://doi.org/10.1001/JAMAINTERNMED.2019.5284.

(28) Nagaraja, V.; Kalra, A.; Puri, R. When to Use Intravascular Ultrasound or Optical Coherence Tomography during Percutaneous Coronary Intervention? *Cardiovasc Diagn Ther* **2020**, *10* (5), 1429. https://doi.org/10.21037/CDT-20-206.

(29) Zheng, S.; Zheng, S.; Fei, Y.; Fei, Y.; Jian, S. Method for Parametric Imaging of Attenuation by Intravascular Optical Coherence Tomography. *Biomedical Optics Express, Vol. 12, Issue 4, pp. 1882-1904* **2021**, *12* (4), 1882–1904. https://doi.org/10.1364/BOE.420094.

(30) Aumann, S.; Donner, S.; Fischer, J.; Müller, F. Optical Coherence Tomography (OCT): Principle and Technical Realization. *High Resolution Imaging in Microscopy and Ophthalmology* **2019**, 59–85. https://doi.org/10.1007/978-3-030-16638-0_3.

(31) Mancuso, J. J.; Halaney, D. L.; Elahi, S.; Ho, D.; Wang, T.; Ouyang, Y.; Dijkstra, J.; Milner, T. E.; Feldman, M. D. Intravascular Optical Coherence Tomography Light Scattering Artifacts: Merry-Go-Rounding, Blooming, and Ghost Struts. **2014**, *19* (12), 126017. https://doi.org/10.1117/1.JBO.19.12.126017.

(32) Lee, J.; Prabhu, D.; Kolluru, C.; Gharaibeh, Y.; Zimin, V. N.; Dallan, L. A. P.; Bezerra, H. G.; Wilson, D. L. Fully Automated Plaque Characterization in Intravascular OCT Images Using Hybrid Convolutional and Lumen Morphology Features. *Scientific Reports 2020 10:1* **2020**, *10* (1), 1–13. https://doi.org/10.1038/s41598-020-59315-6.

(33) Kang, D. O.; Nam, H. S.; Kim, S.; Yoo, H.; Kim, J. W. Feasibility and Safety of Non-Contrast Optical Coherence Tomography Imaging Using Hydroxyethyl Starch in Coronary Arteries. *Scientific Reports 2023 13:1* **2023**, *13* (1), 1–12. https://doi.org/10.1038/s41598-023-40363-7.

(34) Billings, C.; Langley, M.; Warrington, G.; Mashali, F.; Johnson, J. A. Magnetic Particle Imaging: Current and Future Applications, Magnetic Nanoparticle Synthesis Methods and Safety Measures. *International Journal of Molecular Sciences 2021, Vol. 22, Page 7651* **2021**, *22* (14), 7651. https://doi.org/10.3390/IJMS22147651.

(35) Conolly, S.; Krishnan, K.; Grant, G.; Cheng, M. W.; Bliss, T.; Du, F.; Rao, J.; Song, G.; Pisani, L.; Doyle, T.; Wu, L. C.; Zhang, Y.; Steinberg, G.; Qu, H.; Huang, S.; Wu, X. L. C.; Zhang, X. Y.; Steinberg, X. G.; Qu, X. H.; Huang, X. S.; Cheng, X. M.; Bliss, X. T.; Du, X. F.; Rao, X. J.; Song, X. G.; Pisani, X. L.; Doyle, X. T.; Conolly, X. S.; Krishnan, X. K.; Grant, X. G.; Wintermark, X. M. A Review of Magnetic Particle Imaging and Perspectives on Neuroimaging. *American Journal of Neuroradiology* **2019**, *40* (2), 206–212. https://doi.org/10.3174/AJNR.A5896.

(36) Han, X.; Li, Y.; Liu, W.; Chen, X.; Song, Z.; Wang, X.; Deng, Y.; Tang, X.; Jiang, Z. The Applications of Magnetic Particle Imaging: From Cell to Body. *Diagnostics* **2020**, *10* (10). https://doi.org/10.3390/DIAGNOSTICS10100800.

(37) Setyawati, M. I.; Wang, Q.; Ni, N.; Tee, J. K.; Ariga, K.; Ke, P. C.; Ho, H. K.; Wang, Y.; Leong, D. T. Engineering Tumoral Vascular Leakiness with Gold Nanoparticles. *Nature Communications 2023 14:1* **2023**, *14* (1), 1–15. https://doi.org/10.1038/s41467-023-40015-4.

(38) Hur, J. U.; Choi, J. S.; Choi, S. C.; An, G. S. Highly Dispersible Fe3O4 Nanoparticles via Anionic Surface Modification. *Journal of the Korean Ceramic Society* **2020**, *57* (1), 80–84. https://doi.org/10.1007/S43207-019-00001-3.

(39) Augustine, R.; Hasan, A.; Primavera, R.; Wilson, R. J.; Thakor, A. S.; Kevadiya, B. D. Cellular Uptake and Retention of Nanoparticles: Insights on Particle Properties and Interaction with Cellular Components. *Mater Today Commun* **2020**, *25*, 101692. https://doi.org/10.1016/J.MTCOMM.2020.101692.

(40) Galbn, C. J.; Galbn, S.; Van Dort, M. E.; Luker, G. D.; Bhojani, M. S.; Rehemtulla, A.; Ross, B. D. Applications of Molecular Imaging. *Prog Mol Biol Transl Sci* **2010**, *95* (C), 237–298. https://doi.org/10.1016/B978-0-12-385071-3.00009-5.

(41) Pysz, M. A.; Gambhir, S. S.; Willmann, J. K. Molecular Imaging: Current Status and Emerging Strategies. *Clin Radiol* **2010**, *65* (7), 500. https://doi.org/10.1016/J.CRAD.2010.03.011.

(42) Chen, K.; Chen, X. Design and Development of Molecular Imaging Probes. *Curr Top Med Chem* **2010**, *10* (12), 1227–1236. https://doi.org/10.2174/156802610791384225.

(43) Phelps, M. E. Positron Emission Tomography Provides Molecular Imaging of Biological Processes. *Proc Natl Acad Sci U S A* **2000**, *97* (16), 9226–9233. https://doi.org/10.1073/PNAS.97.16.9226.

(44) Wang, Z. G.; Yu, M. M.; Han, Y.; Wu, F. Y.; Yang, G. J.; Li, D. C.; Liu, S. M. Correlation of Glut-1 and Glut-3 Expression with F-18 FDG Uptake in Pulmonary Inflammatory Lesions. *Medicine (United States)* **2016**, *95* (48), e5462. https://doi.org/10.1097/MD.0000000000005462.

(45) Burt, B. M.; Humm, J. L.; Kooby, D. A.; Squire, O. D.; Mastorides, S.; Larson, S. M.; Fong, Y. Using Positron Emission Tomography with [18F]FDG to Predict Tumor Behavior in Experimental Colorectal Cancer. *Neoplasia* **2001**, *3* (3), 189–195. https://doi.org/10.1038/SJ.NEO.7900147.

(46) Adekola, K.; Rosen, S. T.; Shanmugam, M. Glucose Transporters in Cancer Metabolism. *Curr Opin Oncol* **2012**, *24* (6), 650–654. https://doi.org/10.1097/CCO.0B013E328356DA72.

(47) Zhao, C.; Zhang, Y.; Wang, J. A Meta-Analysis on the Diagnostic Performance of 18F-FDG and 11C-Methionine PET for Differentiating Brain Tumors. *American Journal of Neuroradiology* **2014**, *35* (6), 1058–1065. https://doi.org/10.3174/AJNR.A3718.

(48) Saponara, M.; Ambrosini, V.; Nannini, M.; Gatto, L.; Astolfi, A.; Urbini, M.; Indio, V.; Fanti, S.; Pantaleo, M. A. 18F-FDG-PET/CT Imaging in Cardiac Tumors: Illustrative Clinical Cases and Review of the Literature. *Ther Adv Med Oncol* **2018**, *10*. https://doi.org/10.1177/1758835918793569.

(49) Czernin, J.; Allen-Auerbach, M.; Nathanson, D.; Herrmann, K. PET/CT in Oncology: Current Status and Perspectives. *Curr Radiol Rep* **2013**, *1* (3), 177–190. https://doi.org/10.1007/S40134-013-0016-X.

(50) Xian, J. F.; Chen, M.; Jin, Z. Y. Magnetic Resonance Imaging in Clinical Medicine: Current Status and Potential Future Developments in China. *Chin Med J (Engl)* **2015**, *128* (5), 569–570. https://doi.org/10.4103/0366-6999.151637.

(51) Mullins, R.; Reiter, D.; Kapogiannis, D. Magnetic Resonance Spectroscopy Reveals Abnormalities of Glucose Metabolism in the Alzheimer's Brain. *Ann Clin Transl Neurol* **2018**, *5* (3), 262–272. https://doi.org/10.1002/ACN3.530.

(52) Weinberg, B. D.; Kuruva, M.; Shim, H.; Mullins, M. E. Clinical Applications of Magnetic Resonance Spectroscopy in Brain Tumors: From Diagnosis to Treatment. *Radiol Clin North Am* **2021**, *59* (3), 349–362. https://doi.org/10.1016/J.RCL.2021.01.004.

(53) Horská, A.; Barker, P. B. Imaging of Brain Tumors: MR Spectroscopy and Metabolic Imaging. *Neuroimaging Clinics* **2010**, *20* (3), 293–310. https://doi.org/10.1016/J.NIC.2010.04.003.

(54) Tognarelli, J. M.; Dawood, M.; Shariff, M. I. F.; Grover, V. P. B.; Crossey, M. M. E.; Cox, I. J.; Taylor-Robinson, S. D.; McPhail, M. J. W. Magnetic Resonance Spectroscopy: Principles and Techniques: Lessons for Clinicians. *J Clin Exp Hepatol* **2015**, *5* (4), 320–328. https://doi.org/10.1016/j.jceh.2015.10.006.

(55) Ding, H.; Haroon, A.; Wan, S.; Niendorf, T.; Adeleke, S. Old Discovery Leading to New Era: Metabolic Imaging of Cancer with Deuterium MRI. *Magnetochemistry 2023, Vol. 9, Page 6* **2022**, *9* (1), 6. https://doi.org/10.3390/MAGNETOCHEMISTRY9010006.

(56) Al-Rawi, J. M. A.; Behnam, G. Q.; Taha, N. I. Deuterium Nuclear Magnetic Resonance Spectroscopy. 1—Larmor Frequency Ratio, Referencing and Chemical Shift. *Organic Magnetic Resonance* **1981**, *16* (3), 198–201. https://doi.org/10.1002/MRC.1270160306.

(57) De Feyter, H. M.; Behar, K. L.; Corbin, Z. A.; Fulbright, R. K.; Brown, P. B.; McIntyre, S.; Nixon, T. W.; Rothman, D. L.; De Graaf, R. A. Deuterium Metabolic Imaging (DMI) for MRI-Based 3D Mapping of Metabolism in Vivo. *Sci Adv* **2018**, *4* (8), 7314–7336. https://doi.org/10.1126/SCIADV.AAT7314.

(58) Obara-Michlewska, M.; Szeliga, M. Targeting Glutamine Addiction in Gliomas. *Cancers 2020, Vol. 12, Page 310* **2020**, *12* (2), 310. https://doi.org/10.3390/CANCERS12020310.

(59) Serés Roig, E.; De Feyter, H. M.; Nixon, T. W.; Ruhm, L.; Nikulin, A. V.; Scheffler, K.; Avdievich, N. I.; Henning, A.; de Graaf, R. A. Deuterium Metabolic Imaging of the Human Brain in Vivo at 7 T. *Magn Reson Med* **2023**, *89* (1), 29–39. https://doi.org/10.1002/MRM.29439.

(60) Kaggie, J. D.; Khan, A. S.; Matys, T.; Schulte, R. F.; Locke, M. J.; Grimmer, A.; Frary, A.; Menih, I. H.; Latimer, E.; Graves, M. J.; McLean, M. A.; Gallagher, F. A. Deuterium Metabolic Imaging and Hyperpolarized 13C-MRI of the Normal Human Brain at Clinical Field Strength Reveals Differential Cerebral Metabolism. *Neuroimage* **2022**, *257*, 119284. https://doi.org/10.1016/J.NEUROIMAGE.2022.119284.

(61) Serés Roig, E.; De Feyter, H. M.; Nixon, T. W.; Ruhm, L.; Nikulin, A. V.; Scheffler, K.; Avdievich, N. I.; Henning, A.; de Graaf, R. A. Deuterium Metabolic Imaging of the Human Brain in Vivo at 7 T. *Magn Reson Med* **2023**, *89* (1), 29–39. https://doi.org/10.1002/MRM.29439.

(62) Hendriks, A. D.; Veltien, A.; Voogt, I. J.; Heerschap, A.; Scheenen, T. W. J.; Prompers, J. J. Glucose versus Fructose Metabolism in the Liver Measured with Deuterium Metabolic Imaging. *Front Physiol* **2023**, *14*, 1198578. https://doi.org/10.3389/FPHYS.2023.1198578.

(63) Zhang, G.; Cullen, Q.; Berishaj, M.; Deh, K.; Kim, N.; Keshari, K. R. [6,6′-2H2] Fructose as a Deuterium Metabolic Imaging Probe in Liver Cancer. *NMR Biomed* **2023**, *36* (10), e4989. https://doi.org/10.1002/NBM.4989.

(64) Ruiz-Cabello, J.; Barnett, B. P.; Bottomley, P. A.; Bulte, J. W. M. Fluorine (19F) MRS and MRI in Biomedicine. *NMR Biomed* **2011**, *24* (2), 114–129. https://doi.org/10.1002/NBM.1570.

(65) Vaeggemose, M.; Schulte, R. F.; Laustsen, C. Comprehensive Literature Review of Hyperpolarized Carbon-13 MRI: The Road to Clinical Application. *Metabolites 2021, Vol. 11, Page 219* **2021**, *11* (4), 219. https://doi.org/10.3390/METABO11040219.

(66) Aime, S.; Caravan, P. Biodistribution of Gadolinium-Based Contrast Agents, Including Gadolinium Deposition. *Journal of Magnetic Resonance Imaging* **2009**, *30* (6), 1259–1267. https://doi.org/10.1002/JMRI.21969.

(67) Hall, A. J.; Robertson, A. G.; Hill, L. R.; Rendina, L. M. Synthesis and Tumour Cell Uptake Studies of Gadolinium(III)–Phosphonium Complexes. *Scientific Reports 2021 11:1* **2021**, *11* (1), 1–14. https://doi.org/10.1038/s41598-020-79893-9.

(68) Cai, Y.; Wang, Y.; Zhang, T.; Pan, Y. Gadolinium-Labeled Ferritin Nanoparticles as T1Contrast Agents for Magnetic Resonance Imaging of Tumors. *ACS Appl Nano Mater* **2020**, *3* (9), 8771–8783. https://doi.org/10.1021/ACSANM.0C01563.

(69) Chen, Z.; Yu, D.; Liu, C.; Yang, X.; Zhang, N.; Ma, C.; Song, J.; Lu, Z. Gadolinium-Conjugated PLA-PEG Nanoparticles as Liver Targeted Molecular MRI Contrast Agent. *J Drug Target* **2011**, *19* (8), 657–665. https://doi.org/10.3109/1061186X.2010.531727.

(70) Licciardi, G.; Rizzo, D.; Salobehaj, M.; Massai, L.; Geri, A.; Messori, L.; Ravera, E.; Fragai, M.; Parigi, G. Large Protein Assemblies for High-Relaxivity Contrast Agents: The Case of Gadolinium-Labeled Asparaginase. *Bioconjug Chem* **2022**, *33* (12), 2411–2419. https://doi.org/10.1021/ACS.BIOCONJCHEM.2C00506.

(71) Šimečková, P.; Hubatka, F.; Kotouček, J.; Turánek Knötigová, P.; Mašek, J.; Slavík, J.; Kováč, O.; Neča, J.; Kulich, P.; Hrebík, D.; Stráská, J.; Pěnčíková, K.; Procházková, J.; Diviš, P.; Macaulay, S.; Mikulík, R.; Raška, M.; Machala, M.; Turánek, J. Gadolinium Labelled Nanoliposomes as the Platform for MRI Theranostics: In Vitro Safety Study in Liver Cells and Macrophages. *Sci Rep* **2020**, *10* (1). https://doi.org/10.1038/S41598-020-60284-Z.

(72) Dammes, N.; Peer, D. Monoclonal Antibody-Based Molecular Imaging Strategies and Theranostic Opportunities. *Theranostics* **2020**, *10* (2), 938. https://doi.org/10.7150/THNO.37443.

(73) Liu, Y.; Zhang, N. Gadolinium Loaded Nanoparticles in Theranostic Magnetic Resonance Imaging. *Biomaterials* **2012**, *33* (21), 5363–5375. https://doi.org/10.1016/J.BIOMATERIALS.2012.03.084.

(74) Akhtar, M. J.; Ahamed, M.; Alhadlaq, H.; Alrokayan, S. Toxicity Mechanism of Gadolinium Oxide Nanoparticles and Gadolinium Ions in Human Breast Cancer Cells. *Curr Drug Metab* **2019**, *20* (11), 907–917. https://doi.org/10.2174/1389200220666191105113754.

(75) Pan, D.; Schmieder, A. H.; Wickline, S. A.; Lanza, G. M. Manganese-Based MRI Contrast Agents: Past, Present, and Future. *Tetrahedron* **2011**, *67* (44), 8431–8444. https://doi.org/10.1016/J.TET.2011.07.076.

(76) Jeon, M.; Halbert, M. V.; Stephen, Z. R.; Zhang, M. Iron Oxide Nanoparticles as T1 Contrast Agents for Magnetic Resonance Imaging: Fundamentals, Challenges, Applications, and Prospectives. *Advanced Materials* **2021**, *33* (23), 1906539. https://doi.org/10.1002/ADMA.201906539.

(77) Cui, X.; Zhang, Z.; Yang, Y.; Li, S.; Lee, C. S. Organic Radical Materials in Biomedical Applications: State of the Art and Perspectives. *Exploration* **2022**, *2* (2), 20210264. https://doi.org/10.1002/EXP.20210264.

(78) Matsumoto, K. I.; Nakanishi, I.; Zhelev, Z.; Bakalova, R.; Aoki, I. Nitroxyl Radical as a Theranostic Contrast Agent in Magnetic Resonance Redox Imaging. *Antioxid Redox Signal* **2022**, *36* (1–3), 95–121. https://doi.org/10.1089/ARS.2021.0110.

(79) Matsumoto, K. Ichiro; Yakumaru, H.; Narazaki, M.; Nakagawa, H.; Anzai, K.; Ikehira, H.; Ikota, N. Modification of Nitroxyl Contrast Agents with Multiple Spins and Their Proton T1 Relaxivity. *Magn Reson Imaging* **2008**, *26* (1), 117–121. https://doi.org/10.1016/J.MRI.2007.05.009.

(80) McCabe, J. M.; Croce, K. J. Optical Coherence Tomography. *Circulation* **2012**, *126* (17), 2140–2143. https://doi.org/10.1161/CIRCULATIONAHA.112.117143.

(81) Buccheri, D.; Piraino, D.; Andolina, G.; Cortese, B. Understanding and Managing In-Stent Restenosis: A Review of Clinical Data, from Pathogenesis to Treatment. *J Thorac Dis* **2016**, *8* (10), E1150. https://doi.org/10.21037/JTD.2016.10.93.

(82) Ji, A.; Lou, H.; Qu, C.; Lu, W.; Hao, Y.; Li, J.; Wu, Y.; Chang, T.; Chen, H.; Cheng, Z. Acceptor Engineering for NIR-II Dyes with High Photochemical and Biomedical Performance. *Nature Communications 2022 13:1* **2022**, *13* (1), 1–13. https://doi.org/10.1038/s41467-022-31521-y.

(83) Du, Y.; Liu, X.; Zhu, S. Near-Infrared-II Cyanine/Polymethine Dyes, Current State and Perspective. *Front Chem* **2021**, *9*, 718709. https://doi.org/10.3389/FCHEM.2021.718709.

(84) Antaris, A. L.; Chen, H.; Cheng, K.; Sun, Y.; Hong, G.; Qu, C.; Diao, S.; Deng, Z.; Hu, X.; Zhang, B.; Zhang, X.; Yaghi, O. K.; Alamparambil, Z. R.; Hong, X.; Cheng, Z.; Dai, H. A Small-Molecule Dye for NIR-II Imaging. *Nature Materials 2015 15:2* **2015**, *15* (2), 235–242. https://doi.org/10.1038/nmat4476.

(85) Duan, H.; Wang, T.; Su, Z.; Pang, H.; Chen, C. Recent Progress and Challenges in Plasmonic Nanomaterials. *Nanotechnol Rev* **2022**, *11* (1), 846–873. https://doi.org/10.1515/NTREV-2022-0039.

(86) Kravets, V. G.; Kabashin, A. V.; Barnes, W. L.; Grigorenko, A. N. Plasmonic Surface Lattice Resonances: A Review of Properties and Applications. *Chem Rev* **2018**, *118* (12), 5912–5951. https://doi.org/10.1021/ACS.CHEMREV.8B00243.

(87) Besteiro, L. V.; Kong, X. T.; Wang, Z.; Hartland, G.; Govorov, A. O. Understanding Hot-Electron Generation and Plasmon Relaxation in Metal Nanocrystals: Quantum and Classical Mechanisms. *ACS Photonics* **2017**, *4* (11), 2759–2781. https://doi.org/10.1021/ACSPHOTONICS.7B00751.

(88) Boken, J.; Khurana, P.; Thatai, S.; Kumar, D.; Prasad, S. Plasmonic Nanoparticles and Their Analytical Applications: A Review. *Appl Spectrosc Rev* **2017**, *52* (9), 774–820. https://doi.org/10.1080/05704928.2017.1312427.

(89) Mondal, I.; Raj, S.; Roy, P.; Poddar, R. Silver Nanoparticles (AgNPs) as a Contrast Agent for Imaging of Animal Tissue Using Swept-Source Optical Coherence Tomography (SSOCT). *Laser Phys* **2017**, *28* (1), 015601. https://doi.org/10.1088/1555-6611/AA884B.

(90) Marin, R.; Lifante, J.; Besteiro, L. V.; Wang, Z.; Govorov, A. O.; Rivero, F.; Alfonso, F.; Sanz-Rodríguez, F.; Jaque, D. Plasmonic Copper Sulfide Nanoparticles Enable Dark Contrast in Optical Coherence Tomography. *Adv Healthc Mater* **2020**, *9* (5), 1901627. https://doi.org/10.1002/ADHM.201901627.

(91) Wang, A.; Qi, W.; Gao, T.; Tang, X. Molecular Contrast Optical Coherence Tomography and Its Applications in Medicine. *International Journal of Molecular Sciences 2022, Vol. 23, Page 3038* **2022**, *23* (6), 3038. https://doi.org/10.3390/IJMS23063038.

(92) Zhao, Y.; Wang, Y.; Ran, F.; Cui, Y.; Liu, C.; Zhao, Q.; Gao, Y.; Wang, D.; Wang, S. A Comparison between Sphere and Rod Nanoparticles Regarding Their in Vivo Biological Behavior and Pharmacokinetics. *Scientific Reports 2017 7:1* **2017**, *7* (1), 1–11. https://doi.org/10.1038/s41598-017-03834-2.

(93) Muñoz-Ortiz, T.; Hu, J.; Ortgies, D. H.; Shrikhande, S.; Zamora-Perez, P.; Granado, M.; González-Hedström, D.; de la Fuente-Fernández, M.; García-Villalón, Á. L.; Andrés-Delgado, L.; Martín Rodríguez, E.; Aguilar, R.; Alfonso, F.; García Solé, J.; Rivera Gil, P.; Jaque, D.; Rivero, F. Molecular Imaging of Infarcted Heart by Biofunctionalized Gold Nanoshells. *Adv Healthc Mater* **2021**, *10* (10), 2002186. https://doi.org/10.1002/ADHM.202002186.

(94) Huang, Y.; Hsu, J. C.; Koo, H.; Cormode, D. P. Repurposing Ferumoxytol: Diagnostic and Therapeutic Applications of an FDA-Approved Nanoparticle. *Theranostics* **2022**, *12* (2), 796. https://doi.org/10.7150/THNO.67375.

(95) Keselman, P.; Yu, E. Y.; Zhou, X. Y.; Goodwill, P. W.; Chandrasekharan, P.; Ferguson, R. M.; Khandhar, A. P.; Kemp, S. J.; Krishnan, K. M.; Zheng, B.; Conolly, S. M. Tracking Short-Term Biodistribution and Long-Term Clearance of SPIO Tracers in Magnetic Particle Imaging. *Phys Med Biol* **2017**, *62* (9), 3440. https://doi.org/10.1088/1361-6560/AA5F48.

(96) Perrin, J.; Capitao, M.; Mougin-Degraef, M.; Guérard, F.; Faivre-Chauvet, A.; Rbah-Vidal, L.; Gaschet, J.; Guilloux, Y.; Kraeber-Bodéré, F.; Chérel, M.; Barbet, J. Cell Tracking in Cancer Immunotherapy. *Front Med (Lausanne)* **2020**, *7*. https://doi.org/10.3389/FMED.2020.00034.

(97) Cheng, H. L. M. A Primer on in Vivo Cell Tracking Using MRI. *Front Med (Lausanne)* **2023**, *10*, 1193459. https://doi.org/10.3389/FMED.2023.1193459.

(98) Kratz, H.; Taupitz, M.; De Schellenberger, A. A.; Kosch, O.; Eberbeck, D.; Wagner, S.; Trahms, L.; Hamm, B.; Schnorr, J. Novel Magnetic Multicore Nanoparticles Designed for MPI and Other Biomedical Applications: From Synthesis to First in Vivo Studies. *PLoS One* **2018**, *13* (1), e0190214. https://doi.org/10.1371/JOURNAL.PONE.0190214.

(99) Dogan, N.; Caliskan, G.; Irfan, M. Synthesis and Characterization of Biocompatible ZnFe2O4 Nanoparticles for Magnetic Particle Imaging (MPI). *Journal of Materials Science: Materials in Electronics* **2023**, *34* (5), 1–18. https://doi.org/10.1007/S10854-022-09799-X.

(100) Gao, P.; Liu, Y.; Wang, X.; Feng, X.; Liu, H.; Liu, S.; Huang, X.; Wu, X.; Xiong, F.; Jia, X.; Hui, H.; Jiang, J.; Tian, J. Adhesion Molecule–Targeted Magnetic Particle Imaging Nanoprobe for Visualization of Inflammation in Acute Lung Injury. *Eur J Nucl Med Mol Imaging* **2023**, 1–13. https://doi.org/10.1007/S00259-023-06550-4.

(101) Cook-Mills, J. M.; Marchese, M. E.; Abdala-Valencia, H. Vascular Cell Adhesion Molecule-1 Expression and Signaling During Disease: Regulation by Reactive Oxygen Species and Antioxidants. *https://home.liebertpub.com/ars* **2011**, *15* (6), 1607–1638. https://doi.org/10.1089/ARS.2010.3522.

(102) Kovesdy, C. P. Epidemiology of Chronic Kidney Disease: An Update 2022. *Kidney Int Suppl (2011)* **2022**, *12* (1), 7–11. https://doi.org/10.1016/j.kisu.2021.11.003.

(103) Chen, T. K.; Knicely, D. H.; Grams, M. E. Chronic Kidney Disease Diagnosis and Management: A Review. *JAMA* **2019**, *322* (13), 1294–1304. https://doi.org/10.1001/JAMA.2019.14745.

(104) Luis-Lima, S.; Porrini, E. An Overview of Errors and Flaws of Estimated GFR versus True GFR in Patients with Diabetes Mellitus. *Nephron* **2017**, *136* (4), 287–291. https://doi.org/10.1159/000453531.

(105) Helal, I.; Fick-Brosnahan, G. M.; Reed-Gitomer, B.; Schrier, R. W. Glomerular Hyperfiltration: Definitions, Mechanisms and Clinical Implications. *Nature Reviews Nephrology 2012 8:5* **2012**, *8* (5), 293–300. https://doi.org/10.1038/nrneph.2012.19.

(106) Padala, S. A.; Kallam, A. Clear Cell Renal Carcinoma. *StatPearls* **2023**.

(107) Gray, R. E.; Harris, G. T. Renal Cell Carcinoma: Diagnosis and Management. *Am Fam Physician* **2019**, *99* (3), 179–184.

(108) Miftari, R.; Nura, A.; Topçiu-Shufta, V.; Miftari, V.; Murseli, A.; Haxhibeqiri, V. Impact of Gate 99mTc DTPA GFR, Serum Creatinine and Urea in Diagnosis of Patients with Chronic Kidney Failure. *Acta Inform Med* **2017**, *25* (2), 99–102. https://doi.org/10.5455/AIM.2017.25.99-102.

(109) Levey, A. S.; Titan, S. M.; Powe, N. R.; Coresh, J.; Inker, L. A. Kidney Disease, Race, and Gfr Estimation. *Clinical Journal of the American Society of Nephrology* **2020**, *15* (8), 1203–1212. https://doi.org/10.2215/CJN.12791019.

(110) Taylor, A. T. Radionuclides in Nephrourology, Part 1: Radiopharmaceuticals, Quality Control, and Quantitative Indices. *Journal of Nuclear Medicine* **2014**, *55* (4), 608–615. https://doi.org/10.2967/JNUMED.113.133447.

(111) Irrera, P.; Consolino, L.; Dastrù, W.; Pedersen, M.; Zöllner, F. G.; Longo, D. L. Dynamic Contrast Enhanced (Dce) Mri-Derived Renal Perfusion and Filtration: Experimental Protocol. *Methods in Molecular Biology* **2021**, *2216*, 429–441. https://doi.org/10.1007/978-1-0716-0978-1_25.

(112) Schieda, N.; Blaichman, J. I.; Costa, A. F.; Glikstein, R.; Hurrell, C.; James, M.; Jabehdar Maralani, P.; Shabana, W.; Tang, A.; Tsampalieros, A.; van der Pol, C. B.; Hiremath, S. Gadolinium-Based Contrast Agents in Kidney Disease: A Comprehensive Review and Clinical Practice Guideline Issued by the Canadian Association of Radiologists. *Can J Kidney Health Dis* **2018**, *5*. https://doi.org/10.1177/2054358118778573.

(113) Weinreb, J. C.; Rodby, R. A.; Yee, J.; Wang, C. L.; Fine, D.; McDonald, R. J.; Perazella, M. A.; Dillman, J. R.; Davenport, M. S. Use of Intravenous Gadolinium-Based Contrast Media in Patients With Kidney Disease: Consensus Statements from the American College of Radiology and the National Kidney Foundation. *Kidney Med* **2021**, *3* (1), 142–150. https://doi.org/10.1016/j.xkme.2020.10.001.

(114) Fur, M. Le; Moon, B. F.; Zhou, I. Y.; Zygmont, S.; Boice, A.; Rotile, N. J.; Ay, I.; Pantazopoulos, P.; Feldman, A. S.; Rosales, I. A.; How, I. D. A. L.; Izquierdo-Garcia, D.; Hariri, L. P.; Astashkin, A. V.; Jackson, B. P.; Caravan, P. Gadolinium-Based Contrast Agent Biodistribution and Speciation in Rats. *Radiology* **2023**, *309* (1). https://doi.org/10.1148/RADIOL.230984.

(115) Yanga, H.; Chena, J. Q.; Li, J.; Lva, Y.; Gaoa, S. The Effect of TEMPO in the Hydroxylation of Benzene to Phenol on the [(CH3)4N]4PMo11VO40/Ascorbic Acid/TEMPO/O2 Catalytic System: Formation of Ascorbic Acid Radicals through Hydrogen Exchange of Ascorbic Acid and TEMPO. *Appl Catal A Gen* **2012**, *415–416*, 22–28. https://doi.org/10.1016/J.APCATA.2011.11.032.

(116) Rajca, A.; Wang, Y.; Boska, M.; Paletta, J. T.; Olankitwanit, A.; Swanson, M. A.; Mitchell, D. G.; Eaton, S. S.; Eaton, G. R.; Rajca, S. Organic Radical Contrast Agents for Magnetic Resonance Imaging. *J Am Chem Soc* **2012**, *134* (38), 15724–15727. https://doi.org/10.1021/JA3079829.

(117) Nguyen, H. V. T.; Detappe, A.; Harvey, P.; Gallagher, N.; Mathieu, C.; Agius, M. P.; Zavidij, O.; Wang, W.; Jiang, Y.; Rajca, A.; Jasanoff, A.; Ghobrial, I. M.; Ghoroghchian, P. P.; Johnson, J. A. Pro-Organic Radical Contrast Agents ("pro-ORCAs") for Real-Time MRI of pro-Drug Activation in Biological Systems. *Polym Chem* **2020**, *11* (29), 4768–4779. https://doi.org/10.1039/D0PY00558D.

(118) *Cardiovascular diseases*. https://www.who.int/health-topics/cardiovascular-diseases#tab=tab_1 (accessed 2024-01-13).

(119) Hansson, G. K. Inflammation, Atherosclerosis, and Coronary Artery Disease. *https://doi.org/10.1056/NEJMra043430* **2005**, *352* (16), 1685–1695. https://doi.org/10.1056/NEJMRA043430.

(120) Kong, P.; Cui, Z. Y.; Huang, X. F.; Zhang, D. D.; Guo, R. J.; Han, M. Inflammation and Atherosclerosis: Signaling Pathways and Therapeutic Intervention. *Signal Transduction and Targeted Therapy 2022 7:1* **2022**, *7* (1), 1–24. https://doi.org/10.1038/s41392-022-00955-7.

(121) Bentzon, J. F.; Otsuka, F.; Virmani, R.; Falk, E. Mechanisms of Plaque Formation and Rupture. *Circ Res* **2014**, *114* (12), 1852–1866. https://doi.org/10.1161/CIRCRESAHA.114.302721.

(122) Rifkin, R. D.; Parisi, A. F.; Folland, E. Coronary Calcification in the Diagnosis of Coronary Artery Disease. *Am J Cardiol* **1979**, *44* (1), 141–147. https://doi.org/10.1016/0002-9149(79)90263-7.

(123) Yin, Y.; He, C.; Xu, B.; Li, Z. Coronary Plaque Characterization From Optical Coherence Tomography Imaging With a Two-Pathway Cascade Convolutional Neural Network Architecture. *Front Cardiovasc Med* **2021**, *8*, 670502. https://doi.org/10.3389/FCVM.2021.670502.

(124) Chamié, D.; Wang, Z.; Bezerra, H.; Rollins, A. M.; Costa, M. A. Optical Coherence Tomography and Fibrous Cap Characterization. *Curr Cardiovasc Imaging Rep* **2011**, *4* (4), 276–283. https://doi.org/10.1007/S12410-011-9090-8.

(125) Loftus, I. Mechanisms of Plaque Rupture. *Mechanisms of Vascular Disease: A Reference Book for Vascular Specialists* **2011**, 43–78. https://doi.org/10.1017/UPO9781922064004.005.

(126) Seneviratne, A.; Hulsmans, M.; Holvoet, P.; Monaco, C. Biomechanical Factors and Macrophages in Plaque Stability. *Cardiovasc Res* **2013**, *99* (2), 284–293. https://doi.org/10.1093/CVR/CVT097.

(127) Buccheri, D.; Piraino, D.; Andolina, G.; Cortese, B. Understanding and Managing In-Stent Restenosis: A Review of Clinical Data, from Pathogenesis to Treatment. *J Thorac Dis* **2016**, *8* (10), E1150. https://doi.org/10.21037/JTD.2016.10.93.

(128) Mehilli, J.; Byrne, R. A.; Tiroch, K.; Pinieck, S.; Schulz, S.; Kufner, S.; Massberg, S.; Laugwitz, K. L.; Schömig, A.; Kastrati, A. Randomized Trial of Paclitaxel- Versus Sirolimus-Eluting Stents for Treatment of Coronary Restenosis in Sirolimus-Eluting Stents. The ISAR-DESIRE 2 (Intracoronary Stenting and Angiographic Results: Drug Eluting Stents for In-Stent Restenosis 2) Study. *J Am Coll Cardiol* **2010**, *55* (24), 2710–2716. https://doi.org/10.1016/J.JACC.2010.02.009.

(129) W. van Lammeren, G.; L. Moll, F.; Jan De Borst, G.; P.V. de Kleijn, D.; P.M. de Vries, J.-P.; Pasterkamp, G. Atherosclerotic Plaque Biomarkers: Beyond the Horizon of the Vulnerable Plaque. *Curr Cardiol Rev* **2011**, *7* (1), 22. https://doi.org/10.2174/157340311795677680.

(130) Fujimoto, J. G.; Swanson, E. A. The Ecosystem That Powered the Translation of OCT from Fundamental Research to Clinical and Commercial Impact [Invited]. *Biomedical Optics Express, Vol. 8, Issue 3, pp. 1638-1664* **2017**, *8* (3), 1638–1664. https://doi.org/10.1364/BOE.8.001638.

(131) Wang, L. L. W.; Janes, M. E.; Kumbhojkar, N.; Kapate, N.; Clegg, J. R.; Prakash, S.; Heavey, M. K.; Zhao, Z.; Anselmo, A. C.; Mitragotri, S. Cell Therapies in the Clinic. *Bioeng Transl Med* **2021**, *6* (2), e10214. https://doi.org/10.1002/BTM2.10214.

(132) *Cell and Gene Therapy Market Outlook in 2022 and Beyond*. https://www.cellandgene.com/doc/cell-gene-therapies-investment-outlook-in-beyond-0001 (accessed 2024-01-13).

(133) Bashor, C. J.; Hilton, I. B.; Bandukwala, H.; Smith, D. M.; Veiseh, O. Engineering the next Generation of Cell-Based Therapeutics. *Nature Reviews Drug Discovery 2022 21:9* **2022**, *21* (9), 655–675. https://doi.org/10.1038/s41573-022-00476-6.

(134) Margiana, R.; Markov, A.; Zekiy, A. O.; Hamza, M. U.; Al-Dabbagh, K. A.; Al-Zubaidi, S. H.; Hameed, N. M.; Ahmad, I.; Sivaraman, R.; Kzar, H. H.; Al-Gazally, M. E.; Mustafa, Y. F.; Siahmansouri, H. Clinical Application of Mesenchymal Stem Cell in Regenerative Medicine: A Narrative Review. *Stem Cell Research & Therapy 2022 13:1* **2022**, *13* (1), 1–22. https://doi.org/10.1186/S13287-022-03054-0.

(135) Waldman, A. D.; Fritz, J. M.; Lenardo, M. J. A Guide to Cancer Immunotherapy: From T Cell Basic Science to Clinical Practice. *Nature Reviews Immunology 2020 20:11* **2020**, *20* (11), 651–668. https://doi.org/10.1038/s41577-020-0306-5.

(136) Chivu-Economescu, M.; Rubach, M. Hematopoietic Stem Cells Therapies. *Curr Stem Cell Res Ther* **2016**, *12* (2), 124–133. https://doi.org/10.2174/1574888X10666151026114241.

(137) Amer, M. H.; Rose, F. R. A. J.; Shakesheff, K. M.; Modo, M.; White, L. J. Translational Considerations in Injectable Cell-Based Therapeutics for Neurological Applications: Concepts, Progress and Challenges. *npj Regenerative Medicine 2017 2:1* **2017**, *2* (1), 1–13. https://doi.org/10.1038/s41536-017-0028-x.

(138) Nucci, M. P.; Filgueiras, I. S.; Ferreira, J. M.; de Oliveira, F. A.; Nucci, L. P.; Mamani, J. B.; Rego, G. N. A.; Gamarra, L. F. Stem Cell Homing, Tracking and Therapeutic Efficiency Evaluation for Stroke Treatment Using Nanoparticles: A Systematic Review. *World J Stem Cells* **2020**, *12* (5), 381–405. https://doi.org/10.4252/wjsc.v12.i5.381.

(139) Loftus, L. V.; Amend, S. R.; Pienta, K. J. Interplay between Cell Death and Cell Proliferation Reveals New Strategies for Cancer Therapy. *International Journal of Molecular Sciences 2022, Vol. 23, Page 4723* **2022**, *23* (9), 4723. https://doi.org/10.3390/IJMS23094723.

(140) Lechermann, L. M.; Lau, D.; Attili, B.; Aloj, L.; Gallagher, F. A. In Vivo Cell Tracking Using PET: Opportunities and Challenges for Clinical Translation in Oncology. *Cancers 2021, Vol. 13, Page 4042* **2021**, *13* (16), 4042. https://doi.org/10.3390/CANCERS13164042.

(141) Faucher, L.; Tremblay, M.; Lagueux, J.; Gossuin, Y.; Fortin, M. A. Rapid Synthesis of PEGylated Ultrasmall Gadolinium Oxide Nanoparticles for Cell Labeling and Tracking with MRI. *ACS Appl Mater Interfaces* **2012**, *4* (9), 4506–4515. https://doi.org/10.1021/AM3006466.

(142) Yeung, T.; Gilbert, G. E.; Shi, J.; Silvius, J.; Kapus, A.; Grinstein, S. Membrane Phosphatidylserine Regulates Surface Charge and Protein Localization. *Science (1979)* **2008**, *319* (5860), 210–213. https://doi.org/10.1126/SCIENCE.1152066.

(143) Wang, F.; Yu, L.; Monopoli, M. P.; Sandin, P.; Mahon, E.; Salvati, A.; Dawson, K. A. The Biomolecular Corona Is Retained during Nanoparticle Uptake and Protects the Cells from the Damage Induced by Cationic Nanoparticles until Degraded in the Lysosomes. *Nanomedicine* **2013**, *9* (8), 1159–1168. https://doi.org/10.1016/J.NANO.2013.04.010.

(144) Qu, K.; Yuan, Z.; Wang, Y.; Song, Z.; Gong, X.; Zhao, Y.; Mu, Q.; Zhan, Q.; Xu, W.; Wang, L. Structures, Properties, and Applications of Zwitterionic Polymers. *ChemPhysMater* **2022**, *1* (4), 294–309. https://doi.org/10.1016/J.CHPHMA.2022.04.003.

(145) Lau, S. K.; Yong, W. F. Recent Progress of Zwitterionic Materials as Antifouling Membranes for Ultrafiltration, Nanofiltration, and Reverse Osmosis. *ACS Appl Polym Mater* **2021**, *3* (9), 4390–4412. https://doi.org/10.1021/ACSAPM.1C00779.

(146) Mondini, S.; Leonzino, M.; Drago, C.; Ferretti, A. M.; Usseglio, S.; Maggioni, D.; Tornese, P.; Chini, B.; Ponti, A. Zwitterion-Coated Iron Oxide Nanoparticles: Surface Chemistry and Intracellular Uptake by Hepatocarcinoma (HepG2) Cells. *Langmuir* **2015**, *31* (26), 7381–7390. https://doi.org/10.1021/ACS.LANGMUIR.5B01496.

(147) Smith, L.; Kuncic, Z.; Byrne, H. L.; Waddington, D. Nanoparticles for MRI-Guided Radiation Therapy: A Review. *Cancer Nanotechnology 2022 13:1* **2022**, *13* (1), 1–28. https://doi.org/10.1186/S12645-022-00145-8.

(148) Caspani, S.; Magalhães, R.; Araújo, J. P.; Sousa, C. T. Magnetic Nanomaterials as Contrast Agents for MRI. *Materials 2020, Vol. 13, Page 2586* **2020**, *13* (11), 2586. https://doi.org/10.3390/MA13112586.

Chapter 2: Direct Mapping of Kidney Function by DCE-MRI Urography Using a Tetrazinanone Organic Radical Contrast Agent

Nicholas D. Calvert[1], Alexia Kirby[2], Mojmír Suchý[1], Peter Pallister[3], Aidan A. Torrens[1], Dylan Burger[4], Gerd Melkus[5,6], Nicola Schieda[6], Adam J. Shuhendler[1,2,7*]

[1]Department of Chemistry and Biomolecular Sciences, University of Ottawa, 150 Louis Pasteur Pvt., Ottawa, Ontario, K1N 6N5, Canada

[2] Department of Biology, University of Ottawa, 150 Louis Pasteur Pvt., Ottawa, Ontario, K1N 6N5, Canada

[3]Department of Chemistry, Carleton University, 1125 Colonel By Dr., Ottawa, Ontario, K1S 5B6, Canada

[4] Kidney Research Center, Ottawa Hospital Research Institute, University of Ottawa, 501 Smyth Rd, Ottawa, Ontario, K1H 8L6, Canada

[5]Dept. Medical Imaging, The Ottawa Hospital, 501 Smyth Rd, Ottawa, Ontario, K1H 8L6, Canada

[6]Dept. Radiology, University of Ottawa, 501 Smyth Rd, Ottawa, Ontario, K1H 8L6, Canada

[7]University of Ottawa Heart Institute, 40 Ruskin St., Ottawa, Ontario, K1Y 4W7, Canada

*Corresponding author: adam.shuhendler@uottawa.ca

2.1. Introduction to the Research Article Presented in this Chapter

A potentially new class of ORCAs identified from the literature, known as verdazyls, had yet to be evaluated as an MRI contrast agent. The existing verdazyl literature reported a glucose-functionalized verdazyl, known as glucoverdazyl. After optimizing the synthetic procedure to improve purity and yield, we characterized the MRI properties of this compound. We then used a series of animal models with and without different forms of kidney dysfunction to evaluate glucoverdazyl as a new ORCA that could quantitatively and qualitatively map kidney function as a potential alternative to DCE-MRI with GBCAs. The MRI maps were validated as measurements of glomerular filtration rate (GFR) using a gold-standard transdermal recording technique.

2.2. Author Contributions

N.D.C. and M.S. performed all synthesis and characterization of chemical compounds with support from A.A.T. N.D.C. performed all in vitro physicochemical and cell-based experiments. P.P. performed NMR relaxivity and mechanism of contrast enhancement studies. N.D.C. and A.K. performed animal studies, including model development, implementation, and imaging. N.D.C. wrote the MATLAB code for imaging analysis with support from G.M., and performed all analyses. N.D.C. performed statistical analyses. N.D.C., A.J.S., and A.K. conceived of experiments with support from D.B. and N.S. N.D.C. and A.J.S. co-wrote the paper, and all authors edited. the work and provided input on response to reviewers.

2.3. Copyright

2.4. Abstract

Chronic kidney disease (CKD) and acute kidney injury (AKI) are ongoing global health burdens. Glomerular filtration rate (GFR) is the gold standard measure of kidney function, with clinical estimates providing a global assessment of kidney health without spatial information of kidney or region-specific dysfunction. The addition of dynamic contrast enhanced magnetic resonance imaging (DCE-MRI) to the anatomical imaging already performed would yield a 'one-stop-shop' for renal assessment in cases of suspected AKI and CKD. Towards urography by DCE-MRI, we evaluated a class of nitrogen-centered organic radicals known as verdazyls, which are extremely stable even in highly reducing environments. A glucose-modified verdazyl, glucoverdazyl, provided contrast limited to kidney and bladder, affording functional kidney evaluation in mouse models of unilateral ureteral obstruction (UUO) and folic acid- induced nephropathy (FAN). Imaging outcomes correlated with histology and hematology assessing kidney dysfunction, and glucoverdazyl clearance rates were found to be a reliable surrogate measure of GFR.

2.5. Introduction

Chronic kidney disease (CKD) continues to be a major international healthcare burden, with the global mean prevalence > 13%.[1,2] CKD often develops slowly and without obvious symptoms in the early stages, but becomes progressively more debilitating in later stages with limited chances for reversal.[2] This disease is often attributed to long-term diabetes or hypertension, but is also a potential outcome following an acute kidney injury (AKI), the result of a

sudden and dramatic decline in kidney function.[3,4] CKD outcomes are improved with early interventions, such as renin-angiotensin system blockade[5–7] or sodium-glucose co-transporter 2 (SGLT2) inhibitors[8] necessitating earlier detection.[9] Clinical diagnosis of CKD in North America is defined by proteinuria (albumin-to-creatinine (ACR) > 30 mg/g for >3 months) and/or functional decline (estimated glomerular filtration rate (eGFR) < 60 ml/min/1.73 m^2 for >3 months).[9,10] These diagnostic values have been derived from large clinical studies in an ethnically-biased population, significantly reducing the diagnostic power of these biomarkers of disease.[11] Additionally, underlying causes of CKD can vary between individuals, where some of the most common, including diabetes mellitus, cardiovascular disease, and kidney transplant, can limit the accuracy of eGFR measurements at the patient level, as almost 30% of these patients can present with a 30% deviation from their true eGFR.[12] These issues may be partially mitigated by incorporation of cystatin C into the equation, however eGFR equations also assume steady-state creatinine and cystatin C levels and do not account for alterations in or alternate routes of creatinine production, exacerbating variability.[13] It has become important that more accurate methods for GFR estimation be developed independent from demographic characteristics of the patient.[14] In addition, eGFR values fail to provide physicians with spatial or structural information underlying the renal dysfunction, omitting important diagnostic information for patients with AKI, CKD, and renal malignancies.[15] Kidney biopsy can provide histopathological data predictive of CKD outcomes, delivering spatial data about specific kidney lesions and not just overall kidney function.[16] However, biopsies are invasive procedures with their own inherent risk, precluding their repeated use to spatiotemporally characterize kidney disease. Clinically, GFR is the gold standard as an indicator for kidney function, however few clinical techniques are capable of providing spatial information about kidney function.[17]

Medical imaging has been investigated as an alternative approach to measure kidney function. Imaging-based GFR assessment is of particular interest because it allows for a direct link between structural alterations (i.e. renal artery stenosis, ureteral obstruction) and changes in kidney filtration. In addition to this, GFR may be measured at the single kidney level. This is of particular interest when monitoring patients after partial nephrectomy or after living kidney donation where early increases in single kidney GFR are predictive of beneficial outcomes.[18] Importantly, imaging-based urographic approaches to GFR measurement mitigate errors associated with plasma sampling-based techniques, including sample timing, decay correction, dilution of standards and the handling of small volumes.[19] Camera-based imaging of GFR is, however, currently limited to ^{99m}Tc-diethylenetriaminepentaacetic acid (DTPA) single photon emission computed tomography (SPECT)[14]. The specificity and sensitivity of camera-based GFR as diagnostic for renal failure was 100% and 47.5% for ^{99m}Tc-DTPA, respectively[20]. ^{99m}Tc-mercaptoazyltriglycerine (MAG3) is another SPECT-based method for imaging-based urography that is primarily cleared by tubular secretion, and is often used to evaluate renal plasma flow[14]. However, clearance of this radiotracer corrected for body surface area correlates well with creatinine-based GFR measurements[21]. These nuclear imaging techniques suffer from two sources of error leading to a wider confidence interval of the determined GFR relative to eGFR: background subtraction necessary for the correct measurement of percentage injected dose, and the estimation of renal depth from a population-derived nomogram based on patient height and weight in order to correct for signal attenuation[19,22]. Additionally, SPECT is also associated with limited spatial resolution and structural detail, however which is achievable by other imaging modalities such as magnetic resonance imaging (MRI).[23,24] Dynamic contrast enhanced (DCE) MRI has been of particular

interest as a tool for evaluating GFR in patients with renal artery stenosis, urinary obstruction, and living kidney donors. This technique gives spatial and structural reference to important clinical parameters that can be quantified through contrast enhancement changes over time, such as rate of contrast clearance and time to peak intensity.[25,26] In comparison to other medical specialties, the advances in imaging technique development in clinical nephrology have been slow.

The greatest challenge for kidney DCE-MRI is overcoming both the real and perceived risks associated with the use of traditional gadolinium (Gd)-based MRI contrast agents in patients with suspected or diagnosed renal dysfunction.[27–30] Contrast enhanced-MRI in patients with AKI and severe CKD following typical eGFR screens may be delayed or denied in patients with suspected kidney disease due to concerns of nephrogenic systemic fibrosis (NSF).[27,29] NSF is a debilitating and sometimes fatal syndrome with no known treatment, and while its mechanism for pathogenic initiation is still poorly understood, it was shown to be linked to the accumulation of Gd in kidney tissue.[27,29,31,32] There is an increased risk of NSF in patients with severe renal dysfunction (AKI, dialysis patients, and stage 5 CKD) where lower rates of Gd clearance lead to higher residence times of the contrast agents.[33] This risk appears to be mitigated in group II Gd-based contrast agent (GBCAs), as defined by the American College of Radiology.[34]

Regardless of the Gd-based contrast agent used, even with macrocyclic agents being more stable to linear chelators, there is a risk that low levels of gadolinium can be retained, for example at ppm-levels as phosphonates in the brain, and be slowly cleared over months to years.[35,36] Considering there are 30 million doses of Gd-based contrast agents administered annually worldwide, there is a need for a metal-free alternative for facilitating MRI-based urography.[37] There has been an effort to improve MRI contrast agent safety over the last decade by focusing on chemistries capable of altering water proton relaxation kinetics without the use of coordinated

metal ions.[38] A significant proportion of these efforts has been focused on creating stable nitroxyl radicals lacking α-protons in order to enhance their stability (i.e. 2,2,6,6-tetramethylpiperidine 1-oxyl, TEMPO). In addition to the cytotoxicity associated with free radical molecules, these organic radical contrast agents (ORCAs) are prone to reduction in vivo, quickly losing their radical character and contrast enhancing effects.[39] Efforts to stabilize these radicals with bulky sidechains and/or binding to metal nanoparticles significantly alter their biodistribution and clearance, complicating clinical translation.[40,41]

Our group has taken an alternative approach to developing ORCAs, focusing on the radicals belonging to the 6-oxoverdazyl family. These molecules provide the chemical flexibility required for ORCA optimization, possessing a synthetic route that allows for functionalization of the *1* and *5* positions, as well as the *3* position of the tetrazinanone ring with stabilizing and targeting moieties (Fig. 1).[42,43] Through a combination of other previously reported methods, we have optimized and scaled-up the synthesis of a verdazyl-based ORCA containing *3*-glucosyl and *1,5*-*N,N*-isopropyl groups (4, Fig. 1). While the *3* position glucosyl improves solubility and biocompatibility, the incorporation of the anomeric carbon into the tetrazinanone ring precludes cell uptake through glucose transporters, since the anomeric oxygen is required for substrate interaction with most of the GLUT family.[44,45] We also demonstrate enhanced stability and cyto-compatibility of glucoverdazyl relative to a nitroxyl radical (TEMPO) and spin trapping agent, 5,5-dimethylpyrroline-*N*-oxide (DMPO). The delocalization of the radical throughout the nitrogen-centered π-orbitals creates a more stable ORCA radical in relation to typical nitroxyl radical agents.[46] We have evaluated the use of glucoverdazyl as a DCE-MRI agent through a short-term AKI and long-term AKI-to-CKD mouse model of kidney dysfunction (unilateral ureteral obstruction (UUO), and folic acid nephropathy (FAN), respectively), and have presented the

DCE-MRI images as voxel-wise maps of glucoverdazyl perfusion to evaluate contrast clearance and retention. Finally, we compare the image-derived renal decay time constant of glucoverdazyl in healthy and disease mice to a validated transdermal method for GFR determination currently under clinical translation. With this comparison, we demonstrated that glucoverdazyl imaging can provide accurate and reproducible GFR maps from DCE-MRI, allowing the acquisition of kidney functional information. The present work lays the foundation for a unique class of ORCAs with the potential to provide for contrast enhanced-MRI in patients with renal dysfunction, and for the mapping of GFR onto the kidneys independent of the demographic characteristics of the patient.

2.6. Results and Discussion

2.6.1.Optimized Targeted Synthesis of Glucoverdazyl

A combination of previously reported 6-oxoverdazyl syntheses was used to identify an optimized route to glucoverdazyl yielding a high level of molecular purity and scalability that is required for an in vivo contrast agent (Fig. 1). The previously reported hydrazine side chains in the literature were usually limited to short carbon chains or aryl groups.[44,47–50] We functionalized the side chains with isopropyl groups, as they were bulky enough side chain to help protect the delocalized radical while also improving serum retention after injection[51]. In earlier syntheses, we had generated *N*-Boc isopropyl hydrazine (1) from the *N*-Boc hydrazine precursor following a previously reported synthesis by Calabretta *et al*. in large quantities[52]. However, we found it more economical to purchase isopropyl Boc hydrazine. Compound 2 has been synthesized in a number of reported ways, all of which are di-substitutions of $COCl_2$, either as a phosgene solution or solid triphosgene.[48,53] While we have synthesized glucoverdazyl with both forms of phosgene with similar results, we have chosen to work with the 15% phosgene in toluene solution. The route with

the superior yield and purity was achieved through heptane recrystallization of the crude product after the phosgenation step, as first reported by Paré et al.[48] Following Boc deprotection in ethanolic hydrochloric acid to form a crude intermediate used without further purification, we chose to generate the non-radical tetrazinanone ring (compound 3) with D-glucose in the same manner as was first reported by Le *et al*.[42] Finally, oxidation of compound 3 was also performed as reported by Le et al. using potassium ferricyanide, a much milder oxidant with an easier purification process compared to the more typically used benzoquinone seen in the majority of the available verdazyl literature.[42,54–56] Much of the past literature that has reported on these reactions have been incomplete with respect to characterization. Here we are reporting high purity ^{1}H and ^{13}C NMR spectra, as well as high- resolution mass spectra for each step and associated intermediates (Supplementary Figs. S2–S7). The purity of compound 4 was determined by EPR spectroscopy and analytical high-performance liquid chromatography, demonstrating that our approach to glucoverdazyl yielded 4 fully converted from non-radical 3 (Supplementary Fig. S8).

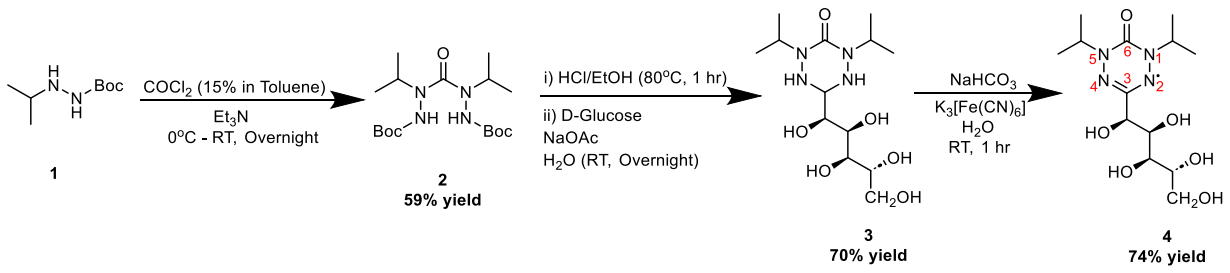

Figure 2.1 Synthesis of glucoverdazyl (4). General synthetic scheme with yields used to synthesize glucoverdazyl. Red numbering on the final compound indicates numbering of the ring.

2.6.2. Characterization of Glucoverdazyl as an MRI-Active Contrast Agent

The EPR spectrum for glucoverdazyl matched that reported previously, with the multiple EPR peaks being characteristic of radical delocalization within the tetrazinanone ring (Fig. 2a).[42,57] The presence of the free radical indicated that glucoverdazyl would potentially result in MRI contrast enhancement.[58] MR imaging of solution phantoms of glucoverdazyl in PBS shows T_1 shortening but no change in T_2 relative to water (Fig. 2b). The relaxivity of glucoverdazyl was expectedly lower than that reported for gadolinium-based contrast agents, but of similar magnitude to other previously reported organic radical compounds, with a longitudinal relaxivity (r_1) of 0.30 ± 0.03 $mM^{-1}s^{-1}$ (Fig. 2c).[41,59,60] In order to look at the possible mechanism of water relaxation for glucoverdazyl, the temperature-dependence of the corrected relaxation rate was examined (Supplementary Fig. S9). The small temperature-dependent increase in R_2 and lack of significant T_2-weighted image enhancement (Fig. 2b) suggests a negligible Curie spin relaxation mechanism.[61] The negligible Curie contribution is unsurprising as the spin quantum number (J or S) ($S = 1/2$) for ORCAs is lower than that for GBCAs, with electronic relaxation times (T_{1e}) being much larger for ORCAs (μs to high ns vs ps or less).[61,62] Therefore, inner-sphere relaxation mechanisms would likely be dominated by Solomon-Bloembergen relaxation and chemical exchange.[61,63] Given the low relaxation rates of glucoverdazyl at high field (especially R_2), it is also possible there is an outer-sphere contribution to the relaxation rate as well.[64]

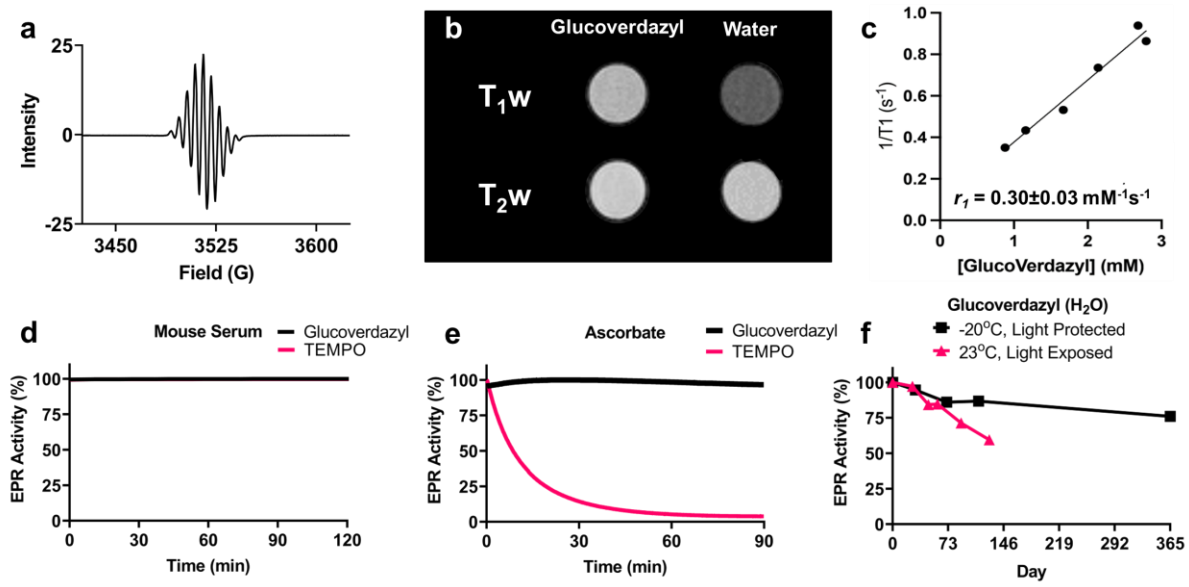

Figure 2.2 Paramagnetic characteristics and stability of glucoverdazyl. **a** EPR spectrum of a 5 mM glucoverdazyl solution in phosphate buffered saline (PBS) acquired at room temperature. **b** T_1 and T_2 weighted MRI images of 3 mM glucoverdazyl solution in PBS acquired at 3 T at 37°C. **c** Longitudinal relaxivity of glucoverdazyl at pH 7.4 in PBS by 3 T MRI. The stability of glucoverdazyl (black) and TEMPO (pink) was determined by EPR during 2 h incubation in (**d**) mouse serum or (**e**) 4 mM sodium ascorbate buffer at pH 7.4. **f** The storage stability of 5 mM glucoverdazyl solutions left exposed to light at room temperature (pink) or left at −20°C protected from light (black) as determined by EPR.

While contrast enhancement was similar to TEMPO, the tetrazinanone radical present in glucoverdazyl was substantially more stable compared to the nitroxyl ORCA counterpart (Fig. 2d, e). Neither glucoverdazyl nor TEMPO showed any change in radical persistence when incubated in mouse serum (Fig. 2d), however in the presence of ascorbate, a biological reductant, there was no loss of the glucoverdazyl radical but complete reduction of the TEMPO nitroxyl radical within 90 min (Fig. 2e). Glucoverdazyl stability was also evaluated in the presence of hydrogen peroxide and glutathione (Supplementary Fig. S10), in the presence of Fenton chemistry (Supplementary Fig. S11), and superoxide generated from the xanthine-xanthine oxidase reaction (Supplementary Fig.

S12). In all cases, glucoverdazyl maintained its radical character. In addition, glucoverdazyl was found to be stable at basic pH (i.e. pH 11) by both EPR and relaxation rate measurements, and demonstrating a small enhancement in relaxation rate at pH 3 ($\varepsilon^* = 1.33$ relative to pH 7) (Supplementary Fig. S13). The stability of the glucoverdazyl radical in solution was evaluated over time at room temperature in direct light or at −20°C in complete darkness. Periodic EPR sampling of these solutions showed that glucoverdazyl maintained over 50% of its radical character after 4 months being stored on the benchtop, while the frozen solution maintained over 80% of its radical activity after 1 year (Fig. 2f). This demonstrated the resiliency of the glucoverdazyl delocalized radical exposed to bioreductive conditions, as well as its shelf-life and storability.

The binding of glucoverdazyl to human serum albumin (HSA) at physiological levels was investigated in vitro in order to better define the putative mechanism of MRI contrast enhancement *in vivo*. The fractional binding of glucoverdazyl was evaluated (Supplementary Fig. S14A), demonstrating negligible glucoverdazyl binding to HSA at concentration below 1 mM and an increase in binding with [HSA] > 1 mM driven by mass action. These results were recapitulated by the investigation of fluorophore displacement from HSA binding site I and site II (Supplementary Fig. S14B). Again, no binding at either site was noted below 1 mM HSA, with a slight increase in fluorophore displacement in both sites I and II suggestive of non-specific interactions driven by mass action. Finally, we evaluated the effect of the presence of HSA on T_1-shortening by glucoverdazyl (Supplementary Fig. S14C). The relaxation rate of a 0.1 mM and 1.0 mM glucoverdazyl solution was measured in the presence of HSA varying from 0% to 22.5% w/v in PBS. Similarly, to what was observed in the HSA binding experiments, there was very little change in glucoverdazyl relaxation rate at HSA concentrations at and below physiological levels (i.e. [HSA] <1

mM), before mass action-induced non-specific binding occurred. These data suggest that glucoverdazyl will not interact with serum albumin once injected *intravenously*.

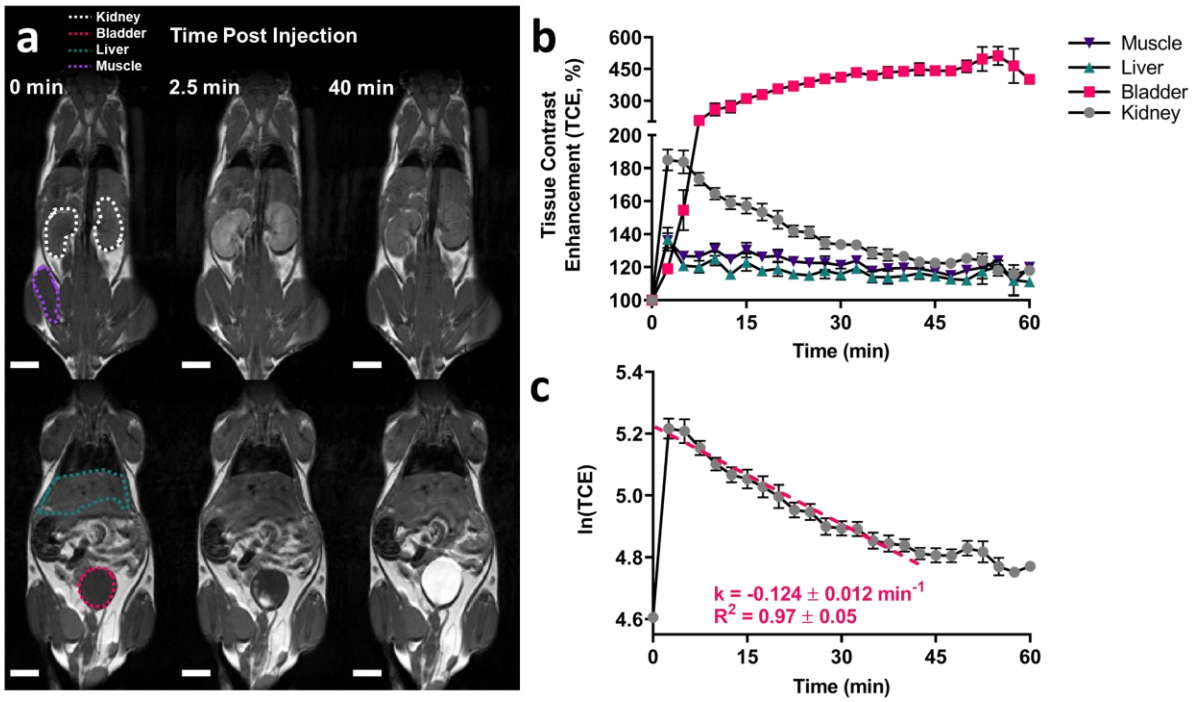

Figure 2.3 Glucoverdazyl localization and clearance in vivo in healthy BALB/c mice. a MRI scans of BALB/c mice were acquired both pre-injection and every 2.5 min post-injection following the administration of glucoverdazyl (3 mmol/kg). The white scalebar represents 5 mm. **b** Regions-of-interest (ROIs)were selected and the average intensity at each timepoint was acquired. Data are presented as mean ± SEM for n = 9 mice. **c** The semi-natural logarithmic transformation and line of best fit (pink) is drawn from t = 2.5 min to t = 40 min of the kidney clearance curve. Data are presented as mean ± SEM for n = 9 mice. The linear regression was determined individually for each mouse, and *k* was calculated as the slope of the fitted line. *k* and R^2 are shown as mean ± SD.

The cytocompatibility of glucoverdazyl was evaluated in H460 human lung carcinoma epithelial cells and demonstrated no cyto- toxicity compared to untreated cells at concentrations up to 10 mM (Supplementary Fig. S15). Glucoverdazyl was evaluated for contrast media suitability in vivo following *intravenous* injections to 9 BALB/c mice. An administered dose of 3 mmol/kg was

chosen based on the difference in r_1 between glucoverdazyl and Gadovist® (~ 10-fold), and considering the standard clinically recommended Gadovist® dose of 0.1 mmol/kg. This dose of glucoverdazyl was still well below the maximum concentration we evaluated for cytocompatibility. Following injection, T_1-weighted images were acquired every 2.5 min following a pre-injection scan, which was used to establish baseline voxel intensity. Limited contrast enhancement was observed in the muscle and liver, with uptake and clearance isolated to the urinary system (Fig. 3a). Overall, contrast enhancement relative to pre-contrast scans reached 127 ± 9% in the muscle, a 121 ± 10% in the liver, and 184 ± 21% in the kidneys 5 min post injection (Fig. 3b). The average clearance time after injection, determined by the return of the kidney ROI to baseline intensity, was ~40 min, coinciding with the plateau of the bladder ROI signal increase. At this timepoint, we observed contrast enhancement of 120 ± 8% in the muscle, 115 ± 7% in the liver, 127 ± 8% in the kidneys, and 438 ± 48% in the bladder. The clearance kinetics of glucoverdazyl through the kidneys matched that of one-phase decay, affording the determination of the renal decay time constant (RDTC, k in min^{-1}) from the slope of the semi-natural log plot of the data (Fig. 3c). Linear regression was applied from the contrast intensity maximum at t = 2.5 min to the timepoint of the most consistent return to baseline at t = 40 min. The k determined from the average data from 9 healthy BALB/c mice was $-0.124 \pm 0.012\ min^{-1}$, with an R^2 of 0.97 ± 0.05, demonstrating excellent reproducibility of this baseline measure of healthy kidney function.

With the observation that glucoverdazyl was being primarily taken up by the kidneys, cytocompatibility studies were repeated with high glucoverdazyl concentrations in human renal proximal tubule cells (hRPT, Supplementary Fig. S16). While glucoverdazyl resulted in no significant increase in cell death compared to untreated cells after a 24 h incubation, >90% of the hRPT were dead after only a 4 h incubation with TEMPO. This stark difference in cytocompatibility

highlights an additional key performance difference between TEMPO and verdazyl- derived ORCAs. The cell uptake of glucoverdazyl by hRPT cells and glucose-starved HepG2 cells was evaluated by EPR spectroscopy, and indicated that glucoverdazyl was not taken up in any detectable manner (Supplementary Fig. S17). Overall, low extraurinary glucoverdazyl biodistribution, the relatively fast renal clearance time of glucoverdazyl, and its demonstrated cytocompatibility suggest that glucoverdazyl may be well suited to MRI-based evaluation of kidney function.

2.6.3. Glucoverdazyl-DCE-MRI of Acute Kidney Injury Through Unilateral Ureteral Obstruction

A unilateral ureteral obstruction (UUO) mouse model was used to determine the effectiveness of glucoverdazyl as a DCE-MRI agent for an AKI caused by obstructive nephropathy. The surgical obstruction of the left ureter prevents fluid clearance, leading to hydronephrosis and dramatically reduced kidney function of the ipsilateral kidney. Both sham (left kidney was touched by a surgical instrument) and surgical UUO (left kidney was ligated) mouse groups were evaluated. The change in voxel-wise intensity over time within the kidneys was determined for the entire left and right kidney (Fig. 4a, *top panel*), as well as their cortex and medullary/renal pelvis (MRP) regions (Supplementary Fig. S18). Voxel-wise mapping of the RDTC (Fig. 4a, *bottom panel*) was used to evaluate changes in kidney function. Hydronephropathy was evident by the ablation of the medullary region on day 3, which continued to worsen at day 7, a hallmark of the UUO model.[65] The kidney contralateral to the ligated ureter in the UUO mice did not show any obvious morphological changes.

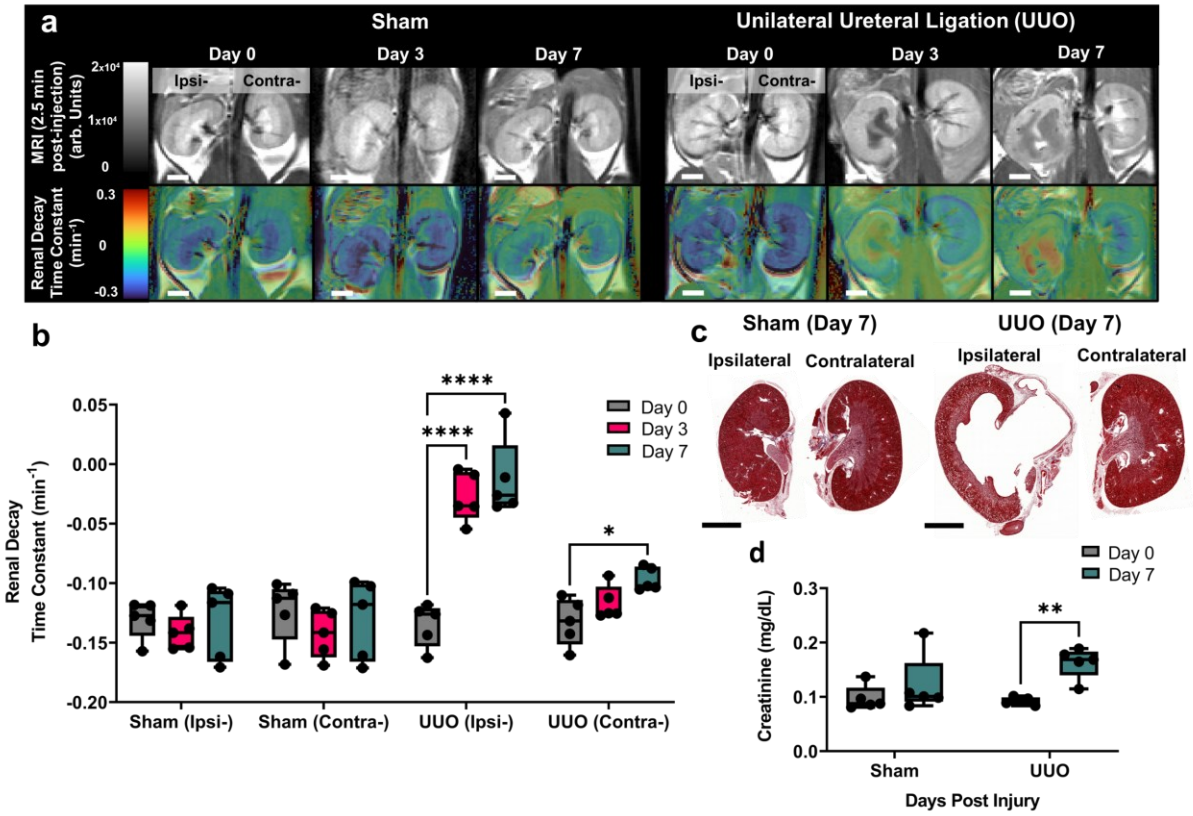

Figure 2.4 Glucoverdazyl-enhanced DCE-MRI in a mouse mode of unilateral ureteral obstruction. **a** T_1-weighted images of kidneys at t = 2.5min post-injection (top) and RDTC maps (bottom) for Sham and UUO groups. The white scalebar represents 2 mm. **b** RDTC values for each kidney at each post-injury time-point. Data are presented as box-and-whisker plots of the single average RDTC value from each kidney (ipsi- or contralateral) individually, from each mouse (n = 5). **c** Representative histology selected from one of the five paired mouse kidneys from sham (left) and UUO (right) treatment groups stained by PAS. The black scalebar represents 6mm. **d** Serum creatinine levels of sham (grey) and UUO (turquoise) mice on the two sampled days. Data are presented as boxplots individual values of SCr. Statistical analysis was done by repeated measures two-way ANOVA followed by a Tukey post-hoc test. In all graphs, *p = 0.019, **p = 0.003, and ****p<0.0001. In all boxplots, whiskers are drawn from the minimum to maximum values, box bounds represent the interquartile range, and the line within the box represents the median.

The RDTC was determined in C57/Bl6 mice prior to surgery in order to define the optimal time interval for glucoverdazyl clearance prior to the analysis of data from diseased mice (Supplementary Fig. S18). In the sham-treated mice, no significant changes in RDTC were noted (Fig. 4b) on days 3 or 7 relative to day 0 across both kidneys. In UUO-treated mice, however, a significant change in RDTC of the ipsilateral kidney was observed, increasing from $k = -0.135 \pm 0.018\ \text{min}^{-1}$ on day 0 to $k = -0.028 \pm 0.014\ \text{min}^{-1}$ on day 3, and $k = -0.013 \pm 0.032\ \text{min}^{-1}$ day 7. The RDTC of the contralateral kidney in UUO mice was unchanged between days 0 and 3 ($k = -0.133 \pm 0.020$ min^{-1} versus $k = -0.117 \pm 0.014\ \text{min}^{-1}$, respectively), but showed a significant increase in RDTC by day 7 ($k = -0.097 \pm 0.010\ \text{min}^{-1}$). Altered physiology of the contralateral kidney following UUO is expected in rodent models, with the induction of macrophage-to-myofibroblast transition,[66] fibrosis,[66,67] and altered cortical mitochondrial function[68] previously reported. Our data demonstrate that glucoverdazyl-mediated DCE-MRI was able to detect the contralateral kidney functional impairment early after ipsilateral ureteral obstruction.

In comparison to the RDTC, mapping area under the curve (AUC) was unreliable for evaluating kidney function using glucoverdazyl (Supplementary Figs. S18, S19). AUC relies heavily on the raw intensity values of the kidney voxel during each scan, and is the average outcome over uptake, retention, and excretion processes. As such, alterations in AUC may indicate abnormalities, but with the underlying deficiency remaining indiscernible across contributing processes. In both the sham and UUO-treated mice, no significant difference in AUC was found between day 0 and any other of the post-injury time points in either the contralateral or ipsilateral kidneys, except for a significant decrease in AUC between days 3 and 7 observed in sham mice. Overall, the alterations in kidney function revealed by RDTC mapping were not recapitulated in the AUC-derived analyses. Histological and serum creatinine (SCr) analysis was performed as

gold standard measures to corroborate pathology we observed through image-based functional evaluation. Both the morphology and fibrosis staining of the sham kidneys and the ipsilateral kidney in UUO-treated mice were unremarkable, while the kidney ipsilateral to ureteral obstruction clearly shows hydronephropathy (Fig. 4c). No significant change in SCr was detected in the sham mice between days 0 and 7 post-surgery, while a significant increase is observed in the UUO mice (Fig. 4d). The observed changes in SCr align well with those previously reported in UUO models, and recapitulate the observed alterations in RDTC.[69–71] The fact that AUC measurements do not parallel the measured alteration in SCr supports the use of RDTC as a measure of kidney function by glucoverdazyl-mediated DCE-MRI.

While the damage caused to the kidney ipsilateral to the ureteral obstruction is evident even on anatomical MRI, the UUO model demonstrated that standard glucoverdazyl-mediated DCE-MRI techniques with simple kinetic mapping can be used to show regional and structural defects across both kidneys, highlighting the functional changes arising in the contralateral kidney even before positive fibrosis staining. A regional analysis of the data discriminating glucoverdazyl clearance from the cortex *versus* medulla & renal pelvis was performed (Supplementary Fig. S18). Here, we are able to clearly discern an impairment in glucoverdazyl clearance caused by a decrease in kidney function, while also mapping where the pathological process is taking place within the kidney, which is valuable towards the evaluation of AKI.[44–46]

2.6.4. Glucoverdazyl-DCE-MRI of Acute-to-Chronic Kidney Injury Through Folic Acid-Induced Nephropathy (FAN)

We next sought to evaluate renal function in a more complex, fibrosis- driven model of kidney disease mediated through folic acid-induced nephropathy (Fig. 5). FAN is the result of tubular folic acid crystal formation following systemic administration of folic acid.[72] This

crystallization causes an initial phase of severe AKI, which is followed by fibrotic renal scarring. The fibrotic scars lead to long term, progressive decline in kidney function, resulting in CKD around 3-weeks post- folate injection. The FAN model was implemented in BALB/c mice rather than the more commonly used C57Bl/6 strain, as BALB/c mice were more resistant to the AKI phase, which had a very high mortality rate in C57Bl/6 mice.

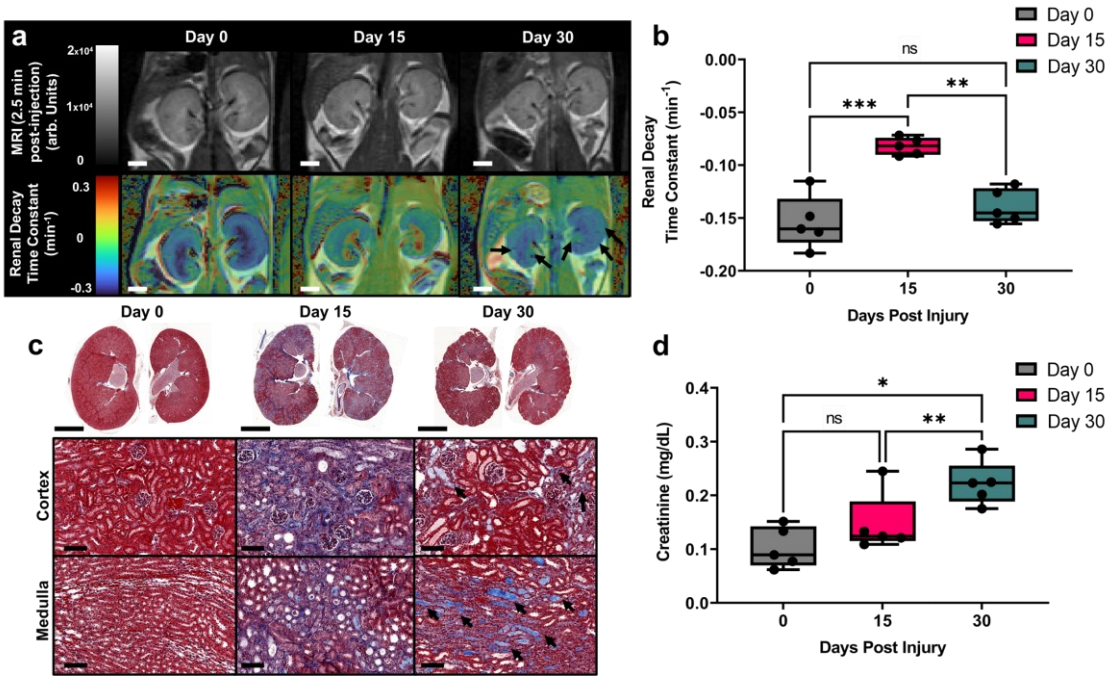

Figure 2.5 Glucoverdazyl-enhanced DCE-MRI of folic acid-induced nephropathy. a T_1-weighted images of kidneys at t = 2.5 min post-injection (top) and RDTC maps (bottom). The white scalebar represents 2 mm. **b** RDTC values for kidneys at each post-injury time point. Data are presented as box-and-whisker plots of the single average RDTC value from both kidneys of each mouse (n= 5). $^{**}p = 0.004$ and $^{***}p = 0.001$. **c** Representative histology selected from one of the five paired mouse kidneys (top) with enlargements of the cortical or medullary regions (bottom) stained by PAS. The top black scalebar represents 6 mm and the bottom black scalebar represents 100 µm. Black arrows indicate positive histological staining for fibrotic areas, represented by a light blue color. **d** Serum creatinine levels of FAN mice at each post-injury time point (n = 5). $^{*}p = 0.025$ and $^{**}p = 0.004$. Statistical analysis was done by repeated measures two-way ANOVA followed by a Tukey post hoc test. In all boxplots, whiskers are drawn from the minimum to maximum values, box bounds represent the interquartile range, and the line within the box represents the median.

Through anatomical imaging, we noted a reduction in overall kidney size from day 0 to day 30 in both kidneys, which has previously been reported for the FAN model[73] (Fig. 5a). Following glucoverdazyl-mediated DCE-MRI, the RDTC was determined for both kidneys prior to the administration of folate, and 15- and 30-days following administration (Fig. 5a, b). A significant increase in RDTC was observed at day 15 ($k = -0.154 \pm 0.025\ \mathrm{min}^{-1}$ on day 0 and $k = -0.082 \pm -0.008\ \mathrm{min}^{-1}$ on day 15), followed by a return to baseline RDTC at day 30 ($k = -0.139 \pm 0.016\ \mathrm{min}^{-1}$). The AKI phase of FAN resulted in a significant increase in medullary and cortical RDTC, indicative of both, poor drainage into the ureter and poor glomerular filtration. The recovery of RDTC by day 30 is anticipated in the early stages of the CKD phase of the disease since AKI often presents with much more severe kidney dysfunction than early stages of CKD, which agreed with the literature using the same post-injury time points.[73] The RDTC maps at day 30 indicate the presence of localized, striated regions within the cortex presenting relatively slower clearance rates (Fig. 5a *right*, black arrows), recapitulating the fibrotic striations observed in kidney histology at day 30 (Fig. 5c, light blue regions are indicators of fibrotic tissue highlighted by black arrows). Therefore, the combination of spatial and temporal information into single kidney maps, as is done in the case of RDTC images (Fig. 5a), afford an increased diagnostic power not afforded by existing nephrological techniques limited either to spatial or kinetic information alone. Importantly, the AUC maps do not provide the same correlative structure-function detail that was obtained from RDTC (i.e. no striations as a result of fibrosis), indicating that AUC is an underpowered method through which kidney function can be evaluated (Supplementary Fig. S21). Data segmented into cortex or medulla & renal pelvis regions were also evaluated (Supplementary Fig. S20).

Kidneys were harvested at days 0, 15, and 30 post-folate injection and evaluated by histology to confirm both AKI and CKD (Fig. 5c), and blood sampling was performed over the same time intervals for SCr determination (Fig. 5d). Histological evaluation revealed substantially increased fibrotic regions in the kidney at day 15, which decreased in severity at day 30 (Fig. 5c). SCr showed a slight elevation on day 15 relative to day 0, which was expected as AKI usually shows only small elevations in SCr.[73,74] However, by day 30 during early stages of CKD, SCr was significantly increased compared to both day 0 and day 15, which is a strong indicator of a severe decrease in kidney function associated with FAN and early stages of CKD.[75–77] Overall, the importance of combining spatial and temporal dimensions in urography was highlighted by the assessment of the FAN model. During severe AKI, minor elevations in SCr were seen, but a much larger increase in RDTC was obtained with differential regional effects across the kidney (Fig. 5a). Of unique value, RDTC maps indicated discrete regions of greater kidney dysfunction (i.e. cortical striations), which may correspond to areas of fibrosis observed in the histological evaluations (Fig. 5c).

2.6.5. Comparison of Glucoverdazyl DCE-MRI to a Validated Measure of GFR

To further develop glucoverdazyl-mediated DCE-MRI as an imaging- based approach to renal functional evaluation, we compared image- derived RDTC values to an established and validated measure of GFR: transdermal fluorescence monitoring.[64–67] The transdermal GFR technique relies on the *intravenous* injection of a fluorescent molecule (i.e. FITC-sinistrin) cleared solely by filtration, and the transdermal monitoring of blood-pool fluorescence over time. The transdermal technique applies a one-phase decay model to determine the RDTC of the fluorescence intensity *versus* time curve, which is then corrected to GFR by a previously determined correction factor.[78–81] We used the transdermal GFR measurements as a benchmark against which the glucoverdazyl-specific correction factor could be derived.

In a second cohort of FAN-induced mice, both transdermal (Fig. 6a) and glucoverdazyl-mediated DCE-MRI (Fig. 6b) measurements were performed on day 0 (black), day 15 (pink) and day 30 (cyan). Both techniques resulted in the hallmark one-phase decay curve, yielding RDTC values after semi-natural log transformations. On day 0, the mean RDTC determined by glucoverdazyl-mediated DCE-MRI ($k = -0.135 \pm 0.022\ \mathrm{min}^{-1}$) was significantly different to the RDTC determined by transdermal fluorescence ($k = -0.075 \pm 0.011\ \mathrm{min}^{-1}$) (Supplementary Fig. S16). The difference in these RDTCs is unsurprising given the different locations for data sampling. While the transdermal measurements evaluate the signal from blood pool only within the first few millimeters under the surface of the skin, the DCE-MRI technique directly evaluates kidney tissue. By applying the transdermal technique, baseline GFR = 1584 ± 238 µl/min/100 g b.w. was determined for BALB/c mice, which is in line with literature values reported.[82] By pooling the baseline DCE-MRI-derived RDTC data obtained for day 0 BALB/c mice, and by using the average GFR measurement from the transdermal technique, we were able to derive a glucoverdazyl-specific correction factor for the conversion of RDTC to GFR. With this factor, we calculated GFR from our RDTC values for each post-injury time point and compared them to the GFR values determined by the transdermal technique (Fig. 6c), demonstrating that there was no significant difference in GFR determined by the two methods.

Deviations in measured GFR between the DCE-MRI and transdermal methods applied were observed (Fig. 6c), and these differences may derive from the very different locations for data sampling: The transdermal method relies on blood pool signal near the skin surface, where DCE-MRI evaluates contrast change within the kidneys directly. During severe AKI on day 15, RDTC is dictated entirely by the reduction in filtration as a result of AKI (Fig. 6d). On day 30, however, the major AKI has healed and early CKD as a result of fibrotic scarring has begun. The fibrotic scarring is

more prevalent in the medulla (Fig. 5c), which means excretion dictates the value of RDTC. Because our MRI method spatially maps contrast agent clearance on the kidney itself, the differentiation of filtration-limited clearance *versus* excretion-limited clearance is possible. Since the transdermal method measures agent in the blood pool (i.e. non-spatially encoded data), this distinction in reduced clearance mechanisms cannot be made. Overall, the data support the application of glucoverdazyl as a DCE-MRI contrast agent suitable for mapping GFR over the volume of the kidney.

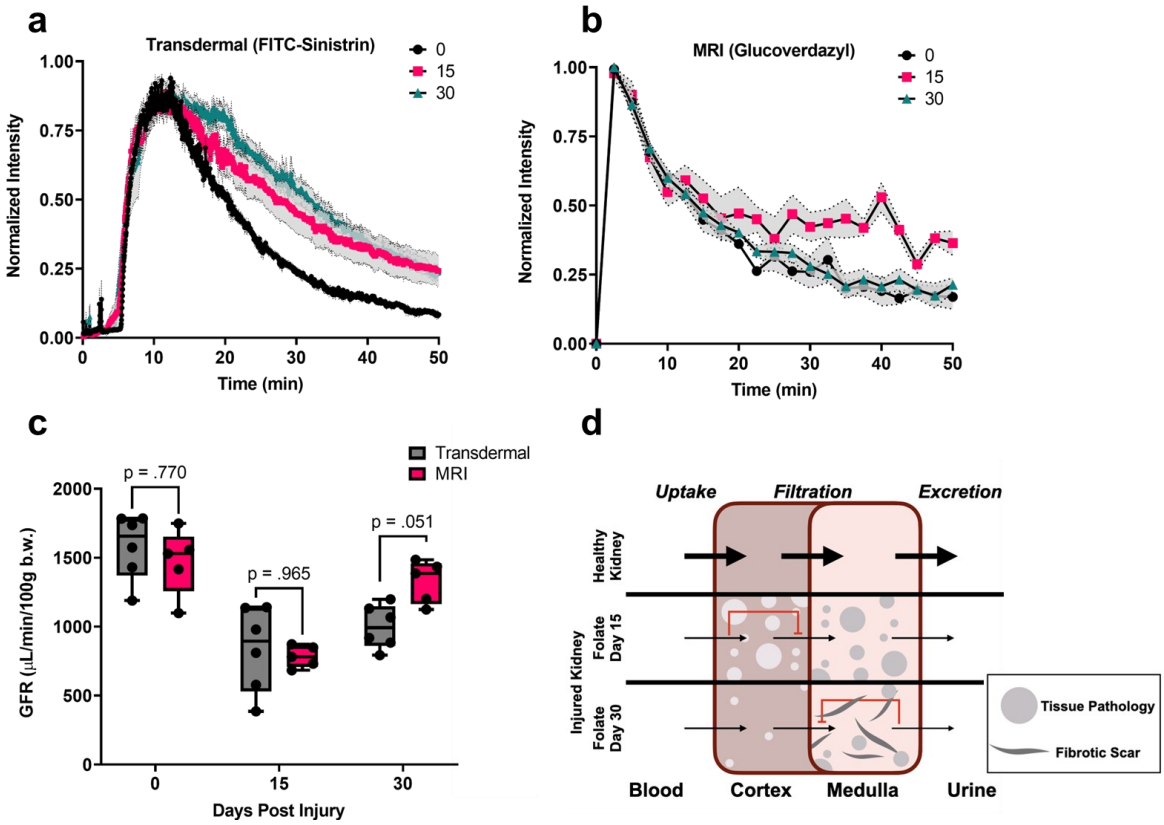

Figure 2.6 Determination of glomerular filtration rate (GFR) by transdermal fluorescence and dynamic contrast enhanced magnetic resonance imaging (DCE-MRI) in folic acid nephropathic (FAN) mice. a Normalized fluorescence intensity of the transdermal fluorescence clearance of FITC-sinistrin in FAN mice on day 0, 15, and 30 (black, pink, and turquoise, respectively). Data are presented as the mean of each time point for each replicate ± SEM for $n = 6$ mice. **b** Normalized DCE-MRI intensity of glucoverdazyl-enhanced scans over time for FAN mice on day 0, 15, and 30 (black, pink, and turquoise, respectively). Data are presented as the mean of each time point for each replicate ± SEM for $n = 5$ mice. **c** GFR values for FAN mice determined by either transdermal fluorescence (grey) or DCE-MRI (pink). Data are presented as box-and-whisker plots of the GFR for each mouse. Statistical analysis was done by mixed measures two-way ANOVA followed by a Tukey post-hoc test. The *p-value* for each test is labelled on the graph. **d** Illustration of glucoverdazyl clearance through the kidney by DCE-MRI to elaborate on differences between transdermal and DCE-MRI measurements. In all boxplots, whiskers are drawn from the minimum to maximum values, box bounds represent the interquartile range, and the line within the box represents the median.

We have optimized and scaled a preparation of a tetrazinanone-derived ORCA, glucoverdazyl, and demonstrated its superior redox stability and cytocompatibility relative to previously used nitroxyl radical contrast agents. Glucoverdazyl appears especially useful for renal DCE-MRI due to its biodistribution limited to the kidneys, ureter, and bladder. Glucoverdazyl has been applied to imaging the UUO model of severe AKI, and FAN model of AKI-to-CKD progression, showing regional functional changes within the kidneys in the form of RDTC. The evaluation of dynamic image sets using RDTC fully corroborated kidney dysfunction in both models. Through benchmarking to a validated transdermal fluorescent recording method of measuring GFR, we demonstrated that glucoverdazyl affords the reliable determination of GFR by DCE-MRI. Importantly, this approach to GFR measurement not only adds a spatial component to urography, but also determines GFR free from the reliance upon patient demographic characteristics, which has been shown to be error-prone. In order to overcome limitations of the current study, future improvements to RDTC measurement will include a higher frequency of imaging and volumetric image acquisition through pulse sequence development, which would increase the confidence and fidelity of our proposed approach to MRI urography. Overall, glucoverdazyl may provide safer MRI-based diagnoses in patients with known or suspected AKI and/or CKD. Given the molecular properties of this organic radical, especially Its inability to enter the cell, cytocompatibility and preliminary bio- compatibility, localization to the kidneys and quick clearance, tetrazinanone-based ORCAs represent an innovative and promising class of metal-free MRI contrast agent.

2.7. Methods

All animal studies were conducted under Animal Use Protocol HIe- 3640-R1 approved by the IACUC at the University of Ottawa.

2.7.1. General reagents

All chemical reagents were purchased from Sigma-Aldrich and used as is unless otherwise reported, with the exception of *N′*-(propan-2-yl)(tert- butoxy)carbohydrazide, which was purchased from AABlocks. All sol- vents were HPLC grade, except for water (18.2 MΩ cm Millipore water).

2.7.2. Experimental procedures

All NMR spectra were acquired on a Bruker AVANCE II 400 MHz or a Bruker Avance III HD 600 MHz NMR spectrometers, operating at 400 MHz or 600 MHz for ^{1}H spectra, and 100 or 150 MHz for ^{13}C spectra, respectively. Chemical shifts are given in ppm. In all spectra, $CDCl_3$ was referenced to 7.26 ppm (^{1}H NMR) and 77.0 ppm (^{13}C NMR); MeOH-D_4 to 3.31 ppm (^{1}H NMR) and 49.0 ppm (^{13}C NMR). All high- resolution mass spectrometry (HRMS) were performed on a Micro- mass Q-TOF I with electrospray ionization. All EPR spectra were acquired on a Bruker EMX plus EPR at room temperature. All MRI acquisitions were performed on a 3 T pre-clinical MRI scanner (MR Solutions, Ltd.). For all MRI image data analysis, only relevant slices of the tissue of interest were included in analysis (i.e., scans for kidney region only used slices with the kidney visible). All data processing, mapping, and quantity generation was done using a custom program written in MATLAB 2020A®. A copy of this program is available from the authors upon request. GraphPad Prism 9.5 was used to generate all graphs, graphical figures, and statistical results.

2.7.3. Synthesis of N-({N'-[(tert-butoxy)carbonyl]-N-(propan-2-yl) hydrazinecarbonyl}(propan-2-yl)amino)(tert-butoxy) formamide (2)

Dry Et_3N (4 ml, 28.8 mmol) was added to a solution of toluene (50 mL, pre-died with 4 Å molecular sieves) followed by the addition of 4 g of *N'*-(propan-2-yl)(tert-butoxy)carbohydrazide (4 g, 23 mmol). The solution was cooled to 0°C while being stirred in the atmosphere of N_2. A 15% phosgene solution in toluene (9 mL, 12.7 mmol) was added dropwise for ~1 min (phosgene is highly toxic, caution is needed when performing the addition), and the reaction mixture was stirred for 1 h at 0°C, then warmed to room temperature (rt) and stirred for an additional 18 h. The reaction was quenched by adding MeOH (50 mL), was stirred for 30 min at rt and was evaporated. The mixture was diluted with 10% solution of NH_4OH (75 mL) and extracted with EtOAc (3 × 15 mL). The combined organic was washed with brine (40 mL), dried with Na_2SO_4, filtered, and evaporated, resulting in a white pow- der. The powder was dissolved in 80 mL of hot, dry heptane and set aside for 18 h at 4°C to induce crystallization of the product. The crystals were filtered off and were washed with hexanes. The product was dried on the high vacuum, (colourless crystals, compound 2, 2.55 g, 59%).

^{1}H NMR (400 MHz, $CDCl_3$) δ 6.40 (s, D_2O exch., 2H), 4.15 (s, 2H), 1.43 (s, 18H), 1.12 (s, 12H).

^{13}C NMR (150 MHz, $CDCl_3$) δ = 155.9, 81.1, 52.6, 50.3, 28.2, 19.2 (broad signal).

HRMS (ESI): Calculated for $C_{17}H_{34}N_4O_5Na$ [M+Na]+: 397.2411, found 397.2427.

2.7.4. Synthesis of 1,3-diamino-1,3-bis(propan-2-yl)urea dihydrochloride

Compound 2 (2.55 g) was resuspended in EtOH (25 mL) in a 100 mL round bottom flask and heated to 80°C (air condenser). Concentrated HCl (10 mL) was added dropwise and the solution was left stirring for 30 min at 80 °C. The solution was cooled to rt and the solvent was evaporated. The crude product was consecutively co-evaporated once with methanol, toluene, and

petroleum ether (50 mL for each). The crude product of sufficient purity for the subsequent step was dried on the high vacuum giving 1,3-diamino-1,3-bis(propan-2-yl)urea dihydrochloride as colourless solid in quantitative yield.

^{1}H NMR (400 MHz, MeOH-D_4) δ 4.23 (heptet, *J* = 6.8 Hz, 2H), 1.35 (d, *J* = 6.8 Hz, 12H).

^{13}C NMR (150 MHz, MeOH-D_4) δ = 162.3, 56.2, 18.9.

HRMS (ESI): Calculated for $C_7H_{18}N_4ONa$ [M+Na]+: 197.1355, found 197.1378.

2.7.5. Synthesis of 6-[(1 S,2 R,3 R,4 R)-1,2,3,4,5-pentahydroxypentyl]- 2,4-bis(propan-2-yl)-1,2,4,5-tetrazinan-3-one (3)

1,3-Diamino-1,3-bis(propan-2-yl)urea dihydrochloride, (1.55 g, 6.3 mmol) was resuspended in H_2O (10 mL) with stirring at rt. A 5 mL solution of D-glucose (1.2 g, 6.7 mmol) and NaOAc (1.1 g, 13.4 mmol,) in water was added dropwise over 1 min, followed by stirring at rt for 18 h. The reaction mixture was extracted with *n*-butanol (6 × 10 mL). The combined organic extract was dried with Na_2SO_4, was filtered, and was evaporated. The resulting oil was consecutively co-evaporated with methanol, toluene, and petroleum ether (50 mL of each). The resulting product was dried on the high vacuum overnight and giving pale yellow crystals (compound 3,1.48 g, 70%).

^{1}H NMR (400 MHz, MeOH-D_4) δ 4.53 (m, 2H), 4.06 – 3.95 (m, 2H), 3.84 – 3.70 (m, 2H), 3.68 – 3.57 (m, 2H), 3.53 (d, *J* = 2.7 Hz, 1H), 1.13 (dd, *J* = 6.8, 3.4 Hz, 6H), 1.08 (d, *J* = 6.5 Hz, 6H).

^{13}C NMR (150 MHz, MeOH-D_4) δ = 155.7, 73.0, 72.4, 72.2, 72.0, 70.0, 65.0, 19.8, 19.7, 19.3, 18.9.

HRMS (ESI): Calculated for $C_{13}H_{28}N_4O_6Na$ [M+Na]+: calculated 359.1910, found 359.1907.

2.7.6. Synthesis of 3-oxo-6-[(1 S,2 R,3 R,4 R)-1,2,3,4,5-pentahydrox- ypentyl]-2,4-bis(propan-2-yl)-1,2,3,4-tetrahydro-1,2,4,5-tetrazin- 1-yl (glucoverdazyl, 4)

Compound 3 (1.48 g, 4.41 mmol) was resuspended in H_2O (5 mL with stirring (rt)). In a separate vessel, potassium ferricyanide (4.44 g, 13.5 mmol) was mixed with 80 drops (~ 4.5 mL) of $NaHCO_3$ solution (2 M), followed by the addition of water (5 mL); the mixture was solubilized using an ultrasound bath. Resulting solution was added drop- wise over 1 min to the original reaction mixture with stirring followed by stirring (rt) for about 30 min or until effervescence stopped. The mixture was extracted with *n*-butanol (6 × 10 mL). The combined organic was dried with Na_2SO_4, was filtered, and was evaporated. The resulting oil was consecutively co-evaporated with methanol (50 mL), three times with toluene (50 mL each time), was cooled to 0°C, followed by co- evaporation with petroleum ether (50 mL). The resulting product was dried on the high vacuum overnight to give a bright yellow fine powder (glucoverdazyl 4, 1.09 g, 74%). Given the compound was radical in nature it could not be characterized by NMR; changes in HPLC elution time, as well as HRMS and EPR were used to confirm structure and purity. HPLC traces can be seen in Supplementary Fig. S7.

HRMS (ESI): Calculated for $C_{13}H_{25}N_4O_6Na$ [M+Na]+: calculated 356.1676, found 356.1672.

2.7.7. Phantom MRI of Glucoverdazyl

Glucoverdazyl was prepared in 1 × PBS in standard NMR tubes. These were inserted into a 50 mL Falcon tube containing ultrasound gel, comprising the MRI phantom. The MRI phantom was placed into a 38-mm-diameter send and receive volume coil and inserted into the MRI scanner. A multislice Rapid Imaging with Refocused Echoes (RARE) pulse sequence was implemented for evaluation of phantoms using the following parameters for T_1-weighted imaging: slice thick- ness of 5 mm, FOV of 40 × 40 mm, averages = 3, matrix size = 96 × 96, TE_{eff} =

11 ms, echo spacing = 7 ms, TR = 720 ms, and acquisition time of 2 min 16 s. For T_2-weighted imaging, all parameters were the same as for T_1-weighted images, except TE_{eff} = 68 ms and TR = 4800 ms, and acquisition time was 7 min 28 s.

For relaxivity measurements, the same imaging phantom was used with contrast agent concentrations of 1 to 3 mM. Contrast agent concentration following imaging was verified by electron para- magnetic spectroscopy. To measure the longitudinal relaxation rate (R_1), an inversion recovery RARE sequence was implemented with the following parameters: Slice thickness of 5 mm, FOV of 50 × 50 mm, average = 1, matrix size = 96 × 96, TE_{eff} = 17 ms, TR = 5000 ms, TI = 50, 75,100, 150, 200, 250, 300, 400, 600, 800, 1200, 2400, and 4800 ms, and acquisition time of 2 min 30 s *per* TI. Longitudinal relaxation rates were extracted using the mapping MATLAB 2 routine written by J. Barral, M. Etezadi-Amoli, E. Gudmundson, and N. Stikov (2009), and modified by J. Rioux (2022). The longitudinal relaxivity (r_1) was extracted from the slope of the plot of $1/T_1$ vs. contrast agent concentration.

2.7.8. Glucoverdazyl Stability Measurements

The EPR was tuned to a 5 mM sample of glucoverdazyl or TEMPO in PBS prior to any stability measurements. Solutions of glucoverdazyl or TEMPO were prepared (20 mM in mouse serum or 5 mM in a 4 mM sodium ascorbate buffer (pH 7.4)). A single spectrum was acquired and the peak height of the most intense peak for either compound was locked. EPR scans were then acquired every 5 s for 2 h (mouse serum) or 1.5 h (ascorbate) to measure percent change in the activity. Storability was measured using a 5 mM solution of glucoverdazyl in water left in a fume hood exposed to light, or wrapped in tinfoil and left in a dark freezer at −20°C. Periodically, these

solutions were sampled and measured by the EPR after it was tuned using a freshly prepared 5 mM sample of glucoverdazyl.

2.7.9. MRI Animal Studies

Mice were housed under 12 h light/dark cycle, and ambient temperature of 20-24 °C and 45 to 65% humidity. All mice were provided water and fed *ad libitum* with Rodent Laboratory Chow. Mice were anesthetized with isoflurane, placed on a heated cradle and inserted into the MRI. Consecutive T_1-weighted RARE images as previously described above were acquired prior to and every 2.5 min thereafter for 60 min after contrast agent injection. *T_1-weighted Imaging:* slice thickness of 1 mm, FOV of 50 × 50 mm, averages = 3, matrix size = 96 × 96, TE_{eff} = 11 ms, echo spacing = 7 ms, TR = 720 ms, and acquisition time of 2 min 16 s. In all cases 3 mmol/kg of contrast agent was injected *intravenously* through a tail vein catheter, which was flushed with saline to ensure full dose of contrast agent was received.

2.7.10. MRI Data Processing and Analysis

Intensity-over-time curves:

SUR files were used to avoid to remove any automatic gain functions associated with the MRI. All scans and slices were normalized to water-filled fiducial marker placed alongside the mice during all scans. A MATLAB routine was used to draw slice- wise regions-of-interest (ROIs) at each scan time point to generate voxel-wise intensity over time data, presented as the mean intensity of the total ROI for each timepoint normalized to 100% for the lowest intensity voxel for the first scan. A graphical representation of the following workflow can be seen in Supplementary Fig. S1.

Renal decay time constant values and image maps:

Using the voxel- wise T_1-weighted intensity values for each imaging time point during the ~45 min scan, a MATLAB script extracted RDTC (k), as follows: A linear regression was fit to the natural logarithm (*ln*) of the intensity values from $t = 2.5$ to 40 min, and the slope of this linear regression yielded the RDTC, k, *per* voxel. The k map was then overlaid on an anatomical reference image to yield the image-based maps of kidney function. An ROI was drawn over each kidney, or over the renal cortex and the medulla of each kidney. RDTC values shown in graphs are the mean of voxel-wise k values within an ROI.

Area-under-the-curve values and image maps:

A baseline correction was applied to each of the voxel-wise intensity-over-time curves by subtracting the lowest voxel value, setting the baseline to 0 across all time points. The integral of this curve for each voxel was acquired using the trapezoids function to generate an area-under-the-curve (AUC) value from $t = 0$ min to $t = 50$ min. AUC values shown in graphs the mean of *per* voxel k values derived from each mouse. Maps of AUC were overlaid on top of the image acquired at $t = 0$ min.

2.7.11. Glucoverdazyl Tissue Localization by DCE-MRI

Glucoverdazyl-enhanced scans were acquired from healthy (9) male BALB/c mice (8 weeks old) as described in the *MRI animal studies* section, and normalized intensity-over-time curves were acquired as described in the *MRI data processing and analysis* section, with ROIs drawn for kidney, liver, bladder, and muscle tissues.

2.7.12. Serum Creatinine Measurements.

Blood was drawn from the saphenous vein at day 0 and at each post-injury time point prior to glucoverdazyl-enhanced MRI. Blood was centrifuged for 10 min (room temperature, 900 xg) and the serum was collected from the fractionated sample. Samples were stored at −80 °C until use. Serum creatinine (SCr) was determined by quantitative HPLC (Agilent 1260 Infinity with diode array equipped with a 2.1 mm × 50 mm, 5 μm particle size Agilent Zorbax 300-SCX column) against a creatinine standard curve by modifying a previously reported method[83]. Briefly, creatinine was dissolved in HPLC mobile phase (15 mM sodium acetate buffer at pH 4.2 with 4% methanol and 1% acetonitrile (AcN) and serially diluted to create a creatinine standard curve from 0 μM to 12.5 μM through integration of the produced HPLC peak at 234 nm (Bruker HyStar PP)). Standards and samples were acquired at a flow rate of 0.5 mL/min with an isocratic mobile phase. Creatinine was extracted from mouse serum samples after thawing by precipitating proteins with a 4:1 ratio of AcN and 0.5% acetic acid to serum. Samples were vortexed, then left at −20 °C for 30 min to allow complete precipitation. Samples were centrifuged at 12,000 xg (10 min, 4°C), and the supernatant transferred to a new tube. Tubes were dried to remove acidified AcN through heated vacuum centrifugation for 45 min at 50°C. The pellet was resuspended in 60 μl of mobile phase and samples were quantified by HPLC, integrating the matched-time elution peak seen in the standard curve at 234 nm.

2.7.13. Animal Models of Kidney Disease

Glucoverdazyl-enhanced scans for all mice in both UUO and FAN dis- ease models were acquired as described in the *MRI animal studies* section, and normalized intensity-over-time curves were acquired as described in the *MRI data processing and analysis* section, with ROIs drawn for kidney tissue. All studies were initiated when animals were 9–10 weeks of age. All

animals were housed in conventional breeding cages, fed standard rodent chow and received water *ad libitum*, and were housed in a facility with a 12-h light cycle.

Unilateral ureter obstruction:

The unilateral ureter obstruction (UUO) mouse model of acute kidney injury (AKI) was performed in C57/Bl6 mice as was previously reported in the literature.[84] Briefly, 10 female C57/Bl6 (8 weeks old) mice were sorted in to groups of 5 for either the sham procedure or UUO procedure. Mice were imaged with glucoverdazyl contrast immediately prior to surgery (day 0). Mice were anesthetized by constant isoflurane inhalation. The left kidney of the mouse was accessed laparoscopically and the left ureter was either touched gently with a surgical instrument (sham group) or tied shut with a suture (UUO group). The wound was sutured closed and mice were imaged by glucoverdazyl contrast MRI 3-days and 7-days post injury. On day 7, mice were sacrificed by cervical dislocation. The kidneys were removed and fixed in paraformaldehyde, after which they were sectioned and stained with PAS, with images acquired using a slide scanner.

Folic acid-induced nephropathy (glucoverdazyl contrast MRI):

The folic acid-induced nephropathy (FAN) model of AKI-to-chronic kidney disease (CKD) injury was performed in BALB/c mice following a modified procedure previously reported in the literature.[85–89] We observed a high mortality rate at doses of 250 mg/kg of folic acid (FA) administered to CD1 and C57/Bl6 mice. BALB/c mice have been shown to be more resistant to obstruction-mediated injuries and to more reliably generate CKD.[69,90] Five male BALB/c mice (8 weeks old) were imaged by glucoverdazyl-enhanced MRI at day 0. Immediately following scans, mice were injected *intraperitoneally* with 125 mg/kg FA in a 0.3 M sodium bicarbonate solution. Daily *subcutaneous* fluid support was necessary for the first 5 days following FA

injection. By day 7, mice were stabilized and housed normally without fluid assistance. Mice were re-imaged by glucoverdazyl-enhanced MRI 15-days and 30-days post injury. On day 30, mice were sacrificed by cervical dislocation. The kidneys were removed and fixed in paraformaldehyde, then sectioned and stained with PAS. Images were acquired using a slide scanner. A group of mice underwent the same disease induction without any glucoverdazyl-enhanced MRI and were sacrificed at day 15 to obtain histology for this time point.

2.7.14. Folic Acid-Induced Nephropathy (Transdermal Fluorescence)

A parallel group of 6 male BALB/c mice (8 weeks old) had kidney dis- ease induced identically to those in the contrast MRI group, except that transdermal fluorescence measurements, as previously described in the literature, were performed instead of MRI.[78–82] Briefly, prior to any data acquisition, hair was removed from the right dorsolateral aspect of the mice. The next day, a transdermal fluorescence monitor (MediBeacon, Inc.) was affixed to the shaved area by a proprietary windowed adhesive patch. The battery was connected to the trans- dermal monitor and a 5 min baseline was established. A solution of FITC-sinistrin (150 µl, 0.2 mg/kg) was injected *intravenously* through the tail vein, and data was collected for 55 min. Day 0 data collection immediately preceded intraperitoneal FA injection, and was repeated 15-days and 30-days post injury, at which point mice were sacrificed by cervical dislocation.

2.7.15. Euthanasia

All animals were euthanized by cardiac puncture under isoflurane anesthesia.

2.7.16. Conversion from RDTC to Glomerular Filtration Rates

Data acquired from transdermal fluorescence was analyzed by proprietary software (MediBeacon, Inc.) to generate RDTC and glomerular filtration rate (GFR) values based pharmacokinetic model fitting. We generated GFR and RDTC data using this software with a one-phase decay model of the raw data with no corrections. MediBeacon uses a previously determined factor that can directly convert RDTC to GFR, based on mouse data they generated and compared to measured GFR through traditional methods.[78–82] Given the consistency of our RDTCs in our 14 measured healthy BALB/c mice, we derived a conversion factor for glucoverdazyl RDTC to GFR based on the average GFR value of the 6 healthy male BALB/c mice measured through transdermal fluorescence. By comparing the difference between our pooled RDTC compared to the transdermal-derived RDTC to normalize the average GFR value, the conversion factor was derived. This conversion was applied to the mean RDTC value presented in the data to generate a GFR comparison between the two methods.

2.7.17. Statistics

Statistical analyses for experiments are reported in the corresponding methods section. Normality was assumed where appropriate for all data sets. Prior to ANOVA, Levene's test was use to confirm equal variance, and visual quantile-quantile plot analysis was used to confirm homoscedasticity.

2.7.18. Reporting summary

Further information on research design is available in the Nature Portfolio Reporting Summary linked to this article.

2.8. Data Availability

All data can be found in the main manuscript or the SI, quantified source data associated with the current study are available at https://doi.org/10.6084/m9.figshare.23538426. Raw animal images can be obtained from the corresponding author upon request due to large file size constraints.

2.9. Code Availability

MATLAB code for generating quantitative RDTC and AUC data, as well as their associated functional maps, is available at https://github.com/ncalvert994/Glucoverdazyl.

2.10. References

1. Bello, A. K. *et al.* Quality of Chronic Kidney Disease Management in Canadian Primary Care. *JAMA Netw Open* **2**, e1910704 (2019).
2. Vanholder, R. *et al.* Fighting the unbearable lightness of neglecting kidney health: the decade of the kidney. *Clin Kidney J* **14**, 1719–1730 (2021).
3. Van Buren, P. N. & Toto, R. Hypertension in Diabetic Nephropathy: Epidemiology, Mechanisms, and Management. *Adv Chronic Kidney Dis* **18**, 28–41 (2011).
4. Chawla, L. S., Eggers, P. W., Star, R. A. & Kimmel, P. L. Acute Kidney Injury and Chronic Kidney Disease as Interconnected Syndromes. *New England Journal of Medicine* **371**, 58–66 (2014).
5. Arry, B. *et al.* Effects of Losartan on Renal and Cardiovascular Outcomes in Patients with Type 2 Diabetes and Nephropathy. *https://doi.org/10.1056/NEJMoa011161* **345**, 861–869 (2001).
6. Ruggenenti, P. *et al.* Renoprotective properties of ACE-inhibition in non-diabetic nephropathies with non-nephrotic proteinuria. *Lancet* **354**, 359–364 (1999).

7. Childs, R. *et al.* Regression of metastatic renal-cell carcinoma after nonmyeloablative allogeneic peripheral-blood stem-cell transplantation. *N Engl J Med* **343**, 750–758 (2000).

8. Perkovic, V. *et al.* Canagliflozin and Renal Outcomes in Type 2 Diabetes and Nephropathy. *New England Journal of Medicine* **380**, 2295–2306 (2019).

9. Levin, A. & Stevens, P. E. Early detection of CKD: the benefits, limitations and effects on prognosis. *Nature Reviews Nephrology 2011 7:8* **7**, 446–457 (2011).

10. Chen, T. K., Knicely, D. H. & Grams, M. E. Chronic Kidney Disease Diagnosis and Management: A Review. *JAMA* **322**, 1294 (2019).

11. Gama, R. M. *et al.* Estimated glomerular filtration rate equations in people of self-reported black ethnicity in the United Kingdom: Inappropriate adjustment for ethnicity may lead to reduced access to care. *PLoS One* **16**, e0255869 (2021).

12. Luis-Lima, S. & Porrini, E. An Overview of Errors and Flaws of Estimated GFR versus True GFR in Patients with Diabetes Mellitus. *Nephron* **136**, 287–291 (2017).

13. Niemantsverdriet, M. S. A. *et al.* GFR estimation is complicated by a high incidence of non-steady-state serum creatinine concentrations at the emergency department. *PLoS One* **16**, (2021).

14. Levey, A. S., Titan, S. M., Powe, N. R., Coresh, J. & Inker, L. A. Kidney Disease, Race, and GFR Estimation. *Clin J Am Soc Nephrol* **15**, 1203–1212 (2020).

15. Romagnani, P. *et al.* Chronic kidney disease. *Nat Rev Dis Primers* **3**, (2017).

16. Srivastava, A. *et al.* The Associations of Plasma Biomarkers of Inflammation With Histopathologic Lesions, Kidney Disease Progression, and Mortality—The Boston Kidney Biopsy Cohort Study. *Kidney Int Rep* **6**, 685–694 (2021).

17. Molitoris, B. A. Measuring glomerular filtration rate in acute kidney injury: Yes, but not yet. *Crit Care* **16**, 158 (2012).

18. van der Weijden, J. *et al.* Early increase in single-kidney glomerular filtration rate after living kidney donation predicts long-term kidney function. *Kidney Int* **101**, 1251–1259 (2022).

19. Taylor, A. T. Radionuclides in Nephrourology, Part 1: Radiopharmaceuticals, Quality Control, and Quantitative Indices. *Journal of Nuclear Medicine* **55**, 608–615 (2014).

20. Miftari, R. *et al.* Impact of Gate 99mTc DTPA GFR, Serum Creatinine and Urea in Diagnosis of Patients with Chronic Kidney Failure. *Acta Informatica Medica* **25**, 99 (2017).

21. Esteves, F. P., Halkar, R. K., Issa, M. M., Grant, S. & Taylor, A. Comparison of Camera-Based 99mTc-MAG3 and 24-Hour Creatinine Clearances for Evaluation of Kidney Function. *http://dx.doi.org/10.2214/AJR.05.1025* **187**, (2012).

22. Taylor, A. T. Radionuclides in Nephrourology, Part 2: Pitfalls and Diagnostic Applications. *Journal of Nuclear Medicine* **55**, 786–798 (2014).

23. Nikken, J. J. & Krestin, G. P. MRI of the kidney—state of the art. *Eur Radiol* **17**, 2780 (2007).

24. Warwick, J. & Holness, J. Measurement of Glomerular Filtration Rate. *Semin Nucl Med* **52**, 453–466 (2022).

25. Irrera, P. *et al.* Dynamic Contrast Enhanced (DCE) MRI-Derived Renal Perfusion and Filtration: Experimental Protocol. *Methods in Molecular Biology* **2216**, 429–441 (2021).

26. Eikefjord, E. *et al.* Use of 3D DCE-MRI for the Estimation of Renal Perfusion and Glomerular Filtration Rate: An Intrasubject Comparison of FLASH and KWIC With a Comprehensive Framework for Evaluation. *http://dx.doi.org/10.2214/AJR.14.13226* **204**, W273–W281 (2015).

27. Weinreb, J. C. *et al.* Use of Intravenous Gadolinium-Based Contrast Media in Patients With Kidney Disease: Consensus Statements from the American College of Radiology and the National Kidney Foundation. *Kidney Med* **3**, 142–150 (2021).

28. Caroli, A., Remuzzi, A. & Lerman, L. O. Basic principles and new advances in kidney imaging. *Kidney Int* **100**, 1001–1011 (2021).

29. Schieda, N. *et al.* Gadolinium-Based Contrast Agents in Kidney Disease: A Comprehensive Review and Clinical Practice Guideline Issued by the Canadian Association of Radiologists. *Can J Kidney Health Dis* **5**, 1–17 (2018).

30. Goldstein, K. M. *et al.* Risk of Nephrogenic Systemic Fibrosis after Exposure to Newer Gadolinium Agents. *Risk of Nephrogenic Systemic Fibrosis after Exposure to Newer Gadolinium Agents* (2019).

31. Wermuth, P. J. & Jimenez, S. A. Nephrogenic Systemic Fibrosis. *Scleroderma: From Pathogenesis to Comprehensive Management* 137–159 (2022) doi:10.1007/978-1-4419-5774-0_13.

32. Le Fur, M. & Caravan, P. The biological fate of gadolinium-based MRI contrast agents: a call to action for bioinorganic chemists. *Metallomics* **11**, 240–254 (2019).

33. Chrysochou, C. *et al.* Low Risk for Nephrogenic Systemic Fibrosis in Nondialysis Patients Who Have Chronic Kidney Disease and Are Investigated with Gadolinium-Enhanced Magnetic Resonance Imaging. *Clin J Am Soc Nephrol* **5**, 484 (2010).

34. Woolen, S. A. *et al.* Risk of Nephrogenic Systemic Fibrosis in Patients With Stage 4 or 5 Chronic Kidney Disease Receiving a Group II Gadolinium-Based Contrast Agent: A Systematic Review and Meta-analysis. *JAMA Intern Med* **180**, 223–230 (2020).

35. Lenkinski, R. E. Gadolinium Deposition and Retention in the Brain: Should We Be Concerned? *Radiol Cardiothorac Imaging* **1**, (2019).

36. Aime, S. & Caravan, P. Biodistribution of gadolinium-based contrast agents, including gadolinium deposition. *J Magn Reson Imaging* **30**, 1259–1267 (2009).

37. Guo, B. J., Yang, Z. L. & Zhang, L. J. Gadolinium Deposition in Brain: Current Scientific Evidence and Future Perspectives. *Front Mol Neurosci* **11**, (2018).

38. Akakuru, O. U. *et al.* The Transition from Metal-Based to Metal-Free Contrast Agents for T1 Magnetic Resonance Imaging Enhancement. *Bioconjug Chem* **30**, 2264–2286 (2019).

39. Fuchs, J. *et al.* Nitroxide radical biostability in skin. *Free Radic Biol Med* **15**, 415–423 (1993).

40. Lee, H. *et al.* Supramolecular and biomacromolecular enhancement of metal-free magnetic resonance imaging contrast agents. *Chem Sci* **11**, 2045–2050 (2020).

41. Rajca, A. *et al.* Organic radical contrast agents for magnetic resonance imaging. *J Am Chem Soc* **134**, 15724–15727 (2012).

42. Le, T. N., Grewal, H., Changoco, V., Truong, V. & Brook, D. J. R. Water soluble, chiral, verdazyl radicals derived from aldoses. *Tetrahedron* **72**, 6368–6374 (2016).

43. Petunin, P. V. *et al.* Verdazyl Radical Building Blocks: Synthesis, Structure, and Sonogashira Cross-Coupling Reactions. *European J Org Chem* **2018**, 4802–4811 (2018).

44. Park, M. S. Molecular Dynamics Simulations of the Human Glucose Transporter GLUT1. *PLoS One* **10**, e0125361 (2015).

45. Patra, M., Awuah, S. G. & Lippard, S. J. Chemical approach to positional isomers of glucose-platinum conjugates reveals specific cancer targeting through glucose-transporter mediated uptake in vitro and in vivo. *J Am Chem Soc* **138**, 12541 (2016).

46. Koivisto, B. D. & Hicks, R. G. The magnetochemistry of verdazyl radical-based materials. *Coord Chem Rev* **249**, 2612–2630 (2005).

47. Kamachi, M., Enomoto, H., Shibasaka, M., Mori, W. & Kishita, M. Magnetic Properties of Polymer Containing Verdazyl in the Side Chain. *Polym J* **18**, 439–441 (1986).

48. Paré, E. C., Brook, D. J. R., Brieger, A., Badik, M. & Schinke, M. Synthesis of 1,5-diisopropyl substituted 6-oxoverdazyls. *Org Biomol Chem* **3**, 4258 (2005).

49. Solea, A. B. *et al.* Versatile synthesis of chiral 6-oxoverdazyl radical ligands – new building blocks for multifunctional molecule-based magnets. *Dalton Transactions* **47**, 4785–4789 (2018).

50. Barclay, T. M., Hicks, R. G., Lemaire, M. T., Thompson, L. K. & Xu, Z. Synthesis and coordination chemistry of a water-soluble verdazyl radical. structures and magnetic properties of M(H $_2$ O) $_2$ (vdCO $_2$) $_2$ ·2H $_2$ O (M = Co, Ni; vdCO $_2$ = 1,5-dimethyl-6-oxo-verdazyl-3-carboxylate). *Chem. Commun.* 1688–1689 (2002) doi:10.1039/B204851E.

51. Al-Husseini, J. K., Stanton, N. J., Selassie, C. R. D. & Johal, M. S. The Binding of Drug Molecules to Serum Albumin: The Effect of Drug Hydrophobicity on Binding Strength and Protein Desolvation. *Langmuir* **35**, 17054–17060 (2019).

52. Calabretta, R., Gallina, C. & Giordano, C. Sodium Cyanoborohydride Reduction of (Benzyloxycarbonyl)- and (tert-Butoxycarbonyl)hydrazones. *Synthesis (Stuttg)* 536–539 (1991).

53. Kumar, V., Shova, S., Maurel, V., Novitchi, G. & Train, C. Crystallographic Insights into the Synthesis and Magnetic Properties of Oxoverdazyl Radicals Functionalized by Benzoic Acid. *Eur J Inorg Chem* **2018**, 517–524 (2018).

54. Le, T.-N., Grewal, H., Changoco, V., Truong, V. & Brook, D. J. R. Water soluble, chiral, verdazyl radicals derived from aldoses. *Tetrahedron* **72**, 6368–6374 (2016).

55. Matuschek, D. *et al.* Profluorescent verdazyl radicals – synthesis and characterization. *Chem Sci* **6**, 4712–4716 (2015).

56. Hicks, R. G., Koivisto, B. D. & Lemaire, M. T. Synthesis of multitopic verdazyl radical ligands. Paramagnetic supramolecular synthons. *Org Lett* **6**, 1887–1890 (2004).

57. Barr, C. L., Chase, P. A., Hicks, R. G., Lemaire, M. T. & Stevens, C. L. Synthesis and characterization of verdazyl radicals bearing pyridine or pyrimidine substituents: A new family of chelating spin-bearing ligands. *Journal of Organic Chemistry* **64**, 8893–8897 (1999).

58. Massolle, A. *et al.* Towards reliable references for electron paramagnetic resonance parameters based on quantum chemistry: the case of verdazyl radicals. *Physical Chemistry Chemical Physics* **20**, 7661–7675 (2018).

59. Tain, R. W., Scotti, A. M., Li, W., Zhou, X. J. & Cai, K. Influence of Free Radicals on the Intrinsic MRI Relaxation Properties. *Adv Exp Med Biol* **977**, 73–79 (2017).

60. Wahsner, J., Gale, E. M., Rodríguez-Rodríguez, A. & Caravan, P. Chemistry of MRI Contrast Agents: Current Challenges and New Frontiers. *Chem Rev* **119**, 957 (2019).

61. Matsumoto, K. I., Nakanishi, I., Zhelev, Z., Bakalova, R. & Aoki, I. Nitroxyl Radical as a Theranostic Contrast Agent in Magnetic Resonance Redox Imaging. *Antioxid Redox Signal* **36**, 95–121 (2022).

62. Caravan, P., Greenfield, M. T. & Bulte, J. W. M. Molecular factors that determine Curie spin relaxation in dysprosium complexes†. *Magn Reson Med* **46**, 917–922 (2001).

63. Berliner, L., Eaton, G. & Eaton, S. Distance Measurements in Biological Systems by EPR. **19**, (2002).

64. Caravan, P., Ellison, J. J., McMurry, T. J. & Lauffer, R. B. Gadolinium(III) Chelates as MRI Contrast Agents: Structure, Dynamics, and Applications. *Chem Rev* **99**, 2293–2352 (1999).

65. Caravan, P. Strategies for increasing the sensitivity of gadolinium based MRI contrast agents. *Chem Soc Rev* **35**, 512–523 (2006).

66. Chevalier, R. L., Forbes, M. S. & Thornhill, B. A. Ureteral obstruction as a model of renal interstitial fibrosis and obstructive nephropathy. *Kidney Int* **75**, 1145–1152 (2009).

67. Xiong, Y. *et al.* Eplerenone Attenuates Fibrosis in the Contralateral Kidney of UUO Rats by Preventing Macrophage-to-Myofibroblast Transition. *Front Pharmacol* **12**, 83 (2021).

68. Figueroa, S. M. *et al.* Upregulation of Cortical Renin and Downregulation of Medullary (Pro)Renin Receptor in Unilateral Ureteral Obstruction. *Front Pharmacol* **10**, 1314 (2019).

69. Xiong, Y. *et al.* Eplerenone Attenuates Fibrosis in the Contralateral Kidney of UUO Rats by Preventing Macrophage-to-Myofibroblast Transition. *Front Pharmacol* **12**, 83 (2021).

70. Bianco, M. *et al.* The contralateral kidney presents with impaired mitochondrial functions and disrupted redox homeostasis after 14 days of unilateral ureteral obstruction in mice. *PLoS One* **14**, (2019).

71. Eddy, A. A., López-Guisa, J. M., Okamura, D. M. & Yamaguchi, I. Investigating Mechanisms of Chronic Kidney Disease in Mouse Models. *Pediatr Nephrol* **27**, 1233 (2012).

72. Vielhauer, V. *et al.* Obstructive Nephropathy in the Mouse: Progressive Fibrosis Correlates with Tubulointerstitial Chemokine Expression and Accumulation of CC Chemokine Receptor 2- and 5-Positive Leukocytes. *Journal of the American Society of Nephrology* **12**, 1173–1187 (2001).

73. Martínez-Klimova, E., Aparicio-Trejo, O. E., Tapia, E. & Pedraza-Chaverri, J. Unilateral Ureteral Obstruction as a Model to Investigate Fibrosis-Attenuating Treatments. *Biomolecules* **9**, (2019).

74. Fink, M., Henry, M. & Tange, J. D. Experimental folic acid nephropathy. *Pathology* **19**, 143–149 (1987).

75. Jiang, K. *et al.* Mechanism and Treatment of Renal Fibrosis: Multiparametric MRI detects longitudinal evolution of folic acid-induced nephropathy in mice. *Am J Physiol Renal Physiol* **315**, F1252 (2018).

76. Doi, K. *et al.* Attenuation of Folic Acid-Induced Renal Inflammatory Injury in Platelet-Activating Factor Receptor-Deficient Mice. *Am J Pathol* **168**, 1413 (2006).

77. Waikar, S. S. & Bonventre, J. V. Creatinine Kinetics and the Definition of Acute Kidney Injury. *Journal of the American Society of Nephrology* **20**, 672–679 (2009).

78. Aparicio-Trejo, O. E. *et al.* Chronic impairment of mitochondrial bioenergetics and β-oxidation promotes experimental AKI-to-CKD transition induced by folic acid. *Free Radic Biol Med* **154**, 18–32 (2020).

79. Yan, L. J. Folic acid-induced animal model of kidney disease. *Animal Model Exp Med* **4**, 329 (2021).

80. Scarfe, L. *et al.* Transdermal Measurement of Glomerular Filtration Rate in Mice. *J Vis Exp* **2018**, (2018).

81. Schreiber, A. *et al.* Transcutaneous measurement of renal function in conscious mice. *Am J Physiol Renal Physiol* **303**, (2012).

82. Friedemann, J. *et al.* Improved kinetic model for the transcutaneous measurement of glomerular filtration rate in experimental animals. *Kidney Int* **90**, 1377–1385 (2016).

83. Shmarlouski, A. *et al.* A Novel Analysis Technique for Transcutaneous Measurement of Glomerular Filtration Rate With Ultralow Dose Marker Concentrations. *IEEE Trans Biomed Eng* **63**, 1742–1750 (2016).

84. Scarfe, L. *et al.* Transdermal Measurement of Glomerular Filtration Rate in Mice. *J Vis Exp* **2018**, 58520 (2018).

85. Schock-Kusch, D. *et al.* Reliability of Transcutaneous Measurement of Renal Function in Various Strains of Conscious Mice. *PLoS One* **8**, e71519 (2013).

86. Yuen, P. S. T. *et al.* A simplified method for HPLC determination of creatinine in mouse serum. *Am J Physiol Renal Physiol* **286**, 1116–1119 (2004).

87. Chaabane, W. *et al.* Renal functional decline and glomerulotubular injury are arrested but not restored by release of unilateral ureteral obstruction (UUO). *Am J Physiol Renal Physiol* **304**, 432–439 (2013).

88. Kang, H. M. *et al.* Defective fatty acid oxidation in renal tubular epithelial cells has a key role in kidney fibrosis development. *Nature Medicine 2014 21:1* **21**, 37–46 (2014).

89. Yuan, Q. *et al.* CPT1α maintains phenotype of tubules via mitochondrial respiration during kidney injury and repair. *Cell Death & Disease 2021 12:8* **12**, 1–12 (2021).

90. Marquez-Exposito, L. *et al.* Acute Kidney Injury is Aggravated in Aged Mice by the Exacerbation of Proinflammatory Processes. *Front Pharmacol* **12**, 1510 (2021).

91. Parchure, M., Ambaye, R. Y., Lalitha, V. S. & Gokhale, S. V. Acute toxicity of folic acid in mice. *Experientia* **41**, 72–73 (1985).

92. Knock, E. *et al.* Strain differences in mice highlight the role of DNA damage in neoplasia induced by low dietary folate. *J Nutr* **138**, 653–658 (2008).

93. Eddy, A. A., López-Guisa, J. M., Okamura, D. M. & Yamaguchi, I. Investigating Mechanisms of Chronic Kidney Disease in Mouse Models. *Pediatr Nephrol* **27**, 1233 (2012).

94. Rabe, M. & Schaefer, F. Non-Transgenic Mouse Models of Kidney Disease. *Nephron* **133**, 53–61 (2016).

2.11. Acknowledgements

The work reported was supported by funding from the Canadian Institutes for Health Research (PJT-180355). N.D.C. and A.K. acknowledge graduate support from the Ontario Graduate Scholarship program. The authors would like to thank F. Mercury for support during MRI acquisitions, Dr. XiaoLing Zhao for the many histological samples she prepared and scanned, as well as Dr. Christopher Boddy and André R. Paquette for use of their HPLC system for serum creatinine measurement.

2.12. Competing Interests

The authors declare no competing interests.

2.13. Additional Information

Correspondence and requests for materials should be addressed to Adam J. Shuhendler.

Peer review information *Nature Communications* thanks Andre Martins and the other, anonymous, reviewer(s) for their contribution to the peer review of this work. A peer review file is available.

2.14. Supplementary Information:

1. General Reagents:

All cell culture reagents and consumables were purchased from ThermoFisher, with the exception of the Epithelial Cell Media and Epithelial Cell Growth Supplement, which were purchased from ScienCell.

2. Experimental Procedures:

All EPR spectra were acquired on a Bruker EMX plus EPR at room temperature. All MRI acquisitions were performed on a 3 T pre-clinical MRI scanner (MR Solutions, Ltd.). For all MRI image data analysis, only relevant slices of the tissue of interest were included in analysis (i.e., scans for kidney region only used slices with the kidney visible). All data processing, mapping, and quantity generation was done using a custom program written in MATLAB 2020A®. A copy of this program is available from the authors upon request. GraphPad Prism 9.5 was used to generate all graphs, graphical figures, and statistical results.

2.1 Phantom MRI, determination of glucoverdazyl longitudinal relaxivity and evaluation of temperature-dependence of relaxation rates.

Contrast agent samples were prepared in 1× PBS in standard NMR tubes, which were then inserted into a 50 mL Falcon tube containing ultrasound gel, comprising the MRI phantom. The MRI phantom was placed into a 38-mm-diameter send and receive volume coil and inserted into the MRI scanner. A multislice Rapid Imaging with Refocused Echoes (RARE) pulse sequence was implemented for evaluation of phantoms using the following parameters for T_1-weighted imaging: slice thickness of 5 mm, FOV of 40 × 40 mm, averages = 3, matrix size = 96 × 96, TE_{eff} = 11 ms, echo spacing = 7 ms, TR = 720 ms, and acquisition time of 2 minutes 16 seconds. For T_2-weighted imaging, all parameters were the same as for T_1-weighted images, except TE_{eff} = 68 ms and TR = 4800 ms, and acquisition time was 7 minutes 28 seconds.

For relaxivity measurements, the same imaging phantom was used with contrast agent concentrations of 1 mM or 0.1 mM contrast agent in 0% to 22.5% HSA in PBS, or 3 mM contrast agent in PBS of pH 3, 7, or 11. Contrast agent concentration following imaging was verified by electron paramagnetic spectroscopy. To measure the longitudinal relaxation rate (R_1), an inversion recovery RARE sequence was implemented with the following parameters: Slice thickness of 5 mm, FOV of 50 × 50 mm, average = 1, matrix size = 96 × 96, TE_{eff} = 17 ms, TR = 5,000 ms, TI = 50, 75,100, 150, 200, 250, 300, 400, 600, 800, 1200, 2400, and 4800 ms, and acquisition time of 2 minutes 30 seconds *per* TI. Longitudinal relaxation rates were extracted using the mapping MATLAB 2 routine written by J. Barral, M. Etezadi-Amoli, E. Gudmundson, and N. Stikov (2009), and modified by J. Rioux (2022). The longitudinal relaxivity (r_1) was extracted from the slope of the plot of $1/T_1$ vs. contrast agent concentration.

High field NMR relaxation measurements were performed at 7.05 T ($\nu_0(^1H)$ = 300.15 MHz) on a Bruker Avance spectrometer. Samples were dissolved in PBS buffer in a mixture of 80:20 H_2O:D_2O. D_2O was used as a field lock. ^1H NMR experiments on pure water at high field with a high Q probe will produce significant radiation damping. So, commonly used inversion recovery experiments for determining T_1 will result in artificially smaller T_1 measurements due to small amounts of transverse magnetization produced with slightly imperfect inversion pulses. This was the case for these samples (data not shown). To alleviate this outcome, a saturation recovery experiment was used to determine T_1. A 3 s CW saturation pulse was used on-resonance prior to the variable delay and read pulse to collect time-arrayed saturation recovery data. Ten – twelve time points were collected at each temperature. T_2 data was collected using a Car-Purcell-Meiboom-Gill (CPMG) sequence with a 20 ms total echo time and an appropriate number of loops to ensure complete loss of signal at each temperature. Eleven time points were collected at each temperature. A relaxation delay of at least 5*T_1 was used for T_1 and T_2 measurements at each temperature. T_1 data was fit using Bruker Topspin 4.1.4 and T2 data was fit using GNAT.[1]

2.2 Glucoverdazyl stability measurements.

The EPR was tuned to a 5 mM sample of glucoverdazyl in PBS prior to any of the stability measurements. Once tuned, glucoverdazyl test solutions were prepared (5 mM in either 10 mM glutathione (GSH), 10 mM hydrogen peroxide (H_2O_2), or 3 mM in PBS of pH = 3, 7, or 11). A single spectrum was acquired and the peak height of the most intense peak for either compound was locked. EPR scans were then acquired every 5 s for 1.5 h (H_2O_2, glutathione, and pH) to measure percent change in the activity.

Glucoverdazyl interaction with hydroxyl radicals generated through Fenton reactions was evaluated through $FeCl_2$ to $FeCl_3$ oxidation catalyzed by H_2O_2. A 20 mM ascorbate buffer (pH = 4.5) containing 1 mM $FeCl_2$ and 10 mM 5,5-dimethyl-1-pyrroline-N-oxide (DMPO). This solution was sparged with N_2 for 30 min and aliquoted into vials containing glucoverdazyl or TEMPO to make a 5 mM concentration of either radical. Immediately prior to EPR scan, 10 mM H_2O_2 was added to the solution. After mixing, the EPR activity was measured, with measurement repeated after 1 h. Aliquots of the 1 h solution were taken and absorbance was measured at 330 nm to determine the amount of $FeCl_3$ produced by $FeCl_2$ oxidation by H_2O_2. Absorbance of TEMPO and glucoverdazyl without Fe(II) were subtracted from the oxidized solutions of each to account for inherent absorbance of these molecules.

Glucoverdazyl interaction with superoxide was evaluated by xanthine (X)/xanthine oxidase (XO) reaction. Solutions of either TEMPO or glucoverdazyl (1.25 mM) in PBS were made containing either 10 mM X, 0.4 U XO, or both. These solutions were incubated under cell culture conditions for 30 min before EPR activity of the solution was measured. Aliquots of the solution were taken and absorbance was measured at 293 nm to determine the production of uric acid, the product of the X/XO reaction. Absorbance of TEMPO and glucoverdazyl without X, XO, or X/XO were subtracted from the oxidized solutions of each to account for inherent absorbance of these molecules.

2.3 Assessment of human serum albumin binding.

Human serum albumin binding assays for both binding and site specificity were adapted from methods by Caravan *et al.,* 2002.[2] A solution of 4.5% w/v human serum albumin (HSA) containing 3 mM glucoverdazyl was prepared. The solution was serially diluted with a 4.5% HSA solution in PBS. The dilutions were incubated under cell culture conditions for 30 min.

Afterwards, free glucoverdazyl was separated from bound glucoverdazyl through ultracentrifugation separation using Centrifree® Ultrafiltration filters (2000 xg, 20 min). The unbound glucoverdazyl in the filtrate was quantified by HPLC using the protocol described in Supplementary section 3.2, after developing a glucoverdazyl HPLC standard curve in PBS. The concentration of bound glucoverdazyl was calculated by subtracting the added concentration of glucoverdazyl from the HPLC determined concentration of free glucoverdazyl.

Site specificity of glucoverdazyl binding was determined by displacement of site-specific fluorophores (dansylamide, site I; dansylglycine, site II). A solution of 4.5% w/v HSA with 3 mM glucoverdazyl was prepared containing 50 mM dansylamide or dansylglycine. These solutions were serially diluted with a 4.5% w/v HSA solution containing 50 mM of either probe but no glucoverdazyl. Another set of solution containing the glucoverdazyl dilutions in HSA but with neither probe was also prepared. These dilutions were incubated under cell culture conditions for 30 min. The dilutions were aliquoted in a black-walled 96-well plate. Fluorescence was measured (ex. 365 nm/em. 480 nm) for each well. Intensity values for glucoverdazyl without probe were subtracted from the same concentration containing probe to account for absorbance incurred by the glucoverdazyl molecule. Corrected fluorescence values were compared to the either fluorescent probe in HSA containing no glucoverdazyl to determine the degree of probe displacement from HSA caused by glucoverdazyl binding.

2.4 Assessment of cell viability in H460 cells.

Large-cell lung cancer cells (H460) were grown in RPMI-1640 (RPMI) media supplemented with 10% fetal bovine serum (FBS) and 1% penicillin-streptomycin (P/S) until 80% confluent, at which point they were passaged. Cells were passaged three times before being seeded in to a 6-well plate and grown until 80% confluent. Cells were seeded to have triplicate

wells of each condition. Cells were then incubated in their regular media supplemented with 0 mM, 2.5 mM, 5 mM, or 10 mM glucoverdazyl, for either 4 h or 24 h. At the respective time points, the media was aspirated and cells were washed three times with 37ºC Dulbecco's phosphate-buffered saline (PBS). Afterwards, cells were lifted with trypsin-EDTA, centrifuged at 400 xg (5 min, 4ºC), aspirated, then resuspended in a 1 mL PBS solution containing 0.2 µM calcein-acetoxymethyl ester (fluorescently staining live cells green) and 16 µM ethidium homodimer-1 (fluorescently staining dead cells red).

Live and dead cell populations were counted by flow cytometry (Beckman-Coulter Gallios Flow Cytometer) using a 488 nm excitation with a 525 nm / 40 nm bandpass filter for calcein-acetoxymethyl ester (live cells, green) and a 620 nm / 20 nm bandpass filter for ethidium homodimer-1 (dead cells, red). After performing, the viable cell population for each condition was determined by comparing the total number of singly-stained, calcein-AM-positive cell counts to the combined total of cells that were singly-stained as positive for live or dead using Kaluza analysis software (Beckman-Coulter).

2.5 Assessment of viability of human renal proximal tubule (hRPT) cells.

hRPT cells were grown in Epithelial Cell Media (EpiMEM) media supplemented with 10% FBS, 1% P/S, and epithelial cell growth supplement (EpiCGS) until 80% confluent, at which point they were passaged. Cells were passaged three times before being seeded in to a 6-well plate and grown until 80% confluent. Cells were seeded to have triplicate wells of each condition. Cells were then incubated in their regular media supplemented with regular media, 10 mM glucoverdazyl, 10 mM 5,5-dimethyl-1-pyrroline *N*-oxide (DMPO, a nitrone spin trap), or 10 mM (2,2,6,6-Tetramethylpiperidin-1-yl)oxyl (TEMPO, a nitroxy radical), for either 4 h or 24 h. At the respective time points, the media was aspirated and cells were washed three times with

37ºC Dulbecco's phosphate-buffered saline (PBS). Afterwards, cells were lifted with trypsin-EDTA, centrifuged at 400 xg (5 min, 4ºC), aspirated, then resuspended in a 1 mL PBS solution containing 0.2 µM calcein-acetoxymethyl ester (fluorescently staining live cells green) and 16 µM ethidium homodimer-1 (fluorescently staining dead cells red).

Live and dead cell populations were counted through flow cytometry (Beckman-Coulter Gallios Flow Cytometer) using a 488 nm excitation with a 525 nm / 40 nm bandpass filter for calcein-acetoxymethyl ester (live cells, green) and a 620 nm / 20 nm bandpass filter for ethidium homodimer-1 (dead cells, red). After performing, the viable cell population for each condition was determined by comparing the total number of singly-stained, calcein-AM-positive cell counts to the combined total of cells that were singly-stained as positive for live or dead using Kaluza analysis software (Beckman-Coulter).

2.6 Evaluation of glucoverdazyl uptake in hRPT and hepatocarcinoma (HEPG2) cells.

hRPT cells were grown in Epithelial Cell Media (EpiMEM) media supplemented with 10% FBS, 1% P/S, and epithelial cell growth supplement (EpiCGS) until 80% confluent, at which point they were passaged. Cells were passaged three times before being seeded in to 6-well plates and grown until 80% confluent. Cells were seeded to have triplicate wells of each condition. Cells were then incubated in their regular media supplemented with regular media or 10 mM glucoverdazyl, and incubated for 24 h. The media was aspirated and cells were washed three times with 37ºC Dulbecco's phosphate-buffered saline (PBS). Afterwards, cells were lifted with trypsin-EDTA, centrifuged at 400 xg (5 min, 4ºC), aspirated, then resuspended in 100 µl of PBS. The concentrated cell solutions were transferred to EPR tubes. A 1 µl aliquot was retained and diluted to obtain the number of cells in each solution.

HEPG2 cells were grown in RPMI supplemented with 10% FBS and 1% P/S until 80% confluent, at which point they were passaged. Cells were passaged three times before being seeded in to 6-well plates and grown until 80% confluent. Cell media was changed to DMEM supplemented with 10% FBS and 1% P/S, containing no glucose for 1 h. The media was replaced after 1 h containing 0 or 10 mM glucoverdazyl. The cells were then incubated for 24 h. The media was aspirated and cells were washed three times with 37ºC with PBS. Cells were then lifted with trypsin-EDTA, centrifuged at 400 xg (5 min, 4ºC), aspirated, then resuspended in 100 µl of PBS. The concentrated cell solutions were transferred to EPR tubes. A 1 µl aliquot was retained and diluted to obtain the number of cells in each solution.

The EPR was tuned to a 5 mM solution of freshly prepared glucoverdazyl in PBS, then samples were measured by the EPR. Concentration was measured against a previously determined standard curve, then normalized to the number of cells previously determined to obtain nM glucoverdazyl per cell.

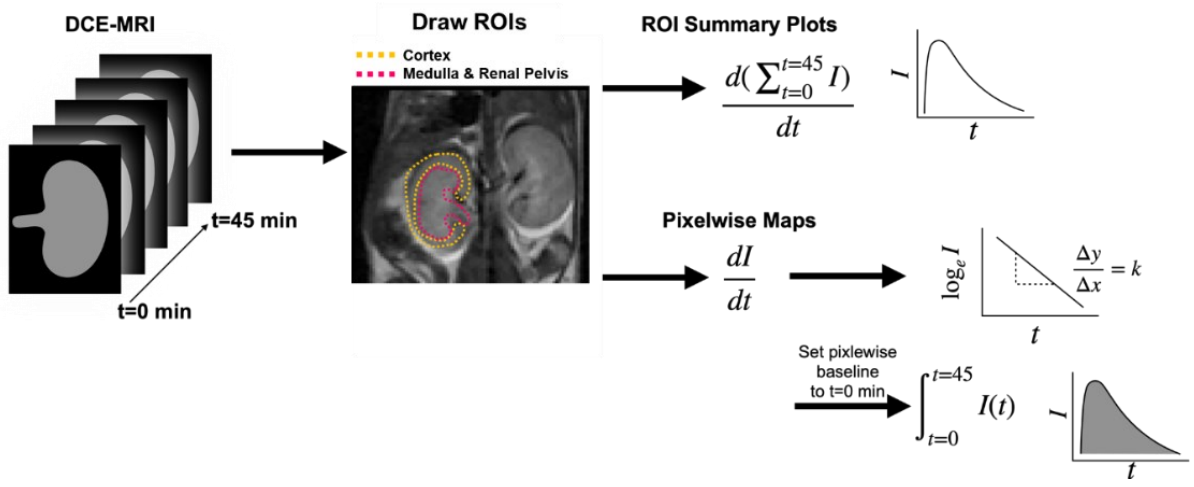

S1. Illustration of DCE-MRI data acquisition and image mapping workflow.

2.7 Statistics

Statistical analyses for experiments are reported in the corresponding methods section. Normality was assumed where appropriate for all data sets. Prior to ANOVA, Levene's test was use to confirm equal variance, and visual quantile-quantile plot analysis was used to confirm homoscedasticity.

3. Characterization Data

3.1 NMR Spectra

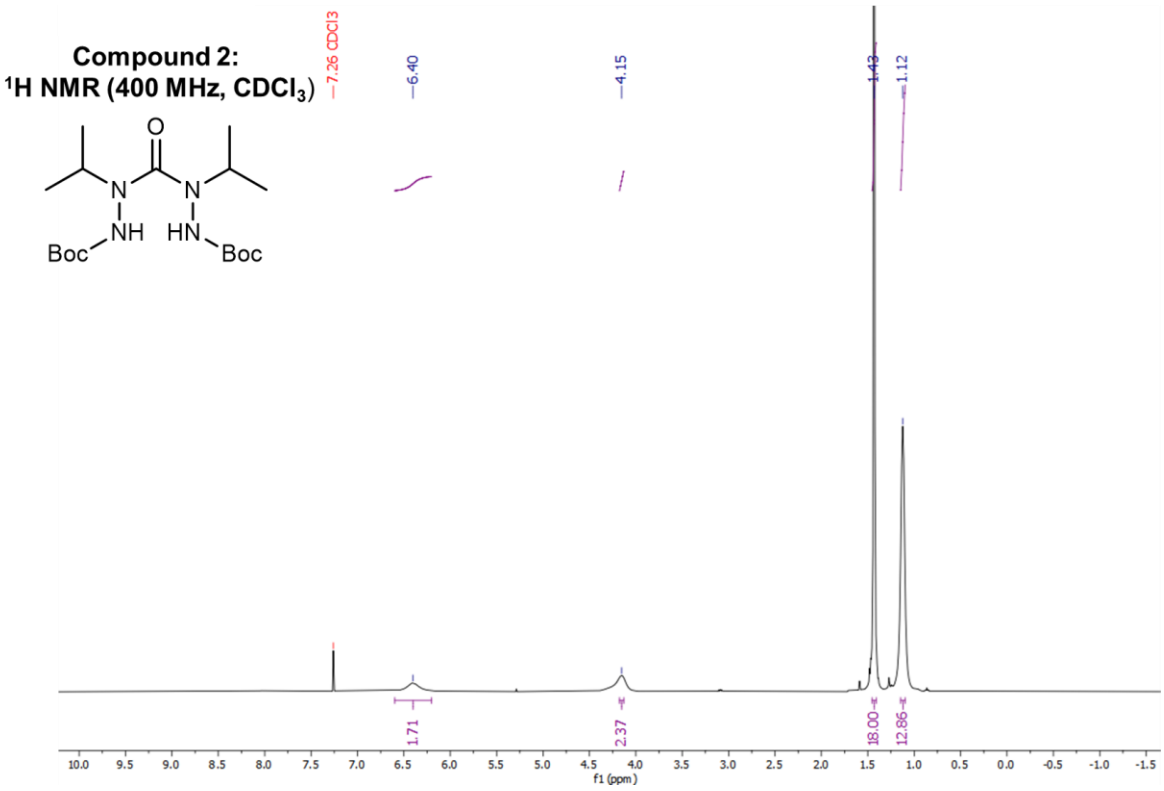

S2. ^{11}H NMR spectrum of compound 2 in $CDCl_3$.

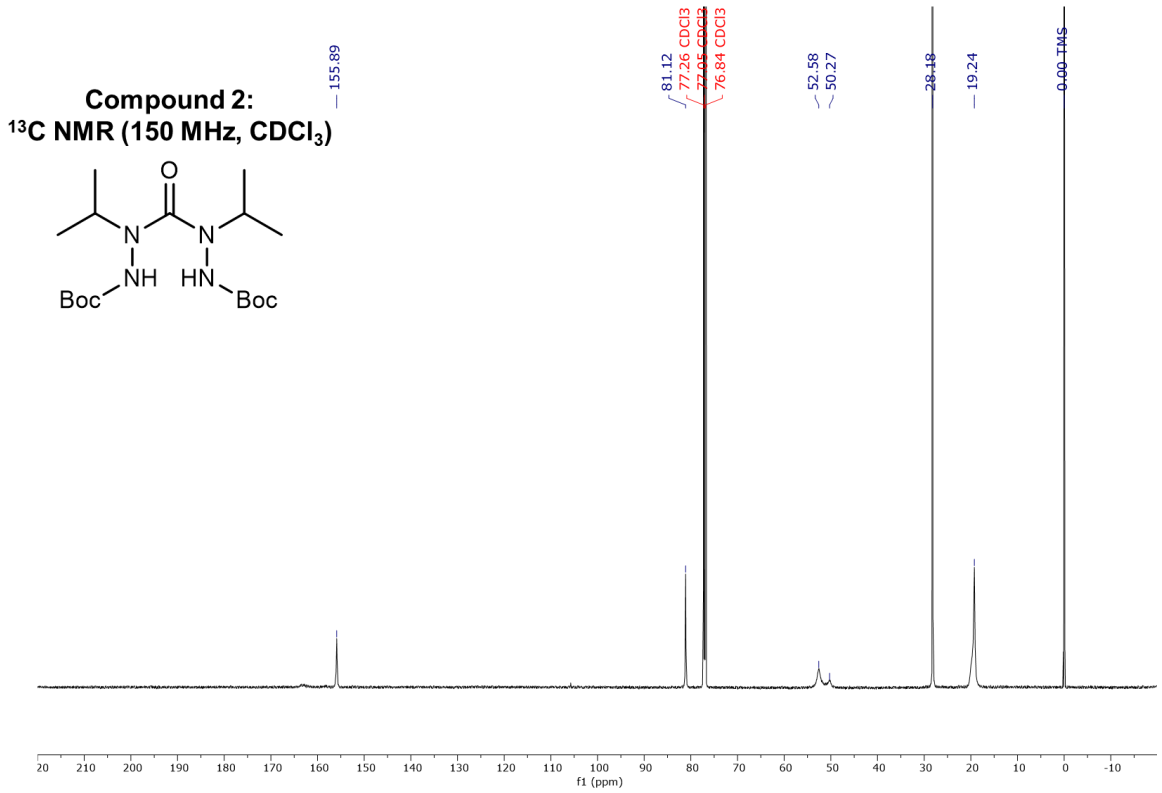

S3. ^{13}C NMR spectrum of compound 2 in $CDCl_3$.

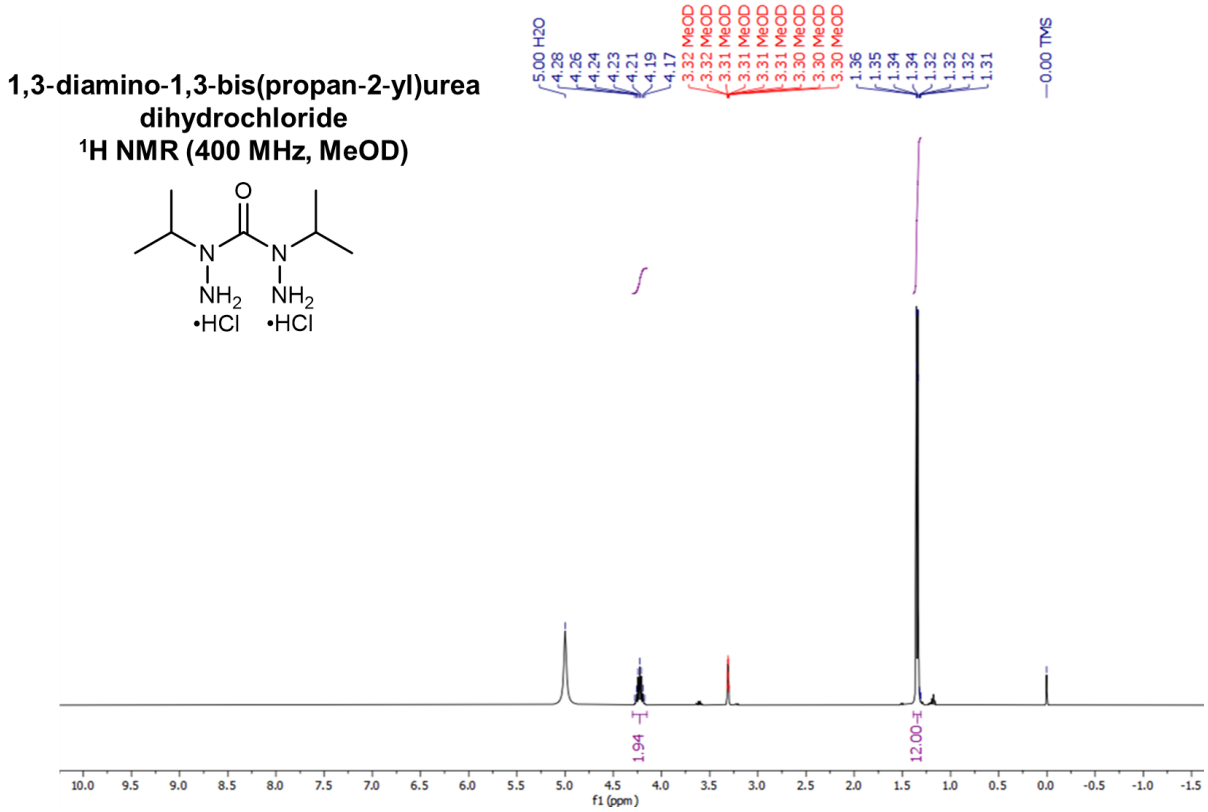

S4. ^{1}H NMR spectrum of 1,3-diamino-1,3-bis(propan-2-yl)urea dihydrochloride in MeOH-D_4.

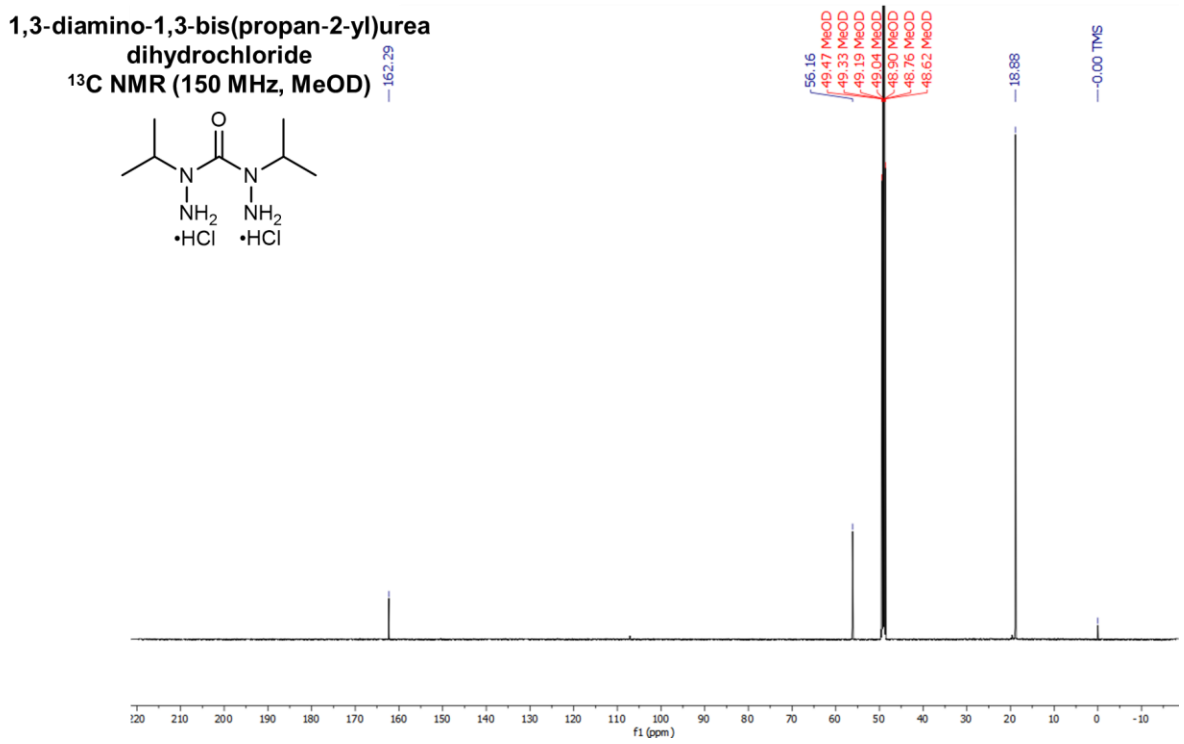

S5. ^{13}C NMR spectrum of 1,3-diamino-1,3-bis(propan-2-yl)urea dihydrochloride in MeOH-D_4.

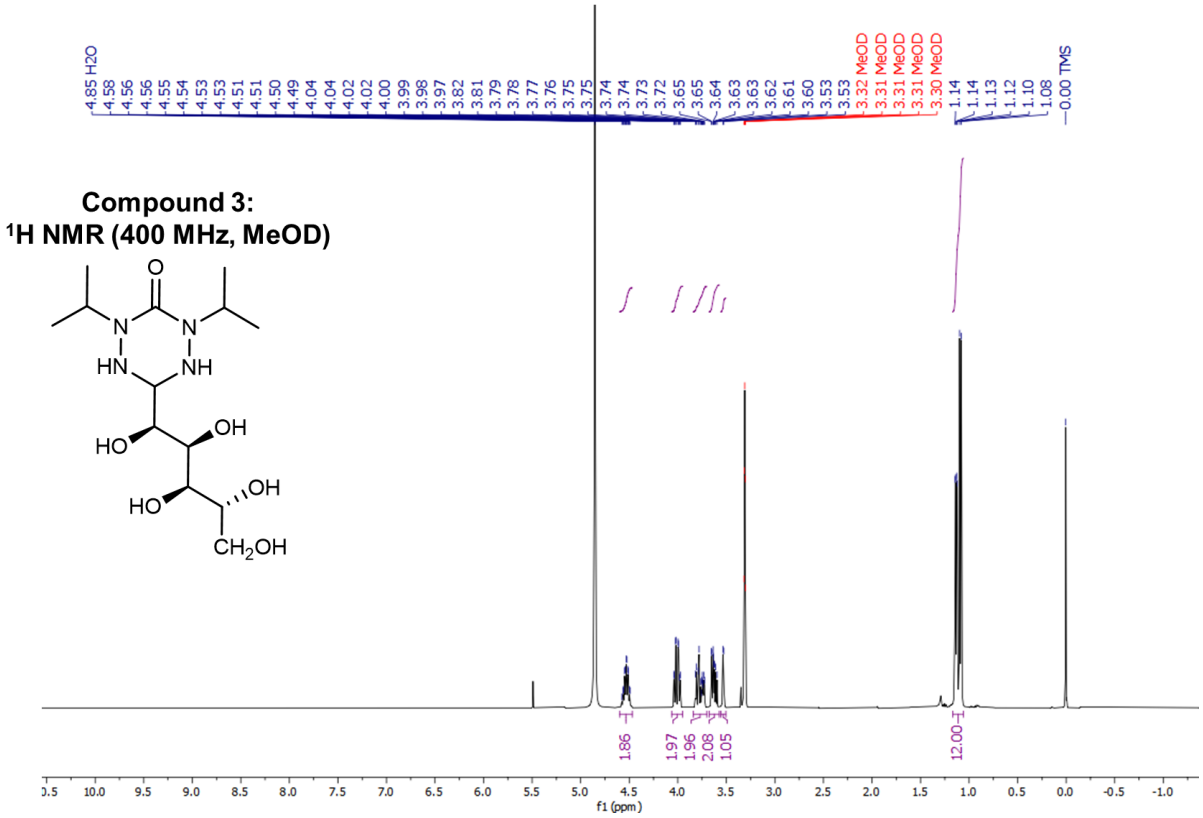

S6. ^{1}H NMR spectrum of compound 3 in MeOH-D_4.

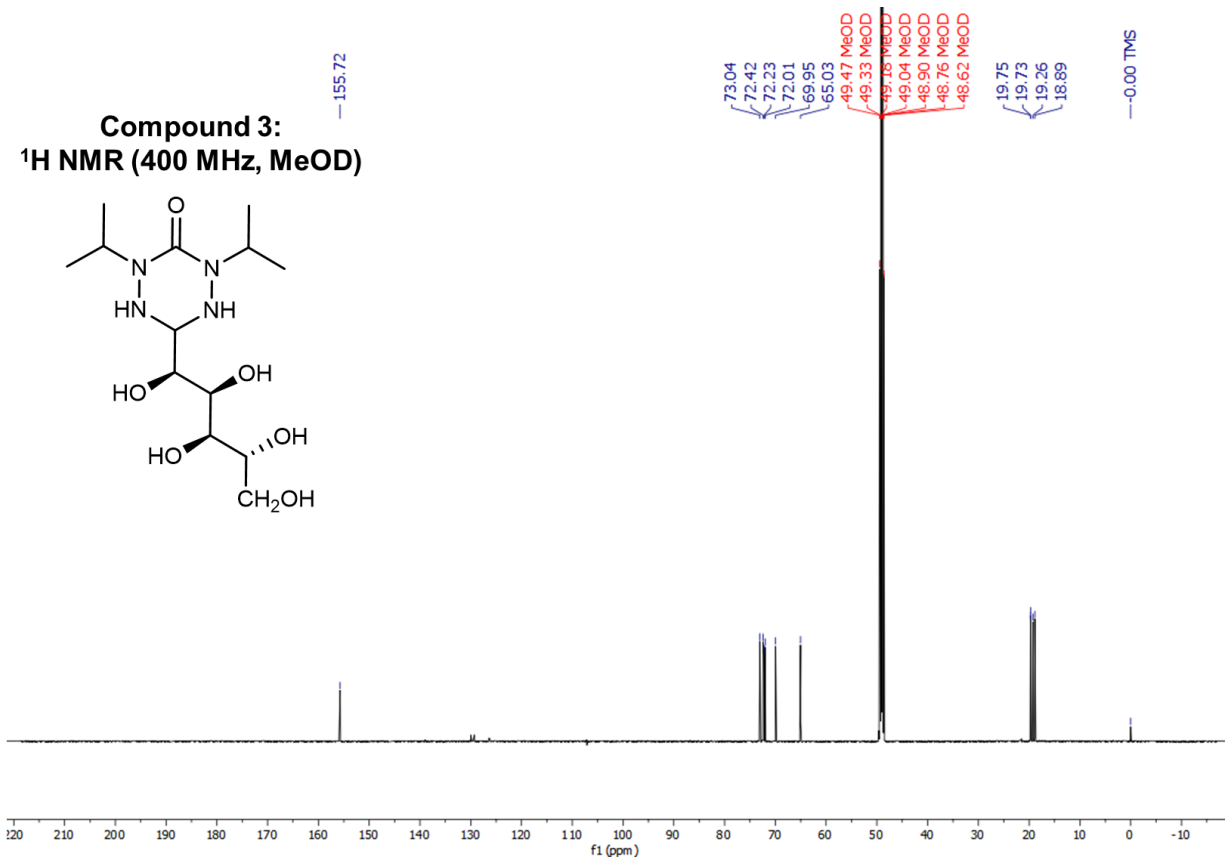

S7. ^{13}C NMR spectrum of compound 3 in MeOH-D_4.

3.2 High-performance liquid chromatography traces of 3 and 4.

In order to verify the completion of radicalization from compound **3** to **4**, we used HPLC traces in conjunction with HRMS and EPR. HPLC analysis was performed on a Prominence HPLC system with diode array detector (Shimadzu North America) using a Luna® C_{18} 100 Å column (4.6 mm x 250 mm, 5µm particle size). A 20 min HPLC gradient with mobile phase consisting of a 0.5% trifluoroacetic acid (TFA) in H_2O gradually increasing from 1% to 100% with AcN containing 0.5% TFA min was used at a flow rate of 1 mL/min. Retention time (t_R) of compound **3** was consistently 10.5 min, while after radicalization and loss of two protons from the verdazyl ring, the t_R increased to 11.8 min. As well, radicalization induced greater absorbance at 452 nm for compound **4**, while no signal at this wavelength is observed in the non-radical compound **3**.

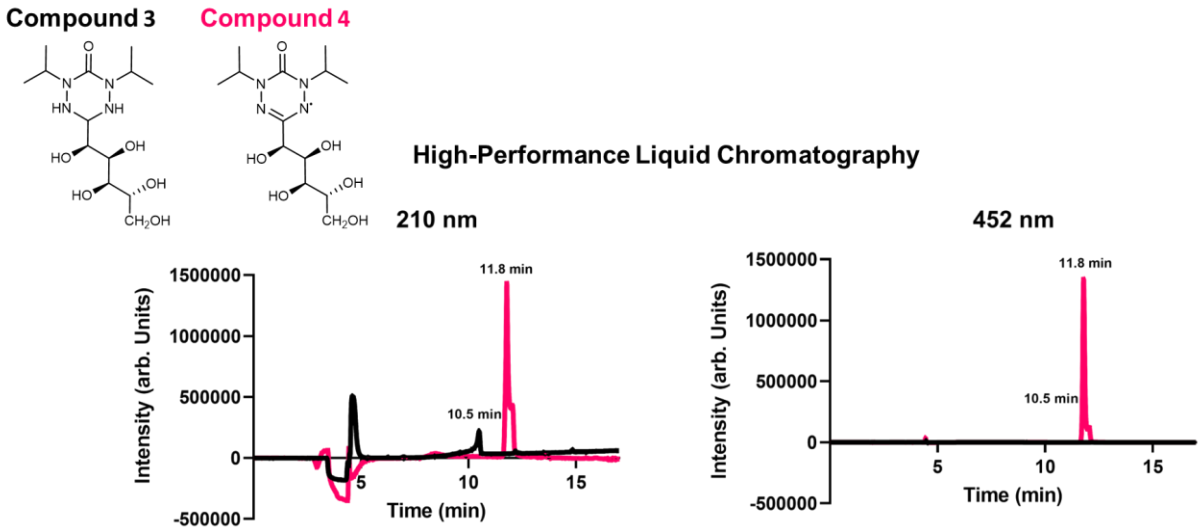

S8. High performance liquid chromatography traces of compounds 3 and 4 to verify radical activity of the compound after radicalization step.

3.4 Temperature-dependence Of Relaxation Rate

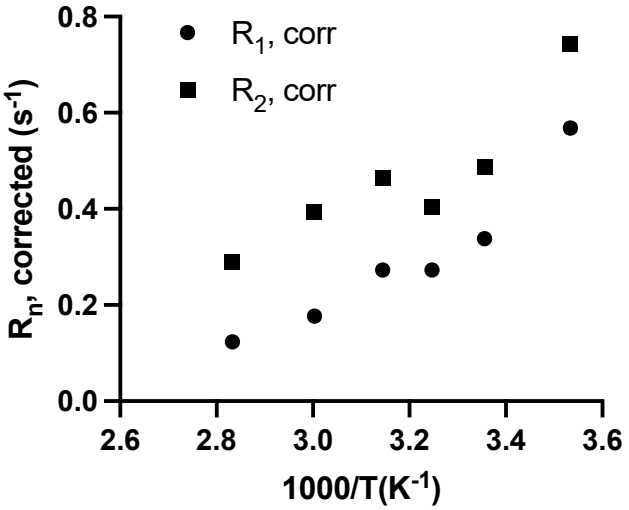

S9. **Temperature-dependency of glucoverdazyl relaxivity.** Temperature-dependence of the longitudinal (circle) and transverse (square) relaxation rates of glucoverdazyl, corrected for buffer effects, at 7.0 T.

3.5 Stability Studies

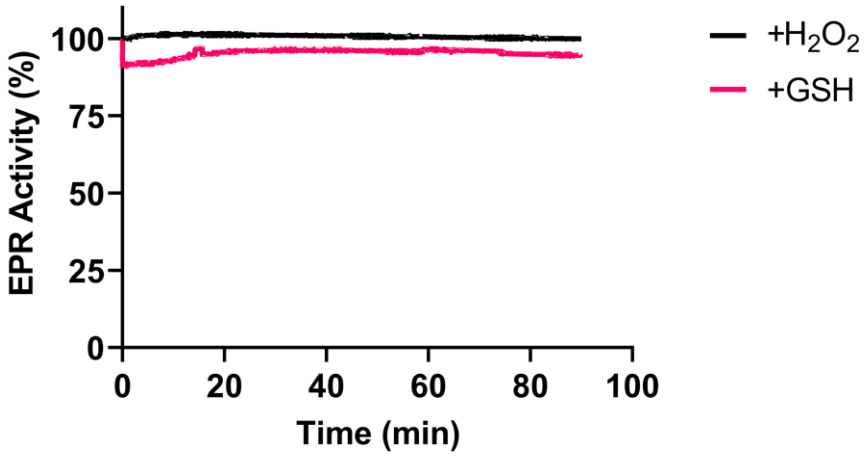

S10. Glucoverdazyl stability in the presence of known oxidizers and reducers. Twenty millimolar of either hydrogen peroxide (H_2O_2) or reduced glutathione (GSH) were added to a solution of 5 mM glucoverdazyl in phosphate-buffered saline (PBS). These solutions were monitored by an EPR that was previously tuned to a 5 mM sample of glucoverdazyl in PBS. Solutions were monitored for 90 min to determine if any loss of radical activity occurred by either oxidation or reduction of glucoverdazyl.

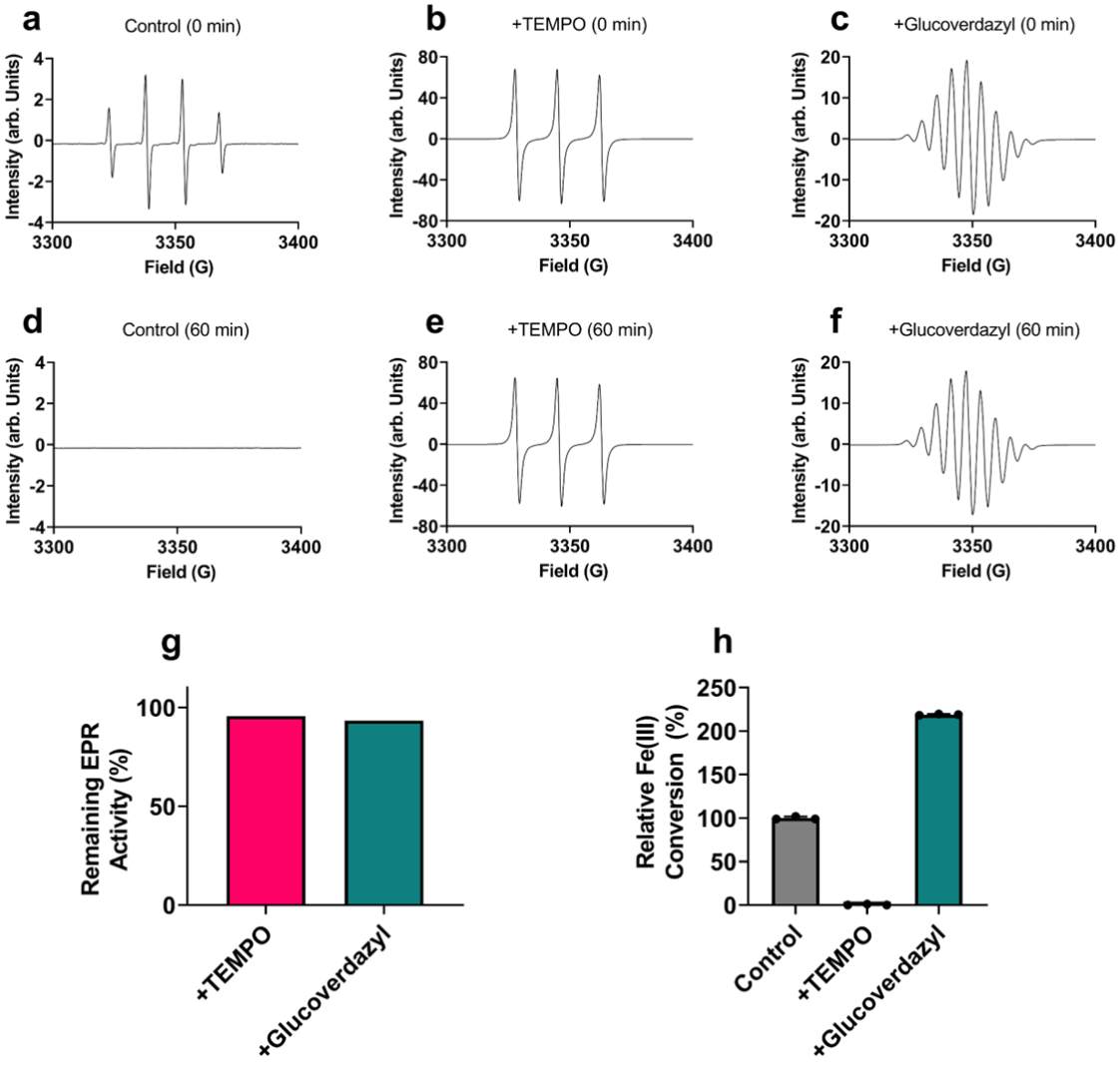

S11. Interactions of TEMPO and glucoverdazyl with Fenton chemistry by H_2O_2 mediated oxidation of $FeCl_2$ to $FeCl_3$. EPR spectra of 10 mM DMPO alone or with 5 mM of either TEMPO or glucoverdazyl before (A, B, C) and 1 h after (D, E, F) the addition of 10 mM H_2O_2 to initiate oxidation of $FeCl_2$ to $FeCl_3$. G) The change in maximum EPR signal before and 1 h after oxidation reaction. H) Conversion of Fe(II) to Fe(III) determined by change in absorbance at 330. Data are presented as means ± standard deviation of n = 3 technical replicates.

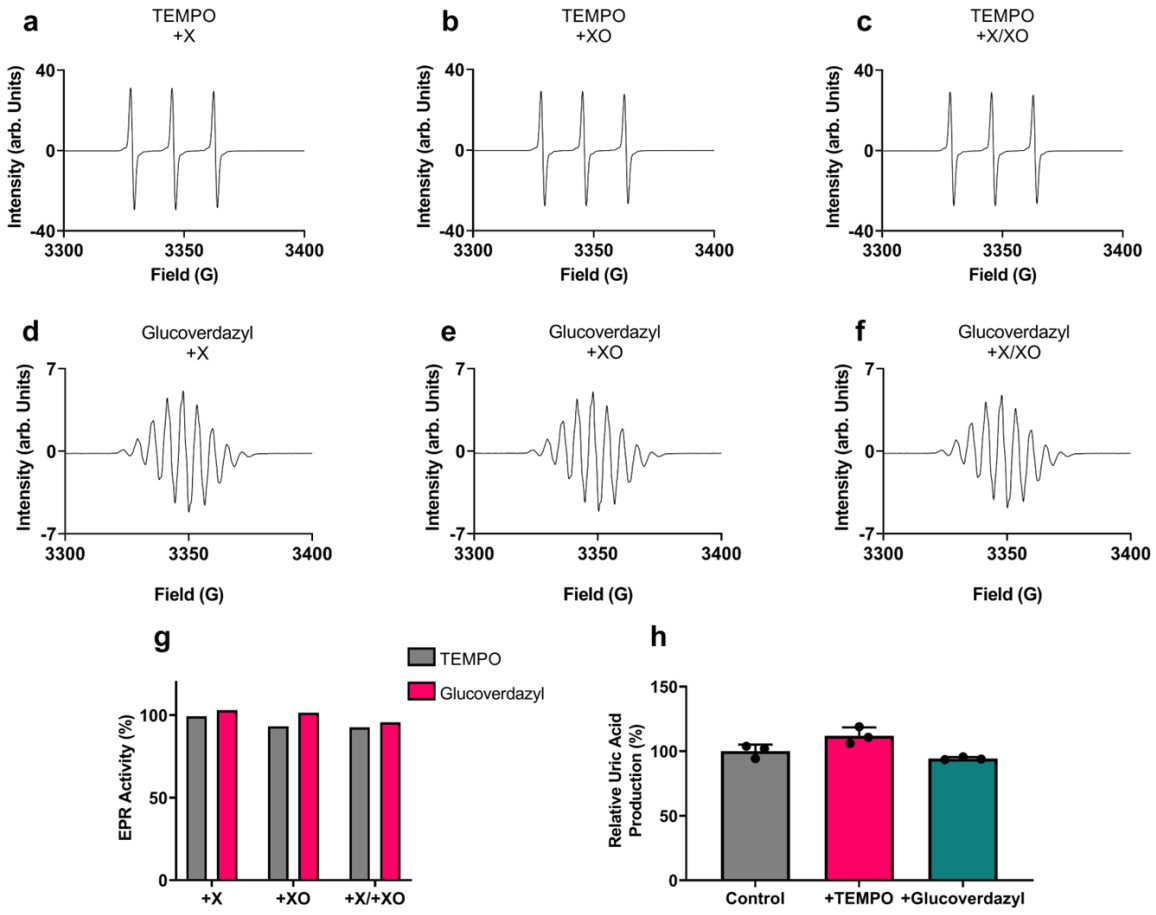

S12. Interactions of TEMPO and glucoverdazyl with superoxide produced by xanthine oxidase. EPR spectra of 1.25 mM TEMPO containing 10 mM xanthine (X, S12. A), 0.4 U xanthine oxidase (XO, S12. B), or both (X/XO, S12. C). S12. D, E, and F are the same but with 1.25 mM glucoverdazyl. The change in EPR maxima compared to the tuned radical is shown in S12. G Relative uric acid production as a result of the X/XO reaction is shown in S12. H by change in absorbance at 293 nm. Data are presented as means ± standard deviation of n = 3 technical replicates.

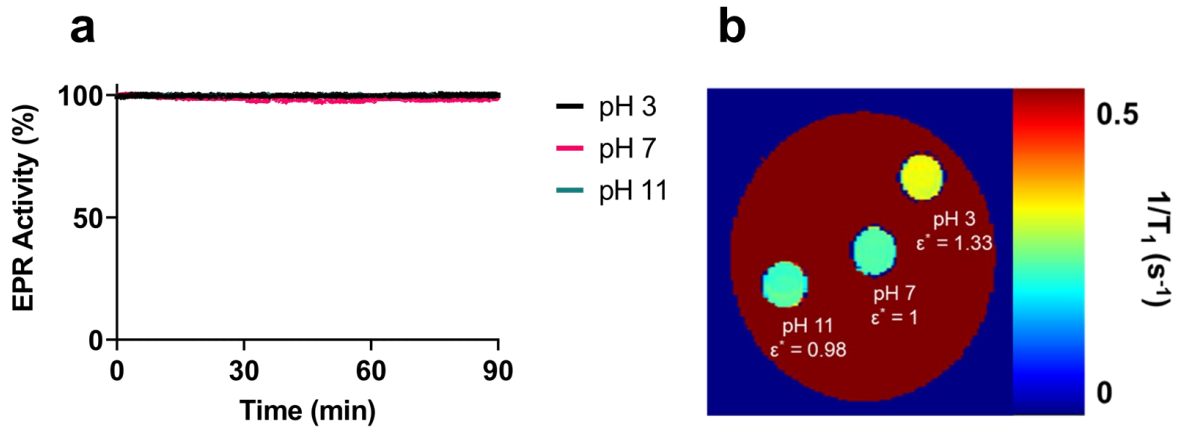

S13. Change in glucoverdazyl radical stability and relaxation by pH. A) Change in EPR activity of a 3 mM glucoverdazyl solution in PBS at pH 3, 7, or 11. B) Relaxation of a 3 mM glucoverdazyl solution in PBS at pH 3, 7, or 11. The change in relaxation compared to pH = 7 is shown as $\varepsilon^* (\frac{1}{T_{1HSA}} / \frac{1}{T_{1PBS}})$.

3.6 Human Serum Albumin Binding.

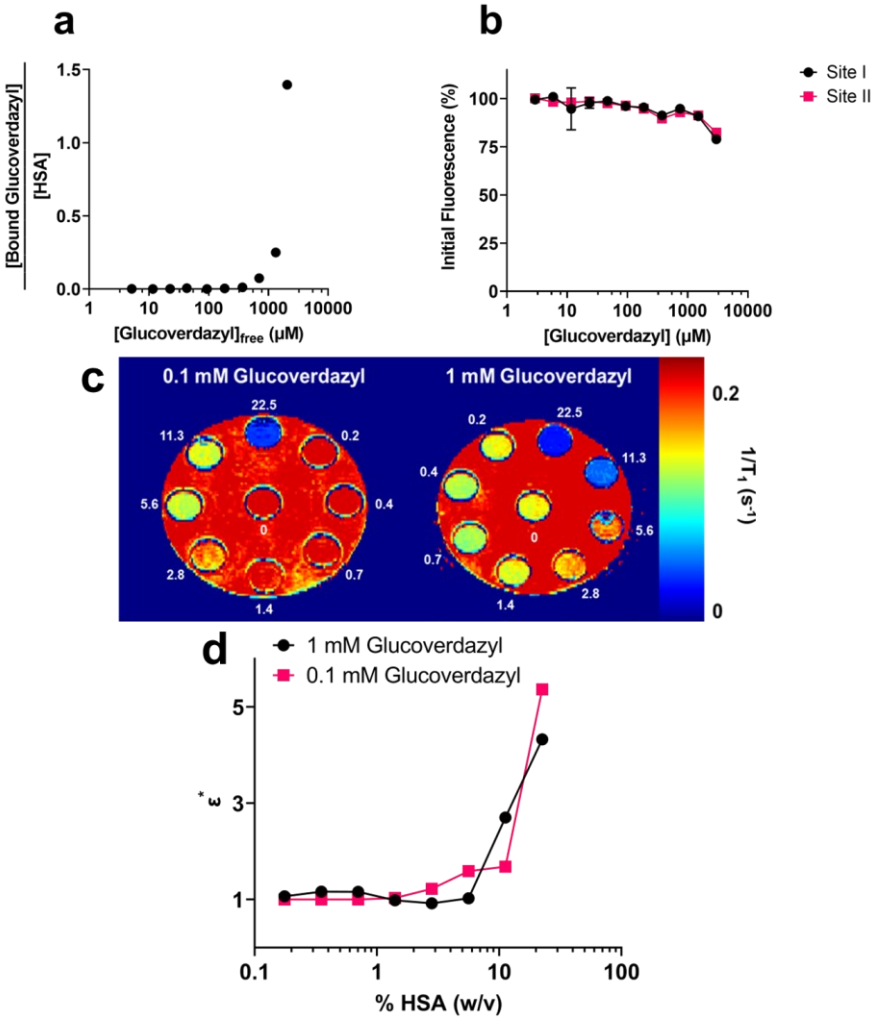

S14. Glucoverdazyl binding to human serum albumin (HSA). A) Glucoverdazyl fraction bound to a 4.5% w/v solution of HSA in PBS as determined by HPLC following ultrafiltration of a glucoverdazyl/HSA solution, separating bound from free fractions. B) Occupation of HSA binding site I or II by glucoverdazyl as determined fluorescently by displacement of site I or site II specific dansylamide or dansylglycine, respectively. Data are presented as means ± standard deviation of n = 3 technical replicates. C) Relaxivity maps of NMR tubes filled with glucoverdazyl (0.1 mM or 1 mM) in either PBS or varying concentrations of HSA (numerically listed in the image as w/v) as determined by MRI at 3 T. D) graphical representation of relaxation enhancement, ε^* ($\frac{1}{T_{1HSA}} / \frac{1}{T_{1PBS}}$) in the presence of HSA.

3.7 Cytotoxicity Evaluations of Glucoverdazyl.

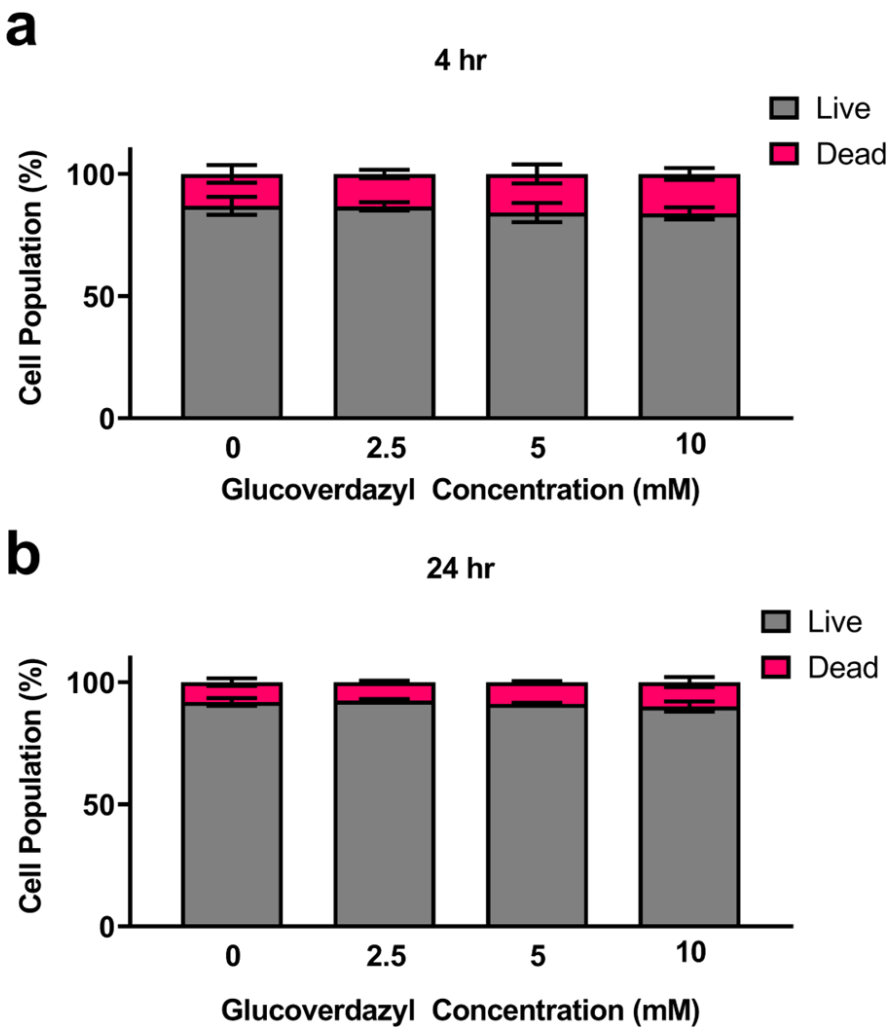

S15. Cytotoxicity evaluation of glucoverdazyl at different concentrations in H460 cells. Cellular viability after 4 h (A) and 24 h (B) incubations with the respective concentration. Data are represented as means ± SD of n = 3 replicates. Statistical analysis was done by one-way ANOVA followed by a Tukey post-hoc test. An example gating strategy used to obtain this data can be seen in Supplementary Figure 23.

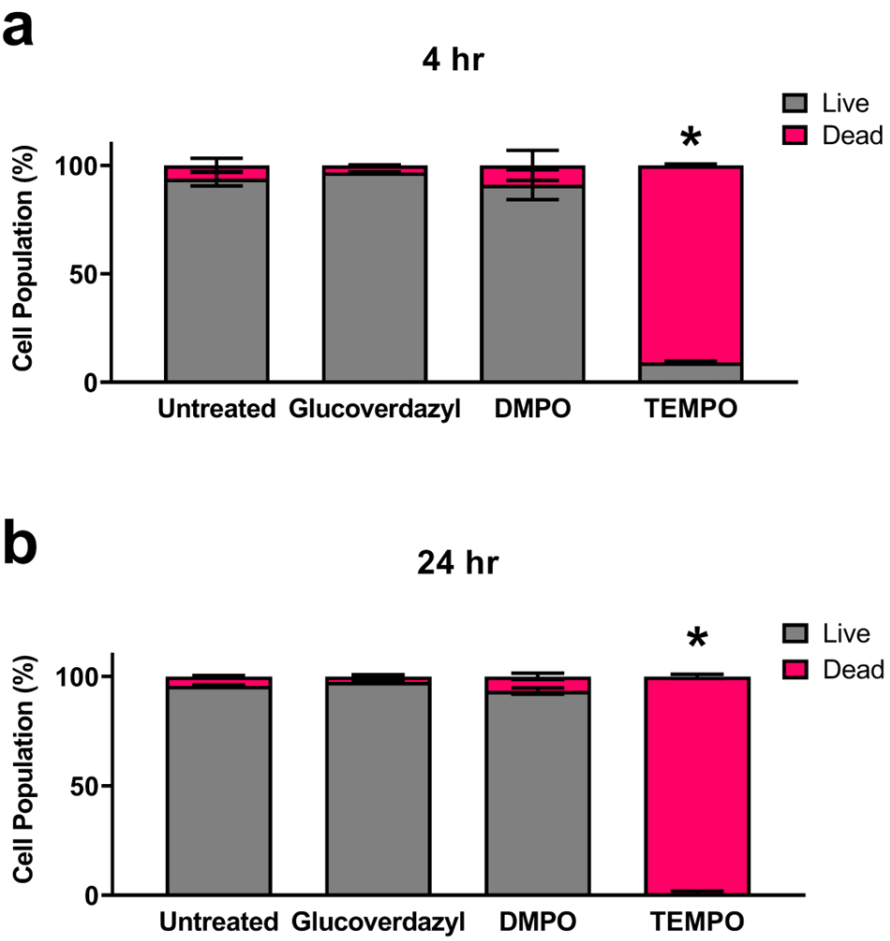

S16. Cellular viability in other radicals and spin traps. Cytotoxicity evaluation of glucoverdazyl, 5,5-dimethyl-1-pyrroline N-oxide (DMPO), and 2,2,6,6-Tetramethylpiperidin-1-yl)oxyl (TEMPO) in human renal proximal tubule cells at 10 mM concentrations after 4 h (A) or 24 h (B) incubations under cell culture conditions. Data are represented as means ± SD of n = 3 replicates. Statistical analysis was done by one-way ANOVA followed by a Tukey post-hoc test. * p<0.0001 of the live and dead cell populations compared to the populations of the other conditions. An example gating strategy used to obtain this data can be seen in Supplementary Figure 23.

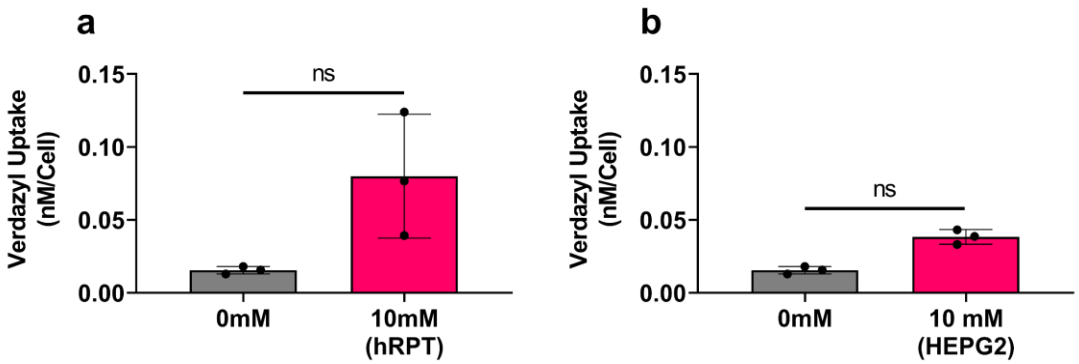

S17. Cellular internalization of glucoverdazyl. Glucoverdazyl uptake in (A) human renal proximal tubules cells (hRPT) under cell culture conditions, and (B) HepG2 hepatocarcinoma cells grown to confluency and starved for 1 h with glucose-free media. In both experiments, uptake was measured by EPR activity after 24 h incubation with 10 mM glucoverdazyl, as compared to a known concentration and normalized to number of cells loaded into the EPR tube. Data are represented as means ± SD of n = 3 replicates. Statistical analysis was done by one-way ANOVA followed by a Tukey post-hoc test.

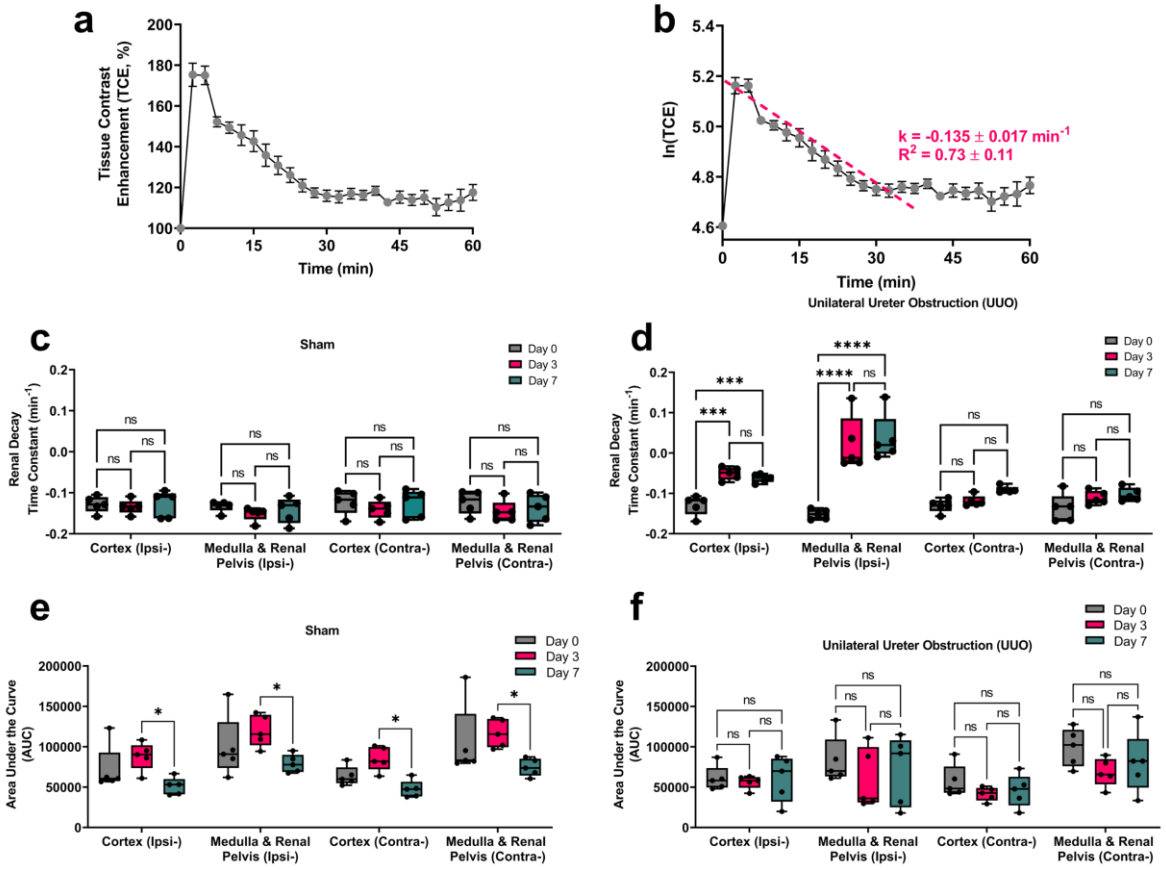

S18. Glucoverdazyl-enhanced DCE-MRI data in the unilateral ureter obstruction (UUO) model. A) Normalized intensity-over-time curves of UUO mice on day 0. Curve is presented as mean normalized intensity ± SEM of n = 10 mice (5 from sham group and 5 from UUO group). B) The semi-natural-log regression curve of A) with the line of best fit from t = 0 min to t = 40 min. Data are presented as mean RDTC (k) and R^2 value ± SD of n = 10 mice (5 from sham group and 5 from UUO group). RDTC values for the cortex and medulla & renal pelvis (MRP) regions-of-interest (ROIs) for the sham group (C) and UUO group (D). Data are presented as box-and-whisker plots of the single average RDTC value from each kidney (ipsi- or contralateral) from each region, individually, from each mouse (n = 5). *** p=0.001 (Day 0 to Day 15) and p = 0.0001 (Day 0 to Day 30), **** p<0.0001. The same data and plots for AUC are shown in E) and F) for the sham and UUO groups, respectively. In E), * p = 0.031 (Sham

Ipsi-), * p=0.030 (UUO Ipsi-), * p = 0.018 (Sham Contra-), and * p = 0.013 (UUO Contra-). Statistical analysis was done by repeated measures two-way ANOVA followed by a Tukey post-hoc test. In all graphs, ns non-significant. In all boxplots, whiskers are drawn from the minimum to maximum values, box bounds represent the interquartile range, and the line within the box represents the median.

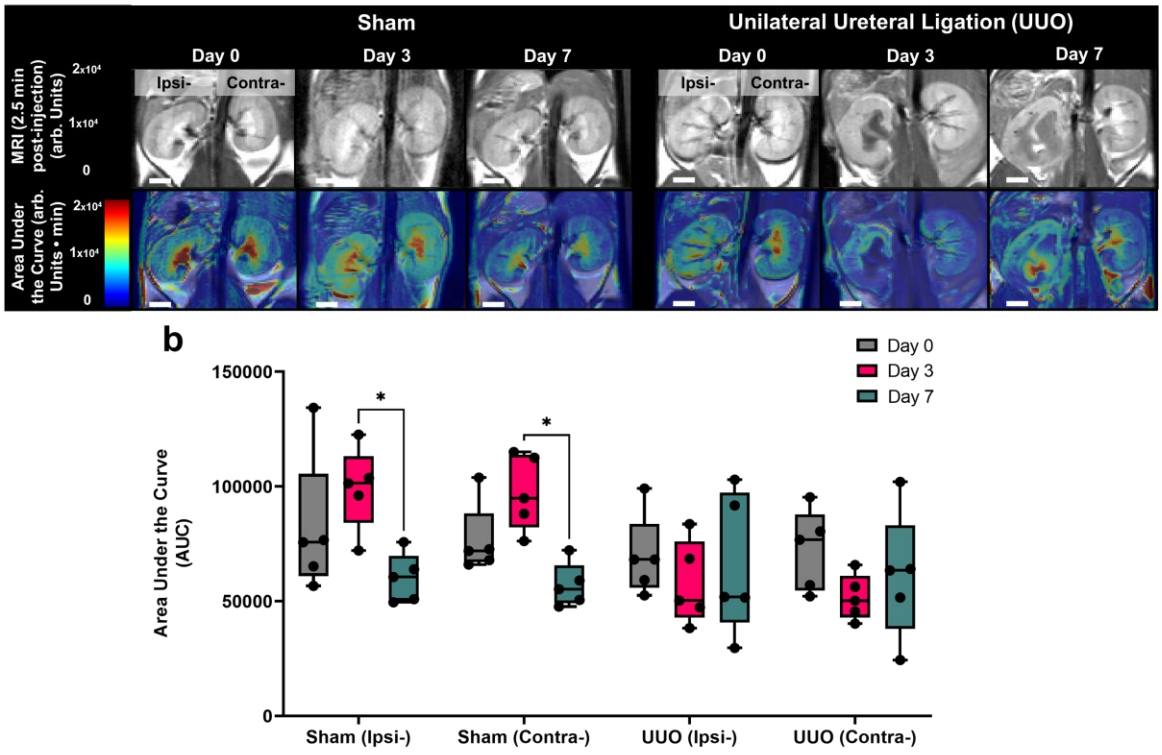

S19. Glucoverdazyl-enhanced DCE-MRI in a mouse mode of unilateral ureteral obstruction. A) T_1-weighted images of kidneys at t = 2.5 min post-injection (*top)* and AUC maps (*bottom)* for Sham and UUO groups. The white scalebar represents 2 mm. B) AUC values for each kidney at each post-injury time-point. Data are presented as box-and-whisker plots of the single average AUC value from each kidney (ipsi- or contralateral) individually, from each mouse (n = 5). * $p = 0.017$ (Sham Ipsi-) and * $p = 0.013$ (Sham Contra-). Statistical analysis was done by repeated measures two-way ANOVA followed by a Tukey post-hoc test. In all graphs, ns non-significant. In all boxplots, whiskers are drawn from the minimum to maximum values, box bounds represent the interquartile range, and the line within the box represents the median.

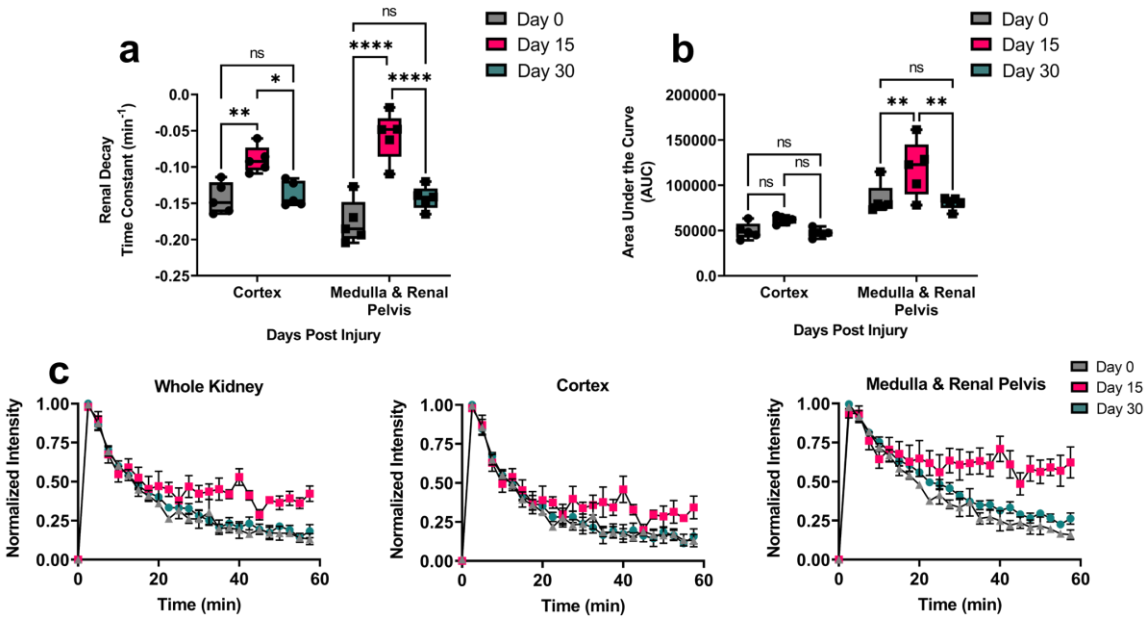

S20. Glucoverdazyl-enhanced DCE-MRI data in the folic acid nephropathy (FAN) model. A) RDTC values for the cortex and medulla & renal pelvis (MRP) regions-of-interest (ROIs). Data are presented as box-and-whisker plots of the single average RDTC value from each mouse (n = 5). * $p = 0.013$, ** $p = 0.006$, and **** $p<0.0001$. B) The same data and plots as in A) but for AUC values are shown. ** $p = 0.005$ (Day 0 to Day 15) and ** $p = 0.002$ (Day 15 to Day 30). C) The normalized intensity-over-time curves for the FAN model over the entire kidney, as well as for the cortex and MRP regions for each of the post injury-time points. Curves are presented as the mean normalized intensity at each time point ± SEM of n = 5 mice. Statistical analysis was done by repeated measures two-way ANOVA followed by a Tukey post-hoc test. In all graphs, ns non-significant. In all boxplots, whiskers are drawn from the minimum to maximum values, box bounds represent the interquartile range, and the line within the box represents the median.

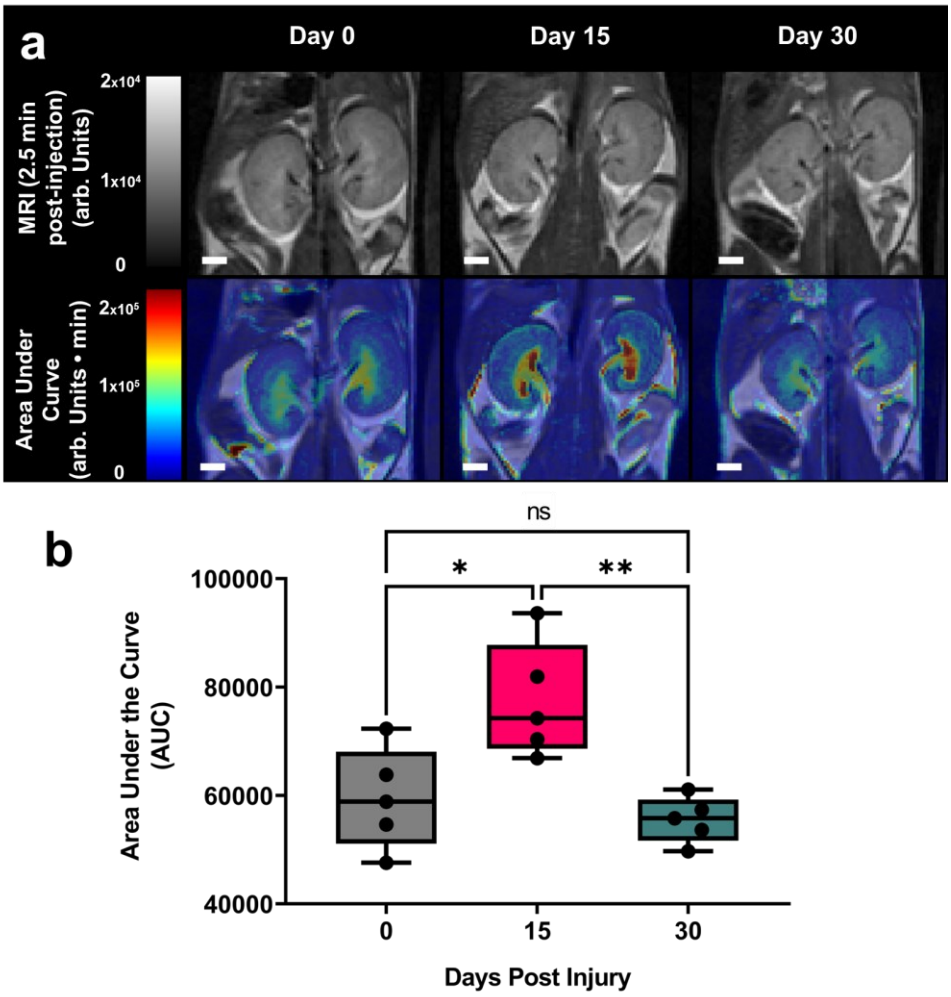

S21. Glucoverdazyl-enhanced DCE-MRI of folic acid-induced nephropathy. A) T_1-weighted images of kidneys at t = 2.5 min post-injection (*top)* and AUC maps (*bottom).* The white scalebar represents 2 mm. B) AUC values for kidneys at each post-injury time point. Data are presented as box-and-whisker plots of the single average AUC value from both kidneys of each mouse (n = 5). * $p = 0.014$ and ** $p = 0.005$. Statistical analysis was done by repeated measures one-way ANOVA followed by a Tukey post-hoc test. In all graphs, ns non-significant. In all boxplots, whiskers are drawn from the minimum to maximum values, box bounds represent the interquartile range, and the line within the box represents the median.

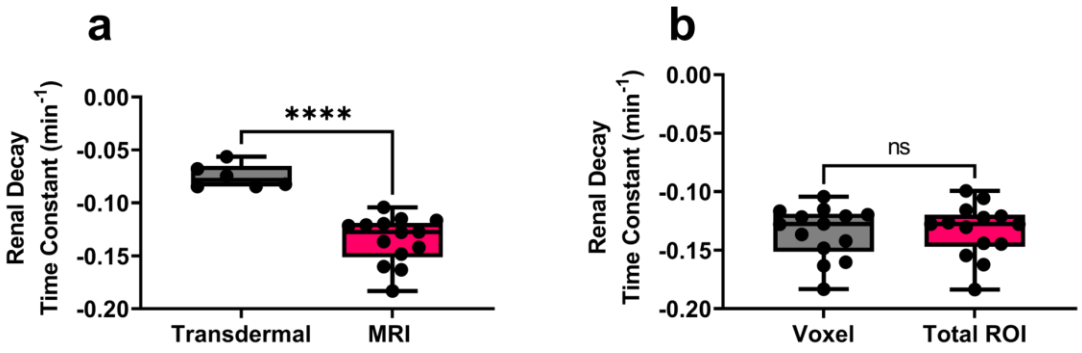

S22. Deriving the renal decay time constant in transdermal compared to MRI. A) Comparison between the transdermal fluorescence RDTC value in healthy BALB/c mice (n = 6) as determined by MediBeacon software and the RDTC value in healthy BALB/c mice (n = 14) as determined by glucoverdazyl DCE-MRI. B) A comparison between RDTC value in healthy BALB/c mice by using intensity measurements derived per voxel or from the entire ROI of a slice at each timepoint (n = 14 mice for both). Data are presented as Data are presented as box-and-whisker plots of the single RDTC (A, transdermal) or single average RDTC (A, MRI and B). Statistical analysis was done by one-way ANOVA followed by a Tukey post-hoc test. In all graphs, ns non-significant and **** $p < 0.0001$

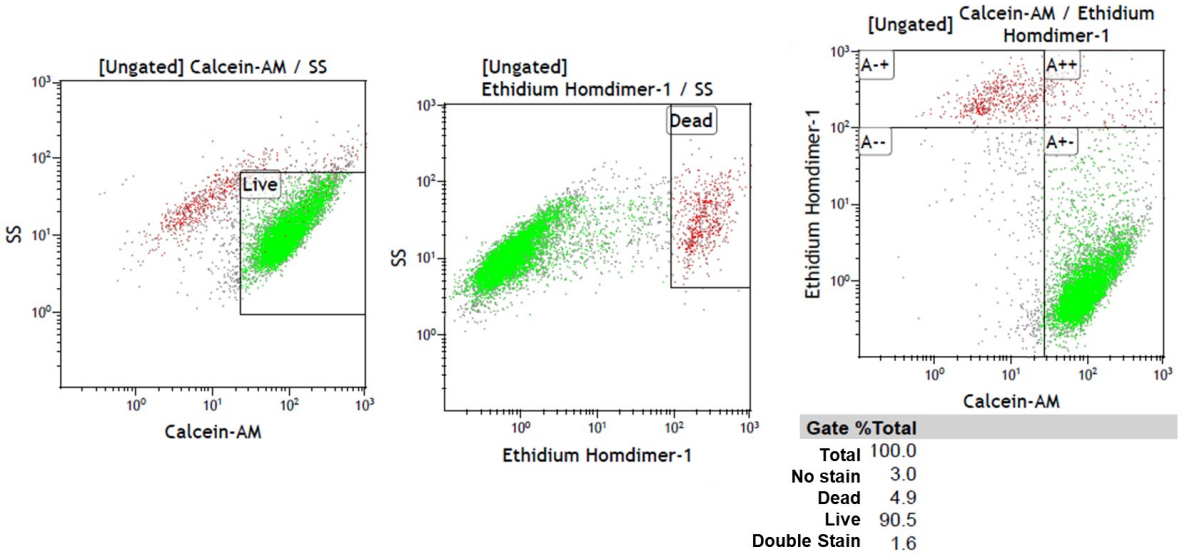

S23. Example gating strategy used for cell viability assays with flow cytometry. Example of the gating strategy used for all cell viability assays. The green region represents singly stained live cells, and the red region represents singly stained dead cells. Double or non-stained cells were not included in analysis.

4. References:

1. Castañar, L., Poggetto, G. D., Colbourne, A. A., Morris, G. A. & Nilsson, M. The GNAT: A new tool for processing NMR data. *Magnetic Resonance in Chemistry* **56**, 546–558 (2018).
2. Caravan, P. *et al.* The interaction of MS-325 with human serum albumin and its effect on proton relaxation rates. *J Am Chem Soc* **124**, 3152–3162 (2002).

Chapter 3: Highly NIR-II Scattering Gold Superclusters for Intravascular Optical Coherence Tomography Molecular Imaging

Nicholas D. Calvert [1], Joshua Baxter [2], Aidan A. Torrens [1], Jesse Thompson [2], Alexia Kirby [3], Jaspreet Walia [4], Spyridon Ntais[4], Eva Hemmer [1], Pierre Berini [2,4], Benjamin Hibbert [5], Lora Ramunno [2], Adam J. Shuhendler [1, 3, 5*]

[1]Department of Chemistry and Biomolecular Sciences, University of Ottawa, 150 Louis Pasteur Pvt., Ottawa, Ontario, Canada, K1N 6N5

[2]Department of Physics, University of Ottawa, 150 Louis Pasteur Pvt., Ottawa, Ontario, Canada, K1N 6N5

[3]Department of Biology, University of Ottawa, 150 Louis Pasteur Pvt., Ottawa, Ontario, Canada, K1N 6N5

[4]School of Electrical Engineering and Computer Science, University of Ottawa, 800 King Edward Ave., Ottawa, Ontario, Canada, K1N 6N5

[5]University of Ottawa Heart Institute, 40 Ruskin St., Ottawa, Ontario, Canada, K1Y 4W7

*Corresponding Author: adam.shuhendler@uottawa.ca

3.1. Introduction to the Research Article Presented in this Chapter

Previous work forcing the assembly of AuNPs into superclusters resulted in a red-shifted LSPR, but had highly heterogeneous morphology and size, and were not aqueously dispersible. We aimed to redevelop this chemical method of producing gold superclusters to be homogeneous, aqueously dispersible, and have a NIR-II LSPR to interact with the IV-OCT light source. We then chemically functionalized these AuSC to target the vascular luminal protein, P-selectin, that is expressed during early phases of inflammation. We applied our AuSCs for use in an animal model of inflammation to show the first instance of *in vivo* IV-OCT MI.

3.2. Author Contributions

N.D.C. performed all AuSC/AuNP syntheses, characterization, *in vitro* IV-OCT experiments, and evaluated targeting performance of AuSC@$(13FS)_2$. N.D.C performed all chemical syntheses with support from A.A.T. All FDTD simulations were performed by J.S.J.B, J.T, and L.R. FIB-TEM and HIM was performed by J.W. and P.B. N.D.C and A.K. developed the rat inflammation model and prepared histological samples. N.D.C and A.J.S. performed all *in vivo* IV-OCT and *in vivo* biodistribution analysis experiments, with support from B.H. N.D.C. and S.N. performed mouse serum stability studies. N.D.C performed all statistical analyses. N.D.C, A.J.S, and B.H. conceived of experiments with support from L.R. and E.H. N.D.C. and A.J.S. co-wrote the paper, and all authors edited the work and provided input.

3.3. Copyright

3.4. Abstract

In North America, intravascular optical coherence tomography (IV-OCT) is performed every few minutes to evaluate atherosclerotic plaques and guide stent placement. Currently, IV-OCT is limited to anatomical imaging, providing structural information about atherosclerotic plaque morphology, thrombus, and dissection. Earlier detection and risk stratification would be possible through molecular characterization of endothelium but necessitates a purpose-engineered IV-OCT contrast agent. We developed gold superclusters (AuSC) tailored to clinical instrumentation and integrated into clinically relevant workflows. AuSC are aqueously dispersible clusters of closely packed small gold nanoparticles, affording plasmon hybridization to maximize light scattering at the IV-OCT laser line (~1350 nm). A polymer coating fosters AuSC uniformity and provides a functionalizable handle, which we targeted to intravascular P-selectin, an early vascular endothelial marker of inflammation. In a rat model of intravascular inflammation, P-selectin-targeted AuSC facilitated IV-OCT molecular imaging, where the strength of the signal correlates with the severity of vascular inflammation. AuSC thus enable *in vivo* molecular imaging, advancing IV-OCT into the molecular age.

3.5. Introduction

Recently, optical biomedical imaging techniques have focused on harnessing photobiophysical interactions in the second near-infrared window (NIR-II, 900 nm – 1700 nm).[1,2] This focus is a result of the unique interaction of incident and emitted NIR-II photons with tissue: minimized light scattering, reduced tissue autofluorescence, and deeper light penetration.[1–3] Extensive research effort has been dedicated to developing biocompatible molecules and materials that are active in the NIR-II region[4–7]. Plasmonic nanomaterials are of special interest due to the tunability of their localized surface plasmon resonance (LSPR) properties, allowing photobiophysical interactions to occur across the visible and NIR spectrum.[8–10] To date, there has been limited innovation in contrast agents for optical coherence tomography (OCT), which is among the most predominant clinical NIR-II imaging technologies.

OCT is primarily used for ocular and intravascular (IV) procedures, where images are created by destructive or constructive interference in backscattered NIR-II light from a laser source relative to a reference mirror.[11–13] IV-OCT is performed using an imaging catheter inserted into the patient's radial or femoral artery, and routed to the aortic vasculature.[14] A rotating NIR-II light source in the catheter is attached to a camera that, upon pull-back, generates a three-dimensional image of the vascular region. IV-OCT is growing in clinical popularity, with procedures being performed every few minutes in the United States,[15] but is limited to providing clinicians with anatomical information about diseased arteries or placed stents.[16] Molecular imaging-guided IV-OCT would allow physicians to extend their evaluation of vascular pathology beyond just anatomical, providing the identification of molecular markers of disease that appear much earlier in disease progression than anatomical changes. Molecular imaging can also provide information not otherwise accessible, such as identifying early biomarkers of

plaques that may rupture as an alternative to current stratification by anatomic plaque features. This would allow physicians to better risk-stratify their patient population.[17,18] A purpose-engineered contrast agent for IV-OCT would justify the use of IV-OCT in almost 7 million more cardiovascular cases in the United States *per* year.[15]

An ideal purpose-built contrast agent for IV-OCT would induce destructive interference (*i.e.*, scattering) of the incident laser light once immobilized by a molecular binding event, resulting in image contrast features within the black vascular lumen. Such contrast agents could be comprised of plasmonic metals, supporting LSPR within the NIR-II region.[19] However, current agents for NIR-II LSPR are often composed of bioactive metals such as Cu or Ag, making them suboptimal for biomedical use.[20–22] Gold nanoparticles (AuNPs), commonly used in a range of biomedical imaging techniques,[23,24] have also been evaluated for OCT.[25,26] Rods and other non-spherical shapes have been shown to support NIR-II LSPRs, but these shapes do not clear the body as effectively as their spherical counterpart, which is an important consideration for intravascular applications.[27] Gold nanoshells have been shown to have excellent NIR-II interactions and have been shown as effective contrast agent in *in vitro* OCT work.[28–31] In addition to NIR-II LSPR and clearance characteristics, an ideal IV-OCT contrast agent enabling molecular imaging would be able to signal relatively rare instances of expression of its biomolecular target. By nature, IV-OCT is dynamic since the imaging catheter is pulled through the vessel to acquire the image. As a result, limited sensor dwell time makes the acquisition of molecular information by IV-OCT challenging. We hypothesize that this challenge can be met with a large contrast agent that fills a larger portion of a voxel, preventing the averaging out of signal within a voxel. In consideration of these performance and materials requirements, there is no instance of a purpose-designed, spherical contrast agent for IV-OCT.

To date, only a single report could be found on the synthesis of gold superclusters interacting with NIR-II light, but which resulted in highly heterogeneously shaped constructs (spheres and networks of fused spheres) that were not aqueously dispersible.[32] Recently, a synthesis of *in vivo* disassembling gold supraclusters was reported,[33] but this ionic assembly was designed to aggregate within the low pH of intratumoral environments and disassemble at physiological pH. While elegant, the resulting AuNP assembly precludes plasmon hybridization, abolishing NIR-II interactions and preventing its use as an IV-OCT contrast agent.

In this study, we report the synthesis of uniform, aqueously dispersible gold superclusters (AuSC) as IV-OCT contrast agents, having ideal characteristics for molecular imaging. We have achieved controlled aggregation of oleylamine-capped AuNPs by varying solvent polarity and have also stabilized AuSC by "cinching" them with large amphiphilic polymers. This polymer coating enables stable aqueous dispersion of AuSC in isotonic media, resulting in biologically relevant supercluster materials. Our solvothermally-driven, one-pot *in situ* nucleation and clustering synthesis approach produces AuSC of unique architecture, supporting a LSPR peak in the NIR-II region that is almost entirely scattering. Furthermore, we have demonstrated the ability to functionalize the stabilizing polymers by attaching biomolecular targeting moieties without sacrificing the physicochemical properties that make AuSC an attractive IV-OCT molecular imaging agent. We functionalized AuSC with a P-selectin ligand mimic to facilitate AuSC binding to highly inflammatory regions of endovasculature with pathology-associated protein expression preceding anatomical changes in the tissue. Finally, using a clinical IV-OCT instrument and imaging catheter, we mapped intravascular inflammation stimulated by *intravenous (iv)* lipopolysaccharide (LPS) injection in rats, thereby demonstrating *in vivo* molecular imaging with IV-OCT.

3.6. Results and Discussion

3.6.1. Synthesis and Characterization of Aqueously Dispersible, NIR-II Scattering Gold Superclusters (AuSC@(Myrj52)$_2$)

In engineering AuSC suitable for *in vivo* imaging, a scalable synthetic method with high batch-to-batch reproducibility was sought. Drawing inspiration from oleylamine capped AuNP clustering initiated by the reduction of $HAuCl_4$ by ethylene glycol through heating,[32] we developed a rapid (~ 5 min) one-pot microwave-assisted method instead of following the more traditional oil bath heating approach. This microwave-assisted method ensured a more homogeneous heating in order to better convert $HAuCl_4$ into AuSCs. Synthetic parameters, including the concentration of gold precursor and capping agents, reaction temperature, and reaction times, were optimized to generate spherical and uniform clusters (Supplementary Table 1). In this work, oleylamine was the chosen capping agent throughout. The most critical parameter for AuSC formation from $HAuCl_4$ was the solvophobic effect, controlled by the polarity of the dispersion solvent. Highly polar solvents, such as methanol, induced tight, branching clusters, whereas highly non-polar solvents, such as hexanes, lacked the proclustering driving force necessary for AuSC formation, and instead yielded discrete AuNPs (Fig. 1).

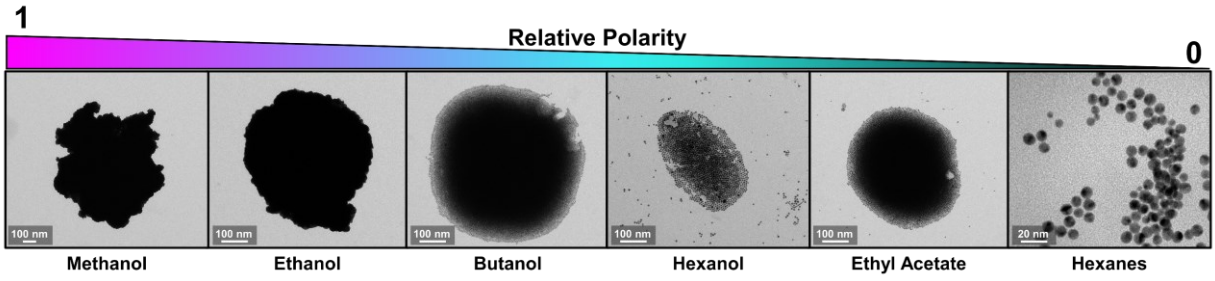

Figure 3.1 Effect of solvent polarity on oleylamine-capped AuNP clustering. Oleylamine-capped AuNPs following microwave synthesis were redispersed in solvents of varying relative polarities, then imaged by TEM.

Of the solvents tested, *n*-butanol generated the most homogenously spherical AuSC (Fig 1) and was used as the solvent for the proclustering step in our AuSC synthesis (Fig. 2A). However, as synthesized, bare AuSC were unstable under electron microscopy, as individual AuNPs were seen disassembling at the AuSC edges (Fig. 2B, C, left panel) and the nanotopography[34] appearing flat and collapsed (Fig. 2D, left panel). These AuSC gave a very broad LSPR peak centered at ~1000 nm (Fig. 2E, black curve), with a highly heterogeneous size and shape distribution of median diameter (d) = 181.1 nm (interquartile range [IQR]: 74 – 403 nm) (Fig. 2F, black bars). AuSC stabilization was achieved using amphiphilic polymers, containing a long aliphatic chain to interact with the hydrophobic oleylamine coating of the AuNPs, and a long hydrophilic portion to interact with aqueous solvents. Many different polymers were tested, with a comprehensive account of their effects on AuSC physicochemical properties shown in Supplementary Fig. 1. While all tested polymers performed similarly, ultimately, polyethylene oxide (40) stearate (Myrj52) was chosen for ease of downstream chemical functionalization, and for its known biocompatibility.[35,36] To achieve the polymer coating, AuSC were mixed in an *n*-butanol solution of Myrj52 to form AuSC@(Myrj52) (Fig. 2A, center panel). Qualitatively, AuSC@(Myrj52) had much tighter intraparticle spacing between the individual AuNPs (Fig. 2B, C, center panel), and appeared more spherical than bare AuSC (Fig. 2D, center *vs.* left panels). The resulting LSPR peak was narrower than in bare AuSC, centered at ~1100 nm (Fig. 2E, orange curve). The observed peak narrowing can be attributed to the narrower size distribution of AuSC@(Myrj52) following stabilization (d = 216 nm (IQR: 79 – 477 nm), Fig. 2F, orange bars). Despite improvement in nanotopography and optical properties, AuSC@(Myrj52) were still not dispersible in water. We hypothesized that a highly concentrated aqueous solution of Myrj52 could be used to further coat AuSC@(Myrj52)

through polymer-polymer interactions, which resulted in aqueously dispersible AuSC@(Myrj52)$_2$ (Fig. 2A, right panel). AuNP packing appeared tighter in AuSC@(Myrj52)$_2$ compared to AuSC@(Myrj52) (Fig. 2B, C, middle *vs.* right panel), and the overall cluster population appeared more homogeneous and with a more spherical nanotopography (Fig. 2D, right panel). After removal from the polymer solution and their dispersion in water, AuSC@(Myrj52)$_2$ displayed a narrower LSPR peak centered ~1350 nm (Fig. 2E, blue curve), attributable to the homogeneous population of AuSC@(Myrj52)$_2$, with d = 419 nm (IQR: 326 – 485 nm) (Fig. 2F, blue bars). An extended LSPR spectra of AuSC@(Myrj52) in *n*-butanol can be seen in Supplementary Fig. 2. Synthesis of AuSC@(Myrj52)$_2$ using 0.9% $NaCl_{(aq)}$ (saline) for the aqueous transfer steps was evaluated and no effect of the isotonic solution on cluster morphology or physicochemical properties was observed (Supplementary Fig. 3).

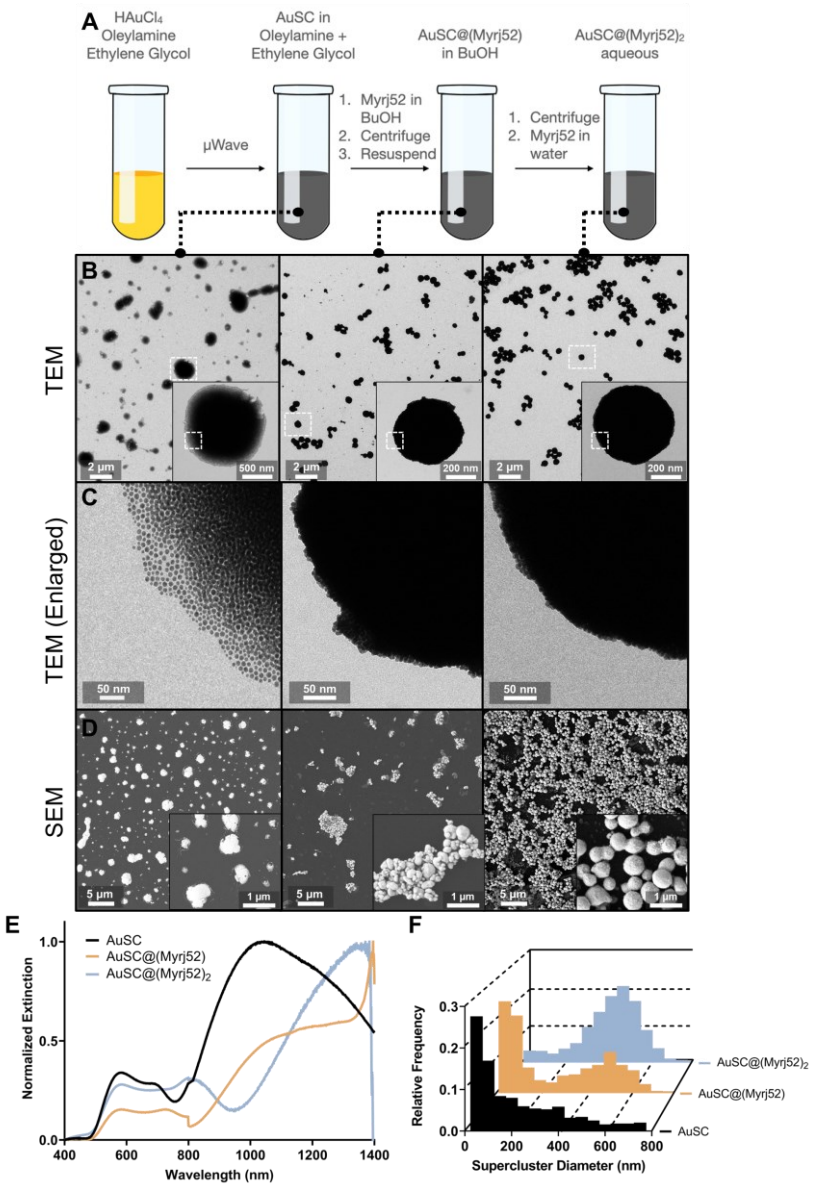

Figure 3.2 Optimized synthesis of AuSC and their physicochemical properties. A) Illustration of the optimized one-pot solvothermal synthetic method, proceeding from $HAuCl_4$ to water-dispersible AuSC (AuSC@(Myrj52)$_2$). B) Transmission electron microscopy images of AuSC after each synthetic step. White boxes in the primary image are magnified in the bottom right corner. White boxes in these magnified images are further magnified in C). D) Scanning electron microscopy images after each synthetic step. Images in the bottom right corner are magnified from the main image. E) Extinction spectra of AuSC after each synthetic step. The spectra for AuSC and AuSC@(Myrj52) were acquired in *n*-butanol, while that of AuSC@(Myrj52)$_2$ was acquired in water. F) Binned relative frequency of cluster diameters derived from two independent AuSC syntheses and extracted from TEM (n = 1015 (black), 1455 (orange), and 5041 clusters (blue)).

3.6.2. Stabilized Intraparticle Interactions Induce NIR-II Redshifting of AuSCs Through Global Plasmon Hybridization

Plasmon hybridization of AuNPs is well-studied,[37,38] but a persistent hybridization of many AuNPs, as present in the AuSC reported here, has yet to be observed or evaluated. Initial calculations were based on the median diameter (d) of AuNPs comprising AuSCs, determined by disassembly of water dispersed AuSC@$(Myrj52)_2$ by addition of a large volume of hexanes and overnight sonication. A significant input of energy in the form of sonication was necessary for AuSC disassembly. AuNPs from disassembled AuSC@$(Myrj52)_2$ (Fig. 3A, left panel) showed a homogeneous population of median d = 9 nm (IQR 8 – 10 nm, $AuNP_9$, Fig. 3A, center panel). Based on this median d, a single AuSC@$(Myrj52)_2$ cluster was calculated to contain ~1×10^9 AuNPs. The large number of AuNPs that comprised AuSC@$(Myrj52)_2$ led us to refer to the LSPR interaction occurring between all AuNPs within the as Global Plasmon Hybridization (GPH). GPH is the result of the close intraparticle spacing within AuSC and is an important factor in ensuring that NIR-II extinction is achieved. The importance of GPH was demonstrated by early attempts at cluster stabilization and aqueous dispersion through silication, which led to a complete loss of NIR-II LSPR activity due to plasmon damping (Supplementary Fig. 4).[39] From these results, we hypothesized that the tetraethyl orthosilicate monomer was small enough to translocate within the cluster and coat the particles individually. The resulting individual plasmonic peak of AuNPs (~550 nm) was broadened (Supplementary Fig. 4), but the NIR-II peak was entirely absent, since plasmonic coupling would be lost between particles, abrogating GPH.

LSPR spectra of $AuNP_9$ were acquired experimentally, and by simulation using the finite-difference time domain (FDTD) method. The two spectra both possess an LSPR peak at

~550 nm (Fig. 3A, right panel), in agreement with previous literature for AuNPs of this size.[40] The disassembly of AuSC@$(Myrj52)_2$ into $AuNP_9$ abolished all NIR-II LSPR activity, an indicator that persistent intraparticle interaction and GPH are necessary. Large AuNPs (d = 500 nm, $AuNP_{500}$) purchased commercially (Nanopartz, 500-CIT-DIH) were used to determine if AuNPs similar in size to our AuSC@$(Myrj52)_2$ but devoid of GPH would generate a similar LSPR spectrum (Fig. 3B, left and center panels). Experimental and FDTD simulated LSPR spectra displayed a broad LSPR peak at ~600 nm (Fig. 3B, right panel). Both simulated and experimental $AuNP_{500}$ showed a broader and redshifted LSPR peak in comparison to $AuNP_9$. A divergence was observed between the simulated and experimental $AuNP_{500}$ spectra, with experimental spectra showing greater extinction in the NIR-II region than predicted through simulation. Together, the simulated and experimental results for monolithic $AuNP_{500}$ further support the importance of GPH in resulting from persistent intraparticle interactions in AuSCs to produce substantial extinction in the NIR-II region.

To further understand the relationship between the nanomaterial architecture and the spectral properties of the AuSC, we sought to expose the internal structure of AuSC@$(Myrj52)_2$ using Ga focused-ion beam (FIB) milling, followed by helium-ion microscopy (HIM) of the milled cross-section (Fig. 3C). Upon inspection, our AuSC@$(Myrj52)_2$ appear composed of tightly packed AuNPs, except for a small ~50 nm diameter void, centered within the AuSC (Fig. 3C, center and right panels highlighted by the black arrow). This void was likely generated in the AuNP proclustering step, where AuNPs moving from the oleylamine to *n*-butanol were assembled around residual oleylamine to stabilize the surface energy during solvent transfer. After purification, this immiscible solvent is removed and leaves a central void behind. Intraparticle spacing was impossible to identify as milling artifacts on exposed AuSC faces could

not be ruled out. Utilizing the HIM images as guide, simulated extinction spectra were generated by FDTD for several different particle organizations and intraparticle unit cells (IUCs) where the volume between AuNPs within a cluster was varied including non-homogeneous (gradient) spacings, and the observed central void. A complete account of these simulations and their resulting LSPR spectra can be found in Supplementary Fig. 5. Variability in IUCs and organizations generated drastically different extinction spectra. Ultimately, an IUC of 13 nm^3 with a 50 nm diameter central void generated an extinction spectrum similar to that acquired experimentally (Fig. 3D). Simulations of the interaction of broadband light with $AuNP_9$, $AuNP_{500}$, and $AuSC@(Myrj52)_2$ can be seen in Supplementary Videos 1-3, respectively. Both simulated and experimental spectra contained the "bull horn" feature from ~600 nm to ~800 nm, likely a result of the LSPR of the individual AuNPs within the cluster, and the large NIR-II stretch from ~1000 nm to ~1400 nm due to the GPH effect. While $AuNP_{500}$ and $AuSC@(Myrj52)_2$ have a similar diameter, the monolithic $AuNP_{500}$ lack the NIR-II peak feature observed in both simulated and experimental spectra. The absorption and scattering components of these spectra were determined by simulation (Fig. 3E) and experimentally (Fig. 3F). Simulated spectra show the low overall contribution of absorption to the extinction spectra, with a broad peak between ~600 nm to ~800 nm, and a smaller broad peak from ~900 nm to ~1200 nm. The scattering component of the simulated extinction spectra is more dominant across the entire spectral range, with small peaks occurring ~600 nm and ~800 nm relative to the scattering-dominant effects of the AuSC at λ>1000 nm (Fig. 3E). The experimental spectral components deviate from the exact features observed in the simulated spectra, but the overall trend is conserved: absorption is slightly less dominant from 400 nm to 900 nm, but beyond 900 nm the scattering component of the spectra is the primary interaction with light (Fig. 3F).

Differences between the simulated and experimental extinction spectra of AuSC@$(Myrj52)_2$, as well as the absorption and scattering spectra, can be attributed to the fact that FDTD simulations look at a single AuSC, while in a real sample there is a population of AuSC with increased heterogeneity relative to the simulated sample as a result of the material complexity of the assembled AuSC@$(Myrj52)_2$ system. While we have constrained the system to a single IUC value, it is likely that the true IUC values are a gradient between the surface and the core of the cluster. In all AuSC simulations, the original AuNP LSPR peak was accompanied by a secondary absorption maximum in the NIR-II region. This secondary NIR-II maximum was never observed in the simulation of discrete $AuNP_9$ or $AuNP_{500}$. The absorptive behavior of AuSC across visible wavelengths is unsurprising, given the gray/black visual appearance of AuSC@$(Myrj52)_2$ in solution (Supplementary Fig. 6), but the extensive NIR-II scattering is critical for use as an IV-OCT molecular imaging contrast agent, optimizing the interference effects elicited by AuSCs on the 1350 nm laser light source.

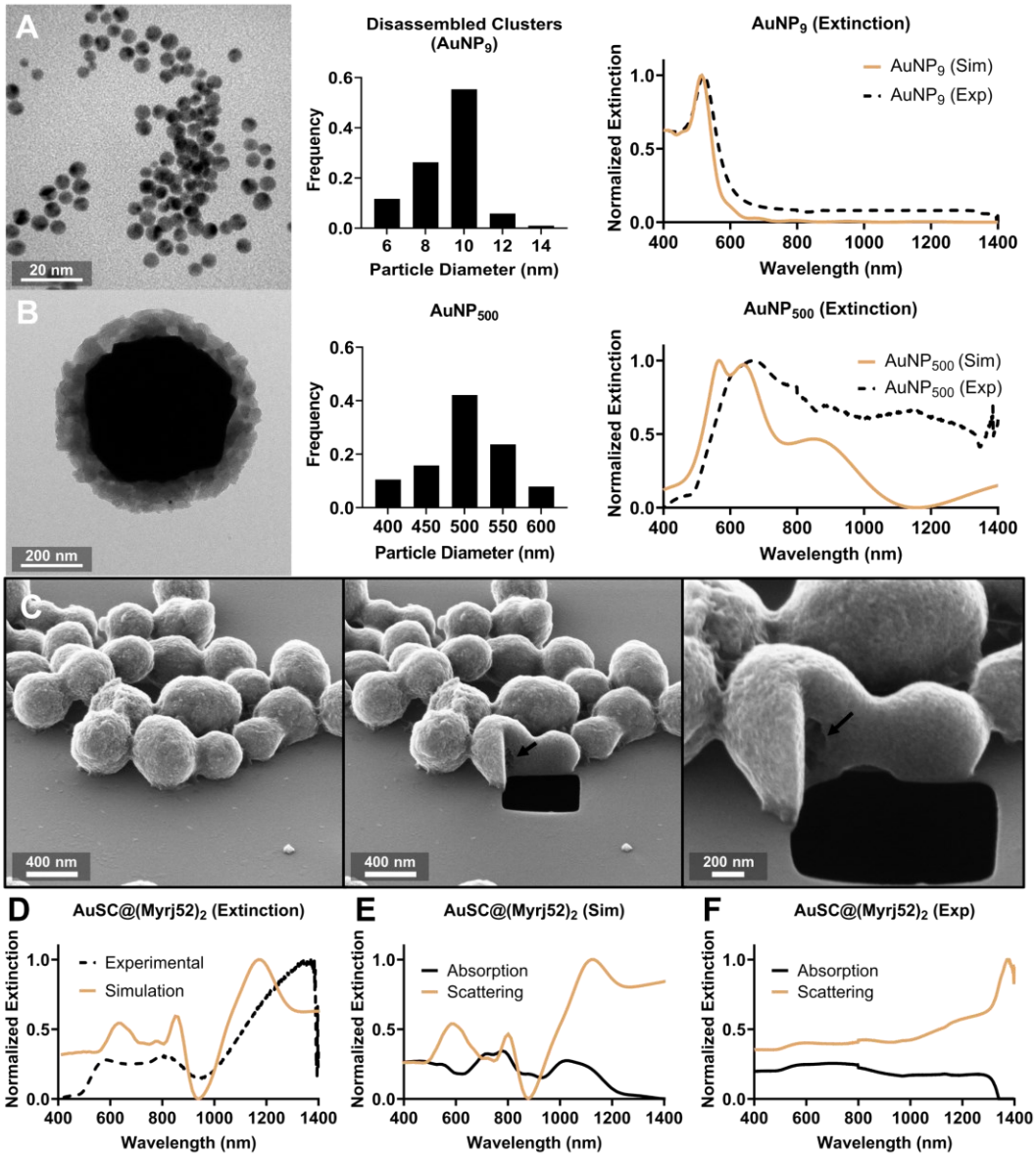

Figure 3.3 Extinction spectra of AuNPs and AuSC@(Myrj52)$_2$ determined experimentally and by FDTD simulations. A) TEM images of disassembled AuSC@(Myrj52)$_2$ dispersed in hexanes (left panel), their size distribution (n = 105 AuNP$_9$, center panel), as well as experimental and FDTD simulated extinction spectra (right panel). B) TEM (left), size distribution (n = 38 AuNP$_{500}$, centre), and experimental and simulated extinction spectra for d = 500 nm (IQR: 468 – 534 nm) AuNPs (AuNP$_{500}$). Binned histograms in A and B are relative frequencies of particle diameters from TEM. C) HIM images before (left panel) and after (center and right panels) gallium ion beam milling of AuSC@(Myrj52)$_2$. A black arrow highlights the central void. D) Experimental and FDTD simulated AuSC@(Myrj52)$_2$ extinction spectra. E) Simulated absorptive and scattering components of the extinction spectra. F) Absorptive and scattering components of the extinction spectra measured experimentally.

3.6.3. AuSC@(Myrj52)$_2$ Enhances IV-OCT Imaging Contrast

Image contrast enhancement of dispersions of AuSC@(Myrj52)$_2$, AuNP$_9$, or AuNP$_{500}$ in saline were evaluated in an imaging phantom using a clinical IV-OCT instrument (Abbott Illumien PCT) and clinical imaging catheter (Optis Dragonfly). The phantom and imaging setup are shown in Supplementary Fig. 7. Imaging of a saline solution provided a baseline for IV-OCT contrast (Fig. 4A). AuSC@(Myrj52)$_2$ generated bright, speckled contrast when imaged by IV-OCT over the concentration range 41 μg/mL to 730 μg/mL (Fig. 4A), with contrast enhancement relative to saline of 63.4 ± 0.9 arb. units and 19.3 ± 0.9 arb. Units, respectively (Fig. 4B). The bright signal produced is the result of backscattering of the IV-OCT laser (central wavelength = 1350 nm) by AuSC@(Myrj52)$_2$ (an absorptive effect would lead to a loss of signal).[41] At the same concentration of 365 μg/mL, AuSC@(Myrj52)$_2$ produced substantial image contrast (54.2 ± 2.3 arb. units) compared to AuNP$_9$ (4.7 ± 0.2 arb. units) and AuNP$_{500}$ (18.4 ± 2.7 arb. units). This highlighted the importance of GPH for IV-OCT signal generation, as LSPR and size-mismatched AuNP$_9$ generated almost no contrast enhancement (Fig. 4C). Size-matched AuNP$_{500}$ did generate some IV-OCT contrast due to their weak broad-range scattering,[42] though the similarly sized and plasmon-matched AuSC@(Myrj52)$_2$ improved this signal by nearly 3-fold (Fig. 4C). This result demonstrated the importance of matching the incident light source to a highly scattering spectral component in generating a strong IV-OCT contrast enhancement; though AuNP$_{500}$ and AuSC@(Myrj52)$_2$ are of similar diameter, the strong NIR-II scattering component of AuSC@(Myrj52)$_2$ allows it to generate significantly more IV-OCT contrast than AuNP$_{500}$.

A vascular phantom was generated by filling silicone tubing with an agarose solution doped with either saline, 500 μg/mL AuSC@(Myrj52)$_2$ in saline, or 500 μg/mL AuNP$_9$ in saline,

and IV-OCT imaging was performed with a clinical system and imaging catheter (Fig. 4D). Four phantom compositions were created and arranged sequentially in the tubing, then evaluated by a single catheter pullback through the agarose gel. Only the AuSC@(Myrj52)$_2$ showed substantial contrast enhancement relative to agarose containing saline only (Figs. 4D-F). Because of this contrast enhancement, fine structural elements within the phantom (*i.e.*, imperfections in agarose) were more prevalent and detailed when enhanced by AuSC@(Myrj52)$_2$ (Figs. 4E and F). Overall, only AuSC@(Myrj52)$_2$ significantly enhanced IV-OCT contrast relative to background, an outcome of matching the nanomaterial photophysical properties to the laser wavelength of the IV-OCT instrument.

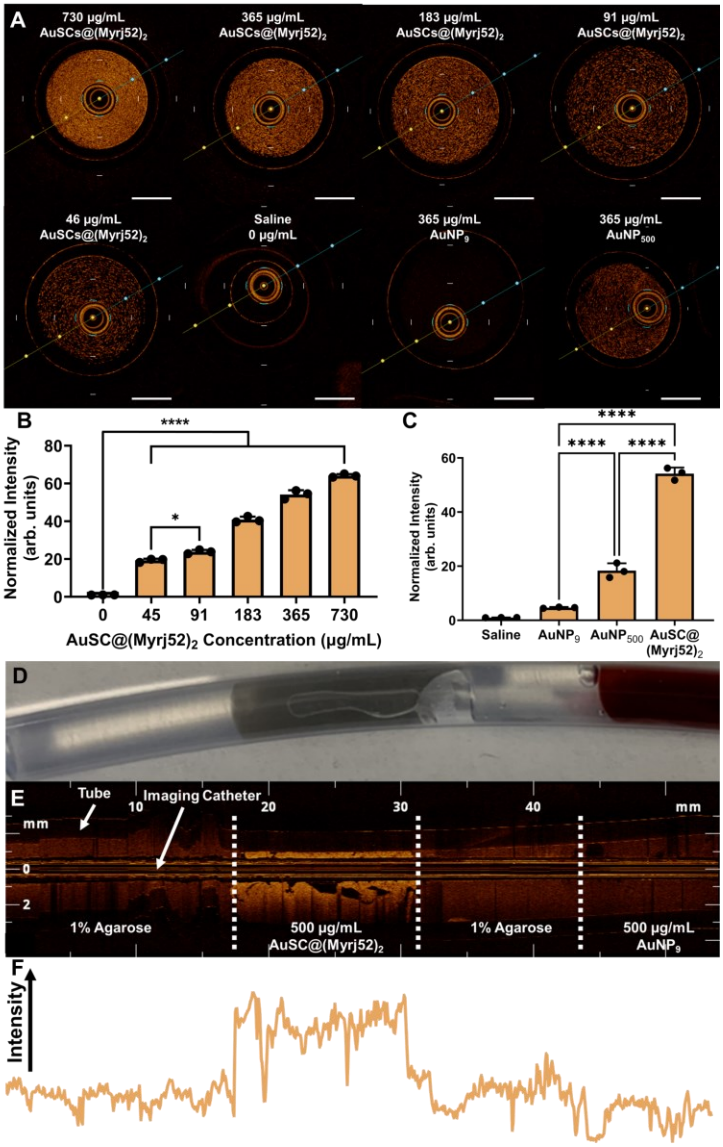

Figure 3.4 Evaluation of AuSC@(Myrj52)2 performance with an IV-OCT instrument. A) Cross-sections of IV-OCT pullback scans of glass capillaries filled with varying concentrations of AuSC@(Myrj52)$_2$, saline, AuNPs of diameter 9 nm (AuNP$_9$), or AuNPs of diameter 500 nm (AuNP$_{500}$). The white scalebar represents 1 mm. B) Contrast enhancement of AuSC@(Myrj52)$_2$ normalized to saline IV-OCT images. Data are presented as means ± standard deviation for n = 3 cross-sections, *p=0.0103 and ****p<0.0001. C) Contrast enhancement of AuNP$_9$, AuNP$_{500}$, and AuSC@(Myrj52)$_2$ normalized to saline. Data are presented as means ± standard deviation for n = 3 cross-sections, ****p<0.0001. For B) and C), statistical analysis was done by one-way ANOVA followed by a Tukey post hoc test. D) Intravascular phantom composed of a silicone tube filled with agarose doped with saline, AuSC@(Myrj52)$_2$, or AuNP$_9$. E) IV-OCT longitudinal scan of the arterial phantom, aligned to the appropriate regions of the above image in D). F) Signal intensity plot aligned to E) of the IV-OCT pullback of the phantom.

3.6.4. Chemical Functionalization AuSC@(Myrj52)$_2$ with a P-selectin Targeting Mimic Facilitates Biomolecular Recognition

With the demonstrated superior signal enhancement of AuSC for IV-OCT, we sought to functionalize AuSC@(Myrj52)$_2$ to approach IV-OCT molecular imaging. Our chosen molecular target was P-selectin, a membrane-anchored protein expressed in vascular endothelium as one of the earliest biomolecular responses to inflammation.[43–45] *In vivo,* the cognate ligands of P-selectin include P-selectin glycoprotein ligand-1 (PSGL-1)[46] and sialyl Lewis-X (SLeX)[47,48], which are both expressed on leukocytes as they roll through vasculature to survey for pathology.[49] Neither PSGL1 nor SLeX were suitable as targeting vectors for AuSC due to their complex structures limiting the scale of their production. However, previous reports have shown that the combined display of L-fucose, D-galactose, and an organosulfate group acts as a P-selectin ligand mimic, simulating the sulfated fucose that is imperative for SLeX binding *in vivo*.[50–53]

The functionalization of Myrj52 was achieved through the activation of the terminal primary hydroxyl group using 4-nitrophenolchloroformate (NPC) (Fig. 5A, **2**), resulting in high overall product conversion with the benefit of released NPC acting as a colorimetric indicator of reaction completeness (Fig. 5A). The anomeric carbons of L-fucose and D-galactose were conjugated to HO-(PEG)$_3$-NH$_2$ groups in the β-anomeric configuration, resulting in a glycoconjugate with nucleophilic handle for polymer conjugation. The resulting functionalized polymers (fuco- (F, Fig. 5A, **2**), galacto- (G, Fig. 5A, **3**), and sulfoMyrj52 (S, Fig. 5A, **4**)) were substituted into the AuSC coating steps, resulting in AuSC@(xyzFGS)$_2$ clusters, where x, y, and z are the molar ratios of each of the F, G, and S functionalized polymers, respectively. Synthetic procedures for the functionalized polymers and a description of all chemical syntheses can be

found in the Supplementary Information. All associated nuclear magnetic resonance (NMR) and high-resolution mass spectrometry characterization of these compounds can be found in Supplementary Figs. 8-46.

AuSC@(xyzFGS)$_2$ were evaluated for their P-selectin binding capabilities *in vitro* at 37 ^{o}C under agitation, an important factor in the P-selectin-ligand interaction.[54] Ratios of 1:2 F:S, 1:2 G:S, and 1:1:1 F:G:S were assayed for their ability to preferentially bind to P-selectin and bovine serum albumin (BSA) (Fig. 5B, top panel), or BSA-coated wells (Fig. 5B, bottom panel) according to Equation 2. Untargeted AuSC@(Myrj52)$_2$ showed a preferential binding of 70.2 ± 20.4%, while AuSC@(12FS)$_2$, AuSC@(12GS)$_2$, and AuSC@(111FGS)$_2$ showed binding values of 287.7 ± 70.2%, 209.8 ± 22.1%, and 227.6 ± 30.6%, respectively (Fig. 5C). We further evaluated F and S ratios 1:3, 1:1, or 3:1 F:S in this P-selectin ligand mimic on the AuSC surface (Fig. 5D). While at lower AuSC@(xyFS)$_2$ concentrations, the 3:1 formulation significantly outperformed the 1:3 and 1:1 combination, at higher concentrations, the F:S ratio had no significant impact, but consistently increased binding relative to AuSC@(Myrj52)$_2$. Ultimately, AuSC@(13FS)$_2$, was chosen for the *in vivo* studies since higher local concentrations were anticipated at the site of imaging due to direct injection of the contrast agent through the imaging catheter, as is done clinically. The selection of AuSC@(13FS)$_2$ is also supported by prior literature demonstrating a greater influence of the organosulfate residue on P-selectin binding compared to the carbohydrate residues.[55–57] AuSC LSPR spectra and spherical morphology (Fig. 5E and F, respectively) were unchanged with fucosylation and sulfation. The hydrodynamic size of AuSC@(13FS)$_2$ (Z-average = 514.1 ± 16.5 nm) was significantly greater than AuSC@(Myrj52)$_2$ (Z-average = 431.3 ± 42.6 nm, p = 0.035, Supplementary Fig. 47A). Zeta

potential remained unchanged between the two clusters (-37.0 ± 0.9 mV for AuSC@$(Myrj52)_2$ and -37.8 ± 0.4 mV for AuSC@$(13FS)_2$), Supplementary Fig. 47B).

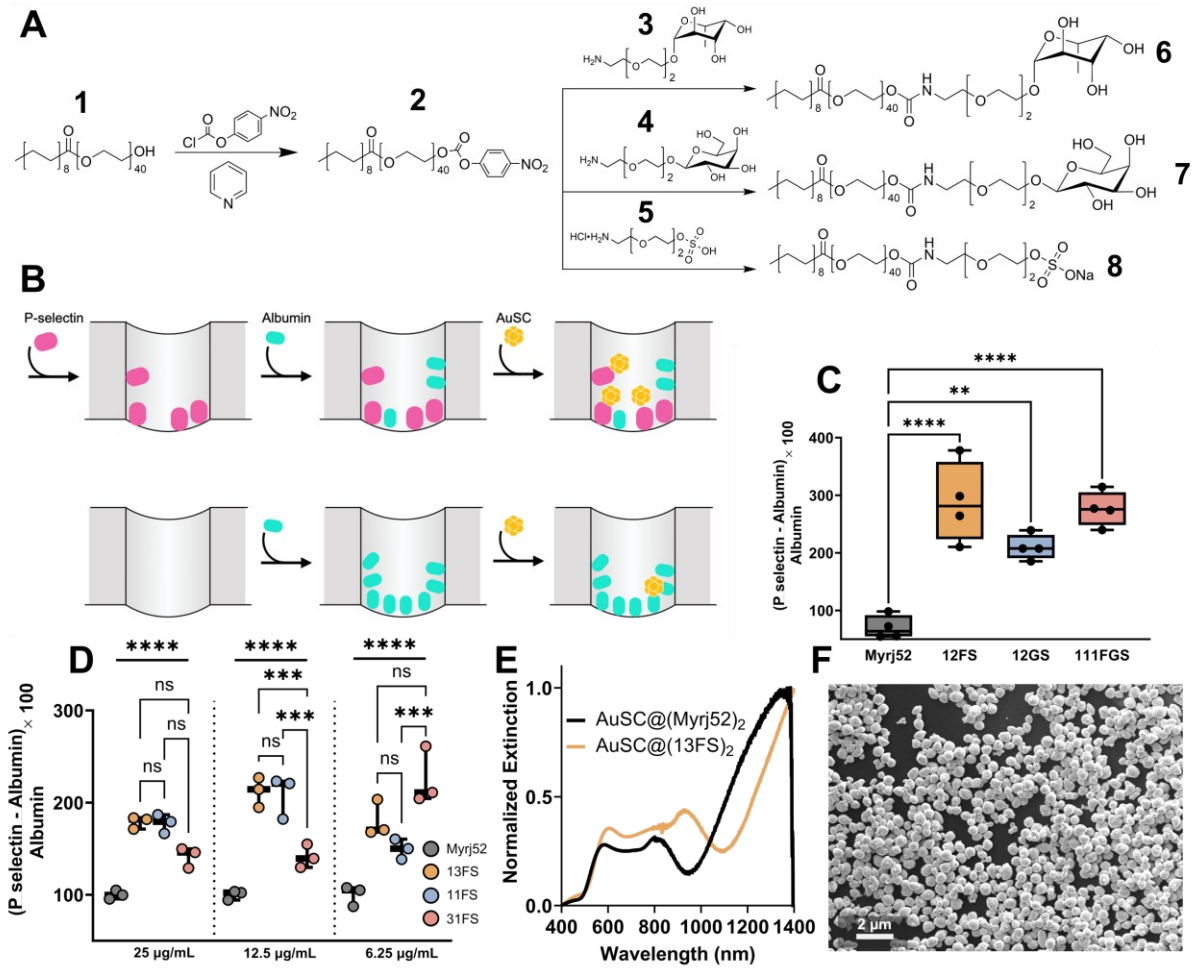

Figure 3.5 Bioactivation of Myrj52 and evaluation of functionalized AuSC binding to P-selectin in vitro. A) Synthetic overview of Myrj52 activation and functionalization. B) Illustration of the P-selectin binding assay. C) Comparison of 25 µg/mL Au AuSC@$(Myrj52)_2$ (gray), 12FS (orange), 12GS (blue), or 111FGS (pink) preferential binding to P-selectin *in vitro*. Data presented are boxplots of n = 3 replicate binding assays. Statistical analysis was done by one-way ANOVA followed by a Tukey post-hoc test. ****p<0.0001, **p=0.002. D) *In vitro* evaluation of different concentrations (25, 12.5, and 6.25 µg/mL of Au) of AuSC@$(Myrj52)_2$ (gray), 13FS (orange), 11FS (blue), and 31FS (pink). Data presented are boxplots of n = 3 replicate binding assays, normalized to the Myrj52 binding value. Statistical analysis was done by two-way ANOVA followed by a Tukey post-hoc test. ****p<0.0001, ***p<0.001. E) Extinction spectra of AuSC@$(Myrj52)_2$ and AuSC@$(13FS)_2$ in water. F) SEM image of AuSC@$(13FS)_2$.

3.6.5. Molecular IV-OCT Enabled by AuSC@(13FS)$_2$ to Map Early Intravascular Inflammation in vivo

In routine stent evaluation by IV-OCT, common radial artifacts due to the stent arise, known as bloom (the result of laser backscattering) and merry-go-round (the result of laser attenuation or shadowing).[58,59] The binding of AuSC@(13FS)$_2$ to endovascular P-selectin would result in the accumulation of metal at the endovascular surface and the generation of both bloom and merry-go-round image features, which we termed as Reflection or scattering events (ROSEs) (Fig. 6A). Intravascular inflammation in rats was induced through the administration of LPS *i.v.*, which was previously reported to stimulate intravascular P-selectin expression in rodents.[60–62] Dosage and incubation times that led to maximal P-selectin expression in rats were determined and validated experimentally, with 4 mg/kg LPS and 4 h resulting in extensive P-selectin expression (Supplementary Fig. 48). IV-OCT using a clinical instrument (Abbott Illumien PCT) and clinical imaging catheter (Optis Dragonfly) was performed on rats injected with LPS or saline (naïve) following the dissection and clamping of their abdominal aorta (AA), and insertion of the imaging catheter. Rats remained alive during this procedure. The AA was chosen as it was the only vasculature large enough to accommodate the 2 mm diameter imaging catheter. Saline was flushed *via* the imaging catheter port until blood was removed, as is performed clinically, and a baseline image was acquired while under 4 mL/min saline flow to maintain vascular patency (Fig. 6B, top panel). The AA was flushed with AuSC@(13FS)$_2$ or AuSC@(Myrj52)$_2$ through the imaging catheter, incubated for 30 s, then flushed with saline to clear unbound clusters prior to image acquisition (Fig. 6B, bottom panel). LPS-treated rats showed little to no ROSEs before and after flushing with AuSC@(Myrj52)$_2$ (Fig. 6B, left panels), while AuSC@(13FS)$_2$ showed numerous ROSEs that were not present prior to contrast flush (Fig. 6B,

center panels). Naïve rats showed no ROSEs before or after AuSC@$(13FS)_2$ flush. (Fig. 6C, right panels). A video of the full vessel length imaged can be seen in Supplementary Video 4.

Quantitative analysis of AuSC binding was performed in a blinded evaluation of the number of ROSEs observed *per* cm length of artery imaged (Fig. 6C). Significantly more ROSEs were generated in LPS-treated rats (Fig. 6C) with AuSC@$(13FS)_2$ (11.2 ± 8.9 ROSEs/cm) compared to AuSC@$(Myrj52)_2$ (1.9 ± 1.5 ROSEs/cm). Some binding in healthy tissue was expected as the plate-binding assay did show some non-specific adhesion of AuSC@$(Myrj52)_2$. A significant reduction in AuSC@$(13FS)_2$ induced ROSE generation was observed in healthy rats (0.2 ± 0.4 ROSEs/cm), which supported the specificity of the AuSC@$(13FS)_2$-P-selectin interaction. The high standard deviation of AuSC@$(13FS)_2$ ROSEs was due to the variability in inflammation severity in the rat LPS model (Supplementary Fig. 49). Blindly scored histological sections of the AA stained with anti-CD62p (anti-P-selectin antibody) showed a linear correlation between P-selectin expression (inflammation severity) and contrast agent binding (ROSEs/cm), suggesting that AuSC@$(13FS)_2$ molecular imaging can indicate arterial disease severity (Fig. 6D, $R^2 = 0.751$, $p < 0.05$). Superclusters were stable even after overnight incubation in mouse serum as indicated by the maintenance of the NIR-II LSPR peak and presence of AuSC by SEM (Supplementary Fig. 50). Therefore, AuSC would still generate strong scattering signal even in the presence of remaining sera factors, though these are routinely flushed prior to IV-OCT clinical imaging. These results support the utility of AuSC@$(13FS)_2$ as an IV-OCT molecular imaging agent for vascular inflammation, and broadly support the application of AuSC as a molecular imaging platform capable of adding molecular-level information to IV-OCT without changing the current clinical workflow.

AuSC@(13FS)$_2$ biodistribution was quantified by ICP-MS analysis (Supplementary Fig. 51) following *i.v.* injection at a dose that was ~5× more concentrated than that used for imaging. All injections were well-tolerated by the animals, with no symptoms of toxic response. Significant Au deposition was only observed in the spleen, which appeared to be the primary route of AuSC@(13FS)$_2$ clearance. This is a common route of blood clearance for nanoparticles of this size.[63,64] Given the low %ID/g wet tissue observed at the earliest timepoint of 1 h post-injection, it is likely AuSC@(13FS)$_2$ clears rapidly. Histological evaluation of tissues involved in blood clearance showed no change in morphology up to 24 h post-injection (Supplementary Fig. 52).

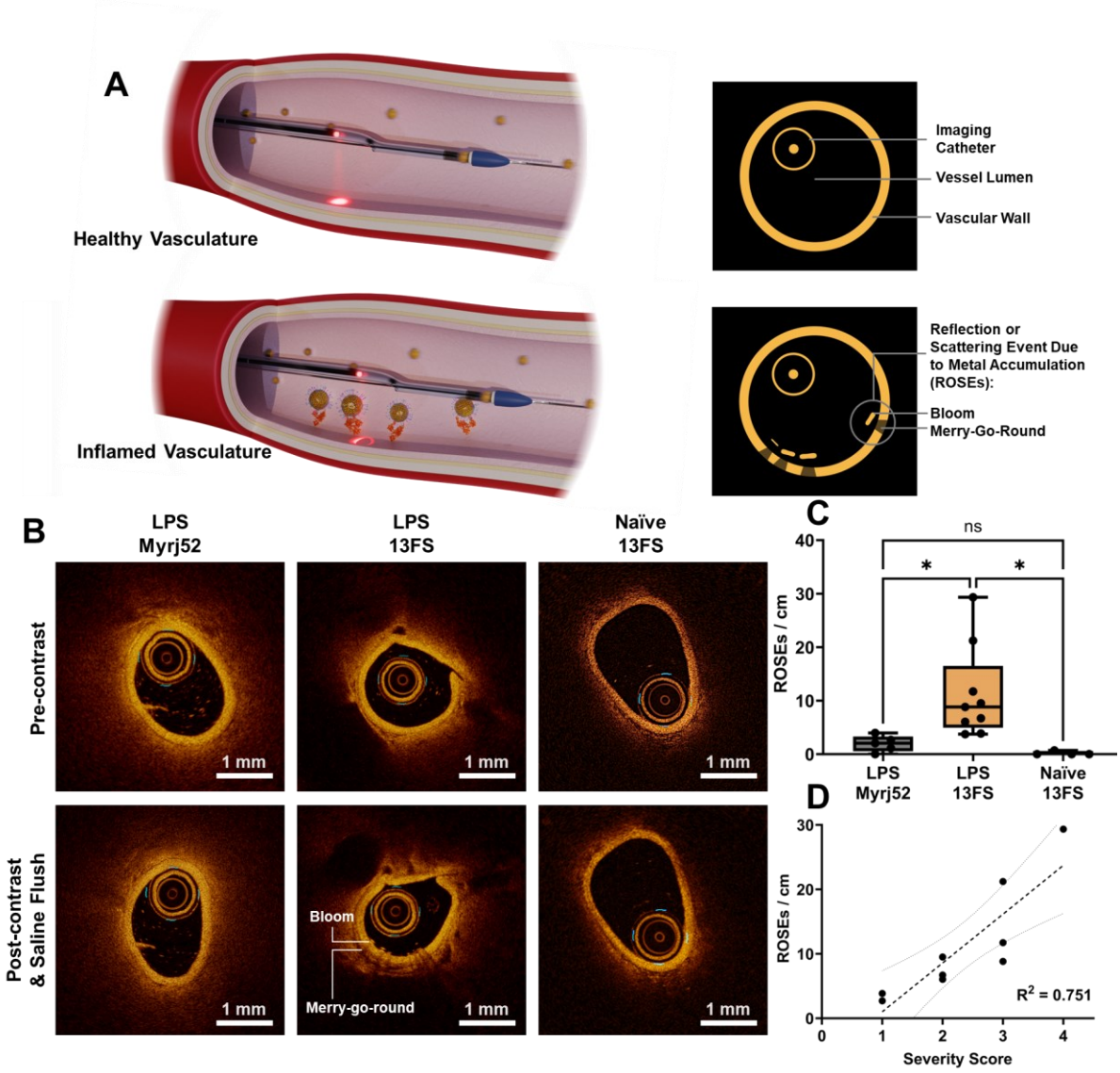

Figure 3.6 i*n vivo* IV-OCT molecular imaging of intravascular inflammation with AuSC@(13FS)$_2$. A) Illustration of the expected binding interactions of AuSC@(13FS)$_2$ in healthy (top) and inflamed (bottom) arteries, and the hypothesized tomographs with AuSC binding-associated reflection or scattering events (ROSEs). B) Two-dimensional IV-OCT cross sections of rat abdominal aorta (AA) before (top panel) and after (bottom panel) AuSC@(Myrj52)$_2$ or AuSC@(13FS)$_2$ flush, following a saline flush in inflamed (left and centre) and healthy (right) rats. C) ROSEs generated per centimeter in the rat abdominal aorta (AA). Data are presented as boxplots of n = 5 (LPS, Myrj52), n = 9 (LPS, 13FS), and n = 4 (naïve, 13FS) rats. *p<0.05. Statistical analysis was done by one-way ANOVA followed by a Tukey post-hoc test. D) Correlation between histological severity score of anti-CD62p rat AAs correlated to their ROSEs/cm for AuSC@(13FS)$_2$ in LPS-treated rats. The dotted line represents a linear fit with R^2 = 0.751. Dashed lines above and below represent the error bands.

3.6.6. Conclusions

Herein we have shown a facile, rapid, and scalable synthetic approach for the one-pot generation and controlled superclustering of oleylamine capped AuNPs. The concept of solvophobically-driven superclustering demonstrated here with $HAuCl_4$ will likely parallel that with using other capping agents and other plasmonic nanoparticles, due to the dependence on solvent-driven assembly. We have also demonstrated the importance of persistent particle stabilization in generating a large redshift through GPH, as well as how changes in IUCs can be used to tailor the LSPR response. Polymer-mediated AuSC stabilization facilitates aqueous dispersion of the clusters without changing their optical properties. Ultimately, solvent and stabilizer can be used in concert to tailor IUC and tune the LSPR of the resulting superclusters.

Towards introducing IV-OCT molecular imaging, we have synthesized three novel polymers bearing fucosyl, galactoyl, and sulfyl functional groups that, in combination, form a P-selectin ligand on our AuSC. The ligand combination resulted in binding to P-selectin both *in vitro* and *in vivo*. The absence of change to the physicochemical properties of AuSC due to the introduction of the target ligand indicates a high degree of physicochemical compatibility for terminal functionalization of Myrj52, allowing these NIR-II scattering superclusters to serve as a platform for molecular imaging in IV-OCT. Finally, we have demonstrated the first instance of *in vivo* molecular imaging with IV-OCT using our AuSC@$(13FS)_2$ contrast agent in live rats with LPS-stimulated P-selectin expression. Given the modularity of the surface functionalization and the tolerability of conjugation strategies to many functional groups and polymers, further efforts to improve on binding, or target different biomolecules of inflammation can create a more personalized approach to diagnostics in IV-OCT without sacrificing the core technology of generating ROSEs by target engagement. AuSC@$(13FS)_2$ target binding and immobilization

generates ROSE artifacts like those seen due to placed stents and stand out in comparison to other IV-OCT image features, allowing the easy identification of regions of endovascular inflammation. Overall, we have demonstrated that these highly NIR-II scattering, P-selectin targeting AuSC@(13FS)$_2$ may serve as the genesis of more personalized cardiovascular medicine through IV-OCT molecular imaging.

3.7. Methods

All animal studies were conducted under Animal Use Protocol HIe-3652 approved by the IACUC at the University of Ottawa. Rats were housed doubly under a 12 h light/dark cycle, and ambient temperature of 20-24°C and 45 to 65% humidity. All rats were provided access to food (Rodent Laboratory Chow) and water *ad libitum*.

3.7.1. General Reagents

All chemical reagents were purchased from Sigma-Aldrich and used as is unless otherwise reported, apart from mouse P-selectin which was purchased from Sino Biologics Inc. (50737-M08H). All solvents were HPLC grade, except for water (18.2 MΩ cm Millipore water).

3.7.2. Experimental Procedures

All AuSC reaction mixtures were degassed and backflushed with N_2 prior to microwave-assisted synthesis on a CEM Discovery SP microwave. For all AuSC syntheses, power was set to 75 W and the reaction was held for 90 s at 115ºC. All AuSC and AuNP concentrations are reported as µg/mL as determined by ICP-OES on an Agilent 700 after 4 h solubilization at 80ºC by aqua regia (3:1 HCl:HNO_3) and dilution in water. LSPR spectra were acquired using a Cary 7000 UV-Vis-NIR spectrometer. All spectra were presented normalized from 0 to 1, with 0 being the lowest signal and 1 being the highest to adequately compare spectra with concentration

dissimilarities, as well as to compare between experimental and simulated spectra. All TEM images were acquired using an FEI Tecnai G2 Spirit Twin TEM, all SEM images were acquired using a JEOL JSM-7500F field emission SEM, all HIM images were acquired using a NAME. All IV-OCT imaging was performed using an Abbott Illumien™ OPTIS™ PCI instrument using Dragonfly™ OPTIS™ imaging catheters and 54 mm high-resolution pullback imaging. All image analyses and quantifications were performed using FIJI. GraphPad Prism 10.0 was used to generate all graphs, graphical figures, and statistical analyses.

3.7.3. General Method for AuSC@(Myrj52)$_2$ and AuSC@(xyzFGS)$_2$ Synthesis

In a typical synthesis, $HAuCl_4 \bullet 3H_2O$ (40 mg, 0.1 mmol) was dissolved in ethylene glycol (2 mL) in a three-neck round bottom flask under stirring at 45ºC. Oleylamine (70%, 4 mL) and ethylene glycol (4 mL) were added to the flask and the entire solution was degassed until effervescence ceased (~45 min). The flask was backflushed with N_2 and the contents decanted into an N_2-purged 35 mL microwave reaction vial. The vial was capped with a Teflon cap and inserted into a CEM Discovery SP microwave reactor, where the solution was heated at 75 W (~0.65ºC / s), with reaction held at 115ºC for 90 s, at which point the solution was cooled by blowing air onto the vessel, which was released from the reactor at 50ºC. These stabilized AuSC were immediately added to a 40 mL solution of n-butanol containing functionalized or unfunctionalized Myrj52 (20 g/L) and was agitated overnight. The solution was centrifuged at room temperature (RT, 1000 xg, 10 min), decanted, replenished with fresh n-butanol (40 mL) not containing polymers, and sonicated back into dispersion. Centrifugation washes were repeated three times, with the mono-coated AuSC pellet after the third centrifugation being re-dispersed by sonication in an aqueous (water or saline) solution of functionalized or unfunctionalized Myrj52 (40 mL, 40 g/L). AuSC in aqueous polymeric solution were shaken overnight, followed

by centrifugation (RT, 1000 xg, 10 min), decanting, and re-dispersion by sonication into fresh aqueous solution (40 mL) not containing the polymers. Centrifugation washes were repeated three times, with the pellet being resuspended in 2 mL of aqueous solvent after the final centrifugation. The doubly-coated AuSC concentrate was twice-purified by size exclusion column chromatography (Pd10 column) eluting with water. Resulting AuSC were allowed to settle overnight, were decanted, and resuspended in 1 – 2 mL of fresh aqueous solution without polymers. Aqueously dispersed AuSC were stored at 4ºC. AuSC concentration (μg/mL Au) was determined by ICP-OES analysis of an aliquot of this solution.

3.7.4. AuSC and AuNP Size Measurements by TEM Image Analysis

AuNPs or AuSC (stabilized, mono-, or di-coated) were drop cast and dried on the carbon-coated side of Cu TEM grid with mesh size 300 and dried overnight. Acquired TEM images were loaded into FIJI and turned into binary images. A watershed function was applied, and the "analyze particles" function was used to automatically measure the area of clusters or particles within the field of view. The resulting area was used to solve for diameter of the AuNPs or AuSC. Sizes were presented as a relative frequency distribution of binned diameters, with the relative frequency describing the amount of occurrence of one bin value. The same grids used for TEM imaging were also used for subsequent SEM imaging.

3.7.5. AuSC and AuNP LSPR Spectra Acquisition

AuNPs or AuSC (stabilized, mono-, or di-coated) were dispersed in their appropriate solvent and placed in a low-volume (700 μL) black-walled cuvette. All extinction spectra were zeroed and blanked by the plain dispersion solvent at 0% and 100% transmission prior to extinction spectra acquisition of samples.

The Cary 7000 UV-Vis-NIR was equipped with an external DRA-2500 attachment; a large integrating sphere that allowed for the separation of scattering and absorptive components of the extinction spectra by collection of the scattered component. We used 1.5 cm glass-walled cuvettes compatible with NIR-II light in a center-mount cuvette holder made for the external DRA-2500 (Agilent). Scattering spectra was zeroed and blanked by water at 0% and 100% transmission prior to acquisition of scattering spectra. The resulting scattering spectra was subtracted from the previously acquired extinction spectra to generate the absorption spectra.

3.7.6. Milling and HIM Imaging of AuSC@(Myrj52)$_2$

A TEM grid drop-casted with AuSC@(Myrj52)$_2$ as previously described was used for all milling and HIM imaging. Grids were loaded into a Zeiss Orion NanoFAB with Ga FIB. Clusters were quartered with the Ga FIB (10 pA, 25 μm aperture, 30 kV landing energy, dwell time 0.1 μs, and 0.15 nC/μm^2 dose). HIM images before and after milling were acquired using a gas-field ion source with different fields of view. Low magnification HIMs were acquired with a beam current of 1.53 pA and a dwell time of 1 μs, while high magnification images were acquired with a beam current of 1.08 pA and a dwell time of 0.5 μs.

3.7.7. FDTD Modelling and Spectra Simulation

The simulated results were obtained through an in-house finite-difference time-domain (FDTD) electrodynamic solver that is parallelized for high performance computing.[65] The solver is deployed on the Digital Research Alliance of Canada High Performance Computing network, using up to a maximum of 800 cores, and running continuously for over 24 h. The simulation domain consists of uniform ($\Delta x = \Delta y = \Delta z$) Yee cells with a side length of 0.5 nm that is excited by a plane-wave broadband raised cosine source (Equation 1),

$$s(t) = \frac{1}{8}(1 - \cos \omega_{max} t)^3 \quad \textbf{Eq. 1}$$

where $\omega_{max} = 2$ PHz. The simulation domain size for the AuSC is 620 nm (1240 cells) in each direction, terminated by 20 convolutional perfectly matched layer cells on each face of the cubic domain. The extinction spectrum is obtained through the scattering and absorption cross sections that are measured via the "Poynting vector flux method".[65]

The superclusters whose results are shown in Fig 3 D-F are modelled as a spherical shell composed of 9 nm diameter gold spheres, arranged in a face-centered cubic (FCC) lattice with an outer radius of 209 nm and an inner radius of 50 nm, and centre-to-centre interparticle spacing of 13 nm. This lattice is embedded into a sphere of the amphiphilic polymer of the same diameter. The superclusters are located within a background material of water. The dispersive behaviour of gold is modelled by a Drude model with two critical points, implemented using the auxiliary differential equation technique.[66] Water and amphiphilic polymers were modelled as non-dispersive media with fixed refractive indices of n = 1.33 and n = 1.46 respectively.

3.7.8. in vitro *IV-OCT Imaging of AuSC@(Myrj52)$_2$:*

Cross-sectional imaging:

To prevent external light interference, imaging was performed inside of a Styrofoam box, which was pierced by a glass Pasteur pipette containing an AuSC suspension. The imaging catheter was inserted into the thin end of the pipette external to the box and the portion of the pipette inside of the box was imaged by pullback. A picture of this setup can be seen in Supplementary Fig. 7. The integrated density of a consistent area and region of the cross-sections generated by the longitudinal imaging was acquired using FIJI and normalized to the weakest contrast enhancer, AuNP$_9$.

Vascular phantom and longitudinal imaging:

A 2% agarose solution was prepared by heating 50 mL of water containing 500 mg of agarose. The hot solution was mixed 1:1 with 1 mg/mL AuSC@$(Myrj52)_2$, 1 mg/mL $AuNP_9$, or water. These solutions were serially injected into a piece of silicone tubing cooled at 4°C for 2 h. The tube was placed in the same Styrofoam box setup, pierced by a glass pipette, and catheterized within the box. IV-OCT pullback imaging was performed to generate a longitudinal image of the phantom. The integrated density across the bottom portion of the longitudinal image was normalized from 0 (lowest integrated density value) to 1 (highest integrated density value) to generate the intensity curve associated with the image.

3.7.9. in vitro *P-selectin Binding Assay*

Highly hydrophobic 96-well plates were incubated with 50 µl of 1X Tris-buffered saline solution containing 1 mM $CaCl_2$ (pH 7.4, TBS) alone or with mouse recombinant P-selectin (2 µg/mL) overnight at 4°C. The wells were washed three times with TBS, and then incubated overnight at 4°C with 150 µl of bovine serum albumin (BSA, 3%) in TBS to block non-coated areas of the wells. The wells were washed three times with 1 mM $CaCl_2$ in Milli-Q water, then incubated with different concentrations or different ratios of AuSC$(xyzFGS)_2$ in Milli-Q water with 1 mM $CaCl_2$ at 37°C on a plate shaker at 700 RPM for 15 min. The wells were washed three times with Milli-Q water to remove unbound clusters. Aqua regia (200 µl) was added to each well and the plate was left at room-temperature over the weekend to digest the remaining clusters. The digest solution was diluted with Milli-Q water and Au concentration was determined by ICP-MS. Preferential binding was expressed as a normalized ratio of the concentration of AuSC@$(xyzFGS)_2$ bound to P-selectin-coated wells compared to BSA-coated wells according to Equation 2:

$$\frac{[BoundAuSC]_{Psel} - [BoundAuSC]_{BSA}}{[BoundAuSC]_{BSA}} \quad \textbf{Eq. 2}$$

3.7.10. Targeting P-selectin n Rat in vivo *Model*

Sprague-Dawley rats (12 weeks old, Charles River) were injected *iv* with LPS (*Escherichia coli* O111:B4, 4 mg/kg in saline) or saline, which was allowed to circulate for 4 h. Rats were anesthetized with isoflurane and dissected to expose the AA. The AA was clamped, severed, and catheterized with the IV-OCT imaging catheter. A syringe pump connected to the injection port of the imaging catheter pumped saline through the AA at 3.5 mL/min. Once clear of blood, a 54 mm high-resolution pullback image was acquired. Flow was interrupted and 100 µl of 500 µg/mL AuSC@$(13FS)_2$ was injected through the imaging catheter and allowed to incubate in the AA for 30 s. Flow of saline at 3.5 mL/min was resumed, and once excess cluster was flushed out another pullback image was acquired. The catheter was removed, and rats were euthanized by exsanguination. The section of catheterized AA was removed and left in 10% formalin in phosphate-buffered saline (pH 7.4) overnight, then replaced by 70% ethanol the next day. Tissue was mounted in paraffin, sliced, and stained with anti-CD62p to evaluate P-selectin expression within the AA. These sections were scored by a blinded participant.

DICOMs of IV-OCT pullbacks were cropped to include usable images of the AA (minimum 3 cm of AA length). Each slice (0.01 cm) was evaluated to determine if a ROSE was visible. A ROSE must have both the bloom and merry-go-round features to be included as a count.

3.7.11. Statistical Analyses

Statistical analyses were performed using GraphPad Prism 10.0 (GraphPad, Inc.). Comparisons across more than two groups was performed by one-way ANOVA followed by Tukey's test for honestly significant differences. Normality was assumed where appropriate for

all data sets. Prior to ANOVA, Levene's test was used to confirm equal variance, and visual quantile-quantile plot analysis was used to confirm homoscedasticity.

3.8. Data Availability

All raw and source data is available on request of the corresponding author.

3.9. Code Availability

Code is available upon reasonable request from Dr. Lora Ramunno.

3.10. References

1. Feng, Z. *et al.* Perfecting and extending the near-infrared imaging window. *Light: Science & Applications 2021 10:1* **10**, 1–18 (2021).
2. Cao, J. *et al.* Recent Progress in NIR-II Contrast Agent for Biological Imaging. *Front Bioeng Biotechnol* **7**, 1–21 (2020).
3. Zhang, N. nan *et al.* Recent advances in near-infrared II imaging technology for biological detection. *J Nanobiotechnology* **19**, 1–14 (2021).
4. Xu, H. *et al.* NIR-II-absorbing diimmonium polymer agent achieves excellent photothermal therapy with induction of tumor immunogenic cell death. *J Nanobiotechnology* **21**, 132 (2023).
5. Yang, Q., Ma, H., Liang, Y. & Dai, H. Rational Design of High Brightness NIR-II Organic Dyes with S-D-A-D-S Structure. *Acc Mater Res* **2**, 170–183 (2021).
6. Li, Z. *et al.* NIR-II Functional Materials for Photoacoustic Theranostics. *Bioconjug Chem* **33**, 67–86 (2022).
7. Su, Y., Yu, B., Wang, S., Cong, H. & Shen, Y. NIR-II bioimaging of small organic molecule. *Biomaterials* **271**, 120717 (2021).

8. Sun, X. *et al.* Effects of nanoparticle sizes, shapes, and permittivity on plasmonic imaging. *Optics Express, Vol. 30, Issue 4, pp. 6051-6060* **30**, 6051–6060 (2022).

9. Zhuang, Y. *et al.* Size and Shape Effect of Gold Nanoparticles in "Far-Field" Surface Plasmon Resonance. *Particle & Particle Systems Characterization* **36**, 1800077 (2019).

10. González, A. L., Noguez, C., Beránek, J. & Barnard, A. S. Size, shape, stability, and color of plasmonic silver nanoparticles. *Journal of Physical Chemistry C* **118**, 9128–9136 (2014).

11. Bezerra, H. G., Costa, M. A., Guagliumi, G., Rollins, A. M. & Simon, D. I. Intracoronary Optical Coherence Tomography: A Comprehensive Review: Clinical and Research Applications. *JACC Cardiovasc Interv* **2**, 1035–1046 (2009).

12. Roleder, T. *et al.* The basics of intravascular optical coherence tomography. *Postepy Kardiol Interwencyjnej* **11**, 74 (2015).

13. Gounis, M. J. *et al.* Intravascular Optical Coherence Tomography for Neurointerventional Surgery. *Stroke* **50**, 218–223 (2019).

14. Megaly, M. *et al.* Radial Versus Femoral Access in Chronic Total Occlusion Percutaneous Coronary Intervention: A Systematic Review and Meta-Analysis. *Circ Cardiovasc Interv* **12**, (2019).

15. Swanson, E. A. & Fujimoto, J. G. The ecosystem that powered the translation of OCT from fundamental research to clinical and commercial impact [Invited]. *Biomed Opt Express* **8**, 1638 (2017).

16. McCabe, J. M. & Croce, K. J. Optical coherence tomography. *Circulation* **126**, 2140–2143 (2012).

17. Yonetsu, T. *et al.* Plaque morphologies and the clinical prognosis of acute coronary syndrome caused by lesions with intact fibrous cap diagnosed by optical coherence tomography. *Int J Cardiol* **203**, 766–774 (2016).

18. Toutouzas, K., Karanasos, A. & Tousoulis, D. Optical Coherence Tomography For the Detection of the Vulnerable Plaque. *European Cardiology Review* **11**, 90 (2016).

19. Wang, A., Qi, W., Gao, T. & Tang, X. Molecular Contrast Optical Coherence Tomography and Its Applications in Medicine. *Int J Mol Sci* **23**, 3038 (2022).

20. Ameh, T. *et al.* Silver and Copper Nanoparticles Induce Oxidative Stress in Bacteria and Mammalian Cells. *Nanomaterials* **12**, (2022).

21. Mondal, I., Raj, S., Roy, P. & Poddar, R. Silver nanoparticles (AgNPs) as a contrast agent for imaging of animal tissue using swept-source optical coherence tomography (SSOCT). *Laser Phys* **28**, (2018).

22. Marin, R. *et al.* Plasmonic Copper Sulfide Nanoparticles Enable Dark Contrast in Optical Coherence Tomography. *Adv Healthc Mater* **9**, 1901627 (2020).

23. Cabuzu, D., Cirja, A., Puiu, R. & Grumezescu, A. Biomedical applications of gold nanoparticles. *Curr Top Med Chem* **15**, 1605–1613 (2015).

24. Si, P. *et al.* Gold nanomaterials for optical biosensing and bioimaging. *Nanoscale Adv* **3**, 2679–2698 (2021).

25. Si, P. *et al.* Gold Nanoprisms as Optical Coherence Tomography Contrast Agents in the Second Near-Infrared Window for Enhanced Angiography in Live Animals. *ACS Nano* **12**, (2018).

26. Nguyen, V. P. *et al.* Gold Nanorod Enhanced Photoacoustic Microscopy and Optical Coherence Tomography of Choroidal Neovascularization. *ACS Appl Mater Interfaces* **13**, (2021).

27. Zhao, Y. *et al.* A comparison between sphere and rod nanoparticles regarding their in vivo biological behavior and pharmacokinetics. *Sci Rep* **7**, 4131 (2017).

28. Hu, J. *et al.* Gold nanoshells: Contrast agents for cell imaging by cardiovascular optical coherence tomography. *Nano Res* **11**, 676–685 (2018).

29. Hu, J. *et al.* Optical Nanoparticles for Cardiovascular Imaging. *Adv Opt Mater* **6**, 1800626 (2018).

30. Muñoz-Ortiz, T. *et al.* Molecular Imaging of Infarcted Heart by Biofunctionalized Gold Nanoshells. *Adv Healthc Mater* **10**, 2002186 (2021).

31. Hu, J. *et al.* Dynamic single gold nanoparticle visualization by clinical intracoronary optical coherence tomography. *J Biophotonics* **10**, 674–682 (2017).

32. Kwon, N. *et al.* Direct Chemical Synthesis of Plasmonic Black Colloidal Gold Superparticles with Broadband Absorption Properties. *Nano Lett* **18**, 5927–5932 (2018).

33. Yu, J. H. *et al.* Highly Excretable Gold Supraclusters for Translatable In Vivo Raman Imaging of Tumors. *ACS Nano* **17**, (2023).

34. Gulumian, M., Andraos, C., Afantitis, A., Puzyn, T. & Coville, N. J. Importance of Surface Topography in Both Biological Activity and Catalysis of Nanomaterials: Can Catalysis by Design Guide Safe by Design? *International Journal of Molecular Sciences 2021, Vol. 22, Page 8347* **22**, 8347 (2021).

35. Witika, B. A. *et al.* Biocompatibility of Biomaterials for Nanoencapsulation: Current Approaches. *Nanomaterials 2020, Vol. 10, Page 1649* **10**, 1649 (2020).

36. Ethylene glycol monostearate | C20H40O3 | CID 24762 - PubChem. https://pubchem.ncbi.nlm.nih.gov/compound/Ethylene-glycol-monostearate#section=Interactions.

37. Rahmani, M. *et al.* Beyond the hybridization effects in plasmonic nanoclusters: Diffraction-induced enhanced absorption and scattering. *Small* **10**, 576–583 (2014).

38. Nordlander, P., Oubre, C., Prodan, E., Li, K. & Stockman, M. I. Plasmon hybridization in nanoparticle dimers. *Nano Lett* **4**, 899–903 (2004).

39. Lee, S. A. & Link, S. Chemical Interface Damping of Surface Plasmon Resonances. *Acc Chem Res* **54**, 1950–1960 (2021).

40. Polavarapu, L., Venkatram, N., Ji, W. & Xu, Q. H. Optical-limiting properties of oleylamine-capped gold nanoparticles for both femtosecond and nanosecond laser pulses. *ACS Appl Mater Interfaces* **1**, 2298–2303 (2009).

41. Aumann, S., Donner, S., Fischer, J. & Müller, F. Optical Coherence Tomography (OCT): Principle and Technical Realization. *High Resolution Imaging in Microscopy and Ophthalmology* 59–85 (2019) doi:10.1007/978-3-030-16638-0_3.

42. Huang, X. & El-Sayed, M. A. Gold nanoparticles: Optical properties and implementations in cancer diagnosis and photothermal therapy. *J Adv Res* **1**, 13–28 (2010).

43. Burger, P. C. Platelet P-selectin facilitates atherosclerotic lesion development. *Blood* **101**, 2661–2666 (2003).

44. Lorenzon, P. *et al.* Endothelial Cell E- and P-Selectin and Vascular Cell Adhesion Molecule-1 Function as Signaling Receptors. *J Cell Biol* **142**, 1381–1391 (1998).

45. Harari, O. A. *et al.* Endothelial cell E- and P-selectin up-regulation in murine contact sensitivity is prolonged by distinct mechanisms occurring in sequence. *J Immunol* **163**, 6860–6 (1999).

46. Moore, K. L. Structure and Function of P-Selectin Glycoprotein Ligand-1. *Leuk Lymphoma* **29**, 1–15 (1998).

47. Beauharnois, M. E. *et al.* Affinity and kinetics of sialyl lewis-X and Core-2 based oligosaccharides binding to L- and P-selectin. *Biochemistry* **44**, 9507–9519 (2005).

48. Zandberg, W. F., Kumarasamy, J., Pinto, B. M. & Vocadlo, D. J. Metabolic Inhibition of Sialyl-Lewis X Biosynthesis by 5-Thiofucose Remodels the Cell Surface and Impairs Selectin-Mediated Cell Adhesion. *J Biol Chem* **287**, 40021 (2012).

49. Beste, M. T. & Hammer, D. A. Selectin catch-slip kinetics encode shear threshold adhesive behavior of rolling leukocytes. *Proc Natl Acad Sci U S A* **105**, 20716–20721 (2008).

50. Pudelko, M., Bull, J. & Kunz, H. Chemical and Chemoenzymatic Synthesis of Glycopeptide Selectin Ligands Containing Sialyl Lewis X Structures. *ChemBioChem* **11**, 904–930 (2010).

51. Revelle, B. M., Scott, D., Kogan, T. P., Zheng, J. & Beck, P. J. Structure-function analysis of P-selectin-sialyl LewisX binding interactions. Mutagenic alteration of ligand binding specificity. *J Biol Chem* **271**, 4289–4297 (1996).

52. Galustian, C. *et al.* Synergistic interactions of the two classes of ligand, sialyl-Lewisa/x fuco-oligosaccharides and short sulpho-motifs, with the P- and L-selectins: implications for therapeutic inhibitor designs. *Immunology* **105**, 350 (2002).

53. Rodgers, S. D., Camphausen, R. T. & Hammer, D. A. Sialyl Lewis(x)-mediated, PSGL-1-independent rolling adhesion on P-selectin. *Biophys J* **79**, 694 (2000).

54. Rutledge, N. S. & Muller, W. A. Understanding Molecules that Mediate Leukocyte Extravasation. *Curr Pathobiol Rep* **8**, 25–35 (2020).

55. Manning, D. D., Hu, X., Beck, P. & Kiessling, L. L. Synthesis of sulfated neoglycopolymers: Selective P-selectin inhibitors. *J Am Chem Soc* **119**, 3161–3162 (1997).

56. Dernedde, J. *et al.* Dendritic polyglycerol sulfates as multivalent inhibitors of inflammation. *Proc Natl Acad Sci U S A* **107**, 19679–19684 (2010).

57. John, A. E. *et al.* Discovery of a potent nanoparticle P-selectin antagonist with anti-inflammatory effects in allergic airway disease. *The FASEB Journal* **17**, 2296–2298 (2003).

58. Mehanna, E. A., Attizzani, G. F., Kyono, H., Hake, M. & Bezerra, H. G. Assessment of coronary stent by optical coherence tomography, methodology and definitions. *Int J Cardiovasc Imaging* **27**, 259 (2011).

59. Mancuso, J. J. *et al.* Intravascular optical coherence tomography light scattering artifacts: merry-go-rounding, blooming, and ghost struts. *J Biomed Opt* **19**, 126017 (2014).

60. Yao, L., Pan, J., Setiadi, H., Patel, K. D. & McEver, R. P. Interleukin 4 or oncostatin M induces a prolonged increase in P-selectin mRNA and protein in human endothelial cells. *Journal of Experimental Medicine* **184**, 81–92 (1996).

61. Misugi, E., Tojo, S. J., Yasuda, T., Kurata, Y. & Morooka, S. Increased Plasma P-Selectin Induced by Intravenous Administration of Endotoxin in Rats. *Biochem Biophys Res Commun* **246**, 414–417 (1998).

62. Fang, H. *et al.* The severity of LPS induced inflammatory injury is negatively associated with the functional liver mass after LPS injection in rat model. *J Inflamm (Lond)* **15**, (2018).

63. Longmire, M., Choyke, P. L. & Kobayashi, H. Clearance Properties of Nano-sized Particles and Molecules as Imaging Agents: Considerations and Caveats. *Nanomedicine (Lond)* **3**, 703 (2008).

64. De Jong, W. H. *et al.* Particle size-dependent organ distribution of gold nanoparticles after intravenous administration. *Biomaterials* **29**, 1912–1919 (2008).

65. Lesina, A. C., Berini, P., Vaccari, A. & Ramunno, L. On the convergence and accuracy of the FDTD method for nanoplasmonics. *Optics Express, Vol. 23, Issue 8, pp. 10481-10497* **23**, 10481–10497 (2015).

66. Vial, A., Laroche, T., Dridi, M. & Le Cunff, L. A new model of dispersion for metals leading to a more accurate modeling of plasmonic structures using the FDTD method. *Appl Phys A Mater Sci Process* **103**, 849–853 (2011).

3.11. Acknowledgements

The authors would like to thank Dr. XiaoLing Zhao for the many histological samples she prepared and scanned, as well as Sabaa Rashid for the focused-ion beam transmission electron microscopy milling and helium ion microscopy images. The authors would also like to thank Dr. Yun Liu and Dr. Jianqun Wang for transmission and scanning electron microscopy imaging of many samples. Finally, the authors would also like to thank Dr. Linda Kempe and Dr. Emmanuel Yumvihoze for their rapid and careful processing of tissue, and ICP-MS analysis for the biodistribution assay. A.J.S. acknowledges funding support from Canada Research Chairs

(950-230754), NSERC Discovery Grant (RGPIN- 2021-03387), and UOHI Precision Medicine Pilot Fund.

3.12. Competing Interests

N.D.C. and A.J.S. have a patent application on the synthesis and application of metal nanoclusters for biomedical imaging (PCT/CA2023/05005).

3.13. Supplementary Information

General Reagents:

All chemical reagents were purchased from Sigma-Aldrich and used as is unless otherwise reported, apart from L-Fucose which was purchased from AABlocks. All solvents were HPLC grade, except for water (18.2 MΩ cm Millipore water).

Experimental Procedures:

All animal studies were conducted under Animal Use Protocol HIe-3652 approved by the IACUC at the University of Ottawa.

All AuSC syntheses, quantifications, characterizations, and simulation data were performed as described in the main manuscript methods section All chemical syntheses were performed at room temperature unless otherwise specified. All evacuation and N_2 purges were done by a PIAB compressed air vacuum and N_2 tank connected to a Schlenk manifold. All NMR spectra were acquired on a Bruker AVANCE II 400 MHz or a Bruker Avance III HD 600 MHz NMR spectrometers, operating a 400 MHz or 600 MHz for ^{1}H spectra, and 100 MHz or 150 MHz for ^{13}C spectra, respectively. Chemical shifts are given in ppm. In all spectra, $CDCl_3$ was referenced to 7.26 ppm (^{1}H NMR) and 77.16 ppm (^{13}C NMR); MeOH-D_4 to 3.31 ppm (^{1}H NMR) and 49.0 ppm (^{13}C NMR); D_2O to 4.79 ppm (^{1}H NMR). All HSQC spectra are edited HSQCs, where CH and CH_3 signals are phased up and CH_2 signals are phased down. These are

presented on the spectra as red and blue blot signals, respectively. Flash column chromatography (FCC) was performed using silica gel of mesh size 230 – 400 Å. All high-resolution mass spectrometry (HRMS) were performed on a Micromass Q-TOF I with electrospray ionization (ESI), a Kratos Concept Mass Spectrometer for electron impact (EI), or a Bruker Autoflex Speed (MALDI, AISM Mass Spectrometry Laboratory, University of Toronto). All IV-OCT imaging was performed using an Abbott Illumien™ OPTIS™ PCI instrument using Dragonfly™ OPTIS™ imaging catheters and 54 mm high-resolution pullback imaging. All image analyses and quantifications were performed using FIJI. GraphPad Prism 10.0 was used to generate all graphs, graphical figures, and statistical analyses.

*Synthesis of 2-[2-(2-azidoethoxy)ethoxy]ethanol (**PEG_3N_3**):*

To a flame-dried round-bottom flask of dry dimethylformamide (DMF, 150 mL) was added 2-[2-(2-chloroethoxy)ethoxy]ethanol (15 g, 89 mmol) and NaN_3 (12.7 g, 2.2 eq, 195 mmol). An air condenser sealed with a septum was placed on the round-bottom flask, and the reaction was evacuated by vacuum while it was heated to 100°C. The reaction was backflushed with N_2 and stirred for 48 h under N_2 at 100°C. The reaction was then cooled to room temperature (RT), transferred to a separatory funnel, and diluted with water (100 mL) and brine (50 mL). The solution was extracted five times with DCM (75 mL). The combined organic was washed three times with brine (100 mL), dried with Na_2SO_4, filtered, evaporated, and dried on the high vacuum overnight. The resulting product was a yellow oil (**PEG_3N_3**, 14.4 g, 93%). **^{1}H NMR:** (600 MHz, $CDCl_3$) δ 3.70 – 3.65 (m, 2H), 3.65 – 3.58 (m, 6H), 3.55 (t, *J* = 4.8 Hz, 2H), 3.34 (t, *J* = 5.3 Hz, 2H), 2.70 (s, 1H). **^{13}C NMR:** (150 MHz, $CDCl_3$) δ 72.53, 70.60, 70.33, 69.98, 61.64, 50.60. **HRMS (EI):** Calculated for $C_6H_{13}N_3O_3$ [M+H]: 176.1035, found 176.0758.

*Synthesis of 2-[2-(2-aminoethoxy)ethoxy]ethanol (**PEG_3NH_2**):*

PEG_3N_3 (10 g, 57 mmol) was added to a round-bottom flask with methanol (MeOH, 75 mL) and palladium on carbon (Pd/C, 500 mg, 5 wt%) under stirring. The flask was evacuated by vacuum and backflushed with N_2 three times. The flask was evacuated again and three balloons of H_2 were pulled into the reaction by vacuum. The reaction was left stirring overnight under H_2 atmosphere. The reaction was filtered over celite and washed with MeOH (50 mL). The filtrate was evaporated, and dried on the high vacuum. The resulting product was a clear-yellow oil (**PEG_3NH_2**, 4.6 g, 54%). **^{1}H NMR:** (600 MHz, $CDCl_3$) δ 3.57 (t, *J* = 4.6 Hz, 2H), 3.54 – 3.52 (m, 2H), 3.51 – 3.49 (m, 2H), 3.45 (t, *J* = 5.0 Hz, 2H), 3.39 (t, *J* = 5.1 Hz, 2H), 2.72 (t, *J* = 5.5 Hz, 2H). **^{13}C NMR:** (150 MHz, $CDCl_3$) δ 72.94, 72.75, 70.23, 70.08, 61.08, 41.36. **HRMS (EI):** Calculated for $C_6H_{15}NO_3$ [M+H]: 150.1130, found 150.1120.

*Synthesis of L-fucose pentaacetate (**3b**):*

L-fucose (**3a**, 5 g, 30.5 mmol) was added to a round-bottom flask containing 30 mL of acetic anhydride and 40 mL of pyridine. After stirring overnight, the reaction was cooled to 0°C on ice, slowly quenched with water (100 mL), and transferred to a separatory funnel. The solution was acidified with 1 N HCl (50 mL) and extracted three times with EtOAc (50 mL). The combined organic was washed again with 1 N HCl, sat. $NaHCO_3$, and brine (50 mL, consecutively). The combined organic was dried with Na_2SO_4, filtered, evaporated, and left on the high vacuum overnight. The resulting product was a brown, viscous oil containing L-fucose pentaacetate in a 2:1 ratio of α:β anomers (**3b**, 9.8 g, 97%). A small amount of L-fucitol pentaacetate is visible in the NMR characterization. The product was used for the next reaction without further purification. NMRs were integrated on the same spectra but independently for the α and β anomers. **^{1}H NMR (α):** (600 MHz, $CDCl_3$) δ 6.30 (d, *J* = 3.1 Hz, 1H), 5.34 – 5.26 (m,

3H), 4.24 (q, *J* = 6.6 Hz, 1H), 2.14 (s, 3H), 2.11 (s, 3H), 1.98 (s, 3H), 1.97 (s, 3H), 1.12 (d, *J* = 6.5 Hz, 3H). **^{13}C NMR (α):** (150 MHz, $CDCl_3$) δ 170.59, 170.24, 170.01, 169.21, 90.01, 70.64, 67.88, 67.34, 66.54, 20.97, 20.73, 20.67, 20.63, 15.98. **^{1}H NMR (β):** (600 MHz, $CDCl_3$) δ 5.65 (d, *J* = 8.3 Hz, 1H), 5.25 – 4.99 (m, 3H), 3.93 (q, *J* = 6.5 Hz, 1H), 2.15 (s, 3H), 2.08 (s, 3H), 2.00 (s, 3H), 1.96 (s, 3H), 1.19 (d, *J* = 6.6 Hz, 3H). **^{13}C NMR (β):** (150 MHz, $CDCl_3$) δ 170.59, 170.24, 170.01, 169.21, 90.01, 70.64, 67.88, 67.34, 66.54, 20.97, 20.73, 20.67, 20.63, 15.98. **HRMS (ESI):** Calculated for $C_{14}H_{20}O_9$ [M+Na]: 355.0977, found 355.1005.

*Synthesis of 1-azido-3,6-dioxaoct-8-yl 2,3,4-tri-O-acetyl-β-L-fucopyranoside (**3c**):*

To a solution of DCM (50 mL) was added **3b** (5 g, 14 mmol) and **PEG_3N_3** (5.4 g, 30.8 mmol, 2.2 eq) under stirring. The solution was evacuated by vacuum, backflushed with N_2, and cooled to 0°C on ice. BF_3•Et_2O (3.5 mL, 28 mmol, 2 eq) was added slowly under N_2. Ice was removed after addition, and the reaction was stirred overnight at RT under N_2 atmosphere. The reaction was quenched slowly by addition of sat. $NaHCO_3$ (75 mL) and transferred to a separatory funnel. The solution was extracted three times with DCM (50 mL). The combined organic was washed with sat. $NaHCO_3$ and brine (75 mL, consecutively), dried with Na_2SO_4, filtered, and evaporated. The resulting crude product was separated by FCC in EtOAc/hexanes (3:2). The eluate was evaporated and dried overnight on the high vacuum. The resulting product was a clear oil (**3c**, 2.9 g, 44%). **^{1}H NMR:** (600 MHz, $CDCl_3$) δ 5.20 (d, *J* = 3.5 Hz, 1H), 5.15 (qd, *J* = 8.0, 2.6 Hz, 1H), 4.99 (dd, *J* = 10.5, 3.5 Hz, 1H), 4.50 (d, *J* = 8.0 Hz, 1H), 3.97 – 3.91 (m, 1H), 3.78 (t, *J* = 6.4 Hz, 1H), 3.70 (ddd, *J* = 11.0, 7.0, 4.0 Hz, 1H), 3.68 – 3.60 (m, 8H), 3.37 (t, *J* = 5.1 Hz, 2H), 2.14 (s, 3H), 2.02 (s, 3H), 1.95 (s, 3H), 1.19 (d, *J* = 6.4 Hz, 3H). **^{13}C NMR:** (150 MHz, $CDCl_3$) δ 170.76, 170.29, 169.63, 101.24, 71.41, 70.81, 70.77, 70.47, 70.36, 70.11,

69.20, 69.02, 69.01, 50.75, 20.87, 20.77, 20.71, 16.13. **HRMS (ESI):** Calculated for $C_{18}H_{29}N_3O_{10}$ [M+Na]: 470.1751, found 470.1751.

*Synthesis of 1-azido-3,6-dioxaoct-8-yl β-L-fucopyranoside (**Deacetylated 3c**):*

A flame-dried round-bottom flask with dry methanol (50 mL) was chilled on ice to 0ºC. Sodium metal (100 mg) was added to the flask and stirred until the metal was fully dissolved. To the *in situ* formed sodium methoxide solution was added **3c** (2 g, 4.5 mmol). The solution was stirred at 0ºC for 45 min, then quenched by the addition of Amberlyst^{TM} 15. This was stirred until the solution became slightly acidic (~ pH 5), at which point the reaction was filtered over celite and washed with MeOH (50 mL). The filtrate was evaporated and separated by a silica plug in DCM:MeOH (9:1). The eluate was evaporated and dried on the high vacuum overnight. The resulting product was a clear oil (**deacetylated 3c**, 1.34 g, 93%). **^{1}H NMR:** (600 MHz, $CDCl_3$) δ 4.25 (d, *J* = 7.7 Hz, 1H), 4.07 – 3.99 (m, 1H), 3.74 – 3.55 (m, 13H), 3.40 (t, *J* = 5.1 Hz, 2H), 1.32 (d, *J* = 6.5 Hz, 3H). **^{13}C NMR:** (150 MHz, $CDCl_3$) δ 103.43, 74.05, 71.59, 71.42, 70.79, 70.68, 70.52, 70.47, 70.09, 68.59, 50.78, 16.47. **HRMS (ESI):** Calculated for $C_{12}H_{23}N_3O_7$ [M+Na]: 344.1444, found 344.1434.

*Synthesis of 1-amino-3,6-dioxaoct-8-yl β-L-fucopyranoside (**3**):*

Deacetylated 3c (1.5 g, 4.7 mmol) was dissolved in a round-bottom flask with MeOH (50 mL) under stirring. Pd/C (150 mg, 10 wt%) was added and the flask was evacuated by vacuum and backflushed with N_2 three times. Three balloons of H_2 were pulled into the reaction by vacuum, and the reaction was stirred for 1.5 h under H_2 atmosphere. The reaction was filtered over celite and washed with MeOH (50 mL). The filtrate was evaporated and dried overnight on the high vacuum. The resulting product was a clear oil (**3**, 1.4 g, quantitative). **^{1}H NMR:** (600 MHz, MeOD) δ 4.23 (d, *J* = 6.5 Hz, 1H), 4.02 – 3.92 (m, 1H), 3.75 – 3.58 (m, 9H), 3.53 (t, *J* =

5.3 Hz, 1H), 3.51 – 3.42 (m, 2H), 2.79 (t, *J* = 5.3 Hz, 2H), 1.26 (d, *J* = 6.5 Hz, 3H). **^{13}C NMR:** (150 MHz, MeOD) δ 104.93, 75.01, 73.27, 72.98, 72.21, 71.93, 71.47, 71.44, 71.12, 69.49, 42.01, 16.76. **HRMS (ESI):** Calculated for $C_{12}H_{25}NO_7$ [M+Na]: 318.1529, found 318.1511.

*Synthesis of 1-azido-3,6-dioxaoct-8-yl 2,3,4-tri-O-acetyl-β-D-galactopyranoside (**4b**):*

To a solution of DCM (50 mL) was added β-D-galactose pentaacetate (**4a**, 4 g, 10.2 mmol) and **PEG_3N_3** (4 g, 22.4 mmol, 2.2 eq) under stirring. The solution was evacuated by vacuum, backflushed with N_2, and cooled to 0ºC on ice. BF_3•Et_2O (2.5 mL, 20.4 mmol, 2 eq) was added slowly under N_2. Ice was removed after addition, and the reaction was stirred overnight at RT under N_2 atmosphere. The reaction was quenched slowly by addition of sat. $NaHCO_3$ (75 mL) and transferred to a separatory funnel. The solution was extracted three times with DCM (50 mL). The combined organic was washed with sat. $NaHCO_3$ and brine (75 mL, consecutively), dried with Na_2SO_4, filtered, and evaporated. The resulting crude product was separated by FCC in EtOAc/hexanes (3:2). The eluate was evaporated and dried overnight on the high vacuum. The resulting product was a clear oil (**4c**, 4.2 g, 81%). **^{1}H NMR:** (600 MHz, $CDCl_3$) δ 5.18 (t, *J* = 9.5 Hz, 1H), 5.06 (t, *J* = 9.7 Hz, 1H), 4.97 (dd, *J* = 9.7, 7.9 Hz, 1H), 4.59 (d, *J* = 8.0 Hz, 1H), 4.28 – 4.17 (m, 1H), 4.15 – 4.05 (m, 2H), 3.92 (ddd, *J* = 11.2, 4.9, 3.7 Hz, 1H), 3.76 – 3.58 (m, 10H), 3.38 (t, *J* = 5.0 Hz, 2H), 2.06 (s, 3H), 2.02 (s, 3H), 2.00 (s, 3H), 1.98 (s, 3H). **^{13}C NMR:** (150 MHz, $CDCl_3$) δ 170.76, 170.36, 169.51, 169.45, 100.92, 72.91, 71.86, 71.37, 70.80, 70.78, 70.50, 70.12, 69.15, 68.51, 62.05, 50.76, 20.82, 20.75, 20.70, 20.68. **HRMS (ESI):** Calculated for $C_{20}H_{31}N_3O_{12}$ [M+Na]: 528.1823, found 528.1805.

*Synthesis of 1-azido-3,6-dioxaoct-8-yl β-D-galactopyranoside (**deacetylated 4b**):*

A flame-dried round-bottom flask with dry methanol (75 mL) was chilled on ice to 0ºC. Sodium metal (200 mg) was added to the flask and stirred until the metal was fully dissolved. To the *in situ* formed sodium methoxide solution was added **4b** (4 g, 7.9 mmol). The solution was stirred at 0ºC for 45 min, then quenched by the addition of Amberlyst^{TM} 15. This was stirred until the solution became slightly acidic (~ pH 5), at which point the reaction was filtered over celite and washed with MeOH (50 mL). The filtrate was evaporated and separated by a silica plug in DCM:MeOH (9:1). The eluate was evaporated and dried on the high vacuum overnight. The resulting product was a clear oil (**deacetylated 4b**, 2.38 g, 89%). **^{1}H NMR:** (400 MHz, MeOD) δ 4.25 (d, *J* = 7.5 Hz, 1H), 4.00 (tdd, *J* = 8.5, 5.9, 2.7 Hz, 1H), 3.81 (d, *J* = 3.3 Hz, 1H), 3.78 – 3.70 (m, 5H), 3.70 – 3.62 (m, 5H), 3.57 – 3.42 (m, 4H), 3.37 (t, *J* = 5.0 Hz, 2H). **^{13}C NMR:** (100 MHz, MeOD) δ 105.08, 76.70, 74.87, 72.51, 71.56, 71.43, 71.10, 70.28, 69.59, 62.51, 51.75. **HRMS (ESI):** Calculated for $C_{12}H_{23}N_3O_8$ [M+Na]: 360.1384, found 360.1383.

*Synthesis of 1-amino-3,6-dioxaoct-8-yl β-D-galactopyranoside (**4**):*

Deacetylated 4b (2 g, 5.9 mmol) was dissolved in a round-bottom flask with MeOH (50 mL) under stirring. Pd/C (200 mg, 10 wt%) was added and the flask was evacuated by vacuum and backflushed with N_2 three times. Three balloons of H_2 were pulled into the reaction by vacuum, and the reaction was stirred for 1.5 h under H_2 atmosphere. The reaction was filtered over celite and washed with MeOH (50 mL). The filtrate was evaporated and dried overnight on the high vacuum. The resulting product was a clear oil (**4**, 1.85 g, quantitative). **^{1}H NMR:** (600 MHz, MeOD) δ 4.29 (d, *J* = 7.8 Hz, 1H), 4.01 (tdd, *J* = 7.0, 3.9, 2.1 Hz, 1H), 3.89 – 3.83 (m, 1H), 3.80 – 3.57 (m, 9H), 3.52 (t, *J* = 5.3 Hz, 2H), 3.28 – 3.22 (m, 2H), 3.23 – 3.14 (m, 1H), 2.82 – 2.75 (m, 2H). **^{13}C NMR:** (150 MHz, MeOD) δ 104.46, 77.97, 77.92, 75.02, 73.40, 71.59,

71.48, 71.44, 71.12, 69.65, 62.74, 42.03. **HRMS (ESI):** Calculated for $C_{12}H_{25}NO_8$ [M+Na]: 334.1462, found 334.1478.

*Synthesis of 2-[2-(2-aminoethoxy)ethoxy]ethyl hydrogen sulfate (**5**):*

A solution of **PEG_3NH_2** (5 g, 33.5 mmol) in DCM (50 mL) and DMF (10 mL) was chilled on ice to 0°C under stirring. Chlorosulfonic acid (2.5 mL ,36.9 mmol, 1.1 eq) was added dropwise very slowly. Ice was removed after addition and the reaction was stirred overnight at RT. The solvent was evaporated and dried on the high vacuum. The crude product was recrystallized in DCM (100 mL). The crystals were filtered off with filter paper, washed three times with DCM (50 mL, consecutively), and dried on the high vacuum overnight. The resulting product was a greasy, white powder (**5**, 4.4 g, 49%). **^{1}H NMR:** (400 MHz, D_2O) δ 4.18 (t, *J* = 4.3 Hz, 2H), 3.80 (t, *J* = 4.6 Hz, 2H), 3.76 (t, *J* = 5.0 Hz, 2H), 3.74 – 3.69 (m, 4H), 3.20 (t, *J* = 5.1 Hz, 2H). **^{13}C NMR:** (100 MHz, D_2O) δ 69.69, 69.46, 68.77, 67.63, 66.36, 39.19. **HRMS (ESI):** Calculated for $C_6H_{14}NO_6S$ [M+Na]: 228.0504, found 228.0542.

*Synthesis of NPC-Myrj52 (**2**):*

To a flame-dried round-bottom flask of dry DCM (100 mL) under stirring was added Myrj52 (**1,** 10 g, 4.9 mmol) and 4-nitrophenyl chloroformate (3 g, 14.9 mmol, 3 eq). The flask was evacuated by vacuum, backflushed with N_2, and allowed to stir for 30 min. Pyridine was added dropwise under N_2 (1.6 mL, 19.6 mmol, 4 eq) and the reaction was stirred for an additional 2 h. The reaction was acidified with 1 N HCl (50 mL) and transferred to a separatory funnel. Brine (25 mL) was added, and the reaction mixture was extracted three times with DCM (50 mL). The combined organic phase was washed with 1 N HCl and brine (75 mL, consecutively). The combined organic phase was dried with Na_2SO_4, was filtered, and then evaporated. The resulting crude product, a pale-yellow wax, was separated by FCC in

EtOAc/MeOH (19:1) to elute the starting material, then switched to DCM:MeOH (4:1) to elute the product. The product eluate was evaporated and dried on the high vacuum overnight, giving a pale-yellow wax (**2**, 9.3 g, 87%). **^{1}H NMR:** (400 MHz, $CDCl_3$) δ 7.17 – 6.62 (m, 1H), 4.26 (t, *J* = 7.8 Hz, 1H), 4.18 (dd, *J* = 9.3, 4.5 Hz, 4H), 3.81 – 3.73 (m, 1H), 3.60 (s, 166H), 3.33 (t, *J* = 4.7 Hz, 4H), 2.28 (t, *J* = 7.6 Hz, 2H), 1.56 (p, *J* = 7.2 Hz, 2H), 1.31 (t, *J* = 5.9 Hz, 3H), 1.20 (s, 28H), 0.83 (t, *J* = 6.6 Hz, 3H). **^{13}C NMR:** (150 MHz, $CDCl_3$) δ 173.86, 157.58, 156.47, 104.39, 104.03, 73.59, 72.75, 72.55, 71.60, 70.98, 70.87, 70.64, 70.58, 70.53, 70.49, 70.47, 70.45, 70.27, 69.94, 69.67, 69.22, 68.39, 64.56, 63.55, 63.37, 41.40, 40.96, 34.23, 31.93, 29.70, 29.67, 29.62, 29.49, 29.37, 29.30, 29.15, 24.93, 22.71, 16.50, 16.42, 14.16. **MALDI (HRMS):** Calculated for $C_{105}H_{199}NO_{46}$ [M+Na]: 2233.3161, found 2233.3185.

*Synthesis of Fucosyl-PEG$_3$-Myrj52 (**6**):*

A solution of **2** (3 g, 1.36 mmol) in dry DCM (25 mL) under stirring was evacuated by vacuum and backflushed with N_2 at 50°C. A solution of **3** (0.80g, 2.72 mmol, 2 eq) in dry DMF (1 mL) was added dropwise under N_2 and allowed to stir for 30 min, at which point triethylamine (Et_3N, 420 µl, 3 mmol, 2.2 eq) was added under N_2 and the reaction was stirred for 48 h. The heat was removed, and the solvent was evaporated and left on a high vacuum for 1 h. The resulting crude product, a bright yellow wax, was separated by FCC in DCM/MeOH (19:1) to elute 4-nitrophenol impurity, then switched to DCM:MeOH (4:1) to elute the product. The product eluate was evaporated and dried on the high vacuum overnight, giving a pale-yellow wax (**6**, 2.5 g, 78%). **^{1}H NMR:** (400 MHz, $CDCl_3$) δ 7.17 – 6.62 (m, 1H), 4.26 (t, *J* = 7.8 Hz, 1H), 4.18 (dd, *J* = 9.3, 4.5 Hz, 4H), 3.81 – 3.73 (m, 1H), 3.60 (s, 166H), 3.33 (t, *J* = 4.7 Hz, 4H), 2.28 (t, *J* = 7.6 Hz, 2H), 1.56 (p, *J* = 7.2 Hz, 2H), 1.31 (t, *J* = 5.9 Hz, 3H), 1.20 (s, 28H), 0.83 (t, *J* = 6.6 Hz, 3H). **^{13}C NMR:** (150 MHz, $CDCl_3$) δ 173.86, 157.58, 156.47, 104.39, 104.03, 73.59,

72.75, 72.55, 71.60, 70.98, 70.87, 70.64, 70.58, 70.53, 70.49, 70.47, 70.45, 70.27, 69.94, 69.67, 69.22, 68.39, 64.56, 63.55, 63.37, 41.40, 40.96, 34.23, 31.93, 29.70, 29.67, 29.62, 29.49, 29.37, 29.30, 29.15, 24.93, 22.71, 16.50, 16.42, 14.16. **HRMS (MALDI):** Calculated for $C_{111}H_{219}NO_{50}$ [M+Na]: 2389.4523, found 2389.4410.

*Synthesis of Galactosyl-PEG$_3$-Myrj52 (**7**):*

A solution of **2** (3 g, 1.36 mmol) in dry DCM (25 mL) under stirring was evacuated by vacuum and backflushed with N_2 at 50ºC. A solution of **4** (0.85g, 2.72 mmol, 2 eq) in dry DMF (1 mL) was added dropwise under N_2 and allowed to stir for 30 min, at which point triethylamine (Et_3N, 420 µl, 3 mmol, 2.2 eq) was added under N_2 and the reaction was stirred for 48 h. The heat was removed, and the solvent was evaporated and left on a high vacuum for 1 h. The resulting crude product, a bright yellow wax, was separated by FCC in DCM/MeOH (19:1) to elute 4-nitrophenol impurity, then switched to DCM:MeOH (4:1) to elute the product. The product eluate was evaporated and dried on the high vacuum overnight, giving a pale-yellow wax (**7**, 2.6 g, 81%). **^{1}H NMR:** (600 MHz, $CDCl_3$) δ 7.17 – 6.71 (m, 1H), 4.32 (d, *J* = 7.9, 1H), 4.27 – 4.16 (m, 4H), 4.18 – 3.95 (m, 2H), 3.97 – 3.85 (m, 2H), 3.86 – 3.41 (m, 166H), 3.39 – 3.28 (m, 2H), 2.29 (t, *J* = 7.6 Hz, 2H), 1.58 (p, *J* = 7.6 Hz, 2H), 1.22 (d, *J* = 2.5 Hz, 30H), 0.84 (t, *J* = 7.1 Hz, 3H). **^{13}C NMR:** (150 MHz, $CDCl_3$) δ 173.88, 157.62, 156.52, 104.54, 104.28, 75.22, 74.90, 73.34, 72.40, 71.39, 71.20, 70.75, 70.71, 70.70, 70.69, 70.66, 70.61, 70.57, 70.55, 70.52, 70.50, 70.48, 70.45, 70.43, 70.36, 70.30, 70.25, 70.03, 69.94, 69.87, 69.74, 69.53, 69.43, 69.25, 68.68, 68.26, 64.60, 63.55, 63.39, 62.69, 62.36, 41.42, 40.97, 34.25, 31.96, 29.73, 29.71, 29.69, 29.65, 29.51, 29.39, 29.32, 29.18, 24.95, 22.73, 14.18. **MALDI (HRMS):** Calculated for $C_{111}H_{219}NO_{51}$ [M+Na]: 2405.4472, found 2405.4506.

*Synthesis of Sulfonyl-PEG$_3$-Myrj52 (**8**):*

A solution of **2** (6 g, 2.72 mmol) and K_2CO_3 (0.83g ,5.98 mmol, 2.2 eq) in dry DCM (50 mL) under stirring was evacuated by vacuum and backflushed with N_2 at 50ºC. A solution of **5** (2.17 g, 8.16 mmol, 3 eq) and K_2CO_3 (1.24 g, 9 mmol, 1.1 eq) in 10:1 DMF:water (11 mL) was added dropwise under N_2 and stirred for 48 h. The heat was removed, and the solvent was evaporated and left on a high vacuum for 1 h. The resulting crude product, a bright yellow wax, was resuspended in DCM with sonication, and was filtered through a celite plug to remove potassium salts before being separated by FCC in DCM/MeOH (19:1) to elute 4-nitrophenol impurity, then switched to DCM:MeOH (4:1) to elute the product. The product eluate was evaporated and dried on the high vacuum overnight, giving a pale-yellow wax (**8**, 3.2 g, 51%). **^{1}H NMR:** 600 MHz, $CDCl_3$) δ 5.95 – 5.45 (m, 1H), 4.19 – 4.12 (m, 5H), 3.72 – 3.49 (m, 166H), 3.32 (dq, *J* = 8.6, 5.5 Hz, 2H), 2.27 (t, *J* = 7.6 Hz, 2H), 1.56 (p, *J* = 7.5 Hz, 2H), 1.20 (d, *J* = 2.3 Hz, 28H), 0.83 (t, *J* = 7.0 Hz, 3H). **^{13}C NMR:** (150 MHz, $CDCl_3$) δ 173.82, 156.59, 156.48, 72.53, 72.38, 70.64, 70.60, 70.56, 70.54, 70.52, 70.49, 70.47, 70.46, 70.44, 70.42, 70.39, 70.37, 70.34, 70.32, 70.30, 70.28, 70.25, 70.22, 70.16, 70.12, 70.10, 70.07, 70.00, 69.93, 69.89, 69.86, 69.84, 69.68, 69.62, 69.20, 66.47, 64.47, 63.87, 63.70, 63.34, 61.64, 61.51, 40.89, 40.79, 34.20, 31.91, 29.68, 29.66, 29.64, 29.59, 29.46, 29.34, 29.27, 29.13, 24.90, 22.68, 14.14. **MALDI (HRMS):** Calculated for $C_{105}H_{208}NO_{49}S$ [M+H]: 2301.3692, found 2301.3521.

Silication of AuSC:

AuSC were synthesized as described in the methods of the main manuscript by microwave synthesis and dispersion in *n*-butanol, except with 40 g/L of polyvinylpyrrolidone (average molecular weight 360 kDa) and shaken overnight. After purification by centrifugation (1000 xg, 10 min, redispersed in fresh *n*-butanol; repeated three times), AuSC were redispersed

in 99% ethanol with either 4.2% v/v (large SiO_2 shell) or 1.3% v/v (small SiO_2 shell) ammonium hydroxide. Tetraethyl orthosilicate (10% v/v) was added to both solutions and were shaken overnight. Both solutions were purified by centrifugation (1000 xg, 10 min, redispersed in fresh ethanol; repeated three times). Both large and small shell encapsulated AuSC were evaluated by TEM and spectroscopy.

Dynamic light scattering and zeta potential measurements:

AuSC@$(Myrj52)_2$ and AuSC@$(13FS)_2$ were diluted with Milli-Q water to 25 µg/mL. After brief sonication, each solution was loaded into a Malvern Zetasizer cuvette (DTS1070). Hydrodynamic size and zeta potential were acquired for each solution on a Malvern Zetasizer Nano-ZS in triplicate.

Optimizing P-selectin expression in rats:

Sprague-Dawley rats (12 weeks old, Charles River) were injected *iv* with LPS (*Escherichia coli* O111:B4, 2 mg/kg or 4 mg/kg in saline) or saline. This was allowed to circulate for 2 or 4 h, at which point rats were anesthetized with isoflurane and euthanized by exsanguination. Rats were dissected to locate the abdominal aorta, which was dissected and fixed in 10% formalin in PBS overnight. This was replaced by 70% ethanol the next day. Tissue was mounted in paraffin, sliced, and stained with anti-CD62p to evaluate P-selectin expression within the AA. Multiple sections for each LPS concentration and the respective timepoints were compared to determine the dose and circulation time that gave maximal intraarterial P-selectin expression.

AuSC@(13FS)$_2$ serum stability:

A concentrated solution of AuSC@(13FS)$_2$ in water was diluted with mouse serum to an Au concentration of 0.5 mg/mL and incubated overnight under cell culture conditions (37ºC, 5% CO_2, humidified). In addition to extinction spectra of the particles in water prior to incubation, spectra of clusters following incubation in mouse serum was acquired, and which was corrected by having a spectra of mouse serum containing no particles subtracted from it, allowing the removal of the high background of the serum. Scanning electron microscopy was performed on clusters in water before and after incubation in mouse serum using a ZEISS Sigma 500. Following incubation, clusters were centrifuged out of mouse serum and resuspended in Milli-Q water prior to being drop casted on copper grids to allow for unobstructed imaging of the clusters.

Biodistribution assay and histological evaluation:

Sprague-Dawley rats (12 weeks old, Charles River) were injected with a dose of AuSC@(13FS)$_2$ that was ~5× more concentrated that that used for imaging experiments (2250 µg/mL Au, 0.3 mL) *intravenously* through the tail vein. A single rat injected with saline (0 hr) was used as a baseline for Au concentration within the tissue. At 1, 4, or 24 h timepoints, rats were anesthetized with isoflurane and euthanized by exsanguination. This blood was placed in a heparinized tube for analysis. Tissues (brain, heart, lung, liver, kidney, spleen, muscle [biceps femoris], stomach, gastrointestinal tract), as well as any available urine and feces, were immediately collected from the rat and stored in falcon tubes at -80ºC for eventual ICP-MS evaluation. Tissue samples from one rat at random were bisected immediately after removal and fixed in 10% formalin in PBS. Fixed tissue samples were replaced by 70% ethanol after 3 days. Tissue was mounted in paraffin, sliced, and stained with hematoxylin and eosin. All rat tissue

and fluid samples were weighed wet, dried overnight at 100ºC, thermally decomposed (R.T. to 550ºC over 12 h, followed by a 4 h hold at 550ºC), incubated overnight in aqua regia and 3% H_2O_2, digested in aqua regia for 4 h at 80ºC, diluted with Milli-Q water, sterile filtered, and evaluated for Au content by ICP-MS.

Statistical analyses:

Statistical analyses were performed using GraphPad Prism 10.0 (GraphPad, Inc.). Two-group comparisons were performed by two-tail Student's t-test. Comparisons across more than two groups was performed by one-way ANOVA followed by Tukey's test for honestly significant differences. Normality was assumed where appropriate for all data sets. Prior to ANOVA, Levene's test was used to confirm equal variance, and visual quantile-quantile plot analysis was used to confirm homoscedasticity.

Supplementary Data:

Supplementary Table 1. AuSC synthesis conditions and resulting physicochemical properties. Modulated conditions of the AuSC synthesis described in the main manuscript and the resulting physicochemical properties.

Entry	Gold Precursor Concentration (mM)	Capping Agent	Microwave Power (W)	Reaction Hold Time (s)	Reaction Hold Temperature (°C)	Post-Microwave Diluent	Transfer Method	Transfer Solvent	Secondary Stabilization	Purification	Suspension Solvent	Center Peak SPR (nm)	Diameter (nm)	Degree of Clustering	Cluster Circularity	Distribution
1	20	Oleylamine (3 M)	300	1	70	Ethanol	Centrifugation (11,300 xg, 1 hr)	Ethanol	N/A	N/A	Ethanol	Low NIR Activity	10	Individual nanoparticles (~10 nm)	N/A	Homogeneous
2	20	Oleylamine (3 M)	300	1	100	Ethanol	Centrifugation (11,300 xg, 1 hr)	Ethanol	N/A	N/A	Ethanol	Low NIR activity	500	Very diffuse	Circular	Heterogeneous
3	20	Oleylamine (3 M)	300	1	120	Ethanol	Centrifugation (11,300 xg, 1 hr)	Ethanol	N/A	N/A	Ethanol	1150 nm (Broad)	600	Very diffuse	Circular	Heterogeneous
4	20	Oleylamine (3 M)	300	1	150	Ethanol	Centrifugation (11,300 xg, 1 hr)	Ethanol	N/A	N/A	Ethanol	1250 nm (Very broad)	600	Diffuse	Uneven circular	Heterogeneous
5	20	Oleylamine (3 M)	300	1	170	Ethanol	Centrifugation (11,300 xg, 1 hr)	Ethanol	N/A	N/A	Ethanol	1250 nm (Very broad)	600	Somewhat diffuse	Uneven circular	Heterogeneous
6	20	Oleylamine (3 M)	300	1	190	Ethanol	Centrifugation (11,300 xg, 1 hr)	Ethanol	N/A	N/A	Ethanol	1250 nm (Very broad)	800	Somewhat diffuse	Abstract	Heterogeneous
7	20	Oleylamine (3 M)	300	300	150	Ethanol	Centrifugation (125 xg, 1 hr)	Ethanol	N/A	N/A	Ethanol	1150 (Broad)	600	Somewhat diffuse	Uneven circular	Heterogeneous
8	20	Oleylamine (3 M)	300	300	225	Ethanol	Centrifugation (125 xg, 1 hr)	Ethanol	N/A	N/A	Ethanol	1250 (Broad)	800	Somewhat diffuse	Abstract	Heterogeneous
9	20	Oleylamine (3 M)	300	900	150	Ethanol	Centrifugation (125 xg, 1 hr)	Ethanol	N/A	N/A	Ethanol	1150 (Broad)	600	Tight	Uneven circular	Heterogeneous

Entry	Gold Precursor Concentration (mM)	Capping Agent	Microwave Power (W)	Reaction Hold Time (s)	Reaction Hold Temperature (°C)	Post-Microwave Diluent	Transfer Method	Transfer Solvent	Secondary Stabilization	Purification	Suspension Solvent	Center Peak SPR (nm)	Diameter (nm)	Degree of Clustering	Cluster Circularity	Distribution
10	20	Oleylamine (3 M)	300	900	225	Ethanol	Centrifugation (125 xg, 1 hr)	Ethanol	N/A	N/A	Ethanol	1250 (Broad)	800	Tight	Abstract	Heterogeneous
11	20	Oleylamine (3 M)	300	1800	150	Ethanol	Centrifugation (125 xg, 1 hr)	Ethanol	N/A	N/A	Ethanol	1150 (Broad)	700	Tight	Intercluster packing	Heterogeneous
12	20	Oleylamine (3 M)	300	1800	225	Ethanol	Centrifugation (125 xg, 1 hr)	Ethanol	N/A	N/A	Ethanol	1250 (Broad)	800	Tight	Intercluster packing	Heterogeneous
13	20 + Entry 12 AuSCs	Oleylamine (3 M)	300	900	200	Ethanol	Centrifugation (125 xg, 1 hr)	Ethanol	N/A	N/A	Ethanol	N/A	1000	Tight	Uneven circular	Homogeneous
14	20	Octadecenethiol (3 M)	300	900	225	Ethanol	Centrifugation (125 xg, 1 hr)	Ethanol	N/A	N/A	Ethanol	N/A	600	Very tight	Uneven circular	Homogeneous
15	20	Oleylamine (3 M)	300	1	100	Ethanol	Sedimentation by gravity	Ethanol	N/A	N/A	Ethanol	N/A	500	Somewhat diffuse	Uneven circular	Homogeneous
16	20	Oleylamine (3 M)	300	900	100	Ethanol	Sedimentation by gravity	Ethanol	N/A	N/A	Ethanol	N/A	> 1500	Tight	Chains of circular clusters	Heterogeneous
17	20	Oleylamine:Octadecenethiol (3 M, 1:1)	300	900	150	Ethanol	Sedimentation by gravity	Ethanol	N/A	N/A	Ethanol	1450 (Sharp)	350	Very tight	Urchin-like, circular	Heterogeneous
18	20	Oleylamine (3 M)	100	60	115	Ethanol	Centrifugation (1000 xg, 10 min)	Ethanol	N/A	N/A	Ethanol	N/A	400	Diffuse	Uneven circular, chains of clusters	Heterogeneous
19	20	Oleylamine (3 M)	100	150	115	Ethanol	Centrifugation (1000 xg, 10 min)	Ethanol	N/A	N/A	Ethanol	N/A	300	Diffuse	Uneven circular, chains of clusters	Heterogeneous
20	20	Oleylamine (3 M)	100	300	115	Ethanol	Centrifugation (1000 xg, 10 min)	Ethanol	N/A	N/A	Ethanol	N/A	350	Somewhat diffuse	Uneven circular,	Heterogeneous

Entry	Gold Precursor Concentration (mM)	Capping Agent	Microwave Power (W)	Reaction Hold Time (s)	Reaction Hold Temperature (°C)	Post-Microwave Diluent	Transfer Method	Transfer Solvent	Secondary Stabilization	Purification	Suspension Solvent	Center Peak SPR (nm)	Diameter (nm)	Degree of Clustering	Cluster Circularity	Distribution
															chains of clusters	
21	20	Oleylamine (3 M)	100	150	115	Petroleum Ether	Centrifugation (1000 xg, 10 min)	Petroleum ether	N/A	N/A	Petroleum ether	N/A	500	Very diffuse	Circular, disassembling clusters	Homogeneous
22	20	Oleylamine (1.5 M)	75	300	115	12.5 g/L Polyethyleneoxide (40) stearate in butanol	Centrifugation (1000 xg, 10 min)	Ethanol	N/A	Centrifugation (1000 xg, 10 min)	Ethanol	1150 (Broad)	400	Very tight	Circular	Homogeneous
23	20	Oleylamine (1.5 M)	75	300	115	12.5 g/L 35 kDa polyvinylpyrrolidone in butanol	Centrifugation (1000 xg, 10 min)	Ethanol	N/A	Centrifugation (1000 xg, 10 min)	Ethanol	1150 (Broad)	450	Very tight	Circular	Homogeneous
24	20	Oleylamine (1.5 M)	75	300	115	20:80 Butanol:Hexanes	Centrifugation (1000 xg, 10 min)	20:80 Butanol:Hexanes	N/A	N/A	20:80 Butanol:Hexanes	520 (Sharp)	600	Very diffuse	Circular, disassembling clusters	Heterogeneous
25	20	Oleylamine (1.5 M)	75	300	115	50:50 Butanol:Hexanes	Centrifugation (1000 xg, 10 min)	50:50 Butanol:Hexanes	N/A	N/A	50:50 Butanol:Hexanes	N/A	400	Diffuse	Uneven circular, chains of disassembling clusters	Heterogeneous
26	20	Oleylamine (1.5 M)	75	300	115	Butanol	Centrifugation (1000 xg, 10 min)	Butanol	N/A	N/A	Butanol	N/A	>1500	Very tight	Abstract chains of clusters	Heterogeneous

Entry	Gold Precursor Concentration (mM)	Capping Agent	Microwave Power (W)	Reaction Hold Time (s)	Reaction Hold Temperature (°C)	Post-Microwave Diluent	Transfer Method	Transfer Solvent	Secondary Stabilization	Purification	Suspension Solvent	Center Peak SPR (nm)	Diameter (nm)	Degree of Clustering	Cluster Circularity	Distribution
27	20	Oleylamine (0.75 M)	75	300	115	12.5 g/L 35 kDa polyvinylpyrrolidone in butanol	Centrifugation (1000 xg, 10 min)	Ethanol	N/A	Centrifugation (1000 xg, 10 min)	Ethanol	N/A	250	Very tight	Abstract chains of clusters	Heterogeneous
28	20	Oleylamine (3 M)	75	300	115	12.5 g/L 35 kDa polyvinylpyrrolidone in butanol	Centrifugation (1000 xg, 10 min)	Ethanol	N/A	Centrifugation (1000 xg, 10 min)	Ethanol	N/A	300	Very tight	Uneven circular	Homogeneous
29	20	Oleylamine (1.5 M)	75	150	115	12.5 g/L 35 kDa polyvinylpyrrolidone in butanol	Centrifugation (1000 xg, 10 min)	Butanol	N/A	Centrifugation (1000 xg, 10 min)	Butanol	1300 (Broad)	250	Very tight	Circular	Homogeneous
30	10	Oleylamine (1.5 M)	75	150	115	12.5 g/L 35 kDa polyvinylpyrrolidone in butanol	Centrifugation (1000 xg, 10 min)	Butanol	N/A	Centrifugation (1000 xg, 10 min)	Butanol	950 (Very broad)	400	Very tight	Circular, jagged edges	Homogeneous
31	40	Oleylamine (1.5 M)	75	150	115	12.5 g/L 35 kDa polyvinylpyrrolidone in butanol	Centrifugation (1000 xg, 10 min)	Butanol	N/A	Centrifugation (1000 xg, 10 min)	Butanol	1100 (Very broad)	500	Very tight	Circular	Homogeneous
32	40	Oleylamine (1.5 M)	75	150	115	15 g/L 10 kDa polyvinylpyrro	Centrifugation (1000 xg, 10 min)	Butanol	N/A	Centrifugation (1000 xg, 10 min)	Butanol	850 (Broad)	450	Very tight	Circular	Homogeneous

Entry	Gold Precursor Concentration (mM)	Capping Agent	Microwave Power (W)	Reaction Hold Time (s)	Reaction Hold Temperature (°C)	Post-Microwave Diluent	Transfer Method	Transfer Solvent	Secondary Stabilization	Purification	Suspension Solvent	Center Peak SPR (nm)	Diameter (nm)	Degree of Clustering	Cluster Circularity	Distribution
						lidone in butanol										
33	40	Oleylamine (1.5 M)	75	150	115	15 g/L 55 kDa polyvinylpyrrolidone in butanol	Centrifugation (1000 xg, 10 min)	Butanol	N/A	Centrifugation (1000 xg, 10 min)	Butanol	1100 (Broad)	450	Very tight	Circular	Homogeneous
34	40	Oleylamine (1.5 M)	75	150	115	15 g/L 360 kDa polyvinylpyrrolidone in butanol	Centrifugation (1000 xg, 10 min)	Butanol	N/A	Centrifugation (1000 xg, 10 min)	Butanol	1000 (Broad)	450	Very tight	Circular	Homogeneous
35	40	Oleylamine (1.5 M)	75	150	115	15 g/L 1300 kDa polyvinylpyrrolidone in butanol	Centrifugation (1000 xg, 10 min)	Butanol	N/A	Centrifugation (1000 xg, 10 min)	Butanol	1000 (Broad)	600	Diffuse	Circular, disassembling clusters	Heterogeneous
36	40	Oleylamine (1.5 M)	75	150	115	15 g/L Polyethyleneoxide (40) stearate in butanol	Centrifugation (1000 xg, 10 min)	Butanol	N/A	Centrifugation (1000 xg, 10 min)	Butanol	1300 (Broad)	250	Tight	Uneven circular, aggregating clusters	Heterogeneous
37	40	Oleylamine (1.5 M)	75	150	115	15 g/L Pluronic F127 in butanol	Centrifugation (1000 xg, 10 min)	Butanol	N/A	Centrifugation (1000 xg, 10 min)	Butanol	1250 (Broad)	450	Very tight	Circular	Homogeneous
38	40	Oleylamine (1.5 M)	75	150	115	15 g/L 360 kDa polyvinylpyrrolidone in butanol	Centrifugation (1000 xg, 10 min)	Butanol	15 g/L Polyethyleneoxide (40) stearate in distilled water	Centrifugation (1000 xg, 10 min), Pd10 column purification	Distilled water	1250 (Broad)	400	Very tight	Circular	Homogeneous

Entry	Gold Precursor Concentration (mM)	Capping Agent	Microwave Power (W)	Reaction Hold Time (s)	Reaction Hold Temperature (°C)	Post-Microwave Diluent	Transfer Method	Transfer Solvent	Secondary Stabilization	Purification	Suspension Solvent	Center Peak SPR (nm)	Diameter (nm)	Degree of Clustering	Cluster Circularity	Distribution
39	40	Oleylamine (1.5 M)	75	150	115	15 g/L Polyethyleneoxide (40) stearate in butanol	Centrifugation (1000 xg, 10 min)	Butanol	15 g/L Polyethyleneoxide (40) stearate in distilled water	Centrifugation (1000 xg, 10 min), Pd10 column purification	Distilled water	1250 (Broad)	450	Very tight	Circular	Homogeneous
40	40	Oleylamine (1.5 M)	75	150	115	15 g/L 360 kDa polyvinylpyrrolidone in butanol	Centrifugation (1000 xg, 10 min)	Butanol	15 g/L Pluronic F127 in distilled water	Centrifugation (1000 xg, 10 min), Pd10 column purification	Distilled water	1150 (Broad)	400	Tight	Circular, some budding	Heterogeneous
41	40	Oleylamine (1.5 M)	75	150	115	15 g/L Polyethyleneoxide (40) stearate in butanol	Centrifugation (1000 xg, 10 min)	Butanol	15 g/L Pluronic F127 in distilled water	Centrifugation (1000 xg, 10 min), Pd10 column purification	Distilled water	1150 (Broad)	450	Very tight	Circular, some budding	Heterogeneous

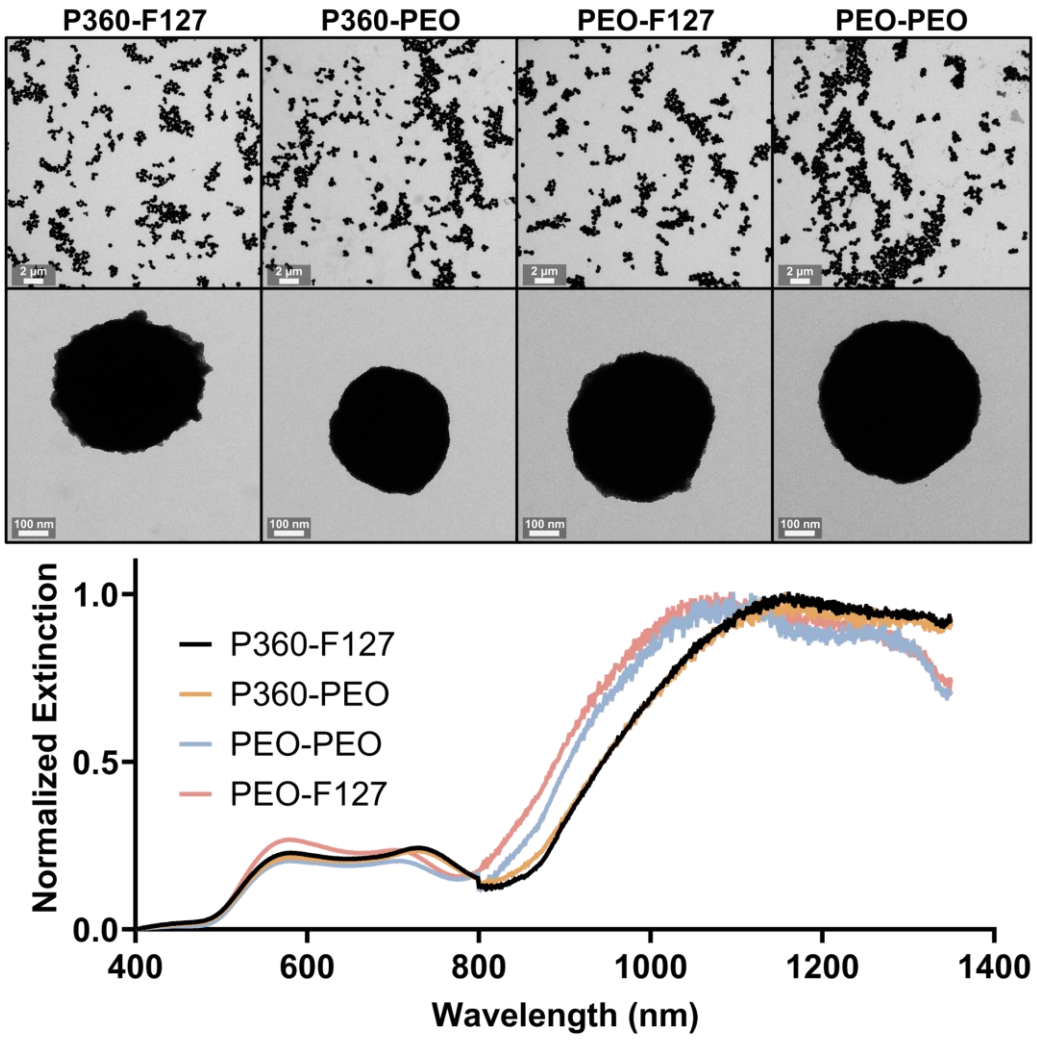

Supplementary Figure 1. Effects of amphiphilic polymer di-coating on AuSC physicochemical properties. TEM images and the resulting LSPR spectra in water of AuSC synthesized as described in the main manuscript with different polymer coating pairings. The first polymer mentioned denotes the polymer used to stabilize AuSC while in *n*-butanol, and the second polymer mentioned was used for coating when drawing the AuSC@(polymer) into aqueous solvent. PEO; polyethylene oxide (40) stearate, P360; polyvinylpyrrolidone (average molecular weight 360 kDa), F127; Pluronic^{TM} F-127.

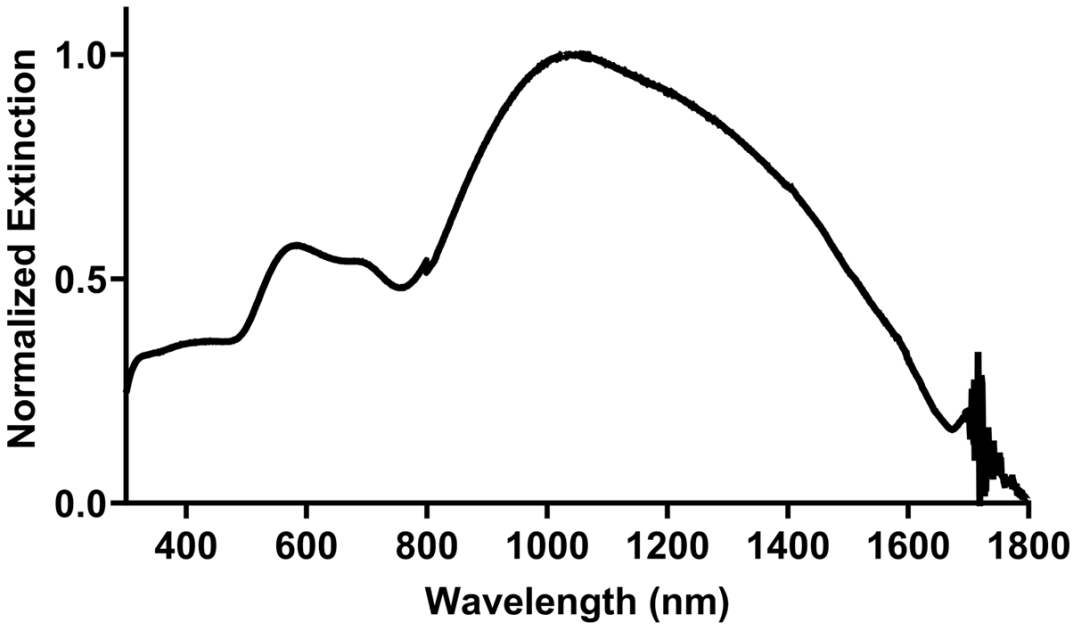

Supplementary Figure 2. Extended LSPR spectra of AuSC@(Myrj52). LSPR spectra of AuSC@(Myrj52) acquired in *n*-butanol showing the extent of the NIR-II-active peak. Spectra in the main manuscript are performed in water and limited to 1400 nm due to the high absorptivity of water in the region around 1400 nm.

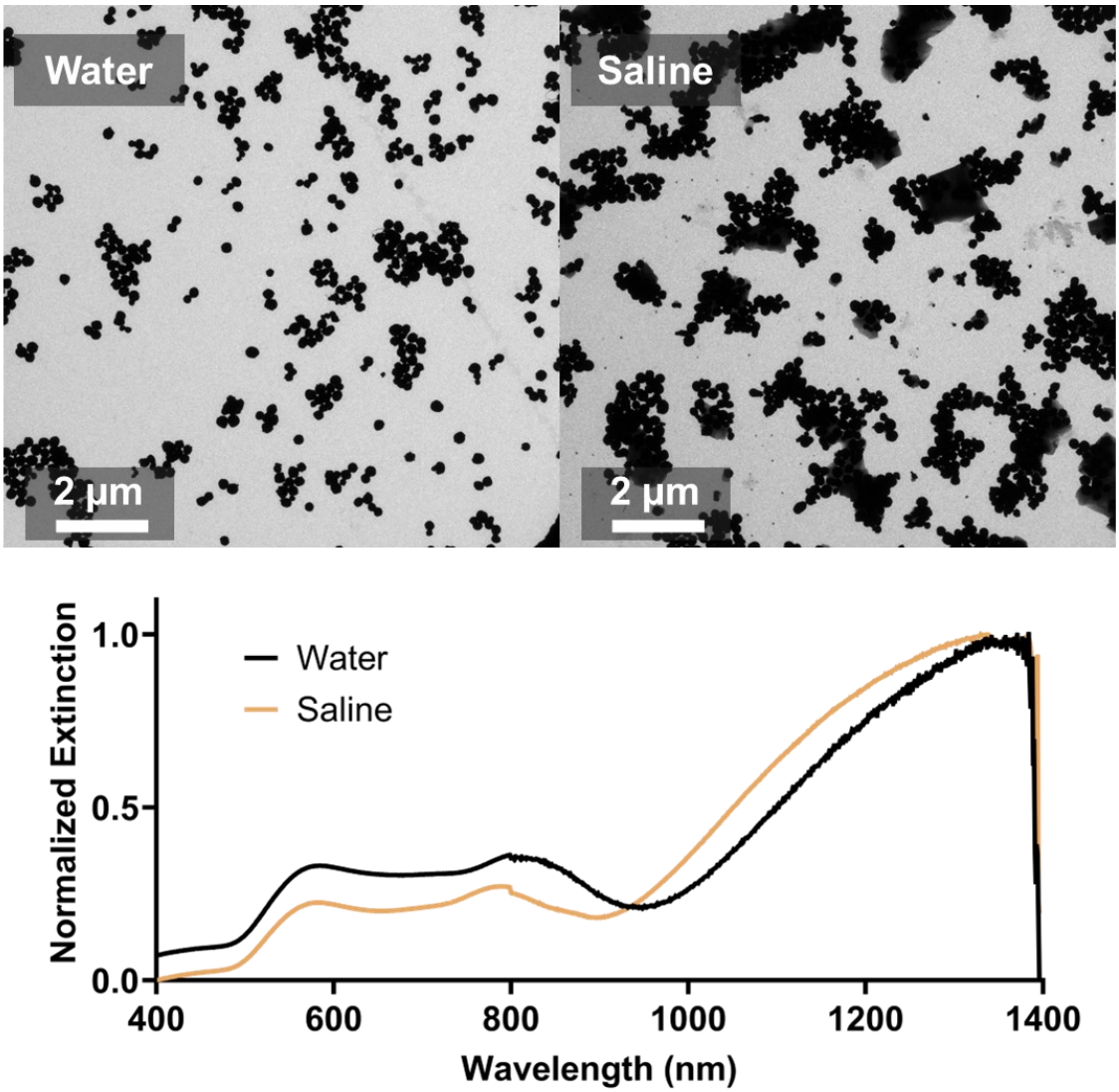

Supplementary Figure 3. Physicochemical properties of AuSC@(Myrj52)$_2$ synthesized in water and saline. AuSC@(Myrj52)$_2$ was synthesized as described in the main manuscript, except the di-coating step of the synthesis was performed as described with water or performed as described with saline instead of water. LSPR spectra was acquired after being blanked to the respective dispersion solvent. Grey shadow artifacts in the saline TEM are due to the formation of NaCl crystals from the dried saline on the TEM grid.

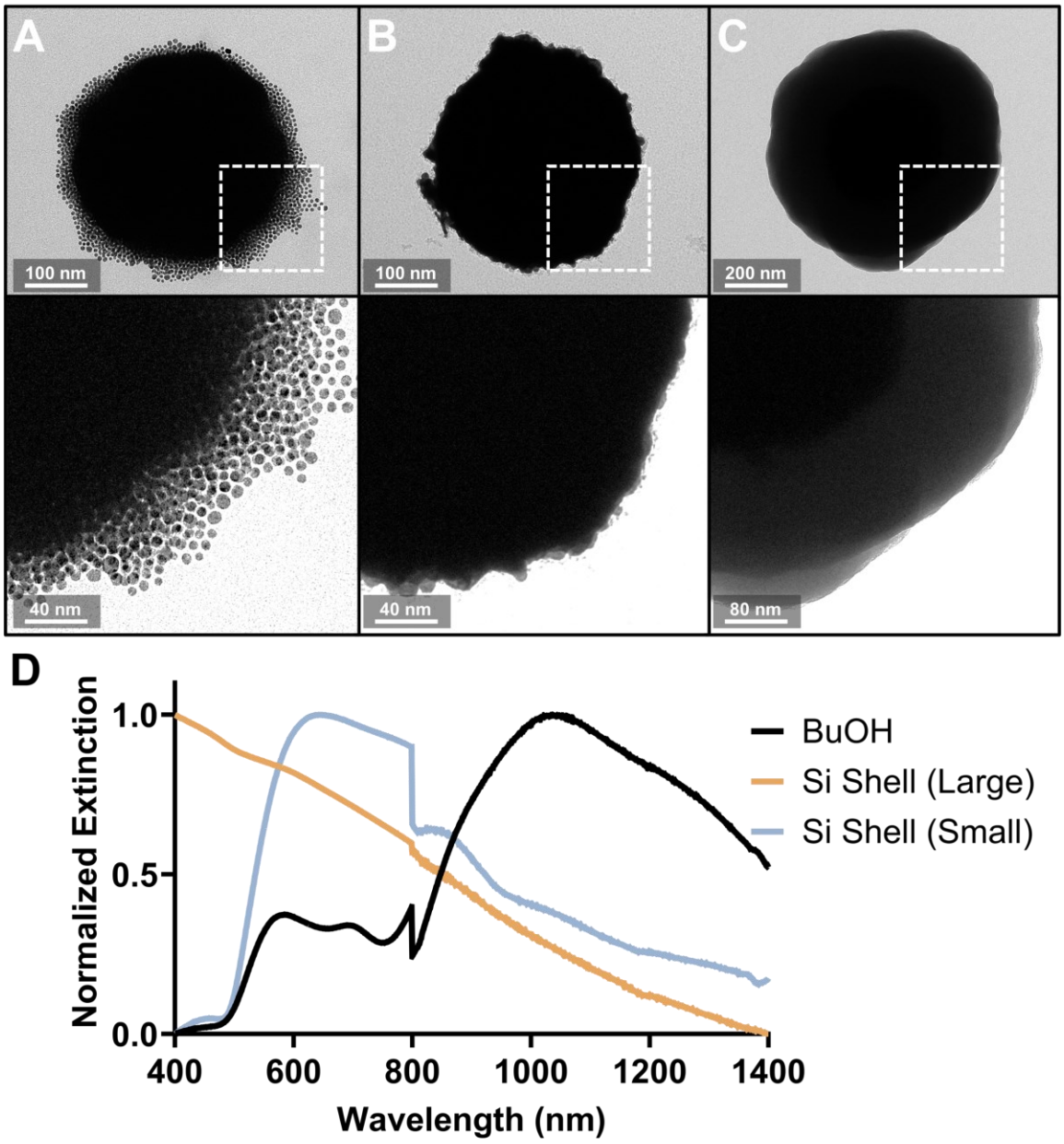

Supplementary Figure 4. Change in AuSC LSPR spectra before and after SiO_2 coating. AuSC dispersed in *n*-butanol without polymer stabilization (A) were coated with a thin (B) or thick (C) shell of SiO_2. Image contrast was boosted digitally to see the cluster more clearly within the shell. D) LSPR spectra of the above AuSC dispersed in *n*-butanol. The sharp vertical drop present in all spectra is a result of detector changeover on the spectrometer.

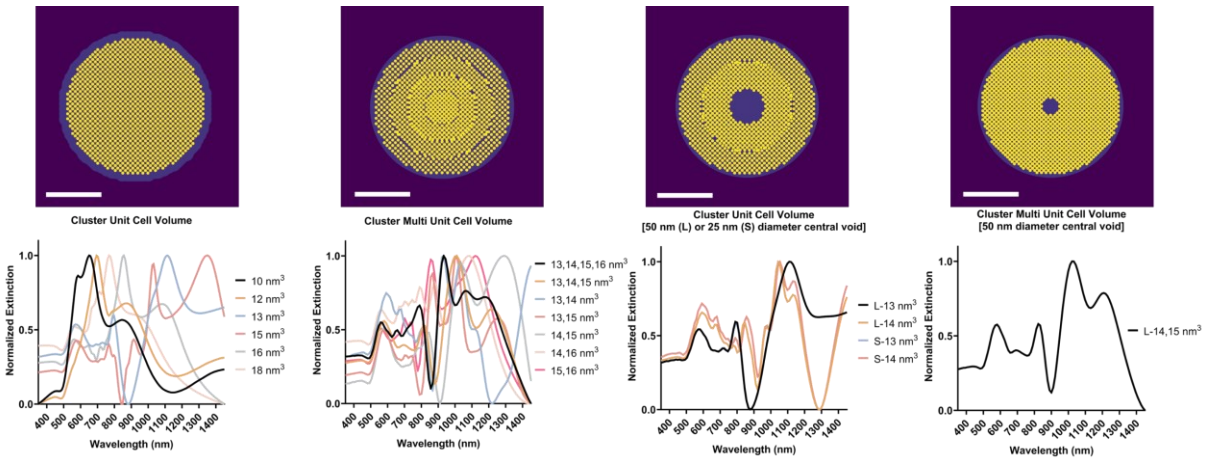

Supplementary Figure 5. Simulated variations in AuSC intraparticle unit cell spacing and orientation and change in LSPR spectra. Finite-difference time domain modelled AuSC and the resulting simulated LSPR spectra for AuSC with different intraparticle unit cell volumes (IUCs), multi-IUCs, as well as single and multi-IUCs with or without a central void.

Supplementary Figure 6. Different concentrations AuSC@(Myrj52)$_2$ suspended in water. Image of varying concentrations of AuSC@(Myrj52)$_2$ from 1 mg/mL to 0 mg/mL (saline, decreasing left to right), suspended in saline in glass vials.

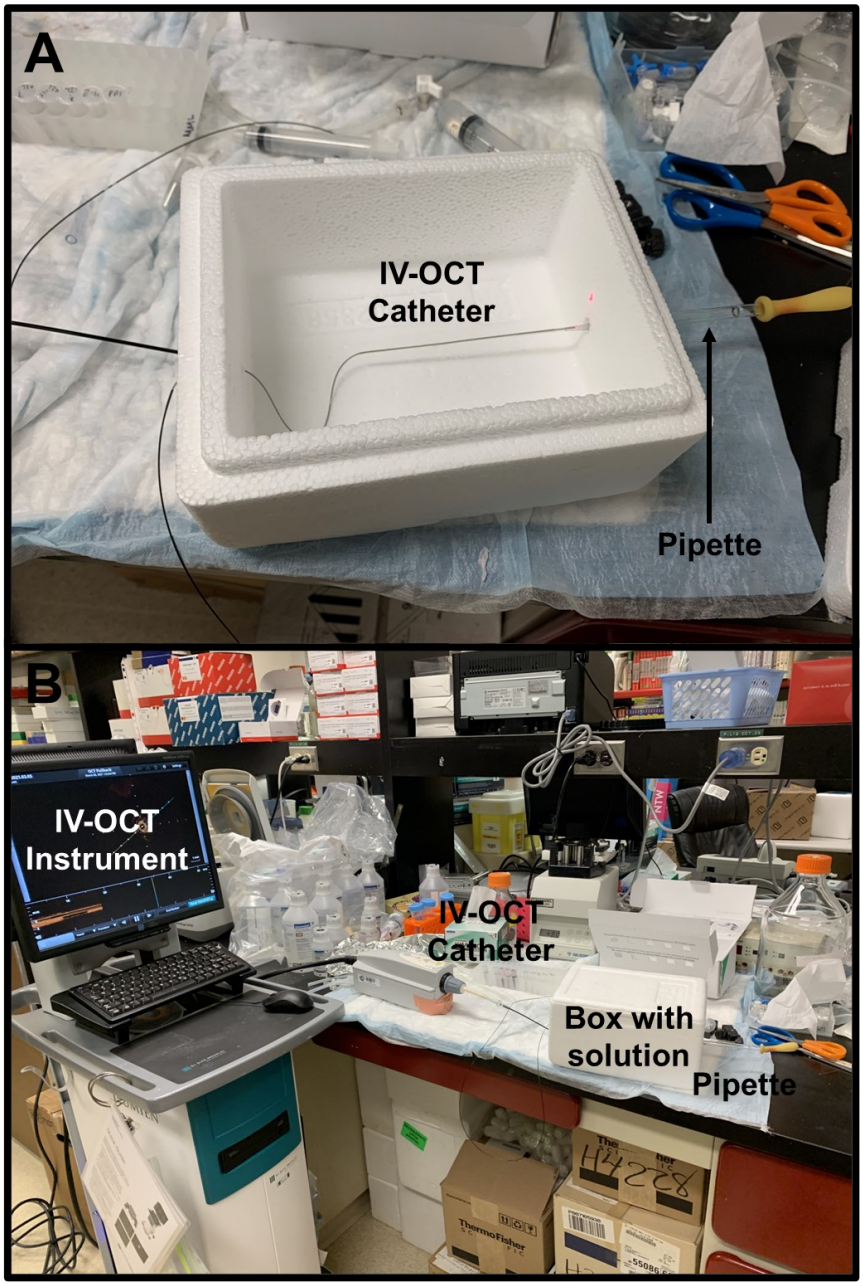

Supplementary Figure 7. Experimental setup for *in vitro* IV-OCT phantom measurements. A clinical IV-OCT instrument (Abbott Illumien™ OPTIS™ PCI) connected to an Dragonfly™ OPTIS™ imaging catheter was used to catheterize a glass pipette containing solutions of AuSC@$(Myrj52)_2$ to image dispersion within the confines of the box. A) Inside of the box containing the inserted pipette catheterized by the IV-OCT imaging catheter. B) Overview of the closed setup connected to the IV-OCT instrument to be imaged.

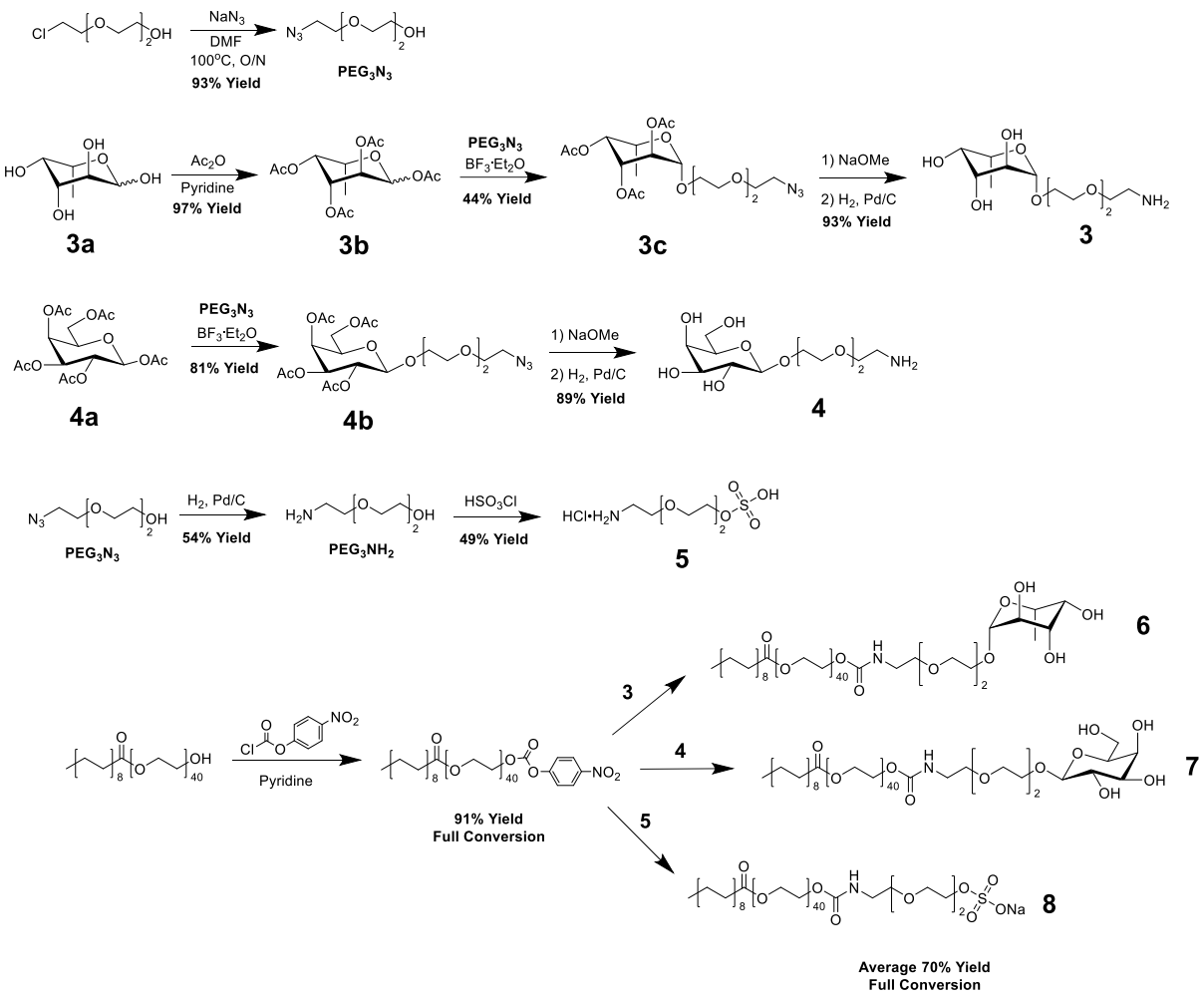

Supplementary Figure 8. Synthetic scheme for precursor molecules used for activated Myrj52 functionalization. General synthetic scheme for the molecules used to functionalize the 4-nitrophenol chloroformate-activated Myrj52 and the resulting functionalization of activated Myrj52.

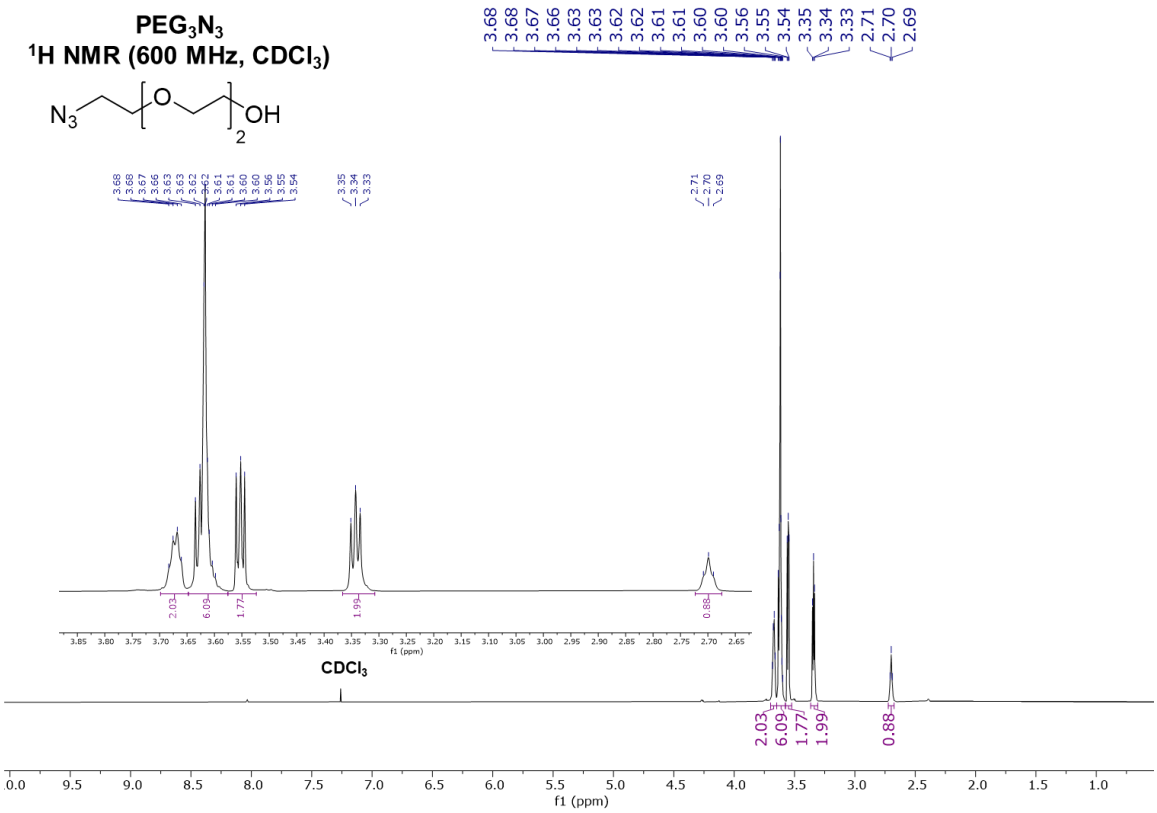

Supplementary Figure 9. ^{1}H NMR spectrum of PEG_3N_3 in $CDCl_3$. Inset spectra is a magnification of the overall NMR from 2.6 ppm – 3.9 ppm.

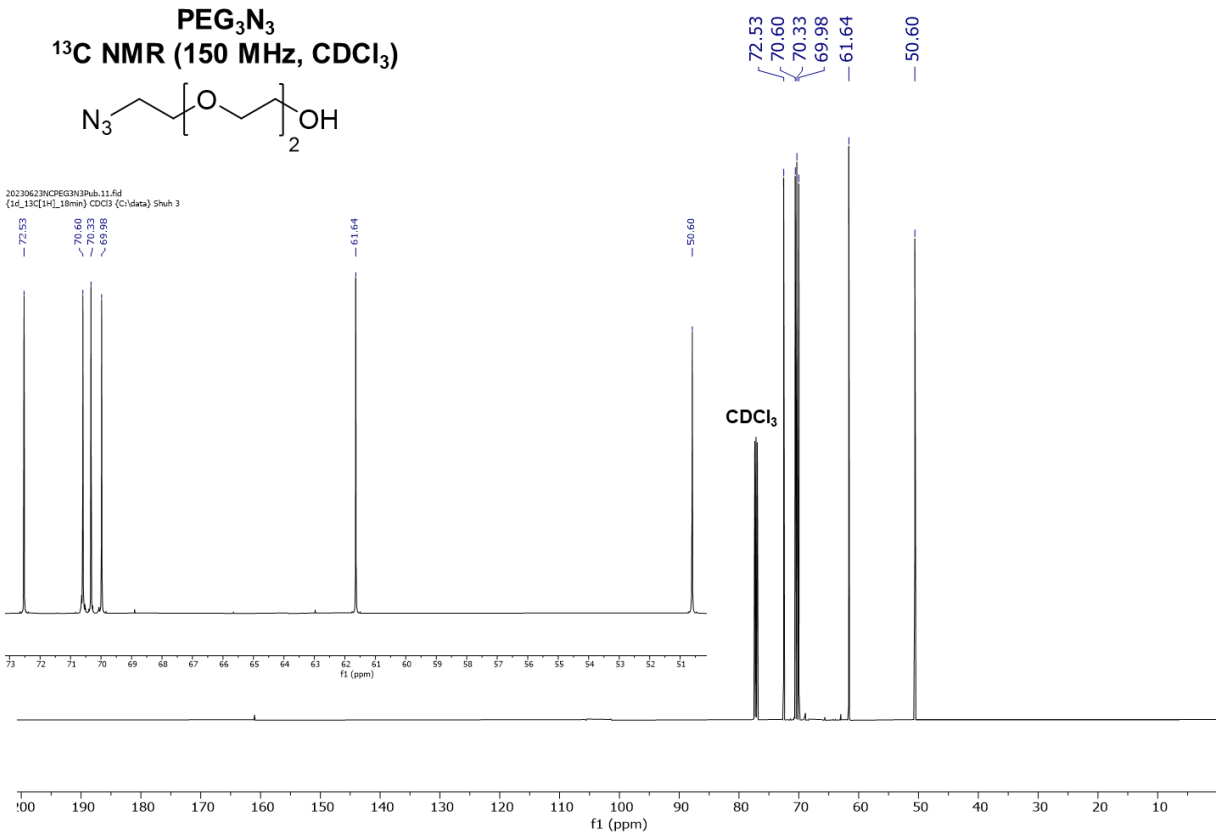

Supplementary Figure 10. ^{13}C NMR spectrum of PEG_3N_3 in $CDCl_3$. Inset spectra is a magnification of the overall NMR from 50 ppm – 73 ppm.

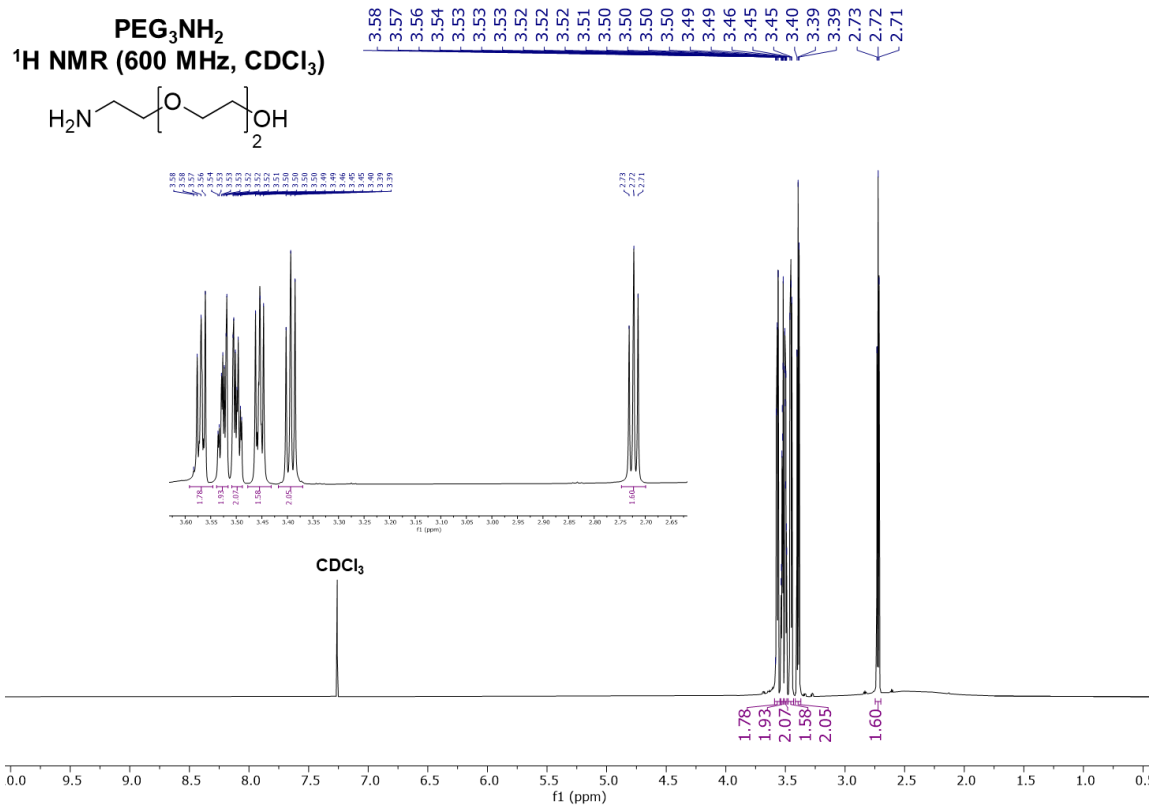

Supplementary Figure 11. ^{1}H NMR spectrum of PEG_3NH_2 in $CDCl_3$. Inset spectra is a magnification of the overall NMR from 2.60 ppm – 3.65 ppm.

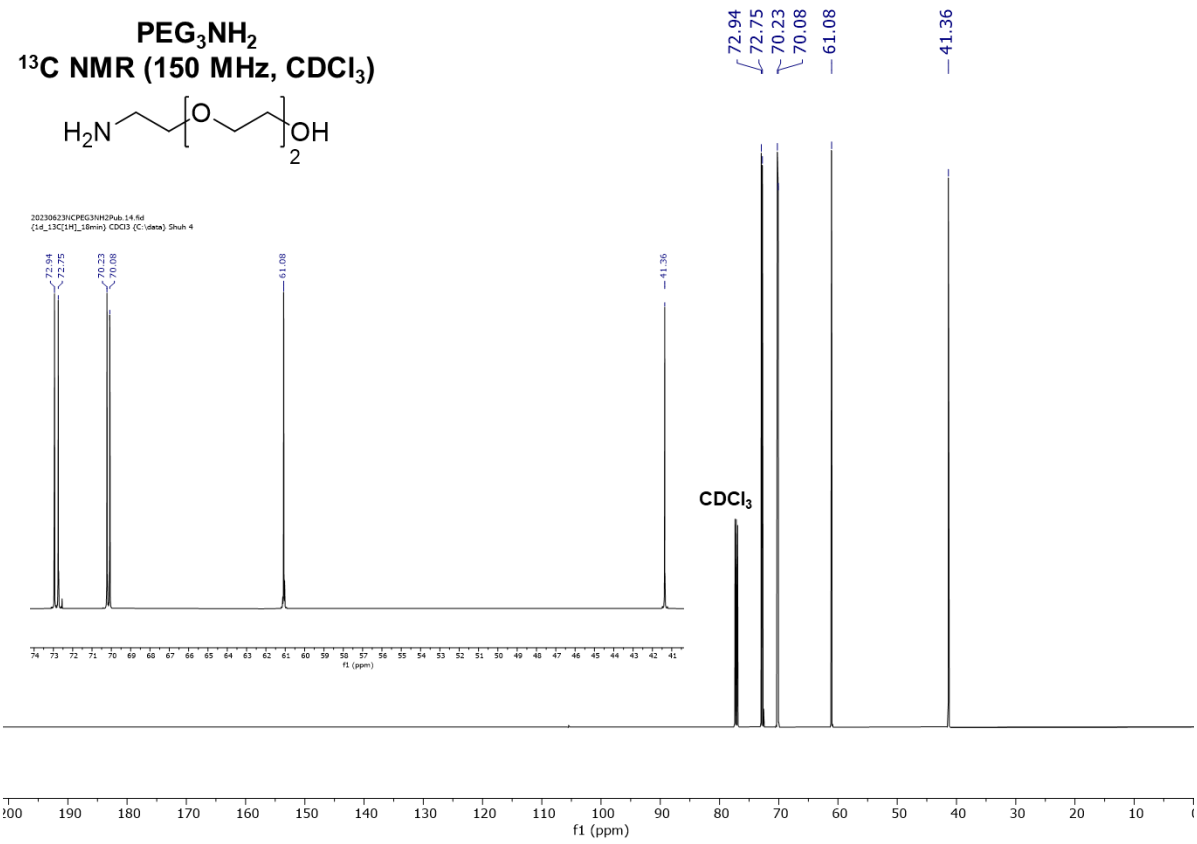

Supplementary Figure 12. ^{13}C NMR spectrum of PEG_3NH_2 in $CDCl_3$. Inset spectra is a magnification of the overall NMR from 40 ppm – 74 ppm.

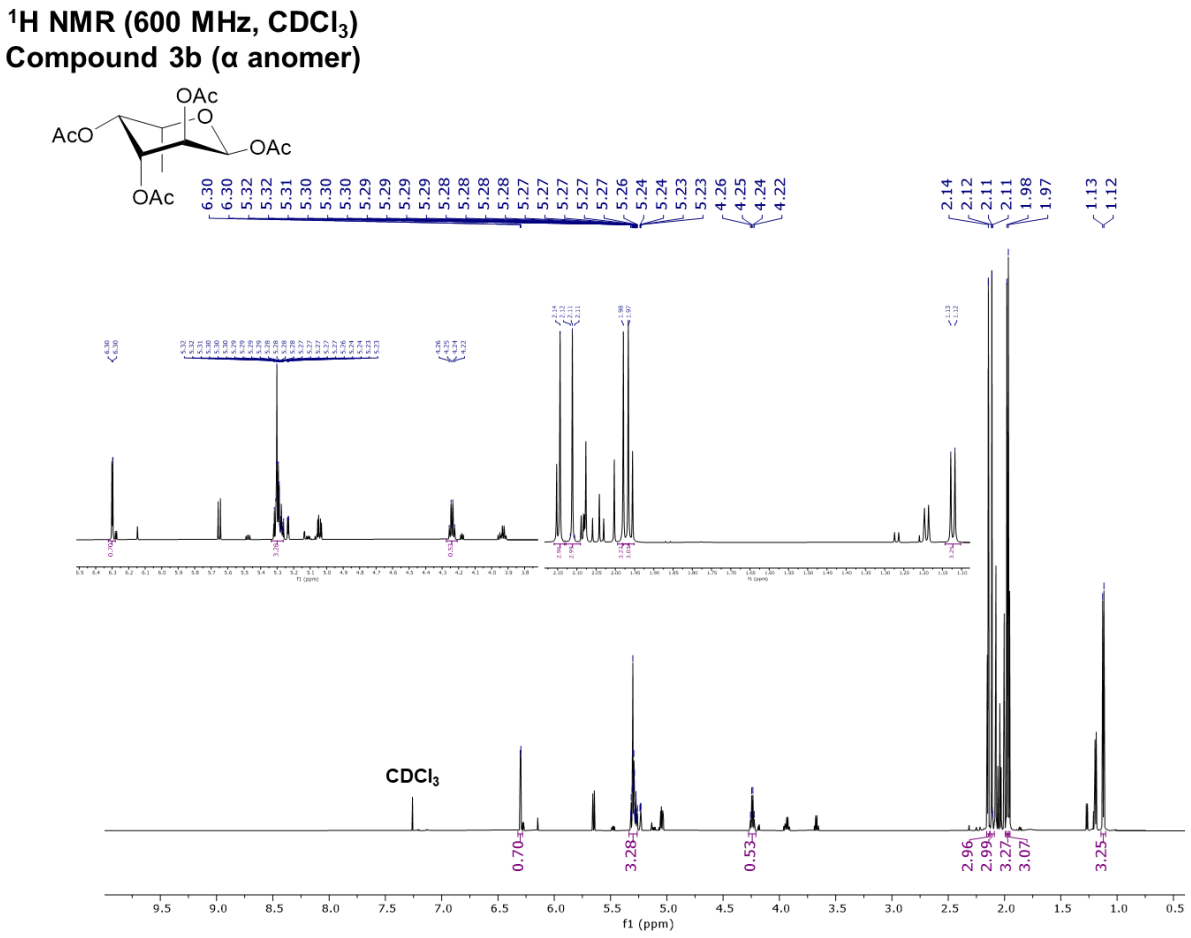

Supplementary Figure 13. ^{1}H NMR spectrum of Compound 3b (α anomer) in $CDCl_3$. Inset spectra is a magnification of the overall NMR from 1.1 ppm – 2.2 ppm and 3.7 ppm – 6.4 ppm.

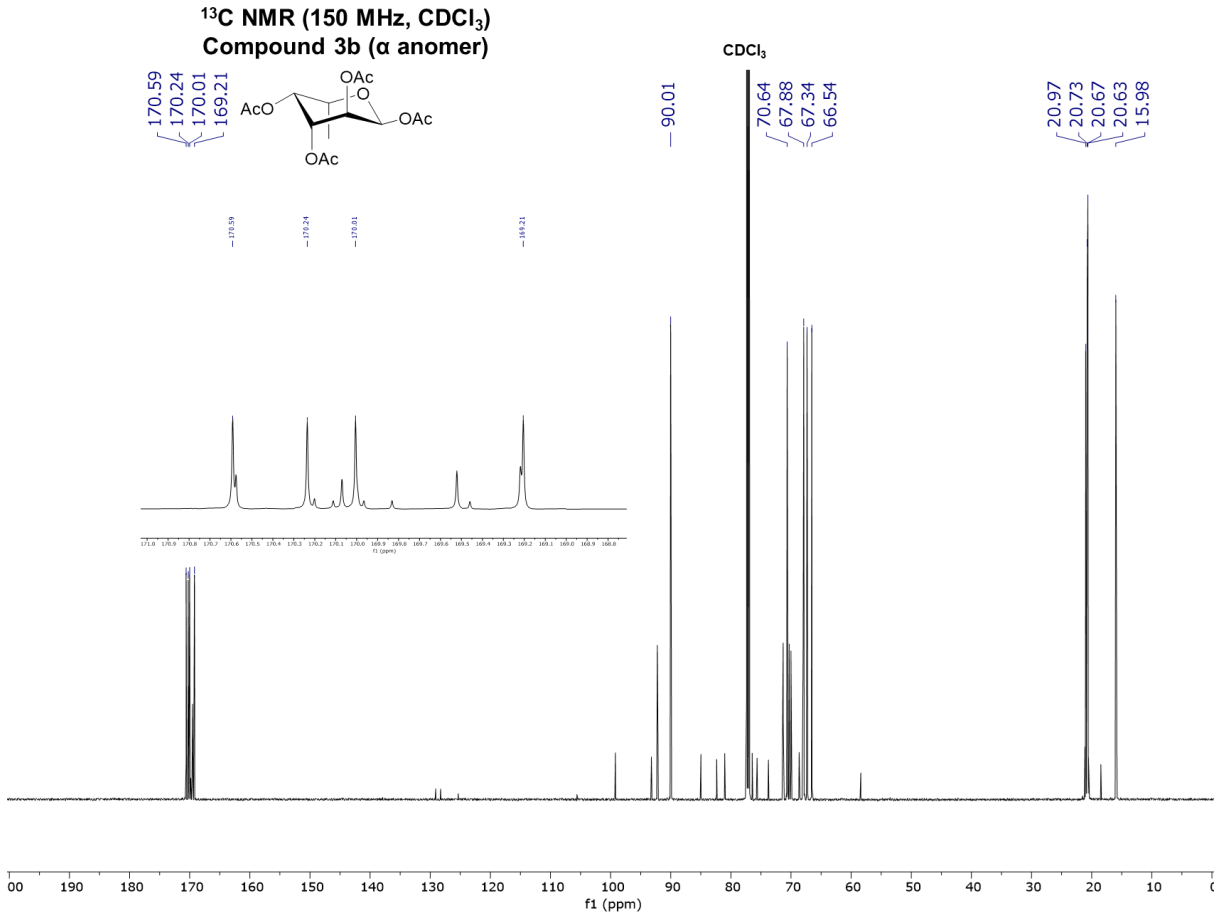

Supplementary Figure 14. ^{13}C NMR spectrum of Compound 3b (α anomer) in $CDCl_3$. Inset spectra is a magnification of the overall NMR from 168.7 ppm – 171.0 ppm.

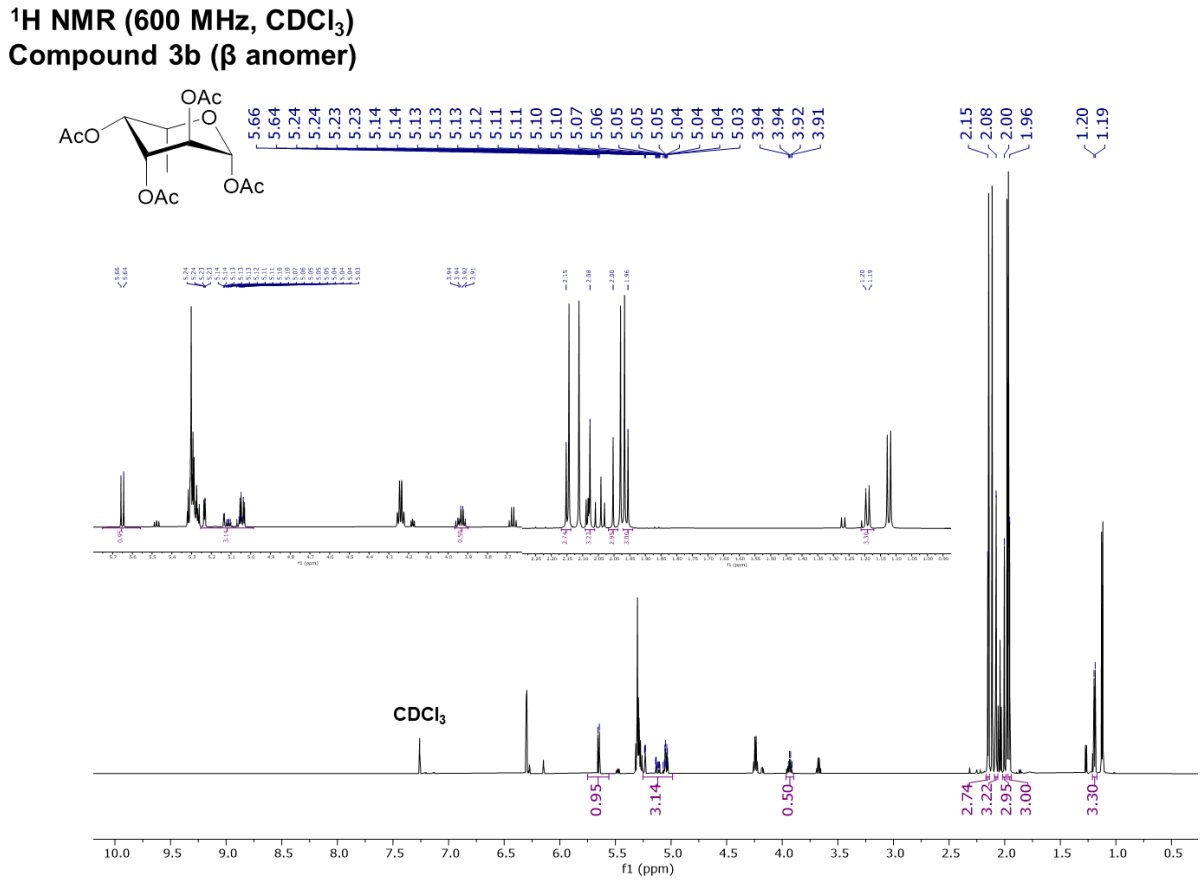

Supplementary Figure 15. ^{1}H NMR spectrum of Compound 3b (β anomer) in $CDCl_3$. Inset spectra is a magnification of the overall NMR from 0.95 ppm to 2.30 ppm and 3.6 ppm to 5.8 ppm.

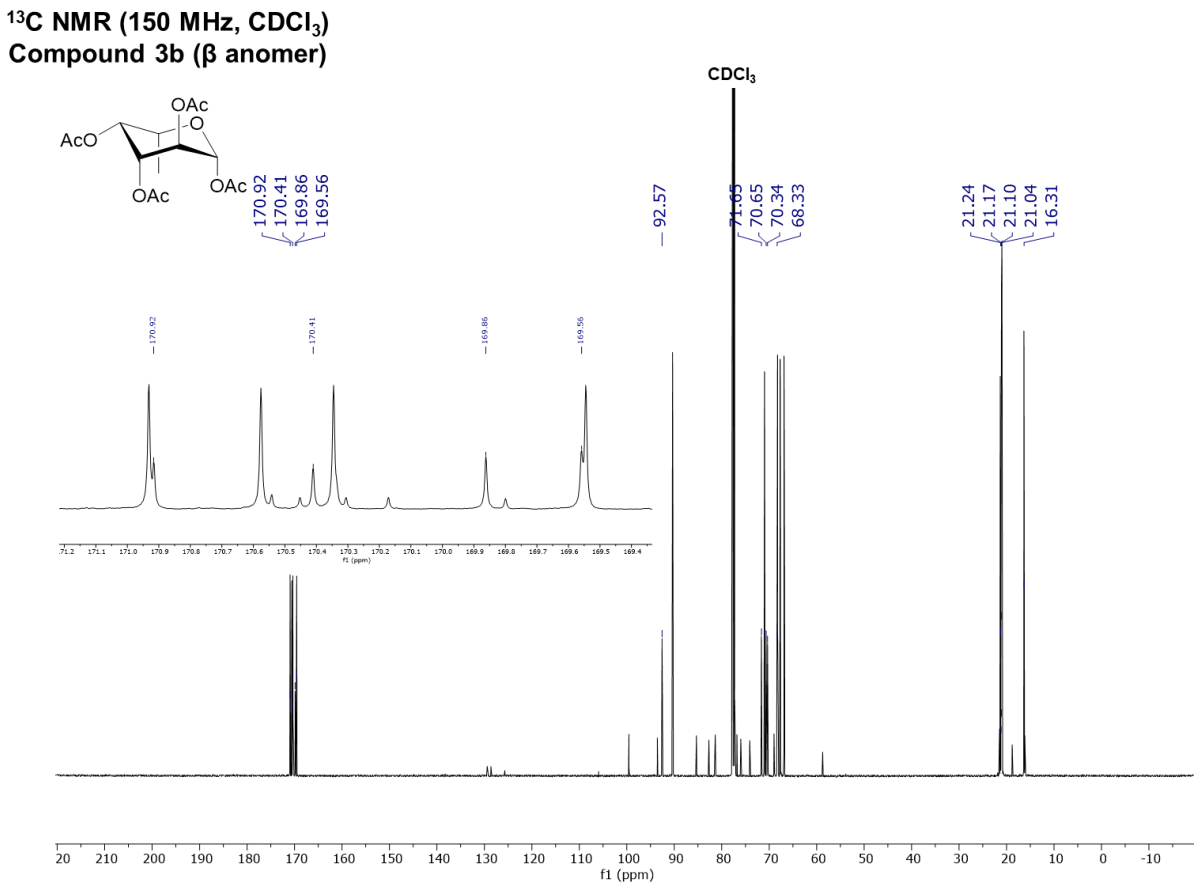

Supplementary Figure 16. ^{13}C NMR spectrum of Compound 3b (β anomer) in $CDCl_3$. Inset spectra is a magnification of the overall NMR from 169.3 ppm – 171.2 ppm.

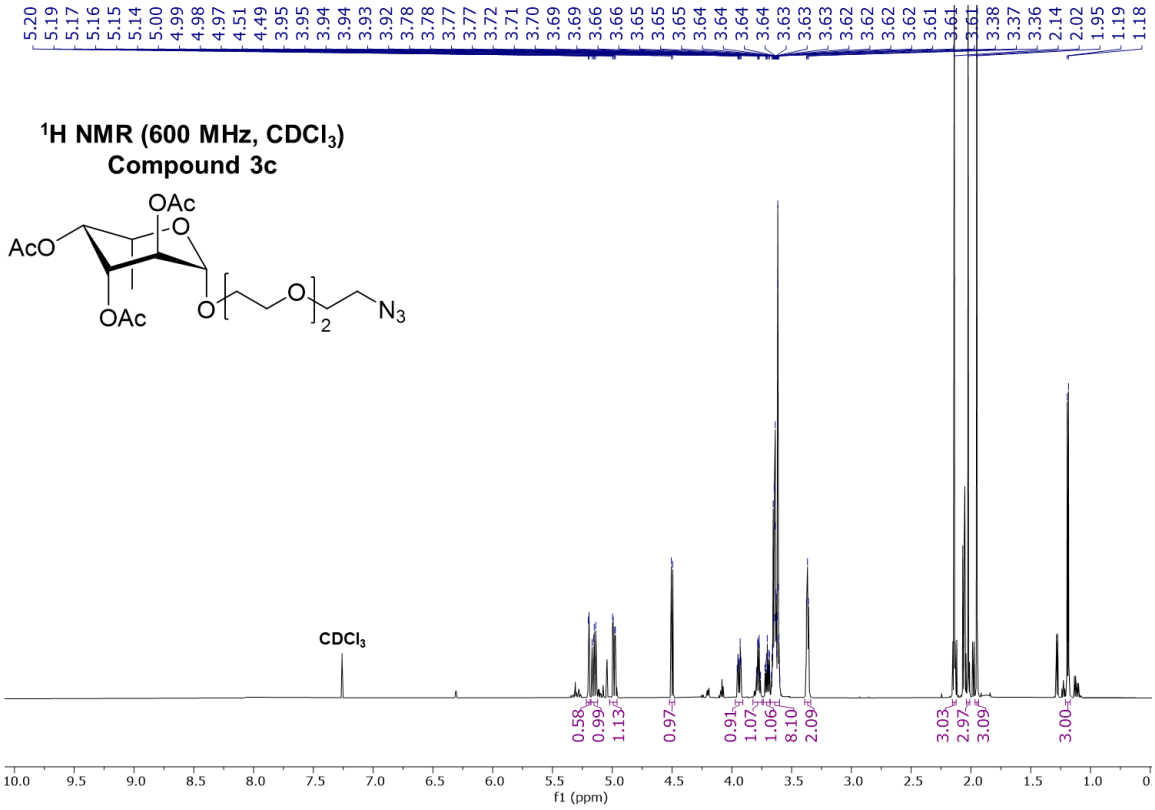

Supplementary Figure 17. ^{1}H NMR spectrum of Compound 3c in $CDCl_3$.

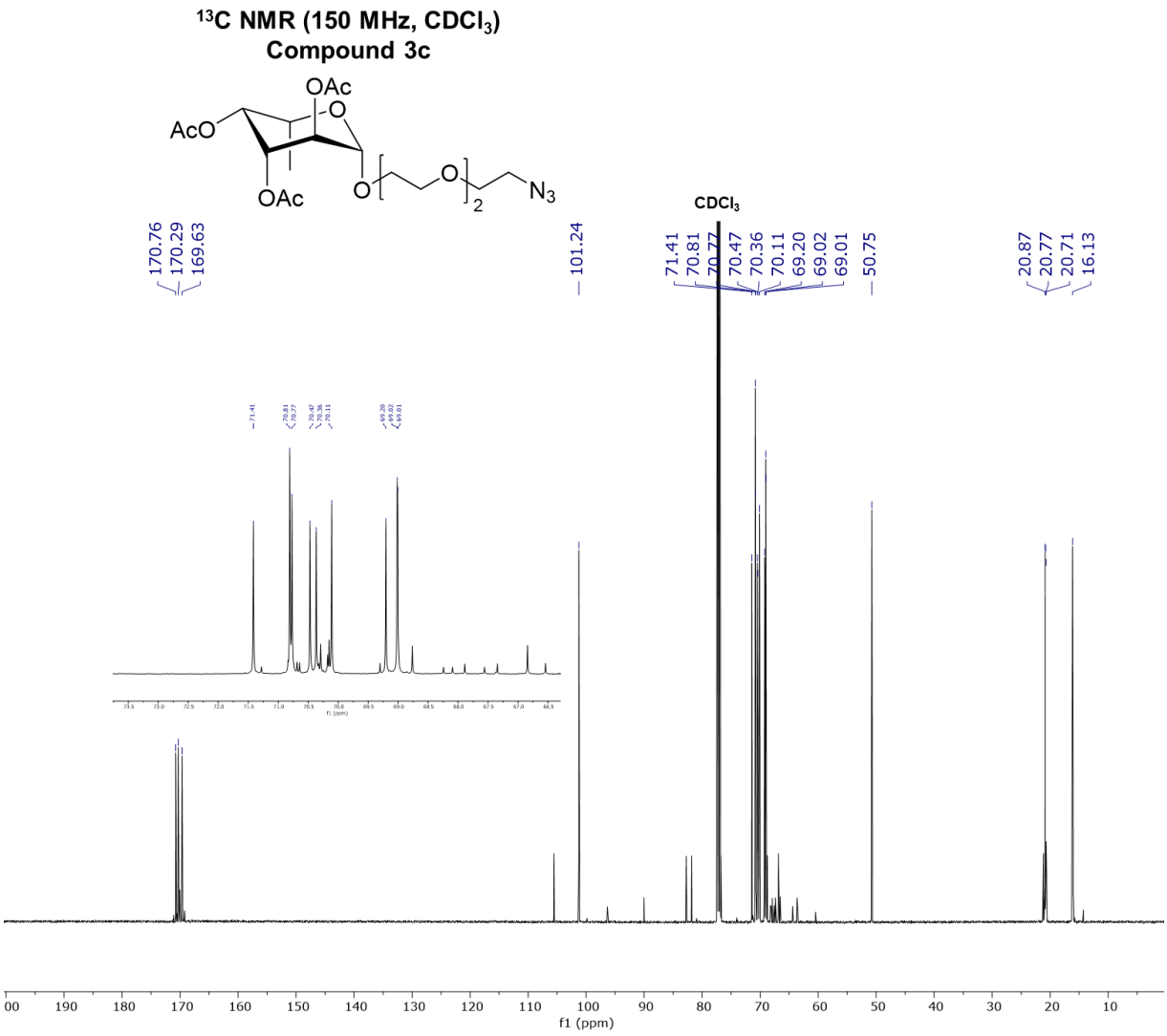

Supplementary Figure 18. ^{13}C NMR spectrum of Compound 3c in $CDCl_3$. Inset spectra is a magnification of the overall NMR from 60 ppm – 74 ppm.

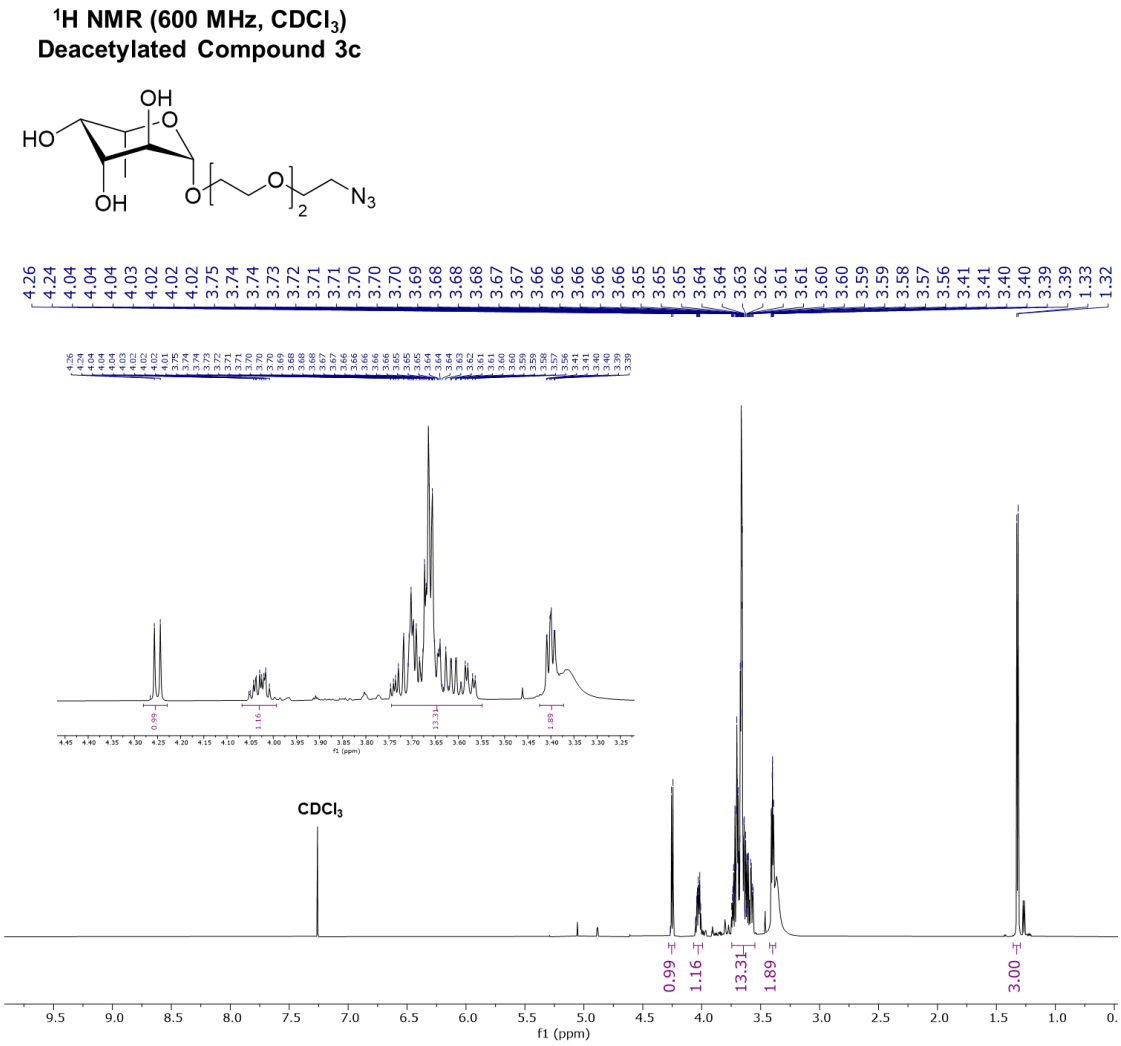

Supplementary Figure 19. ^{1}H NMR spectrum of deacetylated Compound 3c in $CDCl_3$. Inset spectra is a magnification of the overall NMR from 3.2 ppm – 4.5 ppm. The broad peak at 3.35 ppm was generated by the alcohols of **3c**.

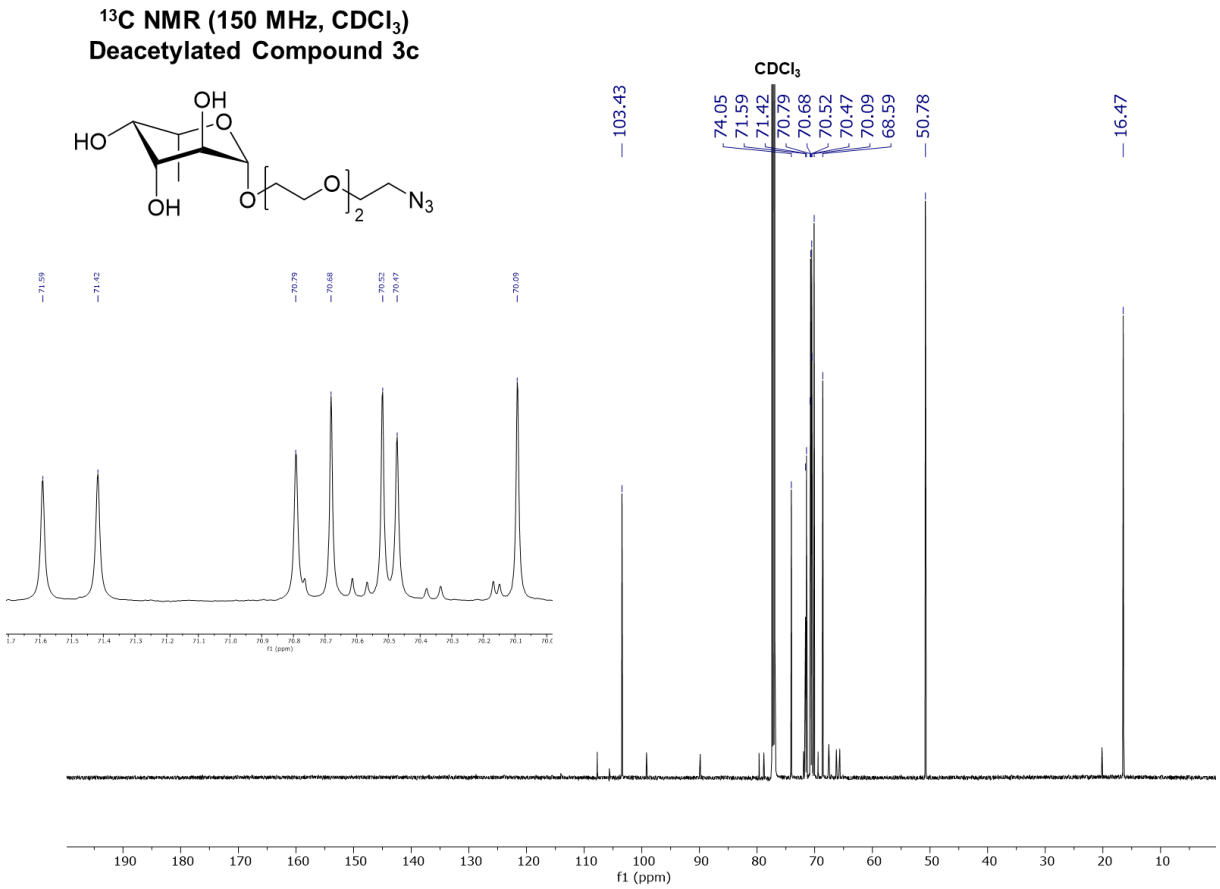

Supplementary Figure 20. ^{13}C NMR spectrum of deacetylated Compound 3c in $CDCl_3$. Inset spectra is a magnification of the overall NMR from 70.0 ppm – 71.7 ppm.

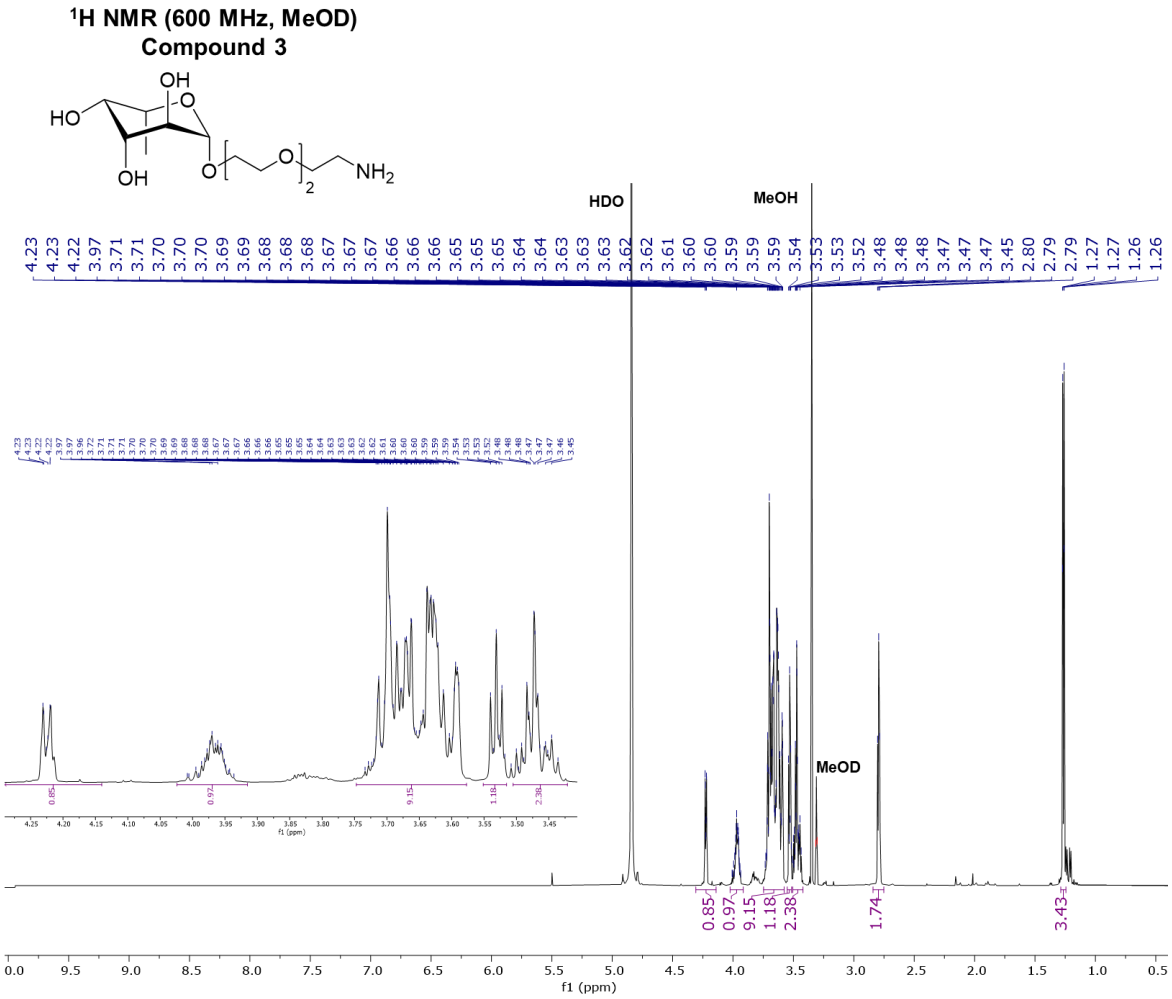

Supplementary Figure 21. ^{1}H NMR spectrum of Compound 3 in MeOD. Inset spectra is a magnification of the overall NMR from 3.4 ppm – 4.3 ppm.

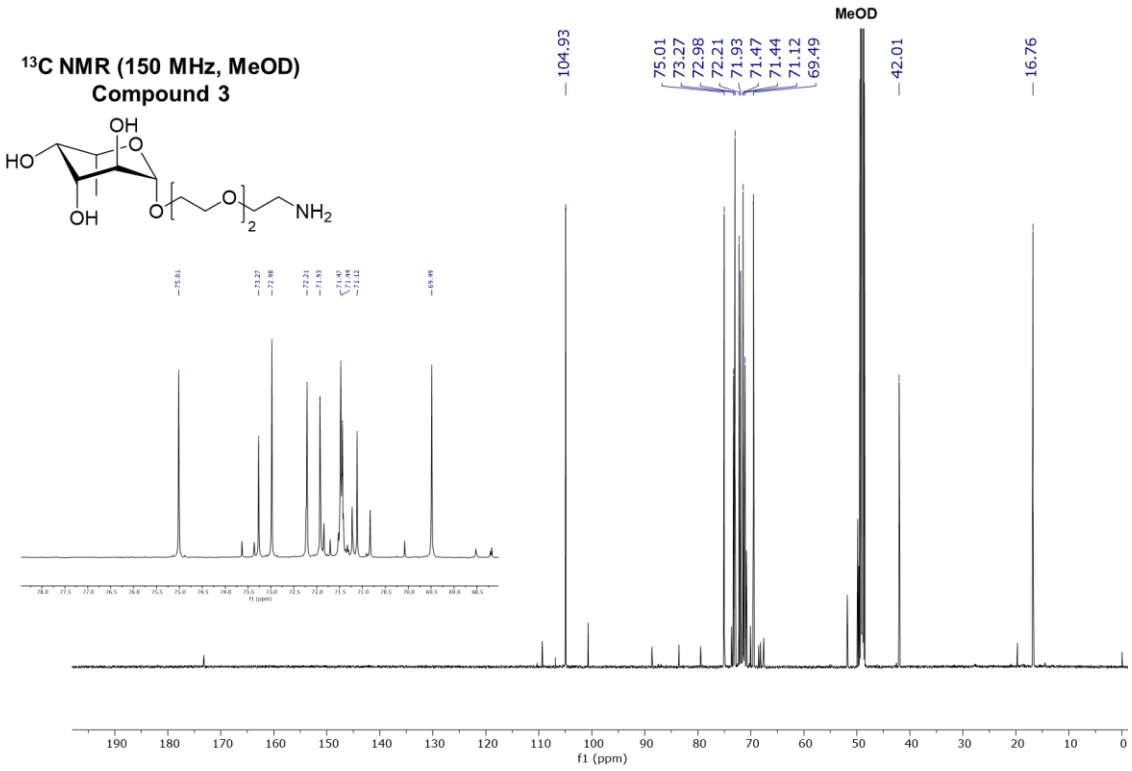

Supplementary Figure 22. ^{13}C NMR spectrum of Compound 3 in MeOD. Inset spectra is a magnification of the overall NMR from 68.0 ppm – 78.5 ppm.

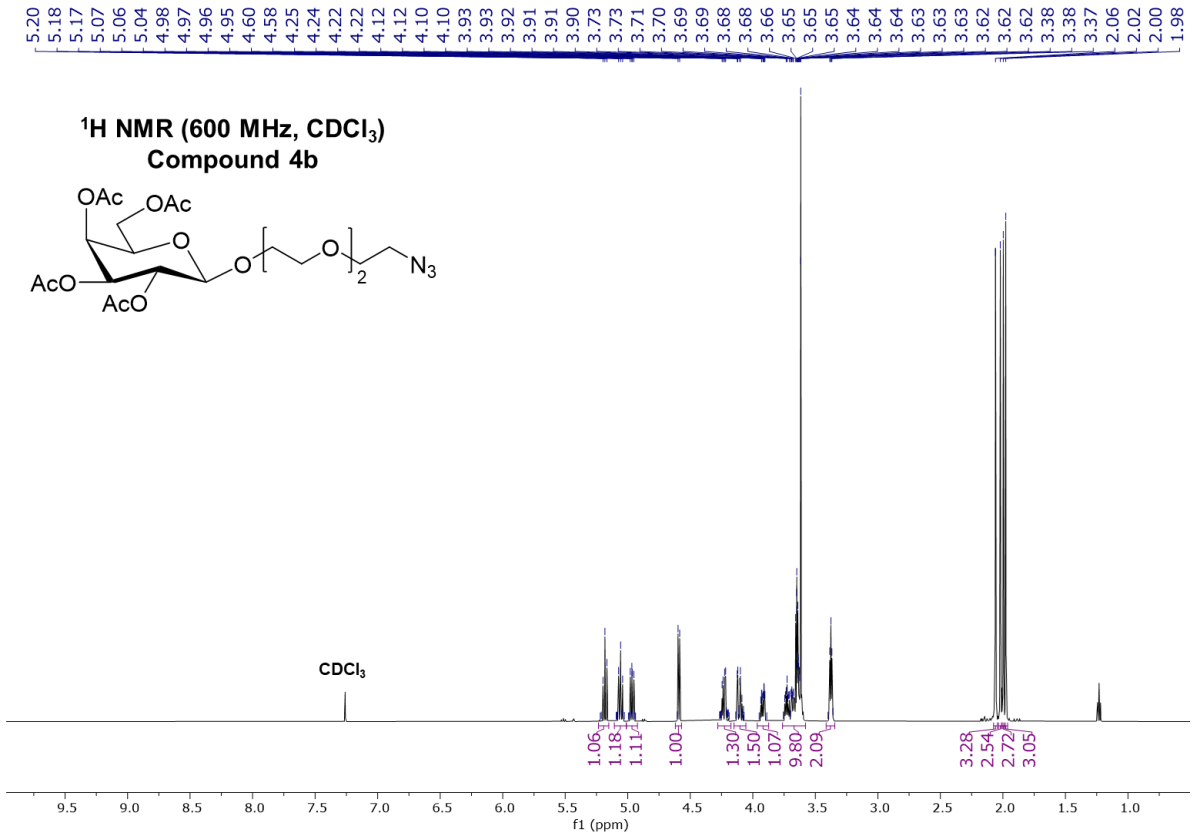

Supplementary Figure 23. ^{1}H NMR spectrum of Compound 4b in $CDCl_3$.

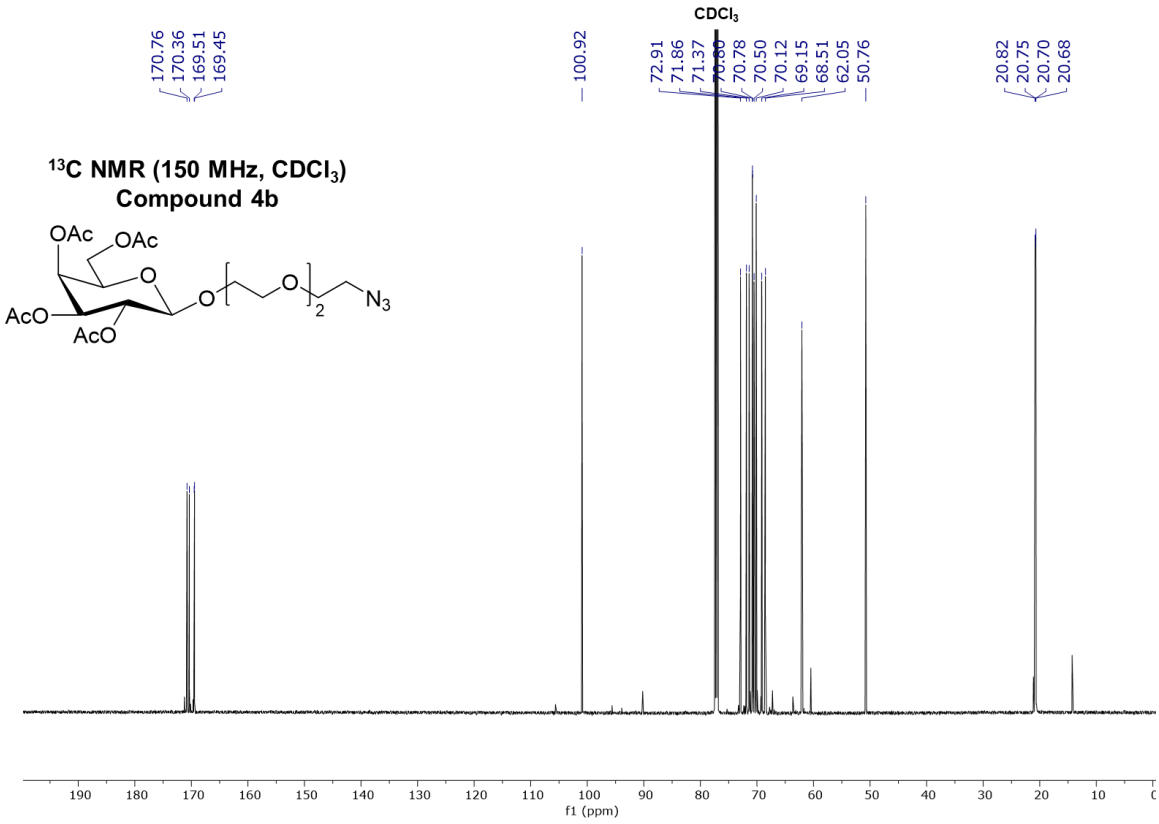

Supplementary Figure 24. ^{13}C NMR spectrum of Compound 4b in $CDCl_3$.

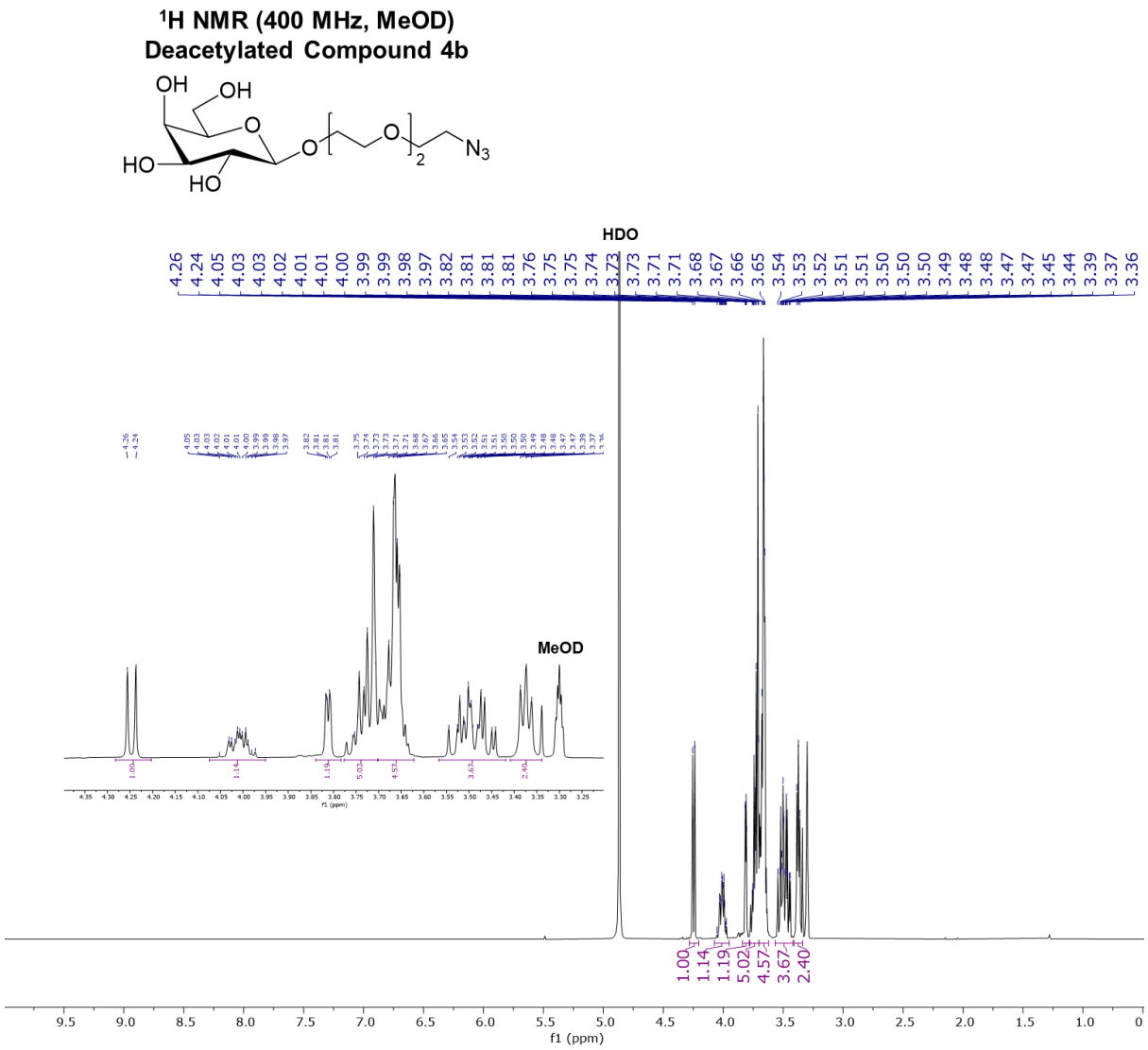

Supplementary Figure 25. ^{1}H NMR spectrum of deacetylated Compound 4b in MeOD. Inset spectra is a magnification of the overall NMR from 3.2 ppm – 4.4 ppm.

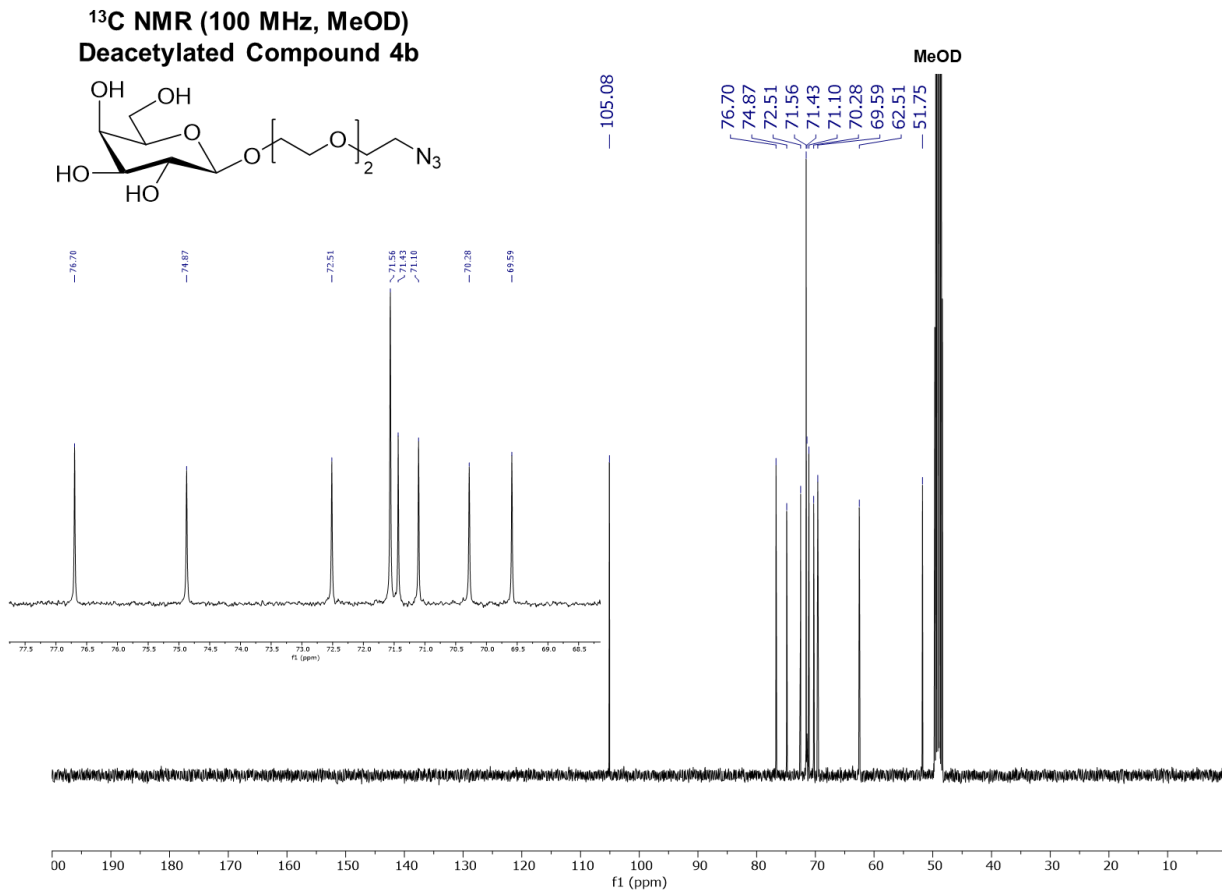

Supplementary Figure 26. ^{13}C NMR spectrum of deacetylated Compound 4b in MeOD. Inset spectra is a magnification of the overall NMR from 68 ppm – 78 ppm.

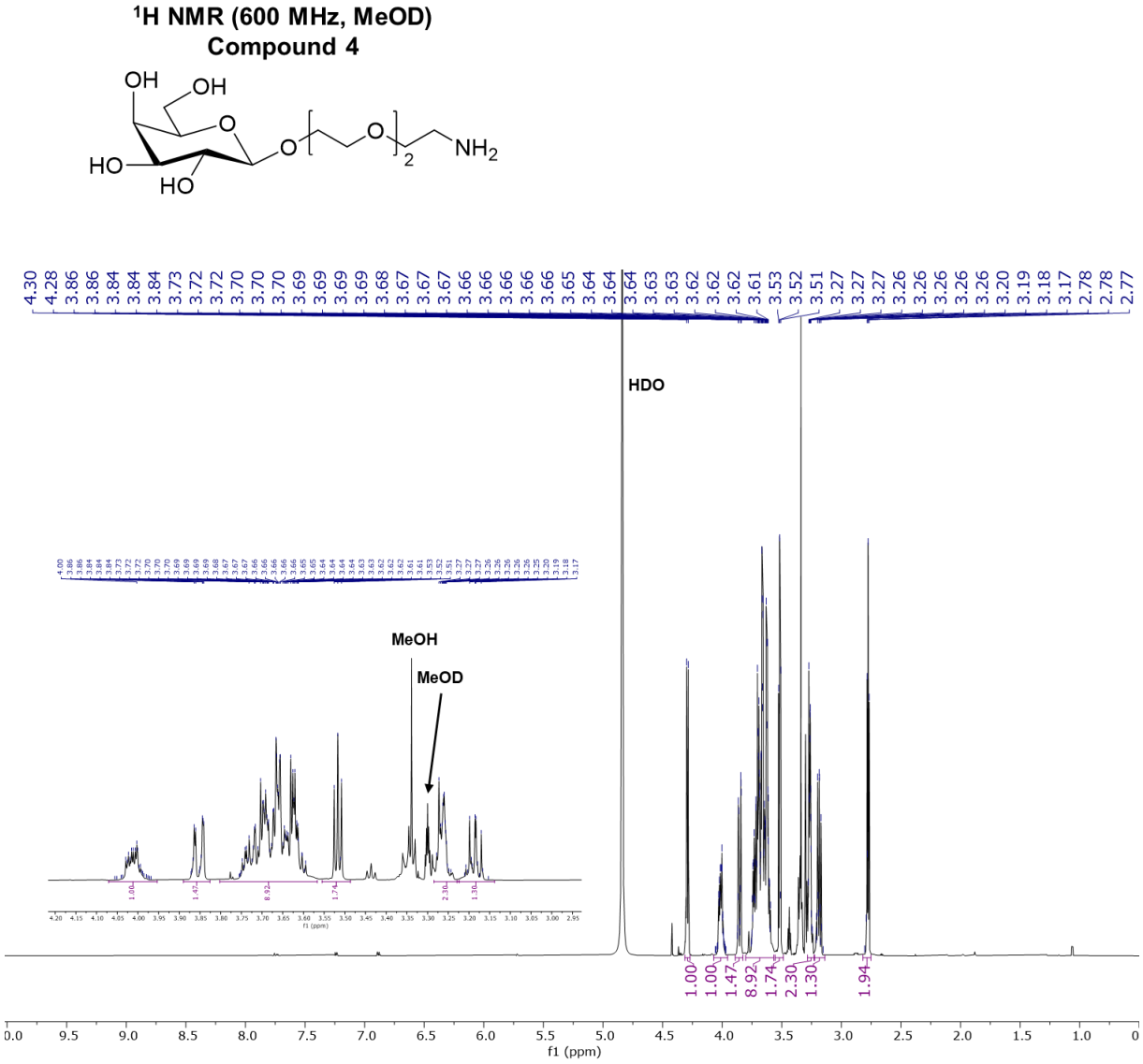

Supplementary Figure 27. ^{1}H NMR spectrum of Compound 4 in MeOD. Inset spectra is a magnification of the overall NMR from 2.9 ppm – 4.2 ppm.

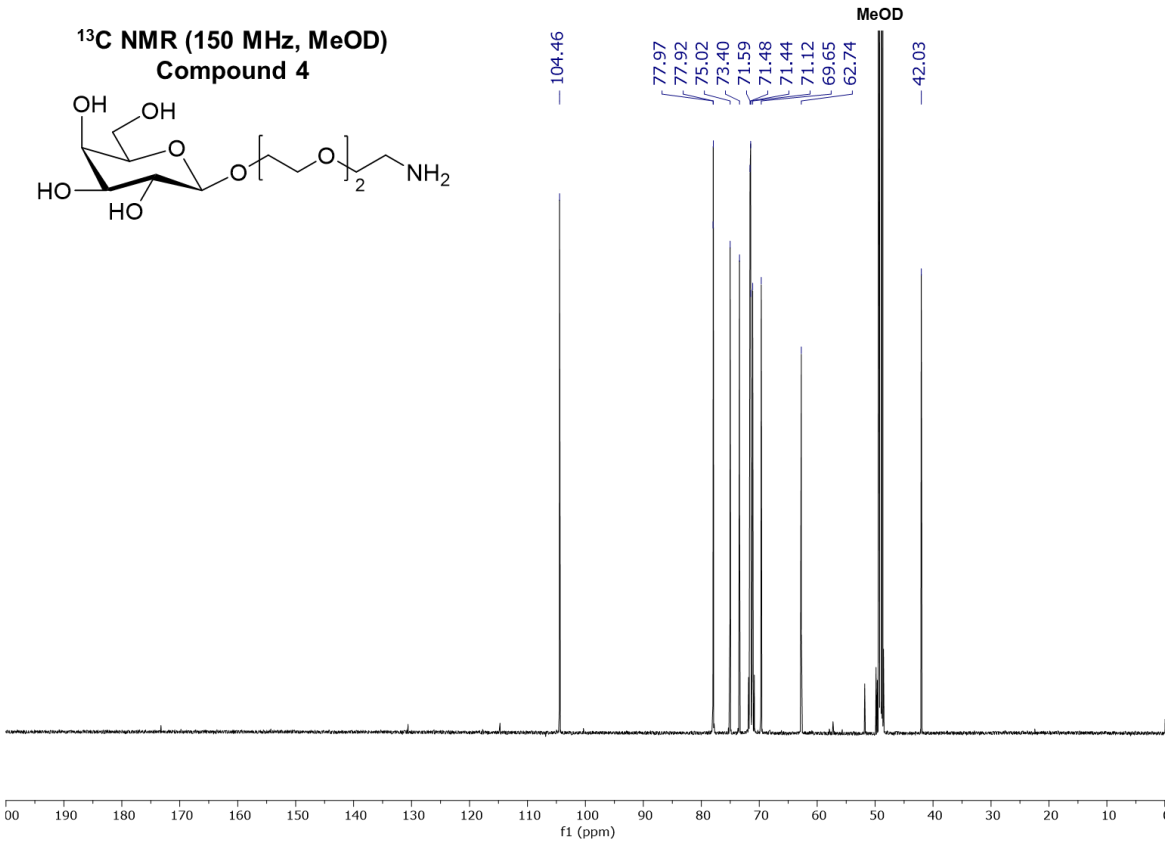

Supplementary Figure 28. ^{13}C NMR spectrum of Compound 4 in MeOD.

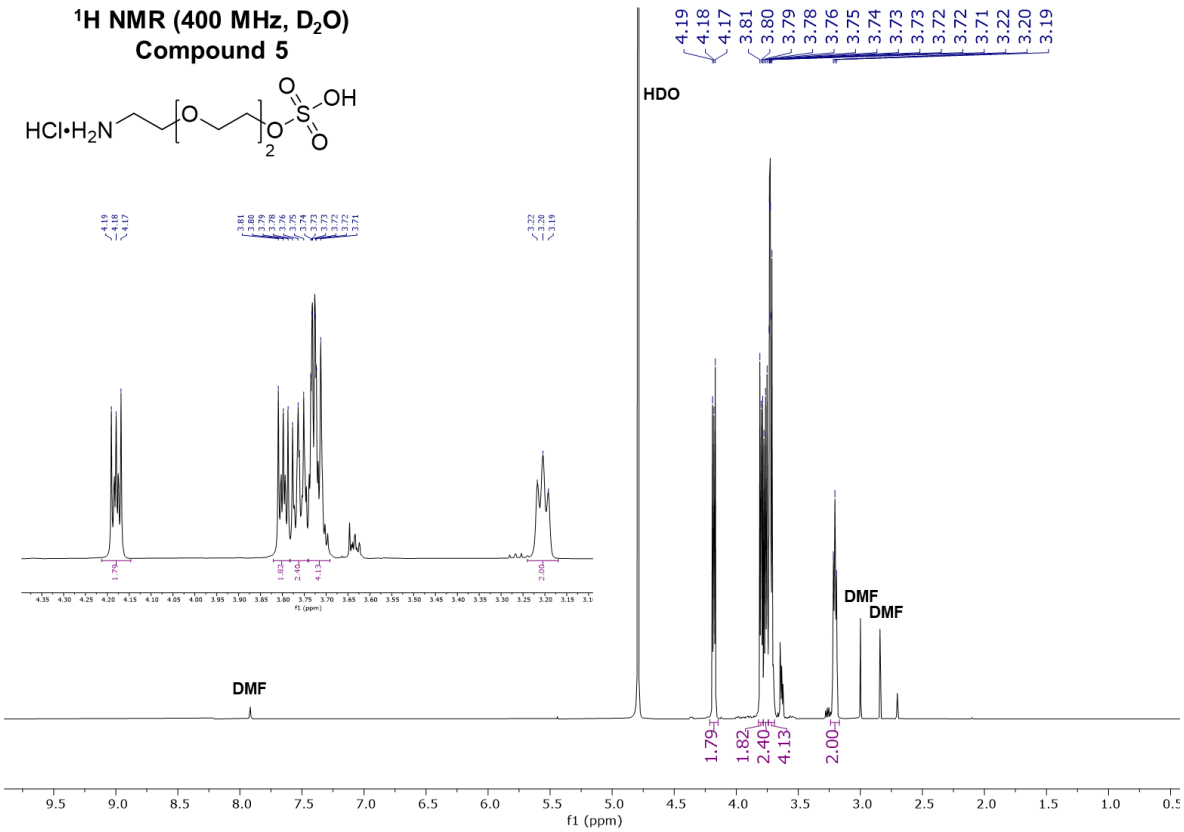

Supplementary Figure 29. ^{1}H NMR spectrum of Compound 4 in D_2O. Inset spectra is a magnification of the overall NMR from 3.1 ppm – 4.4 ppm.

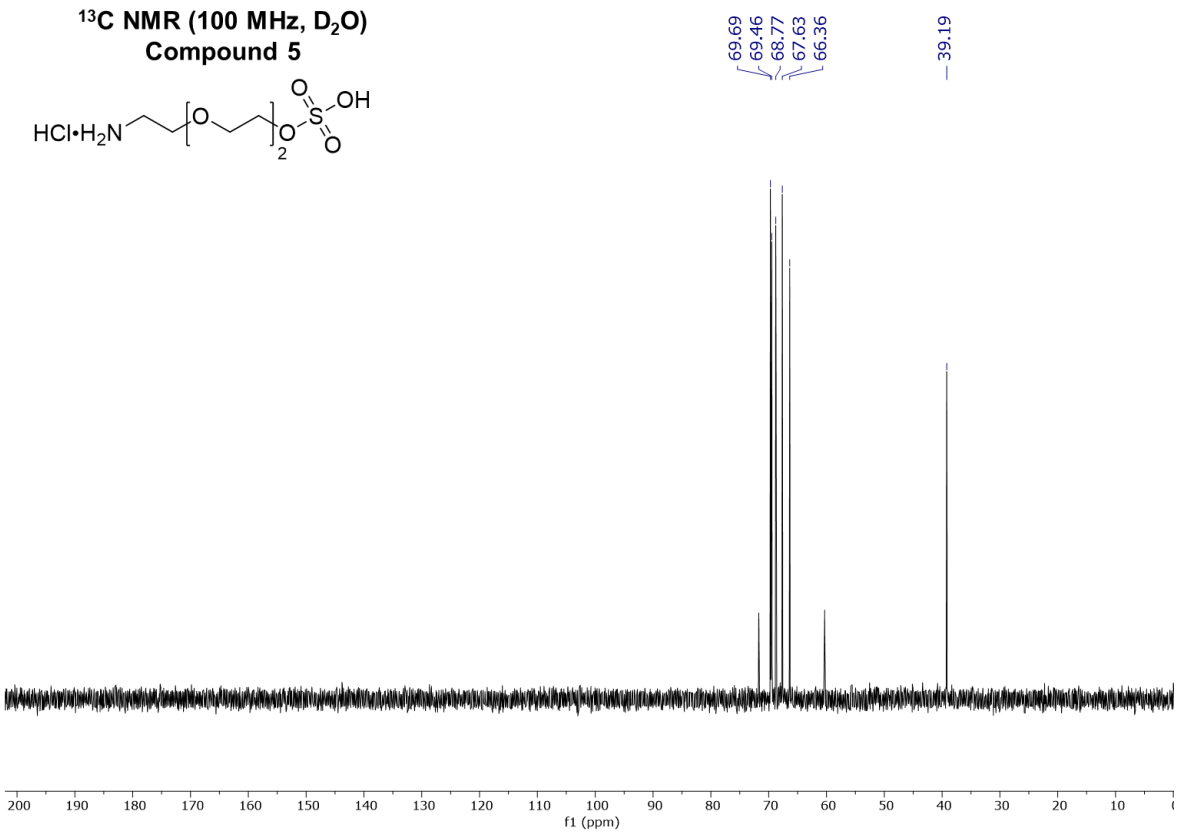

Supplementary Figure 30. ^{13}C NMR spectrum of Compound 4 in D_2O.

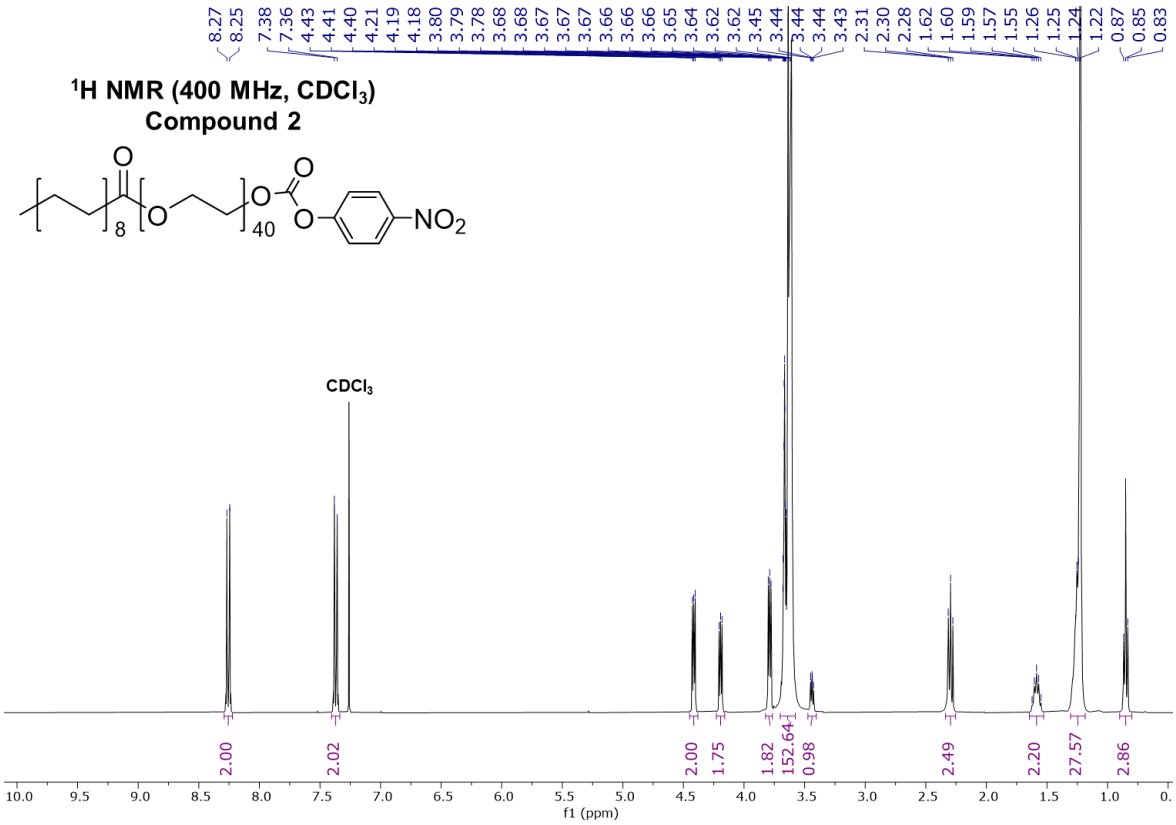

Supplementary Figure 31. ^{1}H NMR spectrum of Compound 2 in $CDCl_3$.

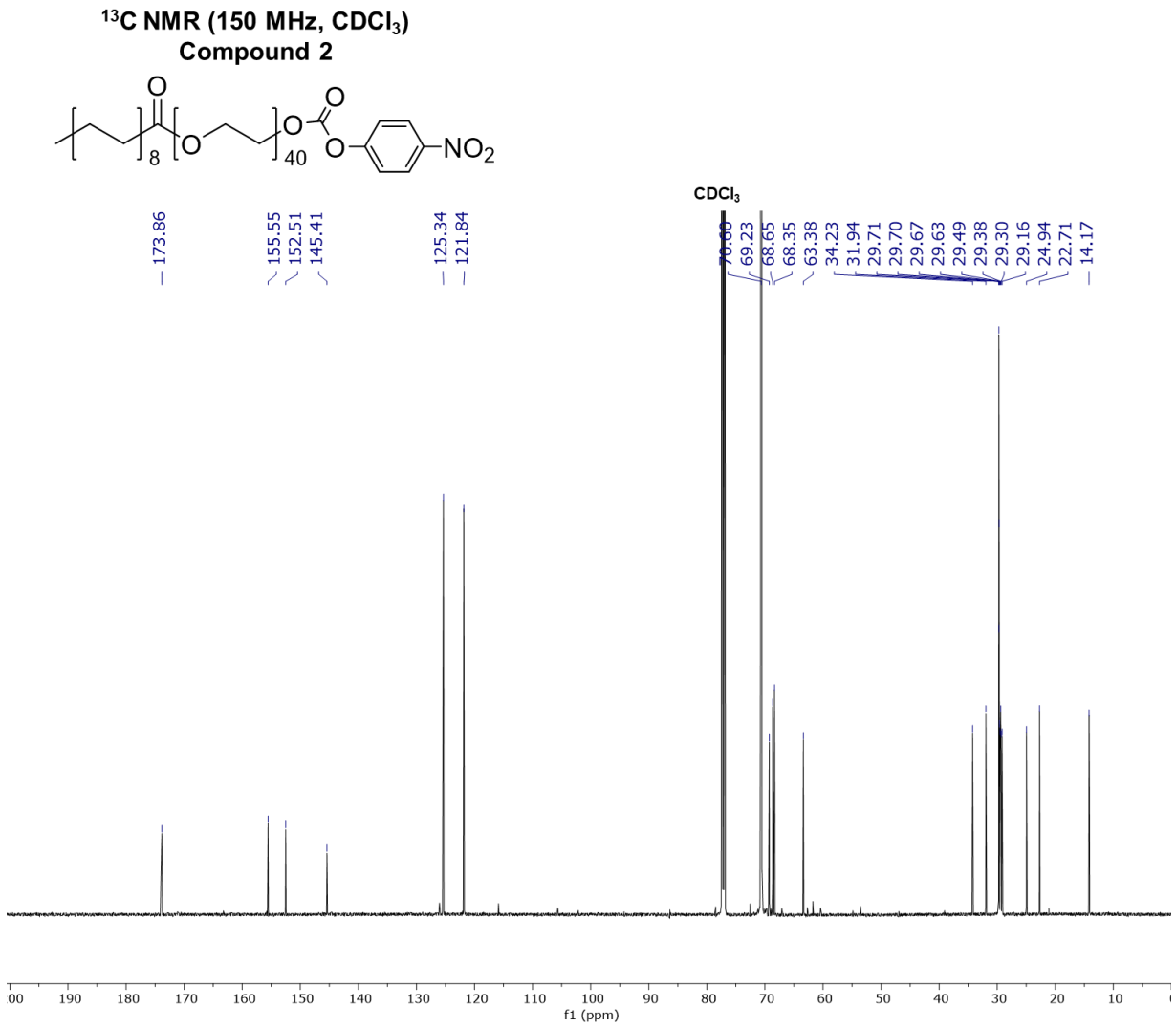

Supplementary Figure 32. ^{13}C NMR spectrum of Compound 2 in $CDCl_3$.

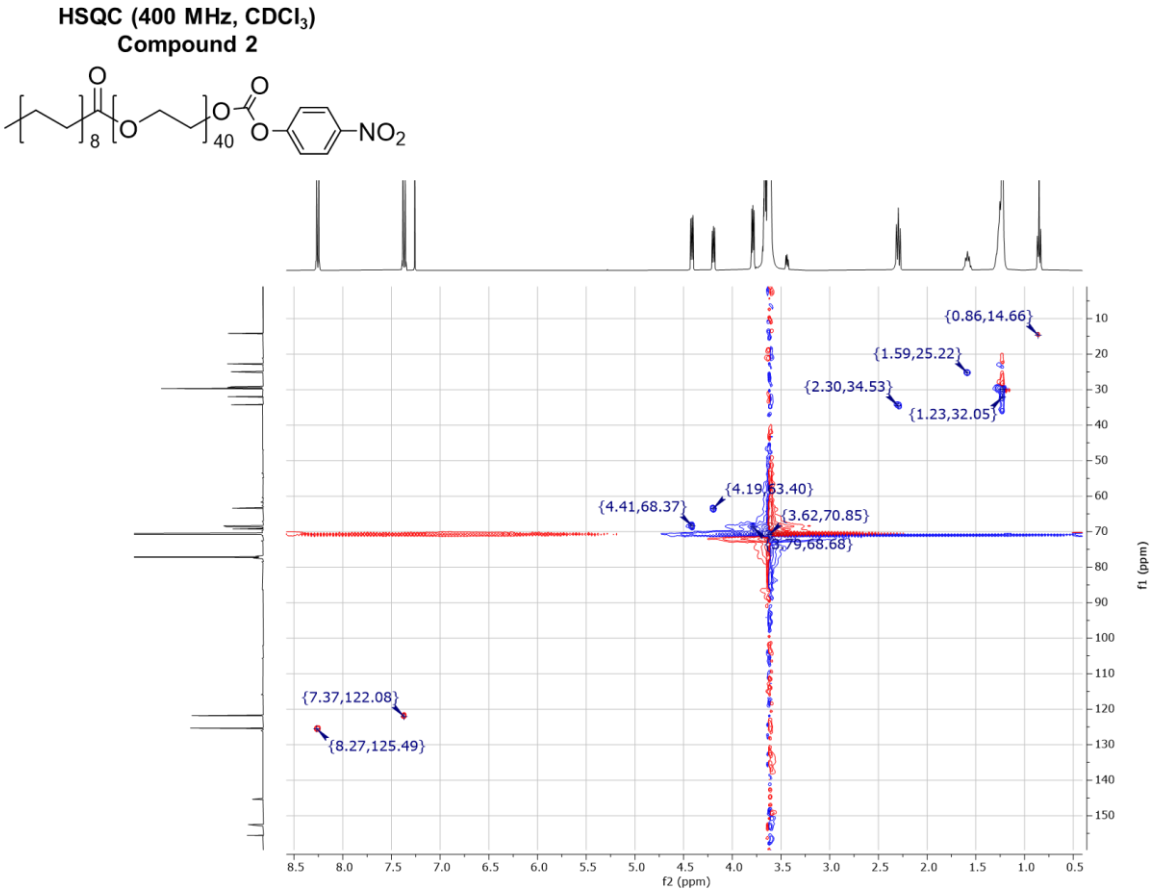

Supplementary Figure 33. HSQC spectrum of Compound 2 in $CDCl_3$. Red blots represent CH or CH_3, blue blots represent CH_2.

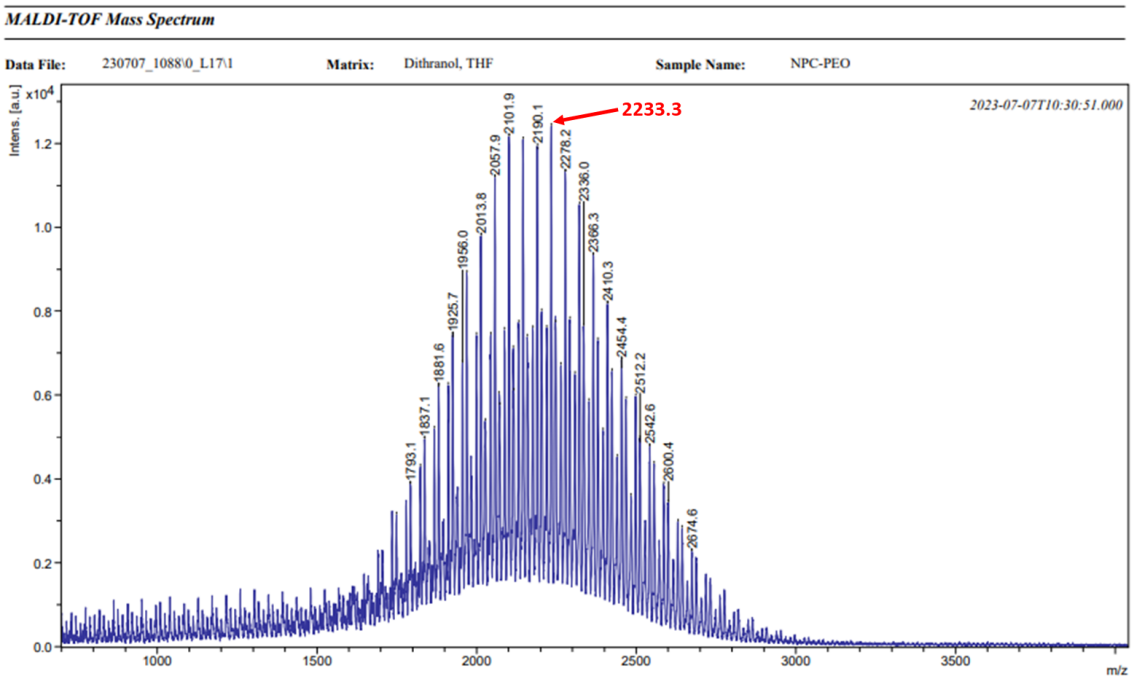

Supplementary Figure 34. MALDI spectrum of Compound 2. The most intense peak is for the M+Na of compound **2** with 40 PEG repeats. The peaks on either side all differ by a mass of ~44 g/mol, which is equivalent to 1 PEG unit. The smaller distribution is the M+H masses of the same compound.

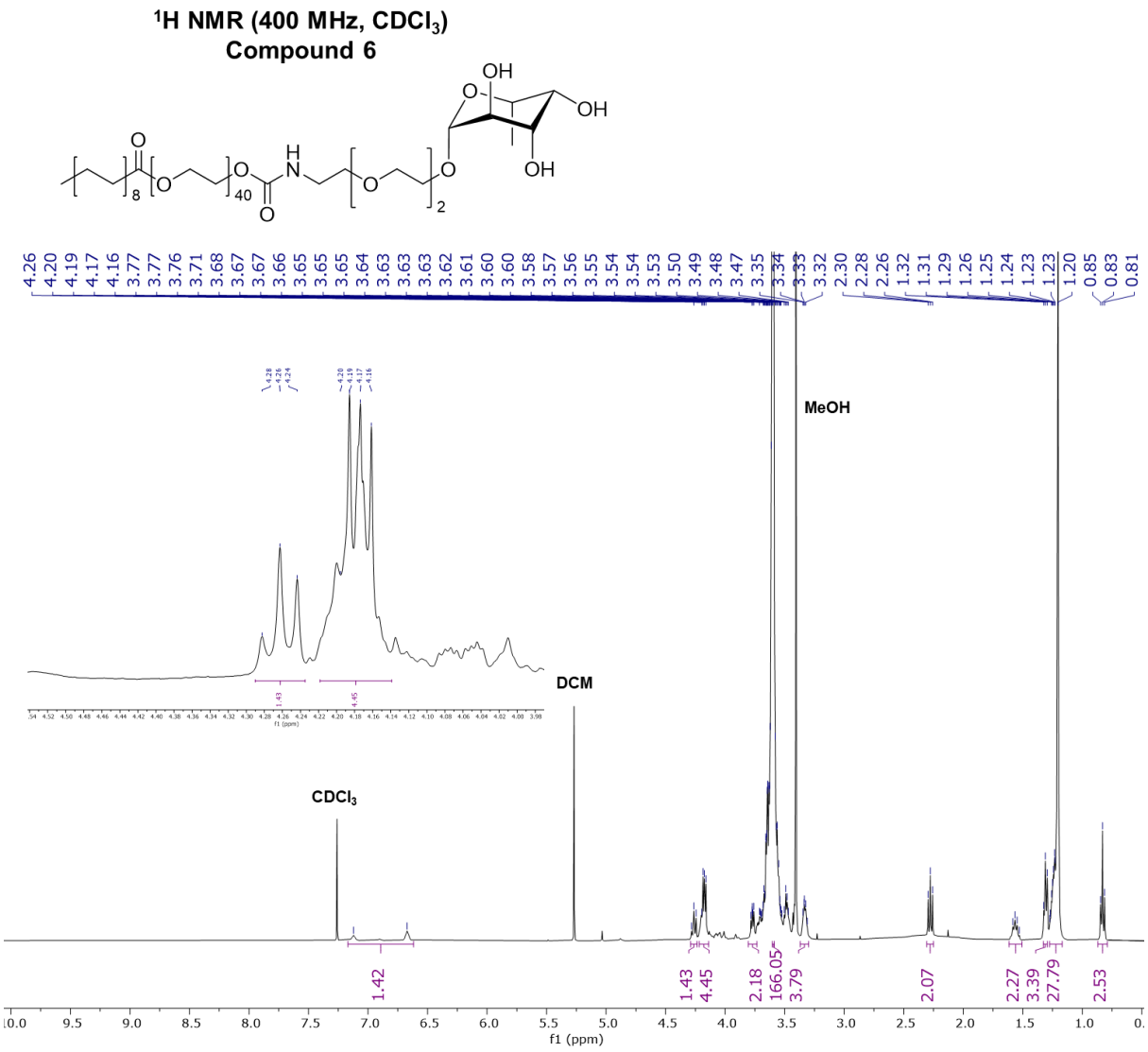

Supplementary Figure 35. ^{1}H NMR spectrum of Compound 6 in $CDCl_3$. Inset spectra is a magnification of the overall NMR from 3.96 ppm – 4.94 ppm, showing the triplet for the fucose anomeric proton (4.26 ppm, 1H) and the multiplet for the CH_2s on either side of the carbamate (4.17 ppm, 4H).

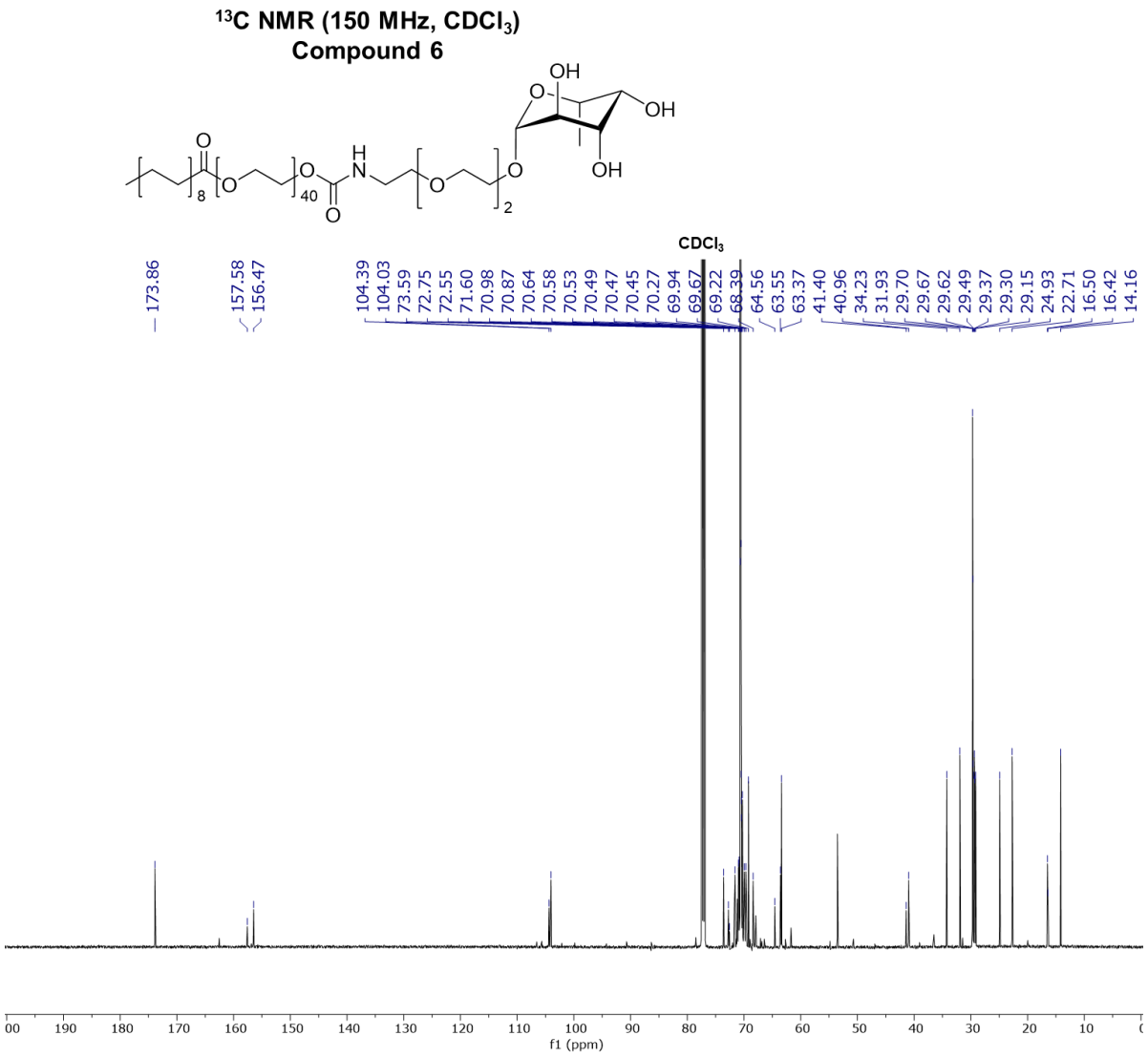

Supplementary Figure 36. ^{13}C NMR spectrum of Compound 6 in $CDCl_3$.

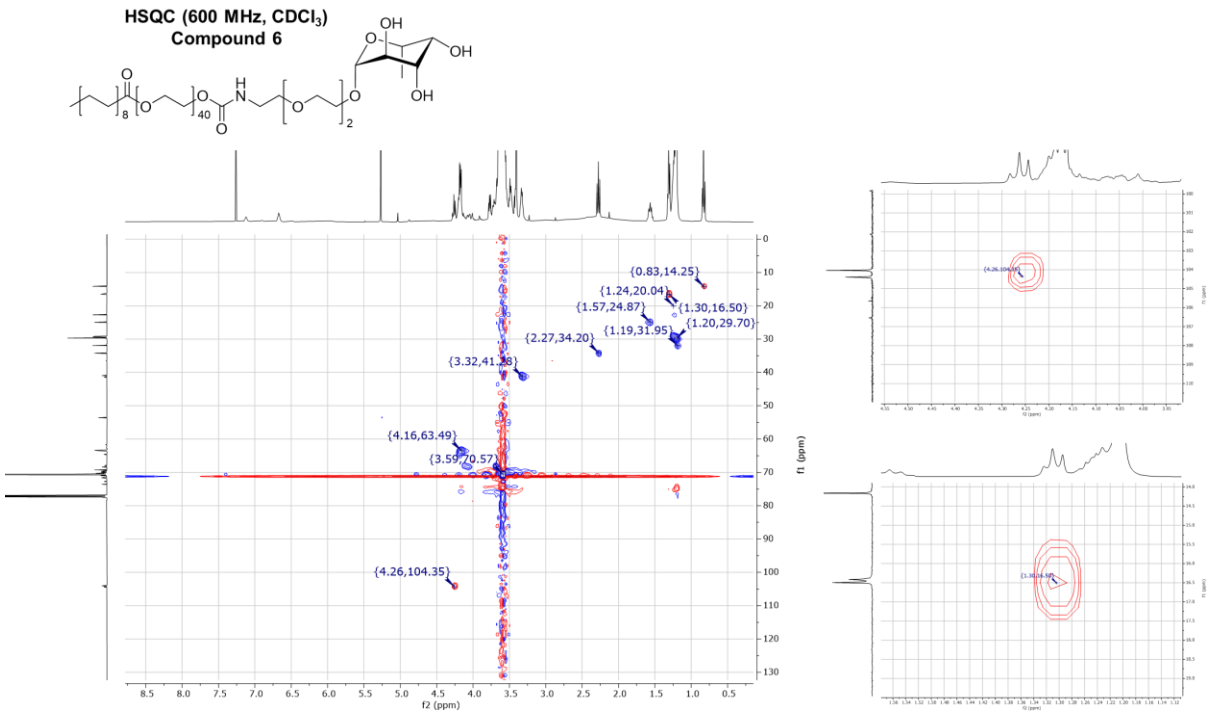

Supplementary Figure 37. HSQC spectrum of Compound 6 in $CDCl_3$. Left, overall HSQC spectrum. Top right; magnification of the correlation between the fucose anomeric proton and the fucose anomeric carbon. Bottom right; magnification of the correlation between the fucose CH_3 proton and the associated carbon. These two signals were used as hallmarks to confirm coupling between compound **2** and compound **3**. In all spectra, red blots represent CH or CH_3, and blue blots represent CH_2.

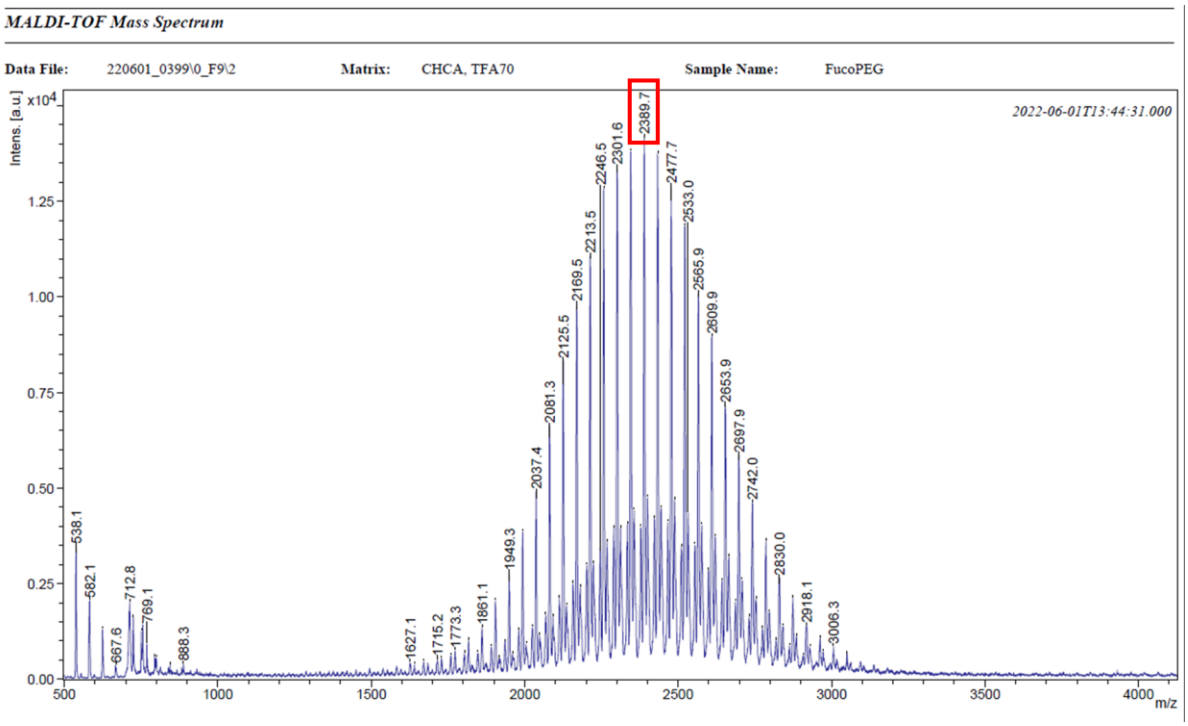

Supplementary Figure 38. MALDI spectrum of Compound 6. The most intense peak is for the M+Na of compound **6** with 40 PEG repeats. The peaks on either side all differ by a mass of ~44 g/mol, which is equivalent to 1 PEG unit. The smaller distribution is the M+H masses of the same compound.

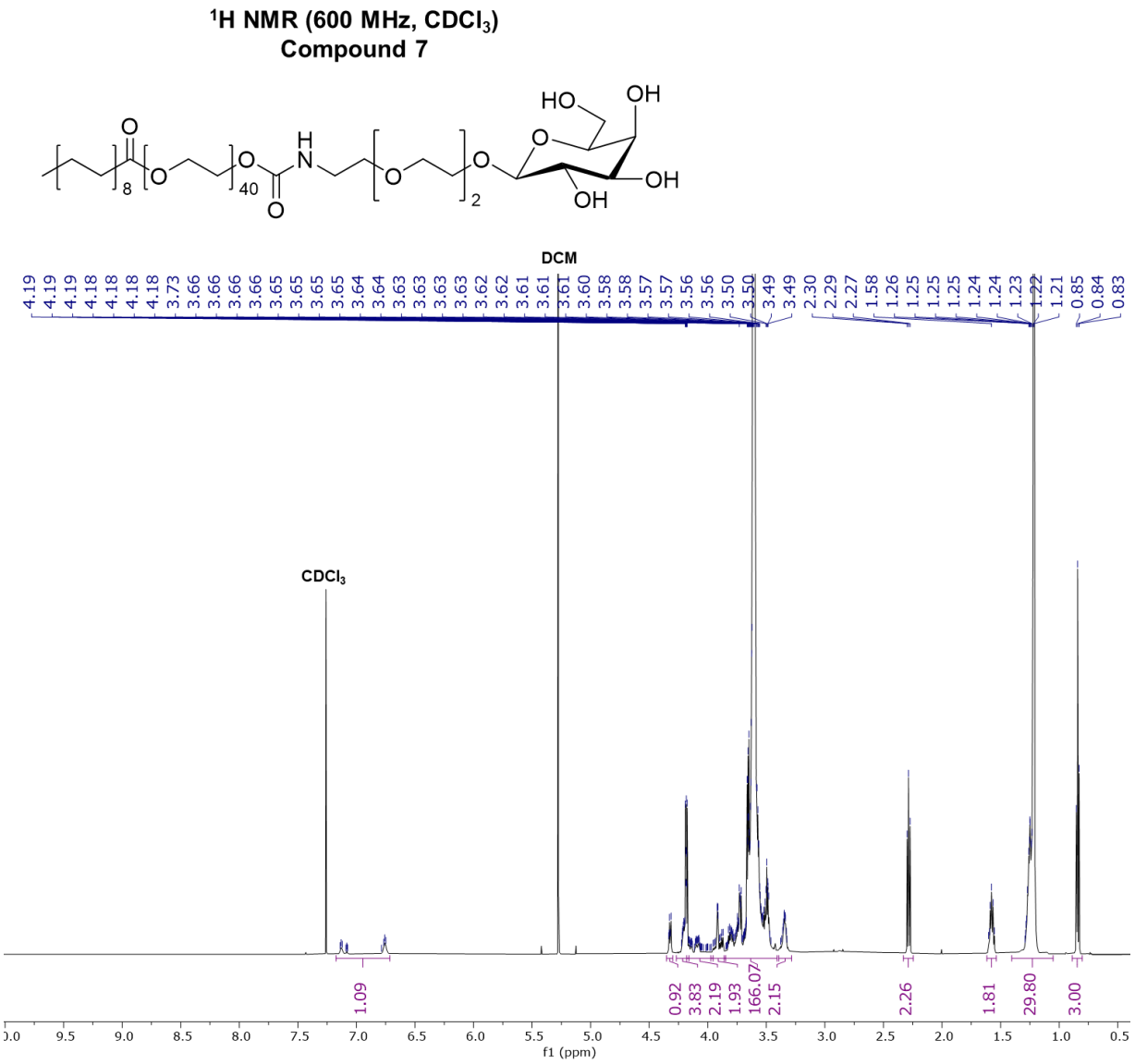

Supplementary Figure 39. ^{1}H NMR spectrum of Compound 7 in $CDCl_3$.

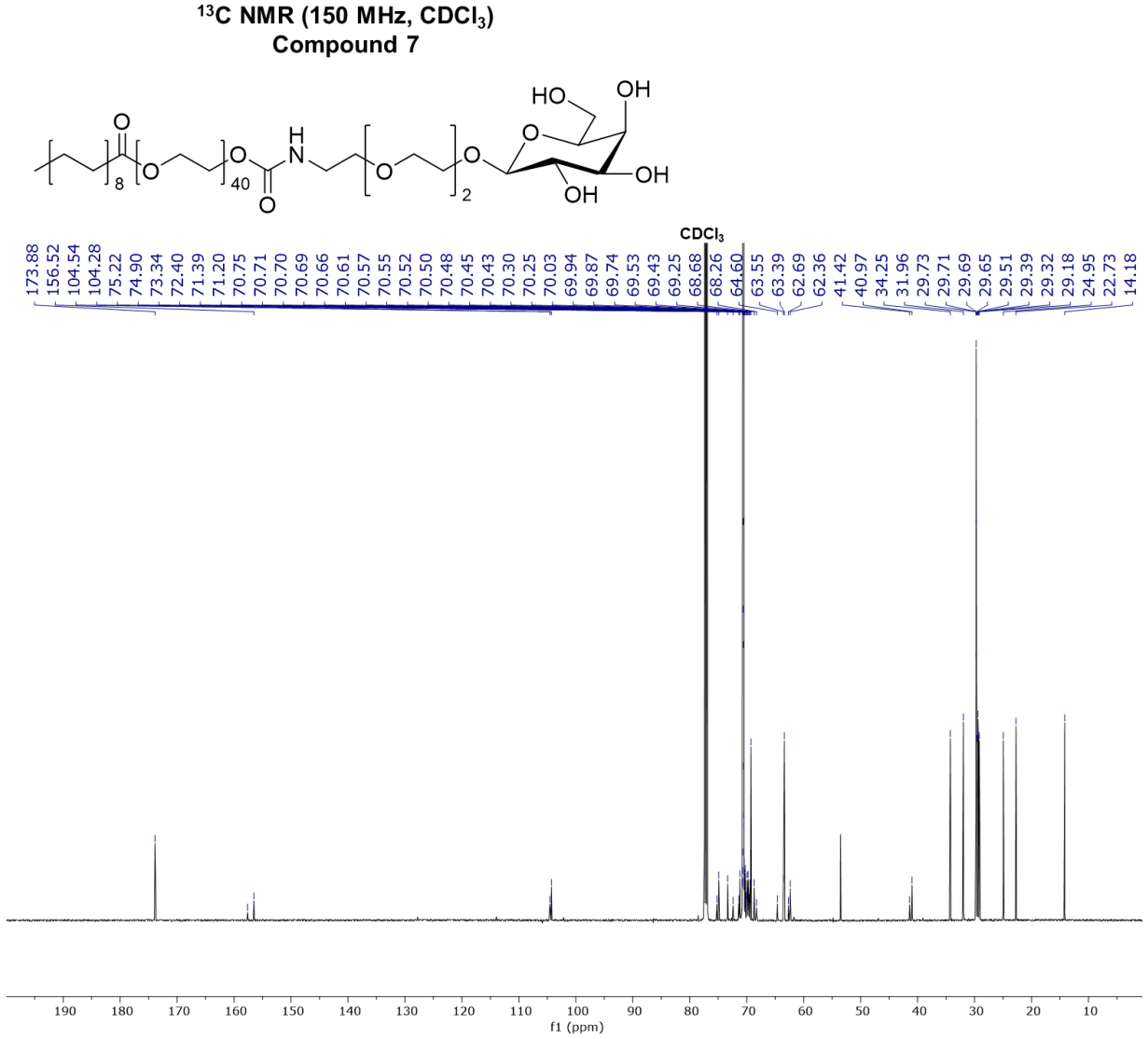

Supplementary Figure 40. ^{13}C NMR spectrum of Compound 7 in $CDCl_3$.

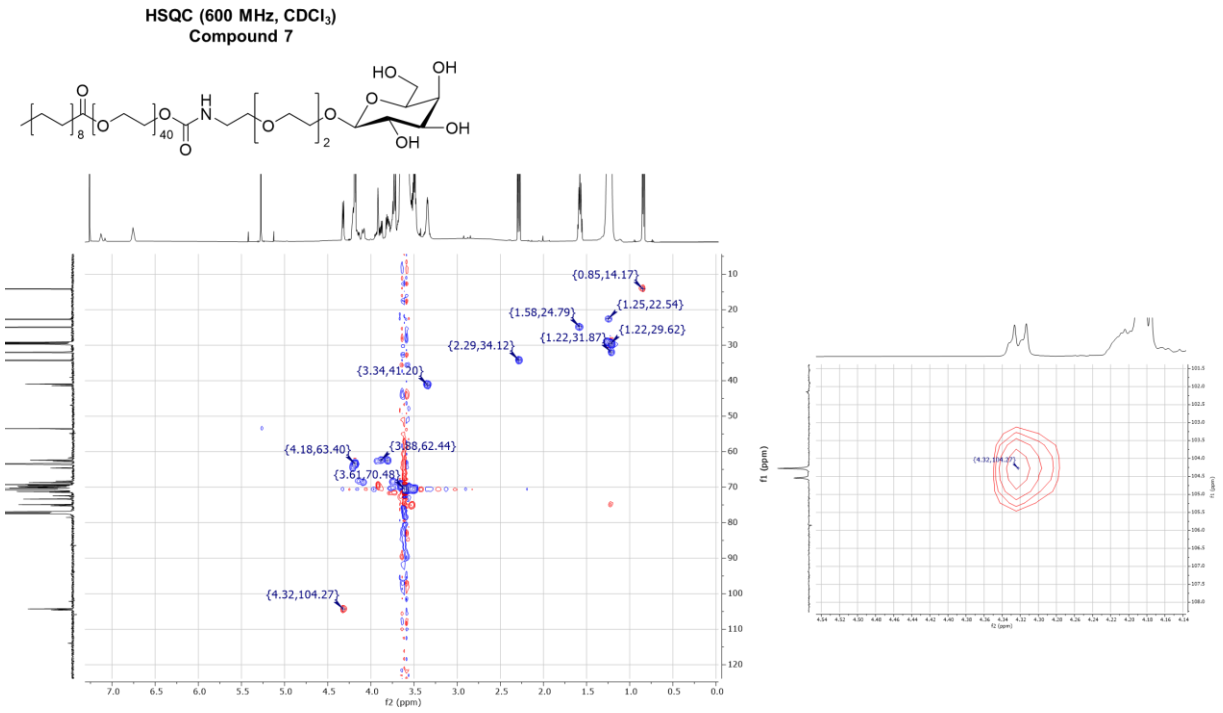

Supplementary Figure 41. HSQC spectrum of Compound 7 in $CDCl_3$. Left, overall HSQC spectrum. Right; magnification of the correlation between the galactose anomeric proton and the galactose anomeric carbon. This signal was used as a hallmark to confirm coupling between compound **2** and compound **4**. In all spectra, red blots represent CH or CH_3, and blue blots represent CH_2.

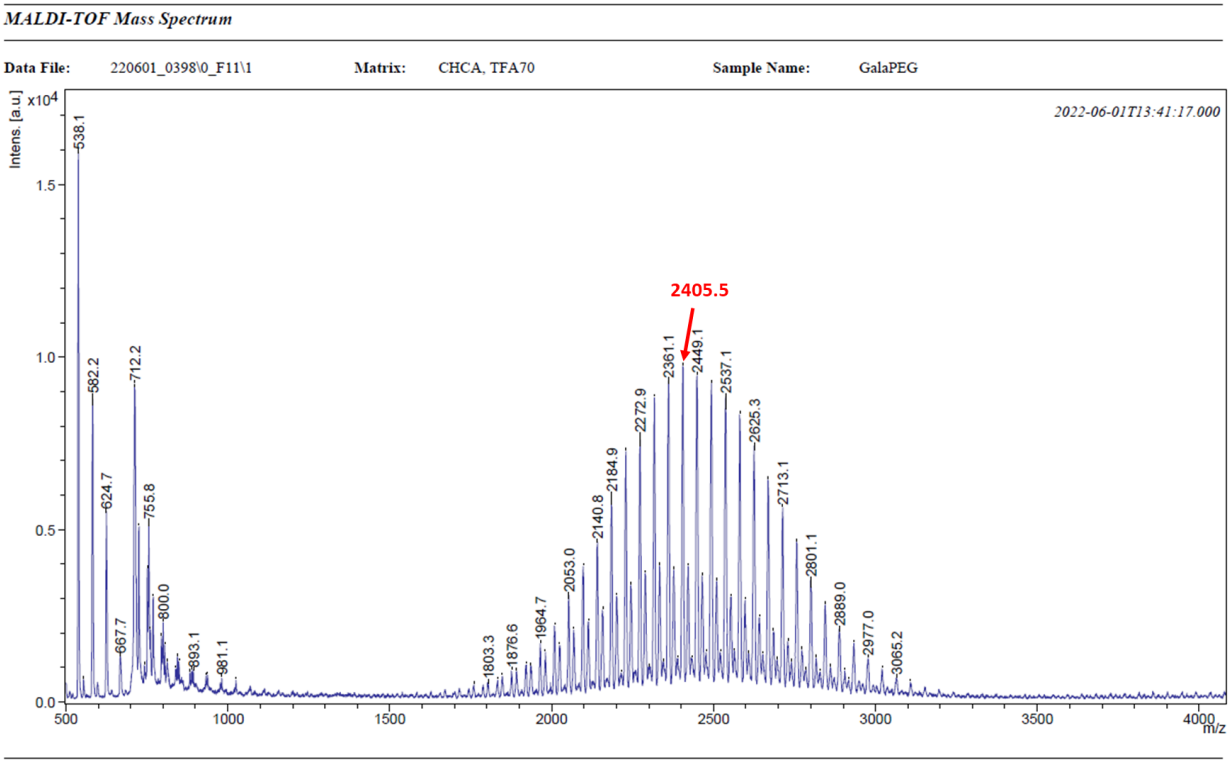

Supplementary Figure 42. MALDI spectrum of Compound 7. The most intense peak is for the M+Na of compound **7** with 40 PEG repeats. The peaks on either side all differ by a mass of ~44 g/mol, which is equivalent to 1 PEG unit. The smaller distribution is the M+H masses of the same compound.

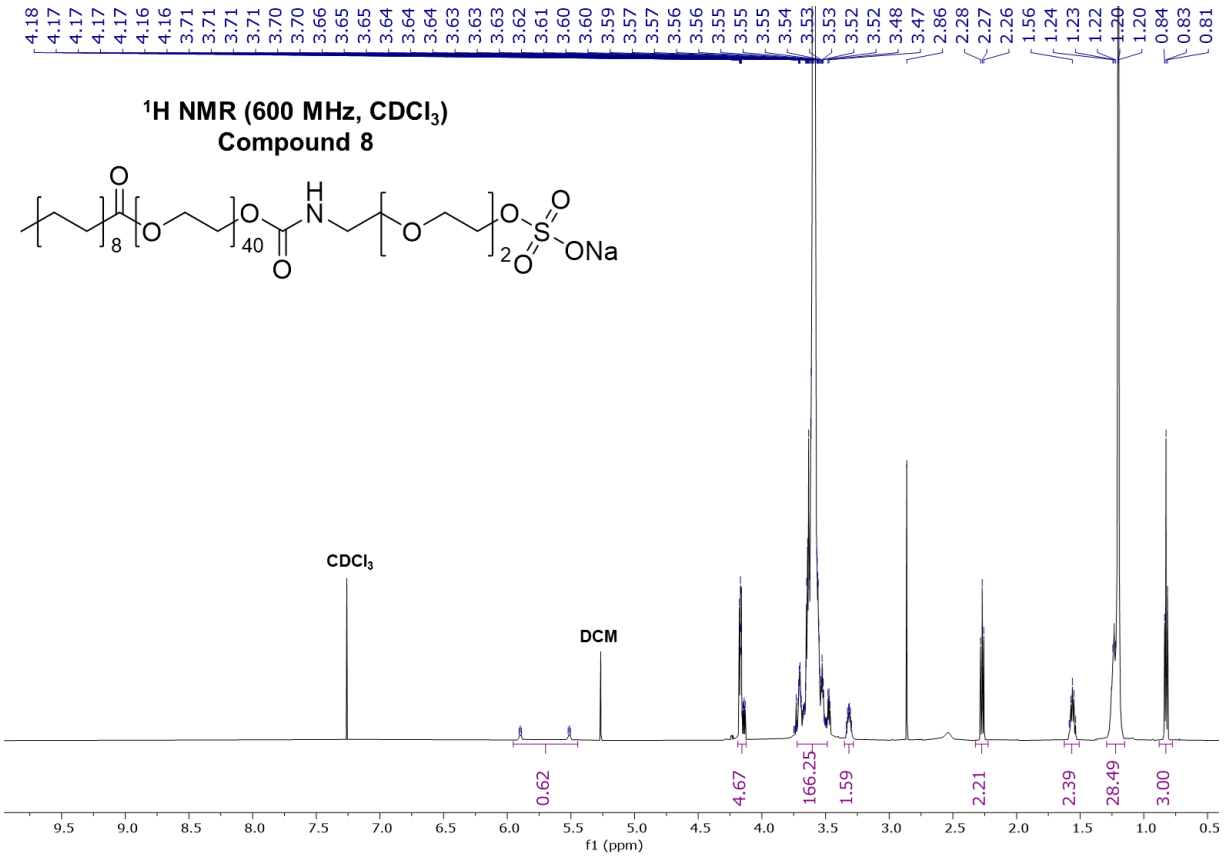

Supplementary Figure 43. ^{1}H NMR spectrum of Compound 8 in $CDCl_3$.

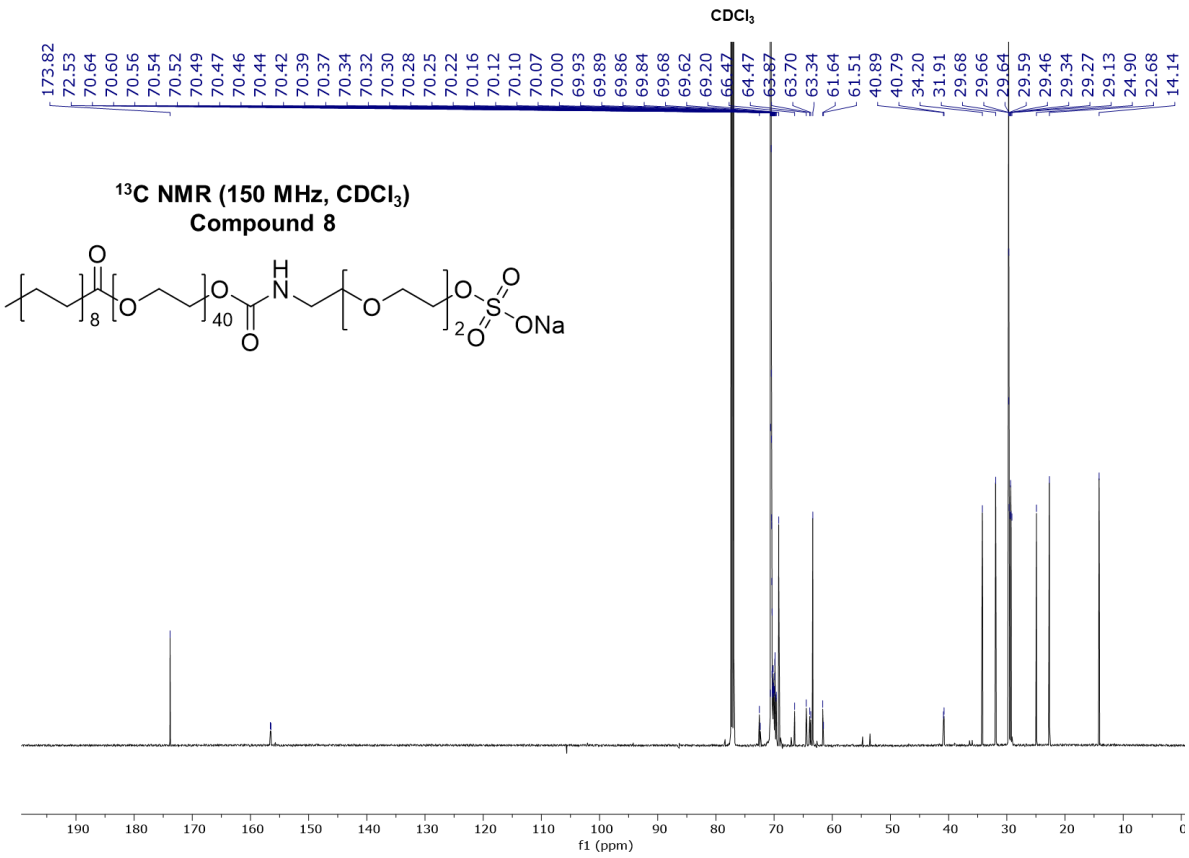

Supplementary Figure 44. ^{13}C NMR spectrum of Compound 8 in $CDCl_3$.

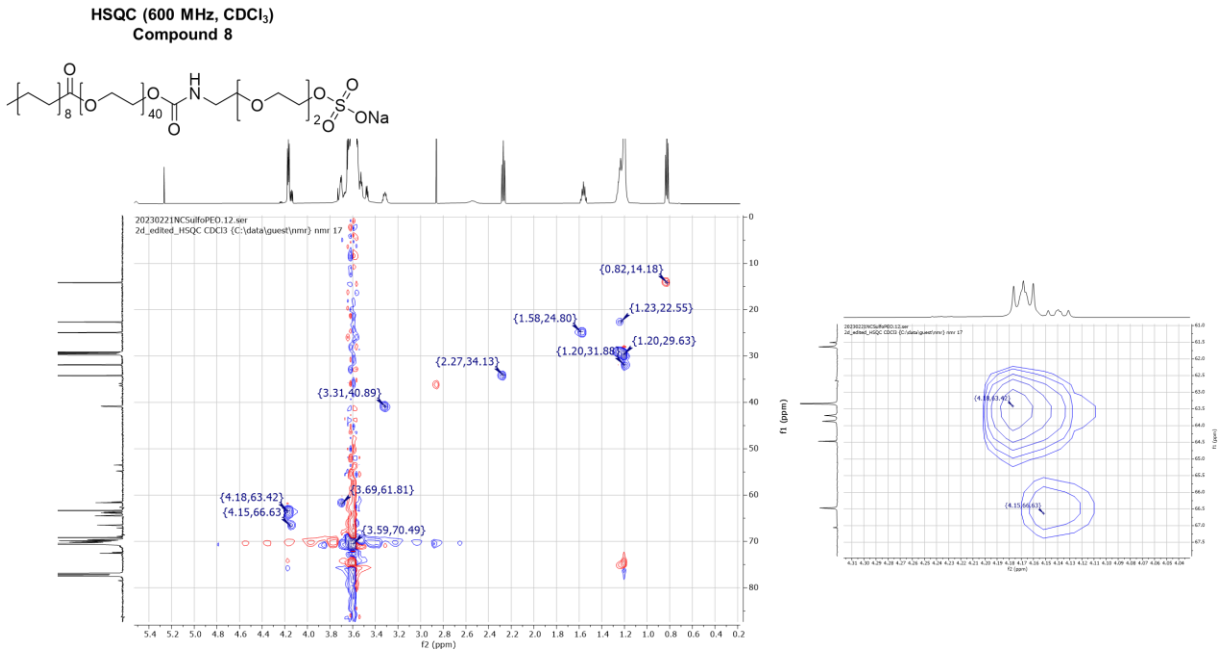

Supplementary Figure 45. HSQC spectrum of Compound 8 in $CDCl_3$. Left, overall HSQC spectrum. Right; magnification of the correlation between the CH_2s on either side of the carbamate, as well as next to the sulfonate, and correlated to the respective associated carbons. This signal was used as a hallmark to confirm coupling between compound **2** and compound **4**. In all spectra, red blots represent CH or CH_3, and blue blots represent CH_2.

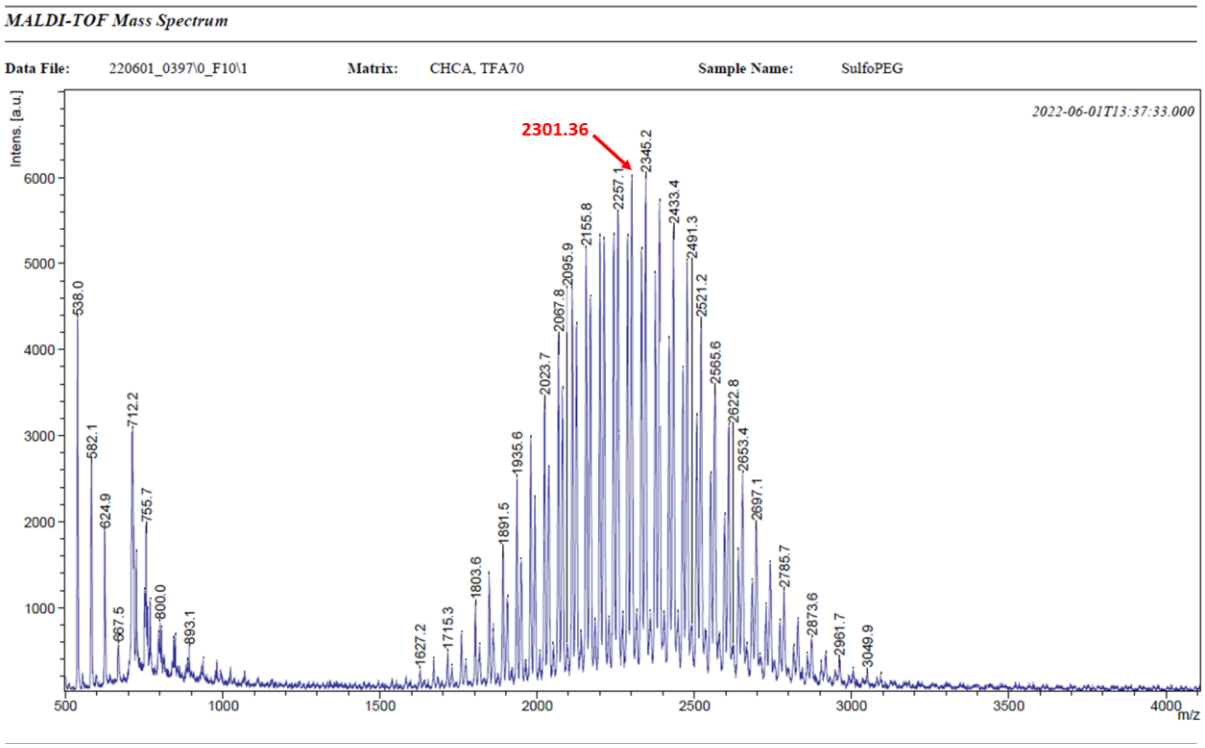

Supplementary Figure 46. MALDI spectrum of Compound 8. The most intense peak is for the M+H of compound **8** with 40 PEG repeats. The peaks on either side all differ by a mass of ~44 g/mol, which is equivalent to 1 PEG unit.

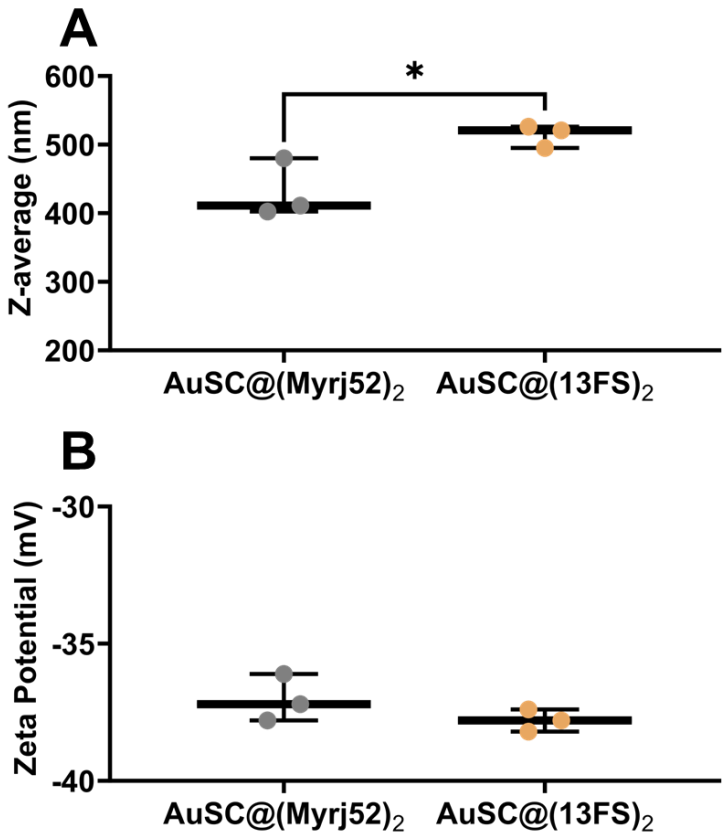

Supplementary Figure 47. DLS and zeta potential of AuSC@(Myrj52)$_2$ and AuSC@(13FS)$_2$. A) Z-average diameter of AuSC@(Myrj52)$_2$ and AuSC@(13FS)$_2$ as determined by DLS. B) Zeta potential values of AuSC@(Myrj52)$_2$ and AuSC@(13FS)$_2$ as determined by DLS. For all graphs, data are presented as boxplots of n = 3 technical replicate measurements. * $p<0.05$ by unpaired t-test.

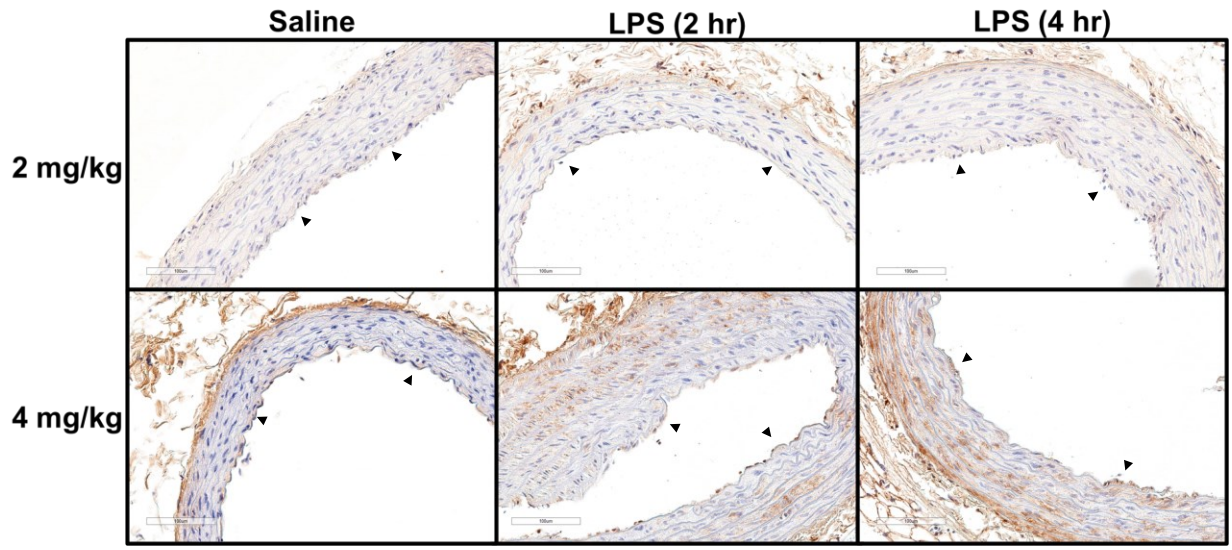

Supplementary Figure 48. Optimization of P-selectin stimulation in rat abdominal aorta after *intravenous* administration of lipopolysaccharide (LPS). Immunohistochemically labelled sections of rat abdominal aorta by anti-CD62p antibody. The variation of LPS induction time and concentration were used to determine the conditions that led to enhanced P-selectin expression. Arrowheads represent luminal aspect of the abdominal aorta.

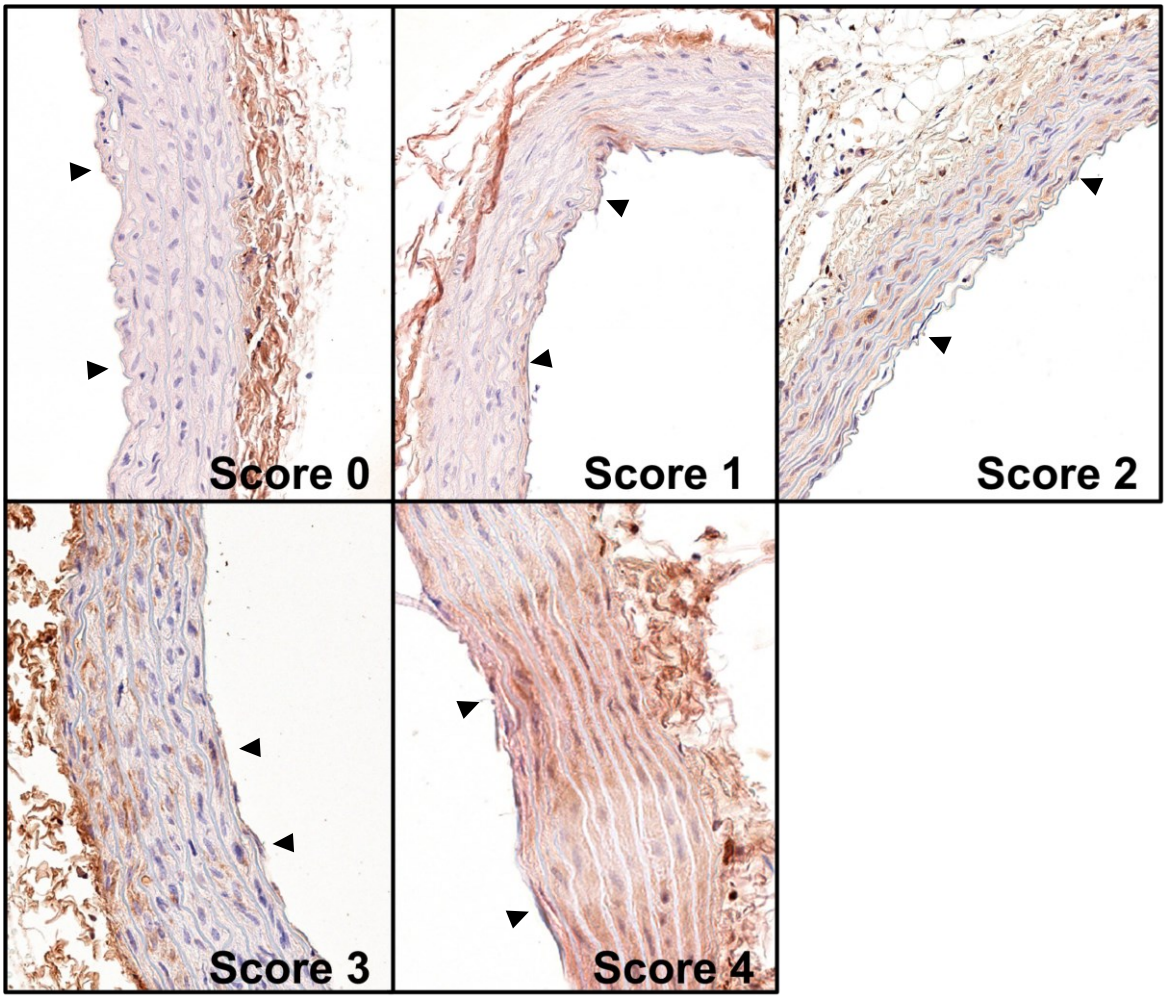

Supplementary Figure 49. Histological scoring examples for P-selectin staining of rat abdominal aorta following stimulation by lipopolysaccharide. Abdominal aorta of rats used in the AuSC@$(13FS)_2$ binding study were fixed and stained with anti-CD62p after imaging. A blinded participant was used to score the histology images with only a healthy and severely diseased image as reference. Representative images are shown for each score as selected by the scorer.

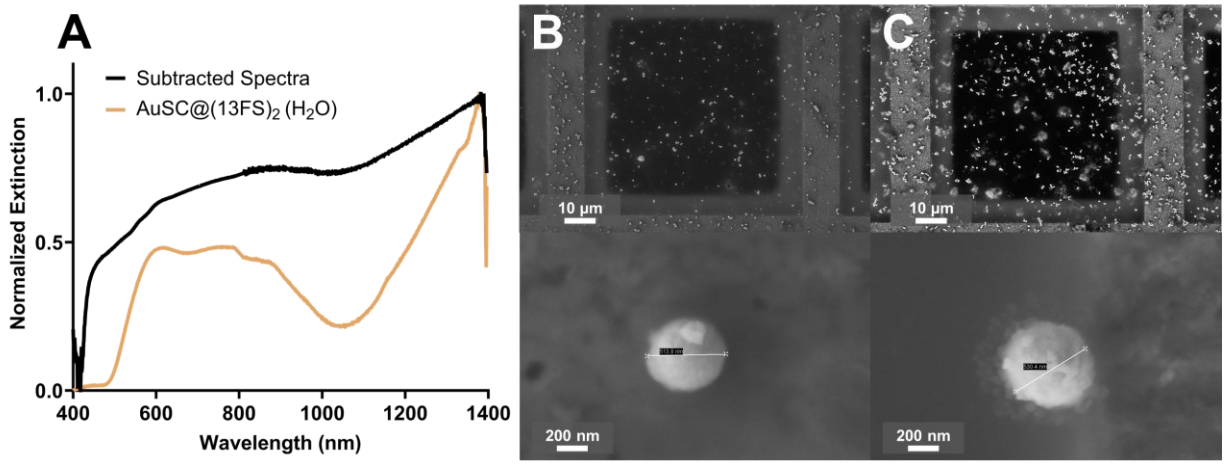

Supplementary Figure 50. Serum stability of AuSC@(13FS)$_2$. AuSC@(13FS)$_2$ was incubated in mouse serum overnight under cell culture conditions (37°C, 5% CO_2, humidified). A) Localized surface plasmon resonance spectra of clusters incubated in mouse serum after subtracting the mouse serum blank spectra (black line), and the pre-incubation clusters dispersed in water (gold line). Scanning electron microscopy (SEM) images of AuSC@(13FS)$_2$ dispersed in water before (B) and after (C) overnight incubation in mouse serum.

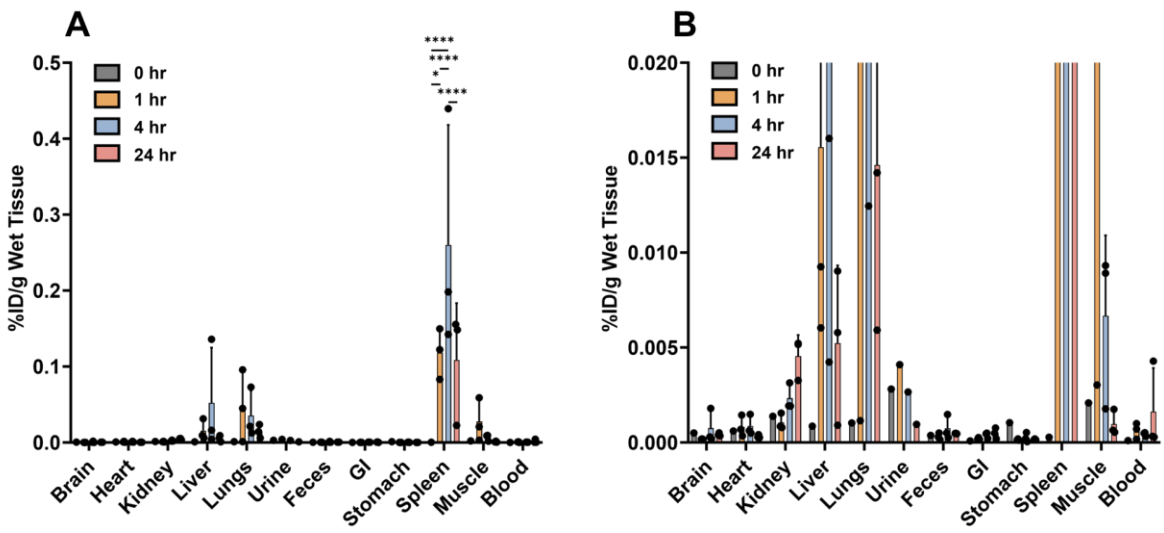

Supplementary Figure 51. Biological distribution of AuSC@(13FS)$_2$ at different timepoints following intravenous injection. Rats were injected with 2250 µg/mL Au AuSC@(13FS)$_2$ and sacrificed at the respective time points, except for 0 h which was injected with saline. Respective tissue was processed and Au concentration within the sample was determined by ICP-MS and normalized to the injected Au mass and wet tissue mass. The data in A) is presented on a lower magnitude axis in B) for clarity. Data are presented as means ± standard deviation for n = 1 (0 hr) or n = 3 rats (1, 4, and 24 hr). Urine samples are n = 1 of pooled samples from each rat due to limitations in fluid collection. Statistical analysis was done by mixed model two-way ANOVA followed by a Tukey post-hoc test. *p=0.0297 and ****p < 0.0001.

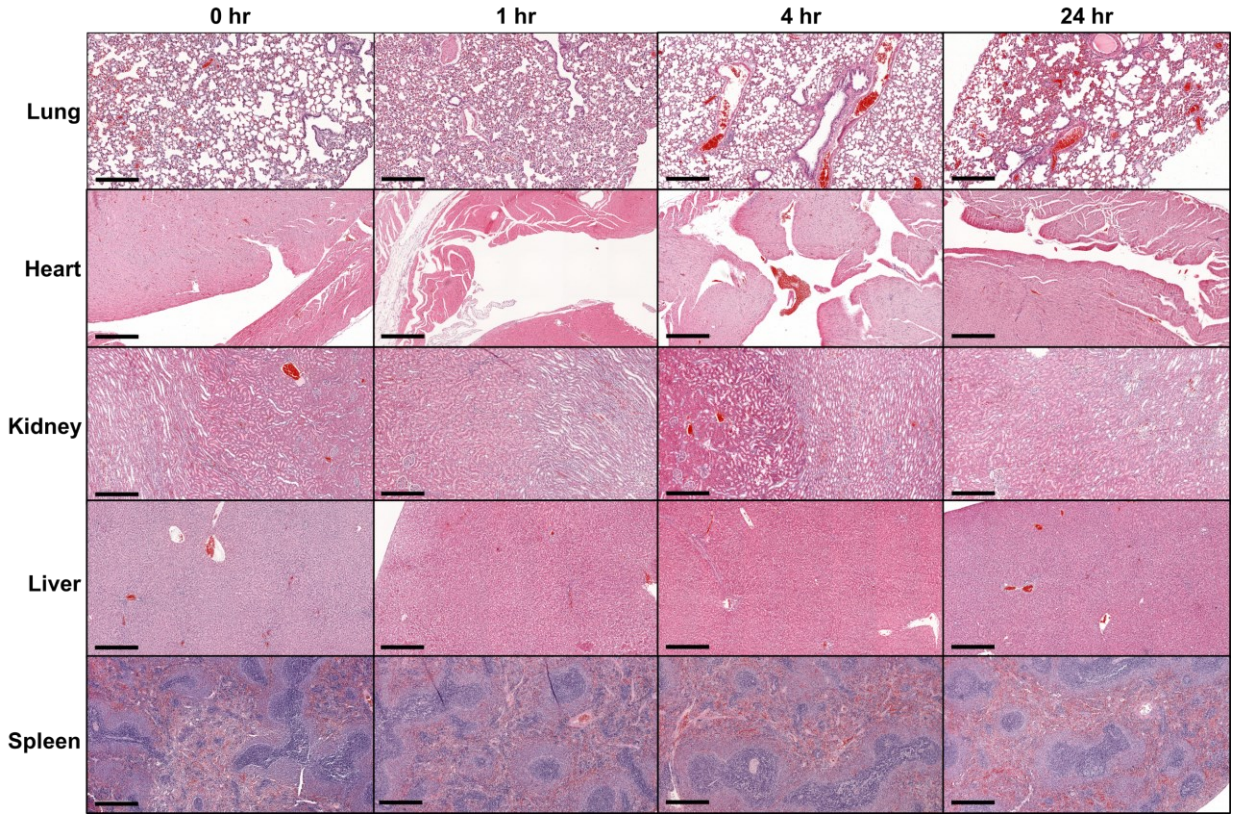

Supplementary Figure 52. Histological evaluation of tissues at different timepoints following intravenous injection of AuSC@(13FS)$_2$. Rats were injected with 2250 µg/mL Au AuSC@(13FS)$_2$ and sacrificed at the respective time points, except for 0 h which was injected with saline. At each timepoint, a portion of the tissue from one rat at random that was removed for ICP-MS analysis was bisected and fixed in 10% formalin. This tissue section was processed for histology and stained with hematoxylin and eosin. Only organs involved in clearance were evaluated.

Chapter 4: The Careful Selection of Zwitterionic Nanoparticle Coating Results in Rapid and Efficient Cell Labelling for Imaging-Based Cell Tracking.

Nicholas D. Calvert [‡ 1], Luciana Yu[‡ 1], Olivia C. Sehl [2], Julia J. Gevaert [2], Natasha N. Knier [2], Angelie Rivera-Rodriguez [4], Carlos M. Rinaldi-Ramos [3, 4], Paula J. Foster [2], Adam J. Shuhendler [* 1, 5, 6]

[1]Department of Chemistry and Biomolecular Sciences, University of Ottawa, 150 Louis Pasteur Pvt., Ottawa, Ontario, K1N 6N5, Canada

[2]Department of Medical Biophysics, Western University; Imaging Research Laboratories, Robarts Research Institute, London, ON N6A 5B7, Canada

[3]Department of Chemical Engineering, University of Florida, 1006 Center Dr. P.O. Box 116005, Gainesville Fl, 32611, United States of America

[4]J. Crayton Pruitt Family Department of Biomedical Engineering, University of Florida, 1275 Center Dr. JG56, P.O. Box 116131, Gainesville FL, 32611, United States of America

[5]Department of Biology, University of Ottawa, 150 Louis Pasteur Pvt., Ottawa, Ontario, K1N 6N5, Canada

[6]University of Ottawa Heart Institute, 40 Ruskin St., Ottawa, Ontario, K1Y 4W7, Canada

‡ Authors contributed equally to this work

*Corresponding Author: adam.shuhendler@uottawa.ca

4.1. Introduction to the Research Article Presented in this Chapter

The MPI SPION literature contains very few investigations into the effect of different surface chemistries on nanoparticle cell uptake. Using anionic PMAO-coated SPIONs with inherently strong MPI contrast-generating properties, we developed hard and soft zwitterionic ligands to functionalize SPIONs. We characterized the surface properties of the SPIONS, and then compared the degree of particle uptake between the zwitterionic and anionic SPIONs in three different cell types, as well as evaluated their trackability over time using MPI in an animal model. This work will further the MPI SPION literature in both guiding surface chemistry selection for different cell tracking purposes, as well as expanding the available effective surface ligands for SPION use. This work is currently under revision in Aggregate (Manuscript ID AGT-2024-0115).

4.2. Author Contributions

N.D.C. and M.S. performed all chemical syntheses, characterizations with assistance from L.Y. A.R.R. and C.M.R.R. performed all syntheses of Fe@PMAO provided to the study. N.D.C. and L.Y. performed all functionalized nanoparticle syntheses and characterizations. N.D.C. and L.Y. performed all cell labelling experiments for TEM and histological evaluations. O.C.S., J.J.G., N.N.K, and P.J.F. performed all cellular and animal MPI experiments. N.D.C performed all statistical analyses. N.D.C, A.J.S, and P.J.F. conceived of experiments with support from C.M.R.R. N.D.C. and A.J.S. co-wrote the paper, and all authors edited the work and provided input.

4.3. Abstract

The increased clinical application of cell-based therapies has resulted in a parallel increase in the need for non-invasive imaging-based approaches for cell tracking, often through labelling with nanoparticles. An ideal nanoparticle for such applications must be biologically compatible as well as readily internalized by cells to ensure adequate and stable cell loading. Surface coatings have been used to make nanoparticle trackers suitable for these purposes, but those currently employed tend to have cytotoxic effects. Zwitterionic ligands are known to be biocompatible and antifouling, however the head-to-head evaluation of specific zwitterionic ligands for cell loading has not yet been explored. Magnetic particle imaging (MPI) detects superparamagnetic iron oxide nanoparticles (SPIONs) using time varying magnetic fields. Because MPI can produce high contrast, real-time images with no tissue depth limitation, it is an ideal candidate for *in vivo* cell tracking. In this work, we have conjugated hard (permanently charged) and soft (pKa-dependently charged) biomimetic zwitterionic ligands to SPIONs and characterized how these ligands changed SPION physicochemical properties. We have evaluated cellular uptake and subcellular localization between zwitterions, how the improvement in cell uptake generated stronger MPI signal for smaller numbers of cells, and how these cells can be tracked in an animal model with greater sensitivity for longer periods of time. Our best-performing surface coating afforded high cell loading within 4 h, with full signal retention *in vivo* over 7 days.

4.4. Introduction

Cell therapies are garnering increasing attention in both research and clinical development due to their potential to treat currently untreatable diseases and complex injuries.[1,2] As of 2021, cell therapies comprised nearly 400 active clinical trials, but less than 10 FDA approved products.[3,4]

Cell therapy involves the administration of autologous or allogenic cells into a patient for a therapeutic purpose, the most common of which include immune cells for targeting cancer, as well as hematopoietic and mesenchymal stem cells for regenerative purposes.[5–7] Following their administration into a patient, these cells are expected to travel to their specific therapeutic destination (tumors and lymph nodes for immune cells, areas of injury for stem cells) to deliver their medicinal payload.[8,9] Survival and oftentimes proliferation of these cells are paramount for eliciting and maintaining their therapeutic action.[10]

In consideration of the *in vivo* environment these highly concentrated cells will face during their journey from injection to their therapeutic site, it is unsurprising that several factors will contribute to an insignificant therapeutic effect. This includes major challenges such as large-scale cell death following administration (sometimes greater than 95%),[11] cells failing to reach their therapeutic destination,[12] and failure to proliferate.[13] These challenges introduce significant uncertainty in cell status and location and limit the therapeutic potential, necessitating a need for better cell tracking for monitoring cell therapies.

Cell tracking plays a crucial role in enabling clinicians to monitor the localization and proliferation of cell-based therapies, maximizing their effective therapeutic potential.[14] The cell tracking process is always initiated by the labelling of the therapeutic cells, either *in situ* or more commonly *ex vivo*.[15–18] These labelled cells can then be imaged and monitored using traditional medical imaging modalities, with the potential for determining both location and status of the administered cells. There are several different imaging techniques that have been used for cell tracking, including positron emission tomography[19] and optical imaging,[20] but one of the most frequently used modalities is magnetic resonance imaging (MRI).[21] MRI cell tracking relies on labelling cells with paramagnetic species, most commonly metal chelates (Gd or Mn)[22–24] or Fe-

based nanoparticles (NPs).[25] Fe-based NP solutions, more specifically superparamagnetic iron oxide NPs (SPIONs) have been the more widely used labelling strategy for cell tracking by MRI,[21] mostly due to intracellular cytotoxicity concerns associated with Gd^{3+} in comparison to Fe^{2+}.[26] Unlike Gd which provides contrast by image brightening, SPIONs produce an image darkening effect (i.e. negative contrast) in MRI,[27] which is non-specific and cannot be directly quantified. Magnetic nanoparticle imaging (MPI) was first developed in the early 2000s as a tracer-based, tomographic technique that allows for specific tracking and quantification of SPIONs.[28] MPI relies on a gradient magnetic field that saturates SPIONs and then sweeps a magnetic field-free region over the image acquisition area to detect excited SPIONs and produce a hotspot image.[29] In comparison to MRI, the MPI signal is much more specific as it only detects SPIONs and has little to no background signal due to lack of endogenous superparamagnetic iron, has high spatial resolution of around 1 mm,[30] and is nearly 10^8 times more sensitive to SPIONs than MRI is to protons.[31] All these properties associated with a tracer-based modality makes MPI an extremely attractive imaging modality for cell tracking and has been where the majority of MPI clinical application research has been focused.[32]

A significant amount of research and development efforts surrounding SPIONs as MPI tracers have been focused on improving SPION magnetization intensity to increase the limit of tracer detection.[33–35] Most of these SPIONs utilize an anionic surface coating, commonly citric acid or carboxydextran, to facilitate SPION cellular uptake and improve nanoparticle aqueous solubility.[36–38] The nature of SPION coating and its role in cellular uptake has been largely understudied. The negative charges help attract SPIONs to positively charged components of the extracellular membrane, but the high hydrophilicity of these strong anions precludes meaningful interaction with most of the cell surface and reduces intracellular uptake.[39] Some neutral

(polyethylene glycol) and cationic (trialkylammonium-based) surface coatings have been evaluated, but these readily form large protein coronas in blood and serum, masking SPIONs from cellular interaction.[40,41] Many cationic coatings are often cytotoxic.[42]

Zwitterionic molecules are charged species with a net neutral charge, and comprise many of the biomolecules endogenous to cells, such as amino acids, proteins, and lipids.[43] Zwitterionic molecules also possess excellent antifouling properties[44] and given their biomimetic electronic state, have been shown to facilitate high intracellular nanoparticle uptake while remaining highly cytocompatible.[45] These properties make zwitterionic molecules an excellent potential surface coating for SPIONs to achieve high levels of non-cytotoxic cell loading leading to greater signal per cell. There have been some reports of zwitterionic SPIONs for MRI based cell tracking,[46,47] but we are aware of none that have systematically evaluated different zwitterionic classes, and none for optimizing *ex vivo* cellular loading with SPION for MPI. In this work, we have functionalized previously described SPIONs possessing excellent MPI magnetic properties[48] and modified them to bear a polymeric (polymaleic anhydride, PMAO) surface coating that was functionalized with “hard” and “soft” zwitterions with permanent or pKa-derived charge-states, respectively. Zwitterion functionalization of originally anionic PMAO-coated SPIONs did not disrupt the measured physicochemical properties or affect their MPI signal generating capacity but did improve stability in cell culture media. Finally, we have shown that the zwitterion-coated SPIONs had much higher levels of intracellular uptake than the anionic PMAO-coated SPIONs in several cell types, including human mesenchymal stem cells (MSCs). The higher degree of uptake observed with zwitterionic SPIONs led to greater MPI signal for longer periods of time than the PMAO-coated nanoparticles when labelled MSCs were injected in mice for *in vivo*

tracking by MPI. These zwitterionic SPIONs may be a key contributor to unlocking the potential for effective cell tracking by MPI.

4.5. Results and Discussion

4.5.1. Synthesis and Dry Characterization of Hard and Soft Zwitterionic SPIONs

The single-core SPIONs were synthesized following the procedure outlined in S. Liu *et al.*[49] The SPION core exhibits an MPI signal that is ~3-times better than commercially available ferucarbotran (Resovist) and is stabilized by a coating of poly(maleic anhydride-alt-1-octadecene, PMAO). In addition to the strong MPI signal generated by the nanoparticle core, the PMAO coating on these nanoparticles readily hydrolyzes in water to polymaleic acid. The presentation of surface carboxylic acids serves as a chemical handle for facile zwitterionic functionalization.[50]

Two biomimetic molecules of the cellular membrane outer leaflet, sulfobetaine (SB) and pyridinium sulfobetaine (PSB), were synthesized and characterized (Supplementary Scheme 1 & Supplementary Fig. 1-9) as our chosen “hard” zwitterions. SB and PSB possessed a permanent positive charge on their nitrogen (dimethylammonium nitrogen for SB and pyridinium nitrogen for PSB), and an effectively permanent negative charge in biological environments on the terminal sulfonate group, due to the negative pKa. Both molecules have been previously reported showing excellent biocompatibility and improvement in cellular uptake when functionalized on nanoparticle surfaces.[51–55] Functionalization of Fe@PMAO was achieved using standard coupling chemistry. The carboxylic acids on the SPION were activated with1-ethyl-3-(3-dimethylaminopropyl)carbodiimide (EDC) to drive amide bond formation to link SB or PSB to Fe@PMAO, resulting in the hard zwitterion functionalized Fe@SB and Fe@PSB SPIONs (Fig. 1A, top scheme). Endogenous natural and semi-natural amino acids L-cysteine and DL-

homocysteine were chosen as the soft zwitterionic molecules. Both cysteine (Cys) and homocysteine (HCys) can enter cells as substrates of the transporter ASCT2 and can also diffuse through SLC transporters.[56,57] The amino acid backbone of these molecules is zwitterionic between the pH ranges of ~3 – ~10. EDC coupling was used to install a maleimide group on Fe@PMAO, followed by a change in buffer and addition of either Cys or HCys (Fig. 1A, bottom scheme). Maleimide allowed the selective use of the thiol as the nucleophilic coupling partner at a controlled pH, preserving the amino acid backbone of both molecules and resulting in the soft zwitterion functionalized Fe@Cys and Fe@HCys SPIONs.

Nanoparticle morphology before and after functionalization was evaluated by transmission electron microscopy (TEM) to detect any morphological changes to the nanoparticle core as a result of chemical functionalization (Fig. 1B). Both hard and soft zwitterion-functionalized nanoparticle morphology appeared unchanged in comparison to Fe@PMAO.

Surface functionalization with zwitterions was evaluated by Fourier-transformed infrared spectroscopy (FTIR). Fe@SB and Fe@PSB (Fig. 1C, left panel) showed characteristic FTIR signals that were not observed for Fe@PMAO: S=O stretch from 1030 – 1070 cm^{-1}, sulfonic acid stretch from 1120 – 1230 cm^{-1}, a decrease in the intensity of the COO^- stretch ~1600 cm^{-1}, and a formation of a conjugated anhydride peak at 1770 cm^{-1}. All signals were in agreement for similar sulfobetaine molecules.[58] The formation of the anhydride peak was of particular interest, and was the result of an iminolization-cyclization reaction following the first amide bond formation between the polymaleic acid and SB or PSB.[59–61] The formed imide is known to be more hydrolysis-resistant than the amide counterpart, and will therefore improve the hydrolytic resistance of these functionalized nanoparticles. FTIR analysis of Fe@Cys and Fe@HCys (Fig.

1C, right panel) proved more challenging given the lack of new and distinct functional groups following functionalization in comparison to those already present in Fe@PMAO. No change in the COO^- stretch ~1600 cm^{-1} was observed, but an increase in the C=O stretch at 1700 cm^{-1} was observed. This stretch is associated with new carboxylic acid groups formed by the reaction between the maleimide and thiol of Cys or HCys, the new carbonyls on the hydrolyzed maleimide, formed polymaleimide, and on Cys or HCys. The appearance of the conjugated anhydride peak attributed to polymaleimide formation was again observed at 1770 cm^{-1}.

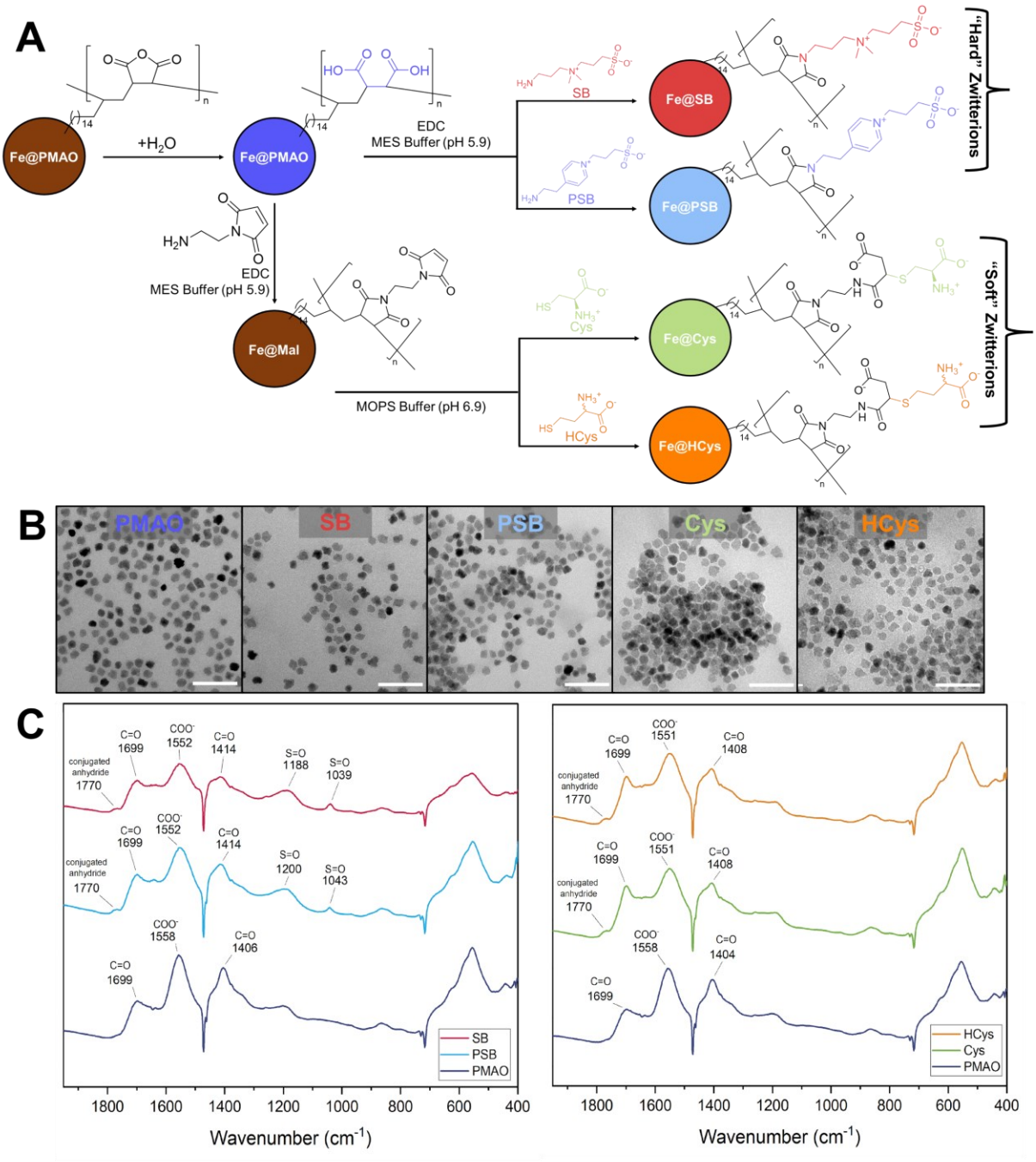

Figure 4.1 Synthesis and dry characterization of hard and soft zwitterionic superparamagnetic iron oxide nanoparticles (SPIONs). A) Synthetic scheme for the synthesis of hard and soft zwitterion surface functionalized SPIONs. B) Transmission electron microscopy images of nanoparticles before and after functionalization. C) Labelled Fourier-transformed infrared spectroscopy of SPIONs before and after functionalization.

4.5.2. Wet Characterization of Hard and Soft Zwitterionic SPIONs

Nanoparticle properties before and after functionalization were evaluated in solution to examine their suitability for cell uptake and to further determine if their initial magnetic properties had changed following functionalization. Changes in magnetic properties would have indicated significant changes to the SPION core, or aggregation behavior in solution.

Zeta potential measurements for all SPIONs were acquired at varying pHs to determine both aqueous dispersibility and the effect of the zwitterionic molecules on the electric double layer (EDL). (Fig. 2A). At basic pH = 11, the surface charge of all nanoparticles remained highly negative, with zeta potentials of -49.91 ± 1.47 mV, -46.86 ± 2.34 mV, -43.82 ± 6.62 mV, -47.44 ± 4.32 mV, and -47.93 ± 3.31 mV for Fe@PMAO, Fe@SB, Fe@PSB, Fe@Cys, and Fe@HCys, respectively. At pH = 11, the functional groups of all five nanoparticles were net negative, contributing to the highly negative value and the high dispersibility of all five nanoparticles. The charged nitrogen in Fe@SB and Fe@PSB had little effect on the overall zeta potential at this pH given the non-terminal position of the positive charge having less contribution on the EDL than the terminal sulfonate. This effect was observed in previous work with nanoparticles also possessing the SB moiety.[62] At physiological pH = 7.4, the zeta potential of all five SPIONs remained similar and negative, though slightly more positive than at pH = 11, with values of -42.57 ± 8.22 mV, -43.50 ± 1.21 mV, -42.22 ± 3.22 mV, -41.78 ± 6.76 mV, and -46.16 ± 1.92 mV for Fe@PMAO, Fe@SB, Fe@PSB, Fe@Cys, and Fe@HCys, respectively. No significant change in nanoparticle zeta potential between pH = 11 and pH = 7.4 was expected. For Fe@PMAO, Fe@SB, and Fe@PSB, the net charge of these functional groups remained the same for pH = 11 and pH = 7.4. For Fe@Cys and Fe@HCys, while the terminal primary amine became positively charged, the carboxylic acid adjacent to the thioether linkage that resulted

from maleimide hydrolysis remained negatively charge, likely contributing to the still negative value zeta potential, though this does not interfere with the ability for the terminal amino acid backbone of cysteine/homocysteine to remain zwitterionic. However, zeta potential values at this pH were similar to other cysteine-functionalized nanoparticles reported previously.[63] At pH = 3, below the pKa of the carboxylic acids, the zeta potentials all nanoparticles became significantly more positive compared to pH = 11 and pH = 7.4 (p<0.05) for all five nanoparticles. Fe@PMAO, Fe@SB, and Fe@PSB possessed similar zeta potentials of -24.38 ± 2.46 mV, -21.83 ± 9.74 mV, and -25.71 ± 3.28 mV, respectively, while Fe@Cys and Fe@HCys possessed significantly more positive charges than the other nanoparticles at pH = 3 (-7.64 ± 6.36 mV and -5.25 ± 4.64 mV, respectively. p<0.05). Interestingly, the soft zwitterion nanoparticles had a much more positive zeta potential value compared to the hard zwitterion nanoparticles. The zeta potential data, in addition to FTIR characterization, supported the successful conjugation of ligands to the PMAO surface through amide bond formation.

Hydrodynamic nanoparticle size (Z-average) was also measured by DLS in phosphate buffered saline (pH = 7.4, PBS) to observe deviations in hydrodynamic size following functionalization, as well as to examine the existence of any aggregation behavior (Fig. 2B). Prior to functionalization, the hydrodynamic size of Fe@PMAO was 81.60 ± 16.83 nm. Hydrodynamic size following hard zwitterion functionalization was not significantly changed, with Fe@SB and Fe@PSB having hydrodynamic sizes of 93.75 ± 25.59 nm and 118.95 ± 17.16 nm, respectively. Functionalization of SPIONs with soft zwitterions, Fe@Cys and Fe@HCys, significantly increased the hydrodynamic size of the nanoconjugates to 278.84 ± 81.51 nm and 275.46 ± 34.00 nm, respectively (p<0.01). This was likely the result of a small degree of aggregation behavior caused by inter- or intraparticle interactions between the terminal opposing charges in PBS. The

dispersion of these nanoparticles in a more ionically complex system (cell culture media supplemented with both fetal bovine serum (FBS) and penicillin/streptomycin (P/S)) resulted in all four zwitterion-functionalized formulations remaining well-dispersed (Fig. 2C). Importantly, while zwitterion functionalized SPION remained well-dispersed, Fe@PMAO aggregated and settled to the bottom of the tubes (Fig. 2C). Though polymaleic acid makes Fe@PMAO highly soluble given the strong negative surface charges, they are more susceptible to forming large protein coronas that cause them to crash out of solution.[64]

The magnetic properties of the nanoparticle formulations were evaluated by magnetic relaxometry in PBS in order to evaluate if surface functionalization would impact their effective MPI contrast properties. Magnetic relaxation curves between all five SPIONs were superimposable (Fig. 2D, top panel). Sensitivity, the maximum peak intensity, remained similar for Fe@PMAO, Fe@SB, and Fe@PSB (52.29 ± 0.27 mg^{-1} Fe, 46.64 ± 0.43 arb. Units/mg Fe, and 59.26 ± 0.37 mg^{-1} Fe, respectively). Fe@Cys and Fe@HCys showed a slight decrease in sensitivity (32.67 ± 0.11 mg^{-1} Feand 30.47 ± 0.35 mg^{-1} Fe, respectively), likely due to peak broadening due to slight nanoparticle aggregation in PBS, agreeing with DLS measurements. Specificity, the full width at half maximum intensity (FWHM), remained similar between Fe@PMAO and the functionalized nanoparticles (0.293 ± 0.002 T/mg Fe, 0.328 ± 0.001 T/mg Fe, 0.280 ± 0.002 T/mg Fe, 0.403 ± 0.003 T/mg Fe, and 0.303 ± 0.001 T/mg Fe, for Fe@PMAO, Fe@SB, Fe@PSB, Fe@Cys, and Fe@HCys, respectively), suggesting that changes to the surface chemistry do not alter the MPI contrast production properties of the PMAO.

The culmination of these wet characterization results showed that zwitterion functionalization of Fe@PMAO improved the solubility characteristics of the nanoparticles while maintaining their already excellent magnetic properties.

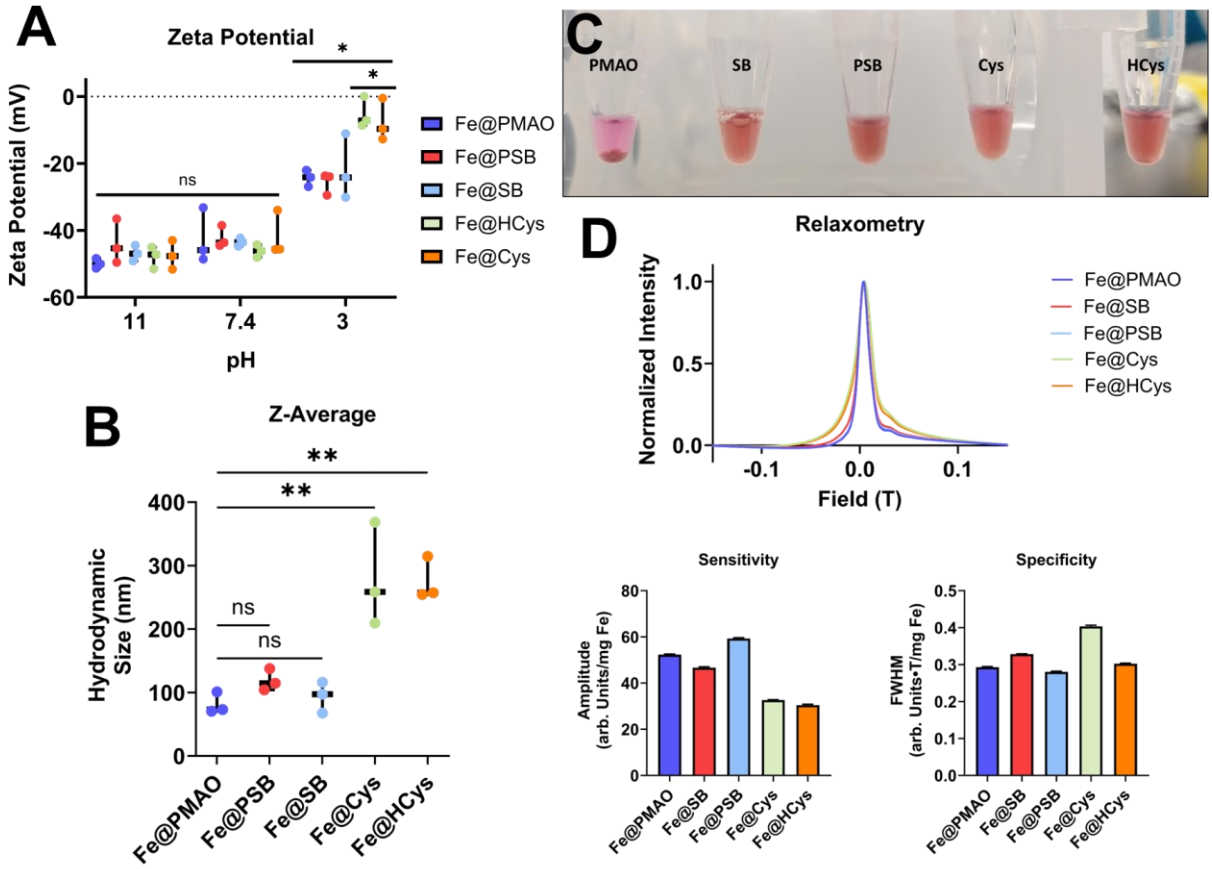

Figure 4.2 Wet characterization of hard and soft zwitterionic superparamagnetic iron oxide nanoparticles (SPIONs). A) Zeta potential measurements of zwitterion surface functionalized SPIONs at varying pHs in 1 mM KNO_3. B) Z-average measurements of zwitterion surface functionalized SPIONs in phosphate-buffered saline (pH 7.4, PBS). C) Photo of Fe@PMAO and zwitterion surface functionalized SPIONs dispersed in Dulbecco's modified Eagle's medium supplemented with 10% fetal bovine serum and 1% penicillin/streptomycin and left on the benchtop overnight. D) Magnetic relaxometry of SPIONs in PBS. Sensitivity and specificity were derived from the relaxometry curves. Data in A) and B) are presented are boxplots of n = 3 individual nanoparticle syntheses. Statistical analysis was done by one-way ANOVA followed by a Tukey post-hoc test. *p<0.05, **p<0.01. Data in D) are presented as lines or bars of n = 3 replicate measurements from one nanoparticle synthesis.

4.5.3. Cellular Uptake, Localization, and Performance of Zwitterionic Surface Functionalized SPIONs

All five nanoparticles were evaluated for cell uptake in three different cell lines representative of cell types typically tracked by imaging methods, including MPI: cancer cells (triple negative human breast cancer MDA-MB-231), stem cells (human mesenchymal stem cells MSC), and immune cells (mouse bone marrow macrophage RAW 264.7). Optimization of nanoparticle incubation concentration and incubation time was first performed, ultimately leading to the use of a nanoparticle concentration of 50 μg/mL Fe for 4 h incubation for effective cell uptake (Supplementary Fig. 10 & 11). No transfection reagents, rocking, or additional reagents beyond the nanoparticles and culture media were used. A histological method using both Perl's Prussian Blue (PPB, visualization of Fe in blue) and Nuclear Fast Red (visualization of cytoplasm and nucleus in pink) was employed to qualitatively evaluate nanoparticle uptake (Fig. 3).

The loading of MDA-MB-231 cells (Fig. 3, left panels) resulted in low Fe@PMAO, Fe@SB, and Fe@PSB uptake, with higher levels of uptake observed during incubation with Fe@Cys and Fe@HCys. The increase in the soft zwitterion nanoparticle uptake was likely the result of the higher levels of expression of amino acid transporters to support higher metabolic demands of the cancer cell line.[65] Incubation of RAW 264.7 cells (Fig. 3, center panels) with SPION formulations appeared to show high levels of uptake with Fe@PMAO, but the majority of the observed PPB stain was in between the cells and not within the cytoplasm (i.e. limited blue-pink overlay). This extracellular accumulation was the result of interactions between the PMAO coating, highly proteinaceous cell culture media, and the positively charged glass coverslips used for culture. From a practical point of view, these interactions are other factors that limit internalization of these highly anionic nanoparticles and make them less reliable for cell tracking.

The hard zwitterion nanoparticles Fe@SB and Fe@PSB, in contrast to Fe@PMAO, resulted in higher uptake in RAW 264.7 cells. The punctate cytoplasmic appearance of these nanoparticles is suggestive of uptake *via* intracellular vesicles. The soft zwitterionic nanoparticles Fe@Cys and Fe@HCys qualitatively showed the highest uptake in this cell line overall, again demonstrating a punctate Fe-stain pattern within the cytoplasmic areas of the cells. For all zwitterionic nanoparticle formulations, there was little to no Fe stain seen outside of the cells, a positive indication of their ease of washing and resistance to aggregation in cell culture media. The loading of MSC (Fig. 3, right panels) was qualitatively similar to the other two cell types: very little intracellular staining of Fe@PMAO. Overall higher and punctate PPB staining was seen in all four zwitterion-functionalized nanoparticles, with the highest qualitative uptake observed again with Fe@Cys and Fe@HCys.

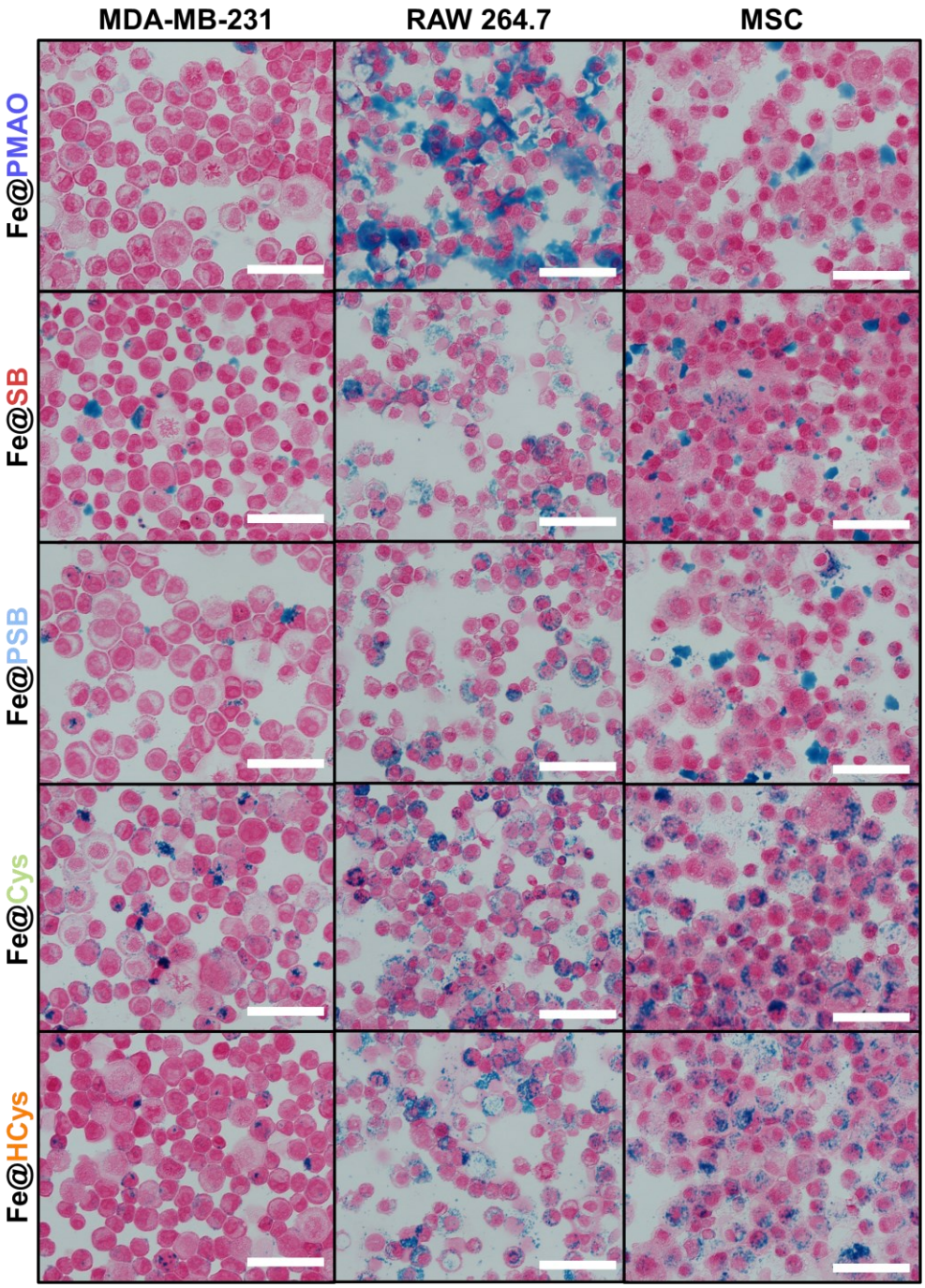

Figure 4.3 Identifying cellular uptake of hard and soft zwitterion functionalized superparamagnetic iron oxide nanoparticles (SPIONs). SPIONs functionalized with or without different zwitterionic functional groups were incubated with each cell type grown to 80% confluency (50 µg/mL Fe concentration for 4 h at 37°C, 5% CO_2, and humidified environment). Cells deposited on a glass slide using a Shandon™ Cytospin™ were washed, fixed, and stained with Perl's Prussian Blue (blue stain) to detect Fe, and with Nuclear Fast Red (pink stain) to detect cellular components prior to imaging. All scalebars represent 50 µm.

To evaluate the method of transport of nanoparticles into cells, cell loading experiments were repeated with incubations at 4ºC, a temperature at which active cellular transport is significantly reduced (Fig. 4)[66]. No Fe staining was observed in MDA-MB-231 cells (Fig. 4, left panels), indicating that nanoparticle uptake in these cells is energy-dependent. For both RAW 264.7 macrophages (Fig. 4, center panels) and MSC (Fig. 4, right panels), neither Fe@PMAO nor the hard zwitterion-functionalized nanoparticles showed any Fe staining, again indicating no nanoparticle uptake in the absence of active transport. However, some intracellular Fe staining, although less than at 37ºC, was observed in both RAW 264.7 and MSC incubated with the soft zwitterion-functionalized nanoparticles. Given that both soft zwitterions are amino acid functional groups, uptake was likely the result of facilitated diffusion, a process that commonly occurs with critical metabolites, such as amino acids and glucose, where carrier proteins and pores are able to translocate these molecules.[67] That soft zwitterion-functionalized nanoparticles could generate cell labelling even in energetically unfavorable cellular conditions is a potentially powerful feature for these formulations.

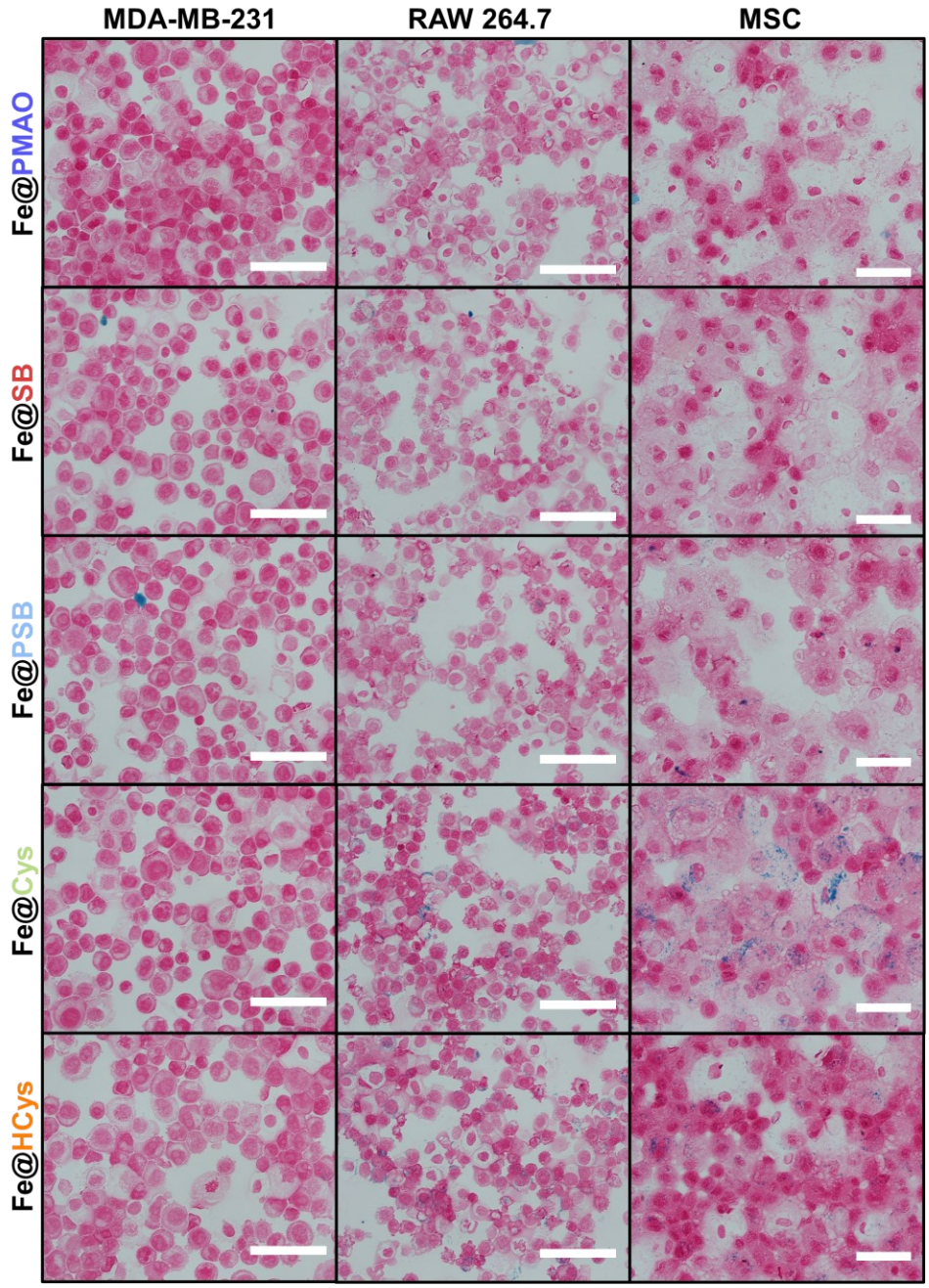

Figure 4.4 Identifying cellular uptake of hard and soft zwitterion functionalized superparamagnetic iron oxide nanoparticles (SPIONs) with limited cellular active transport. SPIONs functionalized with or without different zwitterionic functional groups were incubated with each cell type grown once grown to 80% confluency (50 µg/mL Fe concentration for 4 h at 4°C, 5% CO_2, and humidified environment). Cells deposited on a glass slide using a Shandon™ Cytospin™ were washed, fixed, and stained with Perl's Prussian Blue (blue stain) to detect Fe, and with Nuclear Fast Red (pink stain) to detect cellular components prior to imaging. Left and center panel scalebars represent 50 µm and the right panel scalebar represents 35 µm.

In order to confirm the nanoparticle uptake observed through histology and further evaluate their subcellular localization, SPION-loaded cells were evaluated by TEM (Fig. 5). In MDA-MB-231 cells (Fig. 5, left panels), all five nanoparticle formulations result in the formation of endocytotic vesicles encapsulating the nanoparticles. As observed by histology, Fe@PMAO resulted in mostly extracellular nanoparticles very close to the cell surface. Those Fe@PMAO nanoparticles found intracellularly appear to be mostly within multivesicular bodies (MVB). Fe@SB and Fe@PSB were more extensively found in the intracellular spaces, with Fe@PSB localizing primarily within MVBs, and Fe@SB localizing to early endo/lysosomes. Likewise, both Fe@Cys and Fe@HCys were more extensively localized intracellularly relative to Fe@PMAO, with localization for both nanoparticle formulations occurring in the late endo/lysosome. TEM investigation of RAW 264.7 macrophages (Fig. 5, center panels) incubated with Fe@PMAO confirmed what was observed by histology (Fig. 3), with majority of nanoparticles remaining extracellular. Those nanoparticles that were intracellular were localized within the macrophage phagosome. Incubation with all of the zwitterionic-functionalized ligands resulted in a substantially higher degree of nanoparticle intracellular localization than Fe@PMAO. Fe@PSB localized to the phagosome and MVBs, whereas Fe@SB was found to be confined within the phagosome and the early endo/lysosomes. Similarly, Fe@Cys and Fe@HCys were observed within late endo/lysosomes with some phagosome localization. The phagosome uptake observed in all five of these nanoparticle formulations support the greater overall uptake seen in RAW 264.7 cells by histology (Fig. 3). For MSC (Fig. 5, right panels), very little Fe@PMAO uptake was observed. Higher uptake for all zwitterionic nanoparticles was observed in comparison to Fe@PMAO As was observed in the histology, there were no identified sites of Fe@PMAO uptake in MSCs. The subcellular localization of the respective zwitterionic

nanoparticles were similar to what was observed with the other two cell lines: Fe@PSB and Fe@SB primarily localized within MVBs and early endo/lysosomes, while Fe@Cys and Fe@HCys showed overall higher uptake primarily localized within late endo/lysosomes. The observed subcellular localization of the functionalized nanoparticles is corroborated by previous reports of nanoparticle transport into cells, primarily through endo- or pinocytosis.[68,69] While endocytosis of all nanoparticles will likely lead to lysosomal catabolism, the high level of lysosomal localization for Fe@Cys and Fe@HCys is an interesting feature. Amino acids are known activators of RAG proteins on the lysosomal surface as an initiation to recruitment of mTORC1, promoting cellular anabolic activity and potentially driving further cell uptake of the amino-acid labelled nanoparticles.[70,71]

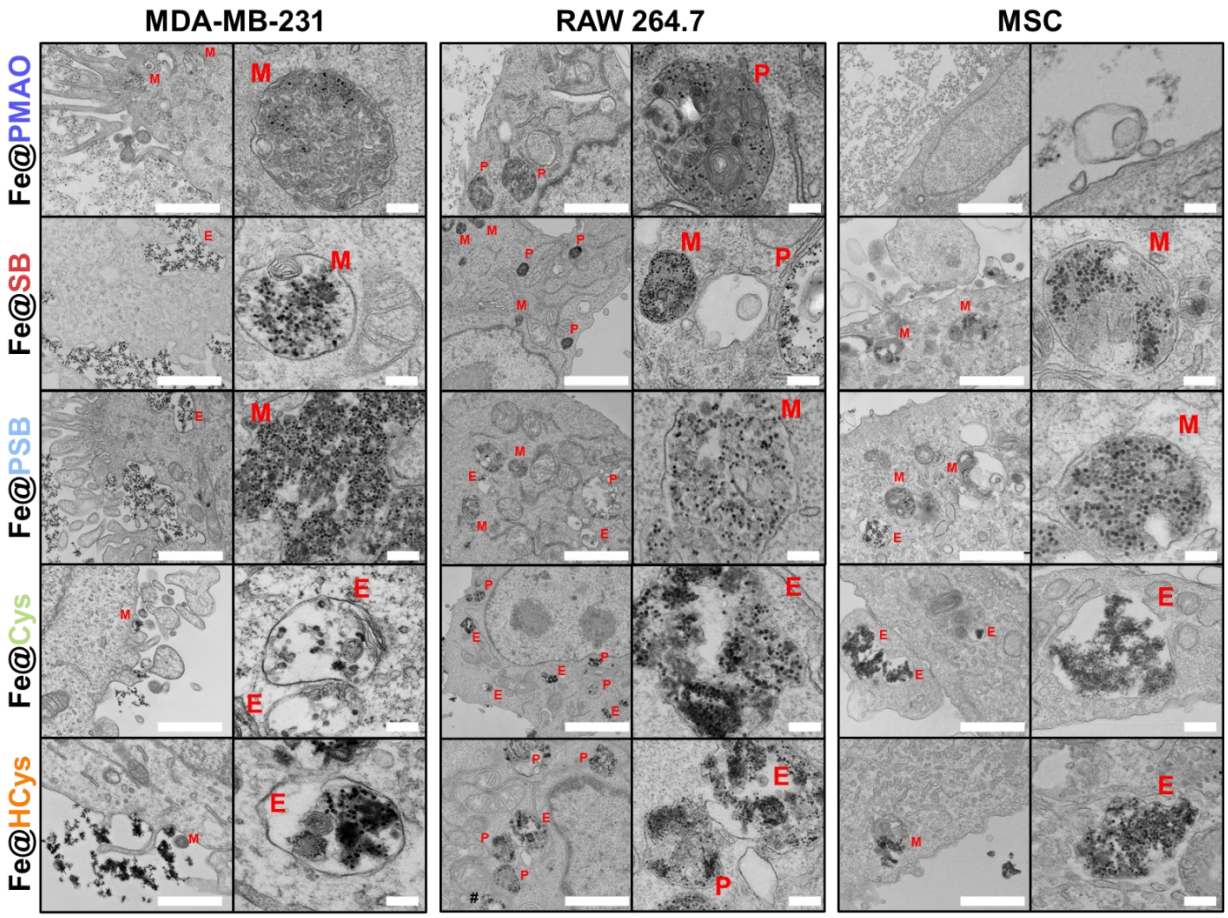

Figure 4.5 Intracellular localization following cellular uptake of hard and soft zwitterion functionalized superparamagnetic iron oxide nanoparticles (SPIONs). SPIONs functionalized with or without different zwitterionic functional groups were incubated with each cell type grown to 80% confluency on glass slides (50 µg/mL Fe concentration for 4 h at 37°C, 5% CO_2, and humidified environment). Cells were washed, fixed, sectioned, and stained for imaging by transmission electron microscopy. **M**: multivesicular body. **E**: endo/lysosome. **P**: phagosome. Large scalebars represent 1 µm and small scalebars represent 150 nm.

4.5.4. in vivo *Cellular Tracking by MPI:*

Given the class-wise similarities in both magnitude of cellular uptake, as well as the mode of transport and subcellular localization, we chose to evaluate the best performer from each of the soft and hard zwitterion categories: Fe@SB for the hard zwitterions due to its more favorable intracellular localization into early endo/lysosomes compared to Fe@PSB, and Fe@HCys for the soft zwitterions due to its overall qualitatively higher level of cell uptake. Cellular uptake experiments were performed once again, except that following the wash step the cells were pelleted and imaged by MPI to quantitatively evaluate nanoparticle uptake into cells (Fig. 6). The MPI signal of the largest cell pellet for each cell type was imaged by MPI (Fig. 6A) and resulted in similar extents of nanoparticle loading as the respective nanoparticle-cell combinations qualitatively observed by light microscopy in Figure 3. Fe@PMAO and Fe@HCys resulted in ~2.2x higher levels of signal intensity as compared to Fe@SB when loaded into MDA-MB-231 cells (Fig. 6B, left panel). Labelling with Fe@PMAO and Fe@HCys generated MPI signal above the limit of detection (LOD), with as little as 19,000 cells. Both Fe@SB and Fe@HCys produced higher MPI signal as compared to Fe@PMAO (1.4x and 2x respectively) when loaded into RAW 264.7 cells (Fig. 6B, center panel). Both hard and soft zwitterion-functionalized nanoparticles generated MPI signal above the LOD with as little as 25,000 cells. Similarly, both Fe@SB and Fe@HCys resulted in higher MPI signal than Fe@PMAO (2.2x and 1.4x respectively) when loaded into MSC (Fig. 6B, right panel). Both Fe@SB and Fe@HCys generated MPI signal above LOD with as little as 15,625 cells. For each cell type, the signal intensity on a per cell basis was compared (Fig. 6C) to determine the labelling efficacy (LE) of the nanoparticles within each cell population. Fe@PMAO and Fe@HCys both had an improved LE over Fe@SB (0.215 ± 0.021 arb. Units/cell and 0.235 ±

0.023 arb. Units/cell compared to 0.112 ± 0.032 arb. Units/cell, respectively. $p < 0.0001$) in MDA-MB-231 cell. However, when incubated with RAW 264.7 cells, Fe@HCys had a significantly greater LE than both Fe@SB and Fe@PMAO (0.364 ± 0.035 arb. Units/cell compared to 0.236 ± 0.035 arb. Units/cell and 0.176 ± 0.014 arb. Units/cell, respectively. $p < 0.0001$), though the LE for Fe@SB was also significantly greater than that of Fe@PMAO ($p < 0.05$). Both Fe@SB and Fe@HCys again resulted in higher LE than Fe@PMAO (0.152 ± 0.045 arb. Units/cell and 0.109 ± 0.023 arb. Units/cell compared to 0.067 ± 0.020 arb. Units/cell, $p < 0.01$ for Fe@PMAO versus Fe@SB) upon incubation with MSC. Ultimately, given the receptor and transporter expression differences between different cell types, it would be valuable to further evaluate a specific cell uptake mechanism for hard versus soft zwitterion-modified nanoparticles prior to use in potential cell therapy.

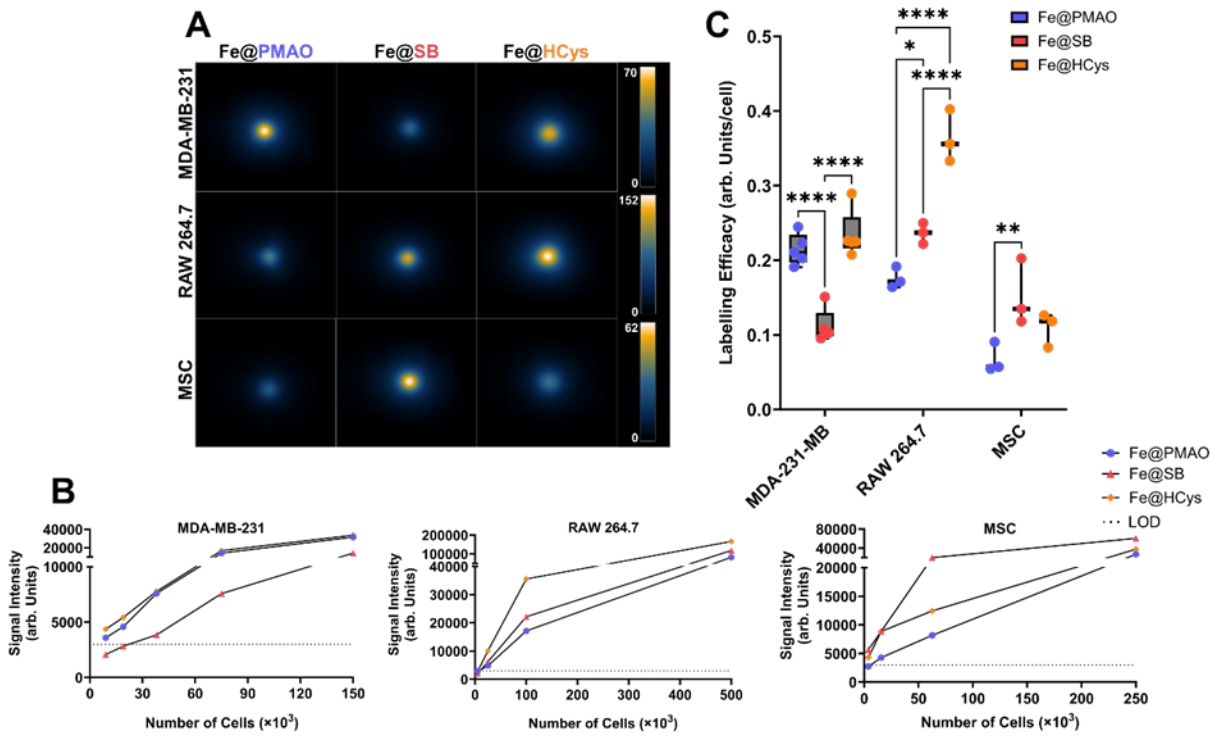

Figure 4.6 Magnetic nanoparticle imaging (MPI) of cell pellets labelled with hard and soft zwitterion functionalized superparamagnetic iron oxide nanoparticles (SPIONs). A) MPI images of cell pellets (150,000, 500,000, and 250,000 cells for MDA-MB-231, RAW 264.7, and MSC, respectively) following labelling with nanoparticles (50 µg/mL Fe concentration for 4 h at 37°C, 5% CO_2, and humidified environment). B) MPI signal of cell pellets containing decreasing numbers of cells from the initial pellet after dilution with phosphate-buffered saline (pH 7.4). LOD represents the limit of detection of the MPI, defined by the signal generated by unlabelled cells. Data are presented as line graphs of continual dilution of a single population of pelleted, labelled cells. C) The labelling efficacy of the nanoparticles for each cell type defined by the signal intensity generated per cell. Data as boxplots of n = 5 (MDA-MB-231) or n = 3 (RAW 264.7, MSC) labelled cell signal pellet signal intensities. Statistical analysis was done by two-way ANOVA followed by a Tukey post-hoc test. *p<0.05, **p<0.01, and ****p<0.0001.

The totality of the results obtained from the histology, TEM, and *in vitro* MPI experiments led us to conclude that the soft zwitterion-functionalized nanoparticles, Fe@HCys, was the best aggregate performer for loading cells with SPION across the three cell lines evaluated. In addition to generating the highest contrast across all three MPI cell labelling experiments, the ability for these nanoparticles to achieve intracellular localization in the absence of active transport is a powerful property from a cell tracking perspective, as it ensures labelling can occur even in suboptimal conditions. Because of this, we chose to evaluate the performance of Fe@HCys in comparison to the non-zwitterionic Fe@PMAO by tracking one of the most therapeutically relevant cell types, MSCs, across 7 days post-injection (Fig. 7).

In vivo MPI tracking of MSC labeled with Fe@PMAO or Fe@HCys over 7 days is shown in Fig. 7. At all 3 imaging timepoints, the MPI signal was significantly higher for MSC labeled with Fe@HCys compared to MSC labeled with Fe@PMAO (Fig. 7C). In agreement with the *in vitro* MPI results (Fig. 6), overall MPI labelling signal by Fe@HCys was stronger than by Fe@PMAO (Fig. 7C). In fact, MPI signal generated from Fe@HCys labelled cells, remained significantly higher than Fe@PMAO throughout the course of the experiment: ~2.0x higher on day 0 (p<0.01), ~2.4x higher on day 3 (p<0.001), and ~2.1x higher on day 7 (p<0.001). Cells labelled with either nanoparticle were able to maintain SPION-generated signal over 7 days without any significant change in signal intensity, though Fe@HCys was able to achieve this with better labelling efficacy and higher MPI signal. Low intensity signal outside of the injection site is observed (red arrows, Fig. 7B), which appears in both mice. In mice administered Fe@PMAO this signal remains stable over the course of 7 days, however is decreases over the course of 7 days in mice administered Fe@HCys. These results highlighted the better labelling

and higher MPI signal provided by Fe@HCys, resulting in higher signal retention in cells *in vivo* over time.

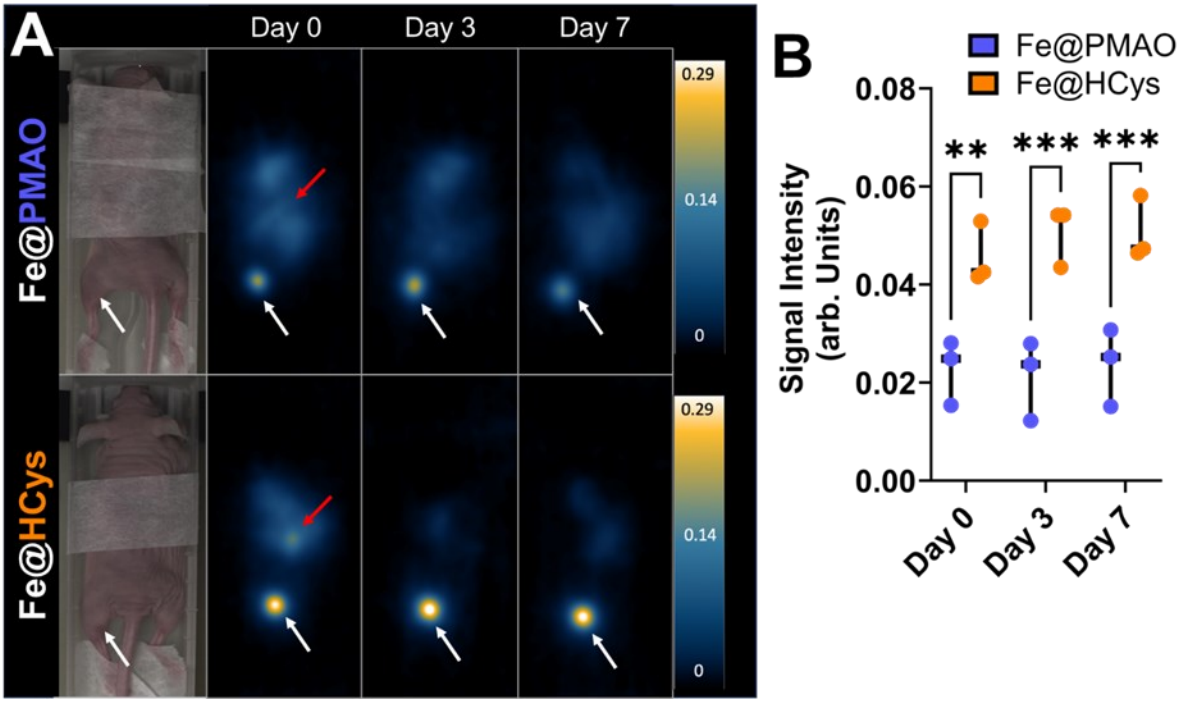

Figure 4.7 Comparing mesenchymal stem cell tracking in mice between soft zwitterion functionalized and anionic superparamagnetic iron oxide nanoparticles (SPIONs).). A) Location of labelled SPION (white arrow) injection in the MPI scan region. and the associated MPI images of the region-of-interest following injection on day 0 and repeat scans on day 3 and 7. Red arrows denote gastrointestinal signal. B) Signal intensity of the labelled cells for each timepoint. Data are presented as cell pellet signal intensities for n = 3 mice. Statistical analysis was done by one-way ANOVA followed by a Tukey post-hoc test. $^{**}p<0.01$, and $^{***}p<0.001$.

4.5.5. Conclusions

The functionalization of SPION with either hard or soft zwitterionic ligands resulted in nanoparticles of similar characteristics and magnetic properties as the precursory Fe@PMAO nanoparticles. However, the functionalized nanoparticles were more colloidally stable when dispersed in cell culture media, while Fe@PMAO aggregated and precipitated out. Cell labelling

experiments with these nanoparticles qualitatively (PPB) and quantitatively (MPI) showed higher uptake and more extensive intracellular localization with zwitterionic functionalization. Most interestingly, the amino acid functionalized soft zwitterionic nanoparticles were able to achieve intracellular localization in metabolically unfavorable conditions that other nanoparticle formulations could not. Overall, the zwitterion functionalized nanoparticles resulted in higher MPI signal for smaller numbers of cells, giving a broader dynamic range by which cells can be confidently identified and tracked. High signal-to-noise tracking of labelled MSCs in mice over 7 days was demonstrated, where Fe@HCys was able to give significantly higher signal over the course of cell tracking than those labelled with Fe@PMAO.

In summary, this study highlights the strength of zwitterionic ligands in enhancing intracellular cell labeling with nanoparticles. While anionic groups contribute to the dispersibility of nanoparticles and draw their proximity to cell surfaces, they fall short in promoting substantial cell uptake. On the other hand, zwitterionic ligands not only maintain outstanding dispersibility *in vitro*, which is key to enhancing cell labelling, but also exhibited greater cell culture media solubility. Additionally, their biomimetic properties facilitate superior intracellular localization. This work has also provided a new route for unlocking the full potential of cellular MPI: focusing on improving the stabilizing functional groups on the nanoparticle surface to maximize rapid, transfection reagent-free cell uptake. In essence, zwitterions emerge as a promising solution for advancing MPI applications in cell tracking.

4.6. Methods

All animal studies were conducted under approved protocols. Mice were housed doubly under a 12 h light/dark cycle, and ambient temperature of 20-24°C and 45 to 65% humidity. All rats were provided access to food (Rodent Laboratory Chow) and water *ad libitum*.

4.6.1. General Reagents

All chemical reagents were purchased from Sigma-Aldrich and used as is unless otherwise reported. All solvents were HPLC grade, except for water (18.2 MΩ cm Millipore water).

4.6.2. Experimental Procedures

All MPI imaging was performed using a MOMENTUM^{TM} MPI (Magnetic Insight Inc., Alameda CA). Non-MPI image analyses and quantifications were performed using Fiji and all MPI image analyses and quantifications were performed using Horos. GraphPad Prism 10.0 was used to generate all graphs, graphical figures, and statistical analyses.

PMAO coating of iron oxide nanoparticles:

Particle coating using PMAO was performed according to published work with some modifications.[72] A solution of PMAO in chloroform at an initial concentration of 0.137 M was added to a solution of oleic acid coated SPIOs in chloroform, at a concentration of 0.1 μM, to reach 300 polymer monomer units per nm^2 of nanocrystal surface. The particle-polymer solution was sonicated for 1 h in a bath sonicator followed by slow evaporation of the solvent under controlled pressure, using a rotary evaporator. A solution of bis(hexamethylene)triamine in chloroform (0.02 M), was added to the PMAO-coated SPIOs to reach a ratio of 10 crosslinker molecules per nm^2 of nanocrystal surface. Chloroform was added to the solution to reach a final concentration of nanoparticles of 0.5 μM Fe_3O_4. The mixture of PMAO-coated SPIOs with

crosslinker was bath sonicated for 30 minutes followed by rotary evaporation for 1 h to ensure complete removal of solvents. A thin film of nanoparticles on the flask wall indicated complete solvent removal. Sodium borate buffer (50 nM, pH 9) was added to cover the thin film of particles in the flask, followed by water bath sonication for 2 h at 60 °C or until the particles detached from the flask wall. Ultrasonication was then performed to obtain a suspension of single nanoparticles. PMAO-coated nanoparticles were purified by magnetic separation using magnetic columns (Myltenyi Biotec, LS Columns) and washed 3x in the magnetic column using the borate buffer to remove free polymer and crosslinker. Particles were then collected in deionized water.

General method for functionalized nanoparticle synthesis:

In a typical synthesis, a volume of Fe@PMAO equivalent to 1.4 mg Fe from the provided stock was centrifuged at 13,000 xg for 30 min to pellet the nanoparticles. The supernatant was aspirated, and the nanoparticles were resuspended by brief sonication with 500 µL of 0.5 mM 2-(*N*-morpholino)ethanesulfonic acid (MES) buffer adjusted to pH = 5.9 with sodium carbonate containing a dissolved 1 mg of EDC. This solution was shaken on a tube shaker for 30 min at 40ºC to activate the carboxylates of the PMAO. For hard zwitterion functionalized nanoparticles, 4 mg of either SB or PSB was added to the tube, and for soft zwitterion functionalized nanoparticles 3 mg of aminoethyl maleimide was added. In all cases, the tube was briefly sonicated and left on the shaker at 40ºC overnight. The nanoparticles were placed on a 1 T magnet to remove the nanoparticles from solution and the supernatant was aspirated and 1 mL of water was added. This was repeated three times to wash any unbound ligand from the nanoparticles. For hard zwitterions, nanoparticles were resuspended in 500 µL of PBS and stored at 4ºC.For soft zwitterions, nanoparticles were resuspended in 3-(*N*-morpholino)propanesulfonic

acid (MOPS) buffer adjusted to pH = 6.9. Two milligrams of either L-cysteine or DL-homocysteine was added to this solution and sonicated briefly. Nanoparticles were again shaken overnight at 40ºC and washed using the same procedures as previously described. Soft zwitterion-coated nanoparticles were resuspended in 500 µL of PBS and stored at 4ºC.

4.6.3. Determining Nanoparticle Concentration by Inductively Coupled Plasma Optical Emission Spectroscopy (ICP-OES)

To determine the concentration of nanoparticles following functionalization, 50 µL of the functionalized nanoparticle stock solution in PBS was added to 3 mL of aqua regia (3:1 HCl:HNO_3) in a glass vial and stirred at 80ºC for 4 h. The vial was cooled to room temperature, diluted with 3 mL of Milli-Q water, and analyzed for Fe concentration against a previously determined standard curve by ICP-OES using an Agilent 7000.

4.6.4. TEM Analysis of Nanoparticle Morphology

Nanoparticles were diluted with Milli-Q water, drop cast, and dried on the carbon-coated side of a Cu TEM grid with mesh size 300 placed on parafilm. TEM images were acquired using an FEI Tecnai G2 Spirit Twin TE.

4.6.5. FTIR Analysis of Nanoparticle Surface Functional Groups

Ten microliters from the nanoparticle stock solutions were drop cast on polyethylene plastic sheets and dried overnight. The dried nanoparticle concentrate was analyzed by FTIR using a Nicolet 6700 FTIR-ATR with background correction performed using polyethylene plastic without any nanoparticles.

4.6.6. Nanoparticle Zeta Potential and Hydrodynamic Size Evaluation by DLS

For zeta potential measurements, 10 µL of nanoparticles were added to 990 µL of 1 mM KNO_3 buffer adjusted to pH = 3 with HNO_3, and pH = 7.4 or pH = 11 with KOH. This solution was added to Malvern Zetasizer cuvettes (DTS1070) and zeta potential was acquired using a Malvern Zetasizer Nano-ZS for triplicate batches. Hydrodynamic size was acquired by dispersing 10 µL of nanoparticles in 990 µL of PBS. The solution was added to Malvern Zetasizer cuvettes (DTS1070), and Z-average size was acquired using a Malvern Zetasizer Nano-ZS for triplicate batches.

4.6.7. Magnetic Relaxometry of Nanoparticles

The RELAX module (MOMENTUMTM) was used for relaxometry measurements. Nanoparticle solutions from their stocks were added to a 0.5 mL microcentrifuge tube (final Fe content of 50 µg) and placed at the center of the sample holder (0 position) in the MPI scanner. The amount of iron in the sample was carefully chosen to avoid saturation of the detector (< 5 arb. Units). Magnetic relaxation curves were acquired by sweeping the magnetic field from -150 to 150 mT to produce relaxation curves. Full width at half maximum (FWHM) and amplitude corresponding to specificity and sensitivity, respectively, were measured directly from these curves.

4.6.8. Dispersibility of Nanoparticles in Cell Culture Media

A stock solution of nanoparticles was added to supplemented Dulbecco's modified Eagle's medium (10% fetal bovine serum (FBS) and 1% penicillin/streptomycin (P/S), supplemented DMEM) to a final concentration of 50 µg/mL Fe, briefly sonicated, and left in an incubator under cell culture conditions overnight (37°C, 5% CO_2, humidified). A picture was taken of the solutions the following day.

4.6.9. Cellular Loading with Nanoparticles

MDA-MB-231 cells and RAW 264.7 bone marrow macrophages were grown in supplemented DMEM, while MSCs were grown in α modified Eagle's medium supplemented with 10% FBS and 1% P/S (supplemented αMEM) under cell culture conditions. Cells were grown to 80% confluency and passaged three times before being seeded into 24-well plates and grown again to 80% confluency.

Once confluent, each nanoparticle was dispersed in the respective supplemented cell culture media to a final concentration of 50 μg/mL Fe and briefly sonicated. The growth media was replaced with this nanoparticle-containing supplemented media. Cells were incubated for 4 h under cell culture conditions. Following incubation, media was aspirated, and cells were washed three times with warm (37ºC) PBS. Cells were removed from the plate by incubation with 0.25% trypsin-EDTA, diluted with supplemented media and centrifuged at 400 xg (5 min, 4ºC). Cell pellets were resuspended in 5 mL of warm PBS and centrifuged at 400 xg (5 min, 4ºC). This was repeated three times to further remove unbound nanoparticles from cells. The final cell pellet was resuspended in 100 μl of warm PBS and an aliquot of this solution was diluted 1:1 with trypan blue to be read by a ThermoFisher Countess II cell counter. Cells were diluted further with warm PBS according to the cell count to a concentration 1.25 mil cells/mL. One hundred microliters of this solution was placed in a CytoSep™ funnel connected to a coverslip, placed in a Shandon™ CytoSpin^3, and spun at 1000 RPM for 5 min. Funnels were removed from the coverslips, dried for 1 min by air, then fixed in a 3:1 v/v methanol:acetic acid solution for 10 min. The slide was washed with distilled water then incubated in a modified PPB solution for 20 min (20 mL solution containing 20% v/v HCl and 20% w/v potassium ferrocyanide). This was washed with distilled water and counterstained with freshly prepared Nuclear Fast Red (20 mg

Nuclear Fast Red, 1 g aluminum sulfate, 20 mL distilled water) for 10 min. After washing with distilled water, slides were dehydrated by 5 min incubations in solutions of distilled water with increasing ethanol concentrations (70%, 95%, and 99%), followed by clearing with xylenes (5 min and 10 min in fresh xylenes each time). Slides were air dried and sealed with coverslips using Epredia CytoSeal^{TM}. Slides were imaged using a Nikon NiU Ratiometric Microscope.

For cellular uptake experiments in the absence of active cell uptake, the entirety of this workflow was repeated identically, with the only exception being nanoparticle-cell incubations were performed at 4^{o}C by placing the incubator in a cold-room, instead of being performed at 37^{o}C.

4.6.10. TEM Analysis of Nanoparticle Subcellular Localization

Cellular uptake was performed as previously described in the methods, except after washing cells in the 24-well plates, they were fixed in 2.5% glutaraldehyde diluted with 0.1 M sodium cacodylate buffer for 2 h. After scraping from the plate and placing into microcentrifuge tubes, cells were rinsed with 0.1 M sodium cacodylate buffer for 10 minutes, three times, followed by fixation for 2 h with 1% osmium tetroxide. Cells were washed again with distilled water and placed in 0.25% uranyl acetate at 4^{o}C overnight. Cells were then dehydrated using increasing concentrations of acetone in water (50%, 70% x2, 95% x2, 100% x3, 10 minutes each) and infiltrated with Epon-Araldite resin (1:3 with acetone for 3 h, 3:1 with acetone overnight, and then 100% Epon-Araldite resin for 3 h twice). Samples were then embedded in 100% Epon-Araldite resin and placed in a 60^{o}C for 48 h to cure.

Cured samples were sectioned using a Reichert-Jung Ultracut E ultramicrotome with a 100 nm diamond knife and placed on Cu grids of mesh size 300. Grids were stained with aqueous 2% uranyl acetate for 10 min, rinsed with distilled water for 5 min twice, stained with

lead citrate for 4 min, rinsed with distilled water, and air dried. Images of sectioned cells was acquired using a JEOL JEM 1230 TEM.

4.6.11. Evaluating MPI Signal of Labelled Cell Pellets

Cell labeling was performed as previously described in the methods, except the final, washed cell pellet (varying number of cells based on cell line) was resuspended in 50 µL of PBS and placed into PCR tubes. An aliquot of this sample was counted using a ThermoFisher Countess. The PCR tubes containing labelled cells were placed in a tube holder and loaded into the bed of the MPI scanner and imaged individually using the following parameters: FOV = 12 cm x 6 cm, gradient strength = 3.0 T/m, dual-channel acquisition (X and Z), excitation amplitude = 20 mT (X channel) and 26 mT (Z channel), imaging time = 1.5 min. After imaging, the pellet was diluted 1:1 with PBS and imaged again. This was repeated until the cell pellet was undetectable.

4.6.12. Cell Tracking of Labelled MSCs in Mice Following Intramuscular Injection

Eight-week-old athymic nude mice were purchased from Charles River. All animals were housed in conventional breeding cages, fed standard rodent chow, received water *ad libitum*, and were housed in a facility with a 12-h light cycle.

Cellular uptake was performed as previously described with MSCs labelled with either Fe@PMAO or Fe@HCys. The cell pellet was resuspended in 300 µl warm, sterile PBS. This labelled cell suspension (500,000 cells) was injected into the hindlimb of three anesthetized mice (isoflurane) mice for Fe@PMAO and Fe@HCys, each. The opposite hindlimb was injected with 300 µl of warm, sterile saline as a control. Following injection, mice were anesthetized by isoflurane and placed in the MPI scanner. MPI images of the hindlimb area were acquired under

anesthesia using thesame imaging parameters described above. These scans were repeated on day 3 and day 7 to follow the change in signal of the labelled cells over time.

4.6.13. Statistical Analyses

Statistical analyses for experiments are reported in the corresponding methods section. Normality was assumed where appropriate for all data sets. Prior to ANOVA, Levene's test was used to confirm equal variance, and visual quantile-quantile plot analysis was used to confirm homoscedasticity**.**

4.7. Conflicts of Interest

The authors declare no conflict of interests.

4.8. Acknowledgements

The authors would like to thank Dr. Mary Ann Trevors for her careful preparation of labelled cells for TEM analysis, Dr. Baptiste Lacoste for use of his TEM, the IMPAKT facility at Western University, and the Canadian Foundation for Innovation.

4.9. References

[1] L. L. W. Wang, M. E. Janes, N. Kumbhojkar, N. Kapate, J. R. Clegg, S. Prakash, M. K. Heavey, Z. Zhao, A. C. Anselmo, S. Mitragotri, *Bioeng Transl Med* **2021**, *6*, e10214.

[2] J. W. M. Bulte, H. E. Daldrup-Link, *Radiology* **2018**, *289*, 604.

[3] C. J. Bashor, I. B. Hilton, H. Bandukwala, D. M. Smith, O. Veiseh, *Nature Reviews Drug Discovery* **2022**, *21:9*, 655.

[4] Cell & Gene Therapy Market Investment Outlook in 2022 & beyond.

[5] R. Margiana, A. Markov, A. O. Zekiy, M. U. Hamza, K. A. Al-Dabbagh, S. H. Al-Zubaidi, N. M. Hameed, I. Ahmad, R. Sivaraman, H. H. Kzar, M. E. Al-Gazally, Y. F. Mustafa, H. Siahmansouri, *Stem Cell Research & Therapy 2022 13:1* **2022**, *13*, 1.

[6] M. Chivu-Economescu, M. Rubach, *Curr Stem Cell Res Ther* **2016**, *12*, 124.

[7] A. D. Waldman, J. M. Fritz, M. J. Lenardo, *Nature Reviews Immunology 2020 20:11* **2020**, *20*, 651.

[8] E. Guerra, R. Di Pietro, M. Basile, M. Trerotola, S. Alberti, *Int J Mol Sci* **2021**, *23*.

[9] J. L. Liesveld, N. Sharma, O. S. Aljitawi, *Stem Cells* **2020**, *38*, 1241.

[10] L. V. Loftus, S. R. Amend, K. J. Pienta, *International Journal of Molecular Sciences 2022, Vol. 23, Page 4723* **2022**, *23*, 4723.

[11] M. H. Amer, F. R. A. J. Rose, K. M. Shakesheff, M. Modo, L. J. White, *npj Regenerative Medicine 2017 2:1* **2017**, *2*, 1.

[12] M. P. Nucci, I. S. Filgueiras, J. M. Ferreira, F. A. de Oliveira, L. P. Nucci, J. B. Mamani, G. N. A. Rego, L. F. Gamarra, *World J Stem Cells* **2020**, *12*, 381.

[13] G. López-Cantillo, C. Urueña, B. A. Camacho, C. Ramírez-Segura, *Front Immunol* **2022**, *13*, 878209.

[14] J. W. M. Bulte, H. E. Daldrup-Link, *Radiology* **2018**, *289*, 604.

[15] S. Waiczies, T. Niendorf, G. Lombardi, *Oncoimmunology* **2017**, *6*.

[16] Y. Kurebayashi, P. L. Choyke, N. Sato, *Nanotheranostics* **2021**, *5*, 27.

[17] F. Progatzky, M. J. Dallman, C. Lo Celso, *Interface Focus* **2013**, *3*.

[18] Y. L. Wu, Q. Ye, L. M. Foley, T. K. Hitchens, K. Sato, J. B. Williams, C. Ho, *Proc Natl Acad Sci U S A* **2006**, *103*, 1852.

[19] L. M. Lechermann, D. Lau, B. Attili, L. Aloj, F. A. Gallagher, *Cancers (Basel)* **2021**, *13*.

[20] V. Sabapathy, J. Mentam, P. M. Jacob, S. Kumar, *Stem Cells Int* **2015**, *2015*.

[21] H. L. M. Cheng, *Front Med (Lausanne)* **2023**, *10*, 1193459.

[22] U. Himmelreich, T. Dresselaers, *Methods* **2009**, *48*, 112.

[23] A. J. Managh, S. L. Edwards, A. Bushell, K. J. Wood, E. K. Geissler, J. A. Hutchinson, R. W. Hutchinson, H. J. Reid, B. L. Sharp, *Anal Chem* **2013**, *85*, 10627.

[24] A. Harizaj, B. Descamps, C. Mangodt, S. Stremersch, A. Stoppa, L. Balcaen, T. Brans, H. De Rooster, N. Devriendt, J. C. Fraire, E. Bolea-Fernandez, O. De Wever, W. Willaert, F. Vanhaecke, C. V. Stevens, S. C. De Smedt, B. Roman, C. Vanhove, I. Lentacker, K. Braeckmans, *Biomater Sci* **2021**, *9*, 4005.

[25] L. Li, W. Jiang, K. Luo, H. Song, F. Lan, Y. Wu, Z. Gu, *Theranostics* **2013**, *3*, 595.

[26] C. Brekke, S. C. Morgan, A. S. Lowe, T. J. Meade, J. Price, S. C. R. Williams, M. Modo, *NMR Biomed* **2007**, *20*, 77.

[27] E. Bull, S. Y. Madani, R. Sheth, A. Seifalian, M. Green, A. M. Seifalian, *Int J Nanomedicine* **2014**, *9*, 1641.

[28] B. Gleich, J. Weizenecker, *Nature* **2005**, *435*, 1214.

[29] X. L. C. Wu, X. Y. Zhang, X. G. Steinberg, X. H. Qu, X. S. Huang, X. M. Cheng, X. T. Bliss, X. F. Du, X. J. Rao, X. G. Song, X. L. Pisani, X. T. Doyle, X. S. Conolly, X. K. Krishnan, X. G. Grant, X. M. Wintermark, *AJNR Am J Neuroradiol* **2019**, *40*, 206.

[30] T. M. Buzug, G. Bringout, M. Erbe, K. Gräfe, M. Graeser, M. Grüttner, A. Halkola, T. F. Sattel, W. Tenner, H. Wojtczyk, J. Haegele, F. M. Vogt, J. Barkhausen, K. Lüdtke-Buzug, *Z Med Phys* **2012**, *22*, 323.

[31] E. U. Saritas, P. W. Goodwill, L. R. Croft, J. J. Konkle, K. Lu, B. Zheng, S. M. Conolly, *J Magn Reson* **2013**, *229*, 116.

[32] O. C. Sehl, J. J. Gevaert, K. P. Melo, N. N. Knier, P. J. Foster, *Tomography* **2020**, *6*, 315.

[33] S. Harvell-Smith, L. D. Tunga, N. T. K. Thanh, *Nanoscale* **2022**, *14*, 3658.

[34] C. Billings, M. Langley, G. Warrington, F. Mashali, J. A. Johnson, *Int J Mol Sci* **2021**, *22*.

[35] A. Tomitaka, H. Arami, A. Ahmadivand, N. Pala, A. J. McGoron, Y. Takemura, M. Febo, M. Nair, *Scientific Reports 2020 10:1* **2020**, *10*, 1.

[36] H. Kratz, D. Eberbeck, S. Wagner, M. Taupitz, J. Schnorr, *Biomedizinische Technik* **2013**, *58*, 509.

[37] N. Dogan, G. Caliskan, M. Irfan, *Journal of Materials Science: Materials in Electronics* **2023**, *34*, 1.

[38] S. Liu, A. Heshmat, J. Andrew, I. Barreto, C. M. Rinaldi-Ramos, *Nanoscale Adv* **2023**, *5*, 3018.

[39] E. Fröhlich, *Int J Nanomedicine* **2012**, *7*, 5577.

[40] R. Gref, M. Lück, P. Quellec, M. Marchand, E. Dellacherie, S. Harnisch, T. Blunk, R. H. Müller, *Colloids Surf B Biointerfaces* **2000**, *18*, 301.

[41] F. Wang, L. Yu, M. P. Monopoli, P. Sandin, E. Mahon, A. Salvati, K. A. Dawson, *Nanomedicine* **2013**, *9*, 1159.

[42] K. I. McConnell, S. Shamsudeen, I. M. Meraz, T. S. Mahadevan, A. Ziemys, P. Rees, H. D. Summers, R. E. Serda, *J Biomed Nanotechnol* **2016**, *12*, 154.

[43] K. Qu, Z. Yuan, Y. Wang, Z. Song, X. Gong, Y. Zhao, Q. Mu, Q. Zhan, W. Xu, L. Wang, *ChemPhysMater* **2022**, *1*, 294.

[44] S. K. Lau, W. F. Yong, *ACS Appl Polym Mater* **2021**, *3*, 4390.

[45] S. Mondini, M. Leonzino, C. Drago, A. M. Ferretti, S. Usseglio, D. Maggioni, P. Tornese, B. Chini, A. Ponti, *Langmuir* **2015**, *31*, 7381.

[46] S. Caspani, R. Magalhães, J. P. Araújo, C. T. Sousa, *Materials 2020, Vol. 13, Page 2586* **2020**, *13*, 2586.

[47] L. Smith, Z. Kuncic, H. L. Byrne, D. Waddington, *Cancer Nanotechnology 2022 13:1* **2022**, *13*, 1.

[48] M. Unni, A. M. Uhl, S. Savliwala, B. H. Savitzky, R. Dhavalikar, N. Garraud, D. P. Arnold, L. F. Kourkoutis, J. S. Andrew, C. Rinaldi, *ACS Nano* **2017**, *11*, 2284.

[49] S. Liu, A. Chiu-Lam, A. Rivera-Rodriguez, R. DeGroff, S. Savliwala, N. Sarna, C. M. Rinaldi-Ramos, *Nanotheranostics* **2021**, *5*, 348.

[50] Q. Yan, H. N. Zheng, C. Jiang, K. Li, S. J. Xiao, *RSC Adv* **2015**, *5*, 69939.

[51] L. Lu, C. Liu, G. Li, L. J. Liu, C. H. Leung, D. L. Ma, *Sens Actuators B Chem* **2018**, *257*, 860.

[52] X. Xin, P. Li, Y. Zhu, L. Shi, J. Yuan, J. Shen, *Langmuir* **2019**, *35*, 1788.

[53] G. Kim, C. E. Yoo, M. Kim, H. J. Kang, D. Park, M. Lee, N. Huh, *Bioconjug Chem* **2012**, *23*, 2114.

[54] W. Wang, X. Ji, A. Kapur, C. Zhang, H. Mattoussi, *J Am Chem Soc* **2015**, *137*, 14158.

[55] T. Goda, Y. Imaizumi, H. Hatano, A. Matsumoto, K. Ishihara, Y. Miyahara, *Langmuir* **2019**, *35*, 8167.

[56] Y. Zhang, Y. Zhang, K. Sun, Z. Meng, L. Chen, *J Mol Cell Biol* **2019**, *11*, 1.

[57] M. Scalise, L. Pochini, L. Console, M. A. Losso, C. Indiveri, *Front Cell Dev Biol* **2018**, *6*, 409495.

[58] Y. Zhou, P. Dong, Y. Wei, J. Qian, D. Hua, *Colloids Surf B Biointerfaces* **2015**, *132*, 132.

[59] Q. Yan, H. N. Zheng, C. Jiang, K. Li, S. J. Xiao, *RSC Adv* **2015**, *5*, 69939.

[60] X. R. Zhang, B. T. Tang, S. F. Zhang, *Molecules 2011, Vol. 16, Pages 1981-1986* **2011**, *16*, 1981.

[61] E. S. Stratford, R. W. Curley, *J Med Chem* **1983**, *26*, 1463.

[62] S. Guo, D. Jańczewski, X. Zhu, R. Quintana, T. He, K. G. Neoh, *J Colloid Interface Sci* **2015**, *452*, 43.

[63] Y. Xu, H. Wang, M. Zhang, J. Zhang, W. Yan, Y. ; Xu, H. ; Wang, M. ; Zhang, J. ; Zhang, W. Yan, A. María Díez-Pascual, *Nanomaterials 2021, Vol. 11, Page 1621* **2021**, *11*, 1621.

[64] J. Mosquera, I. Garciá, M. Henriksen-Lacey, M. Martínez-Calvo, M. Dhanjani, J. L. Mascarenãs, L. M. Liz-Marzán, *ACS Nano* **2020**, *14*, 5382.

[65] M. Van Geldermalsen, Q. Wang, R. Nagarajah, A. D. Marshall, A. Thoeng, D. Gao, W. Ritchie, Y. Feng, C. G. Bailey, N. Deng, K. Harvey, J. M. Beith, C. I. Selinger, S. A. O'Toole, J. E. J. Rasko, J. Holst, *Oncogene* **2016**, *35*, 3201.

[66] B. D. Knapp, K. C. Huang, *Annu. Rev. Biophys.* **2022**, *51*, 499.

[67] G. M. Cooper, **2000**.

[68] Y. Wei, T. Tang, H. B. Pang, *Nature Communications* **2019**, *10*, 1.

[69] Y. Liu, Z. Chen, J. Wang, *Journal of Nanoparticle Research* **2011**, *13*, 199.

[70] M. Shimobayashi, M. N. Hall, *Cell Research 2016 26:1* **2015**, *26*, 7.

[71] Y. Yao, E. Jones, K. Inoki, *Biomolecules* **2017**, *7*.

[72] R. Di Corato, A. Quarta, P. Piacenza, A. Ragusa, A. Figuerola, R. Buonsanti, R. Cingolani, L. Manna, T. Pellegrino, *J Mater Chem* **2008**, *18*, 1991.

4.10. Supplementary Information

General reagents:

All chemical reagents were purchased from Sigma-Aldrich and used as is unless otherwise reported. All solvents were HPLC grade, except for water (18.2 MΩ cm Millipore water).

Experimental procedures:

All chemical syntheses were performed at room temperature unless otherwise specified. All evacuation and N_2 purges were done by a PIAB compressed air vacuum and N_2 tank connected to a Schlenk manifold. All NMR spectra were acquired on a Bruker AVANCE II 400 MHz or a Bruker Avance III HD 600 MHz NMR spectrometers, operating a 400 MHz or 600 MHz for ^{1}H spectra, and 100 MHz or 150 MHz for ^{13}C spectra, respectively. Chemical shifts are given in ppm. In all spectra, $CDCl_3$ was referenced to 7.26 ppm (^{1}H NMR) and 77.16 ppm (^{13}C NMR); MeOH-D_4 to 3.31 ppm (^{1}H NMR) and 49.0 ppm (^{13}C NMR); D_2O to 4.79 ppm (^{1}H NMR).

Synthesis of sulfobetaine and pyridinium sulfobetaine:

Sulfobetaine (SB) was synthesized with modifications to previously reported literature (Scheme 1, top scheme).[1] Only ^{1}H spectra were reported for each step, as this molecule had been previously reported and characterized. Pyridinium sulfobetaine (PSB) was also synthesized with modifications to previously reported literature (Scheme 1, bottom scheme).[2] However, no characterizations of this molecule from the aminoethyl pyridine starting material have been reported previously, so both ^{1}H and ^{13}C spectra have been reported.

*Synthesis of tert-butyl N-[3-(dimethylamino)propyl]carbamate (**1b**):*

Dimethylaminopropylamine (**1a**, 1 g, 9.7 mmol) was added to a round-bottom flask and dissolved in methanol (MeOH, 5 mL). The solution was cooled to 0°C on ice while stirred, at which point Boc_2O (2.1 g, 9.7 mmol, 1 eq) was added dropwise. After 1 h, ice was removed, and the solution was stirred overnight at room temperature. Solvent was evaporated and the crude product was suspended between water and ethyl acetate (EtOAc) in a separatory funnel. The organic layer was collected, and the aqueous layer was extracted three times with EtOAc. The combined organic was dried with Na_2SO_4, filtered, and evaporated. The resulting product was a clear oil (**1b**, 1.6 g, 80%). **^{1}H NMR:** (400 MHz, $CDCl_3$) δ 5.17 (s, 1H), 3.14 (q, *J* = 6.5 Hz, 2H), 2.27 (t, *J* = 7.0 Hz, 2H), 2.17 (s, 6H), 1.60 (p, *J* = 6.8 Hz, 2H), 1.41 (s, 9H).

*Synthesis of (3-{[(tert-butoxy)carbonyl]amino}propyl)dimethyl(3-sulfopropyl)azanium (**1c**):*

1b (1 g, 5.0 mmol) was added to a round-bottom flask and dissolved in dry dimethylformamide (DMF, 5 mL). A solution of DMF (1 mL) containing 1,3 propanesultone (.92 g, 7.5 mmol, 1.5 eq) was added to the starting material and stirred overnight. Toluene (15 mL) was added, and both solvents were evaporated. Chilled diethyl ether (0°C) was added to the crude product and was mixed with a glass rod by hand to form a semi-solid wax. The wax was vacuum filtered with three diethyl ether washes and left on a high vacuum overnight to give the resulting product as a pale wax (**1c**, 1.5 g, 95% yield). **^{1}H NMR:** (400 MHz, MeOD) δ 3.53 (t, *J* = 8.5 Hz, 2H), 3.35 (t, *J* = 8.4 Hz, 2H), 3.16 (t, *J* = 6.6 Hz, 2H), 3.10 (s, 6H), 3.00 (s, 1H), 2.88 (t, *J* = 6.9 Hz, 2H), 2.26 – 2.14 (m, 2H), 2.02 – 1.90 (m, 2H), 1.44 (s, 9H).

*Synthesis of (3-aminopropyl)dimethyl(3-sulfopropyl)azanium (**SB**):*

A solution of 4 M HCl in 1,3 dioxane (10 mL) was added to a round-bottom flask and was cooled to 0°C on ice under stirring. **1c** (1.5 g, 4.6 mmol) was dissolved in 5 mL of dichloromethane (DCM), added to the round-bottom flask, and stirred for 30 min. The ice was

removed, and the solution was stirred at room temperature for 1 h. The solvent was evaporated and was redissolved in a hot solution of DCM:isopropyl alcohol (IPA):MeOH (10:5:1). This solution was allowed to cool to form crystals of the product. The resulting crystals were dissolved in water, flash frozen in liquid nitrogen, and freeze-dried overnight to give the resulting product as a pale green wax (**SB**, 1.2 g, quantitative yield). **^{1}H NMR:** (400 MHz, D_2O) δ 3.50 (t, *J* = 8.4 Hz, 2H), 3.43 (t, *J* = 8.6 Hz, 2H), 3.13 (s, 6H), 3.07 (t, *J* = 6.4 Hz, 2H), 2.97 (t, *J* = 7.1 Hz, 2H), 2.30 – 2.08 (m, 4H).

*Synthesis of tert-butyl N-[2-(pyridin-4-yl)ethyl]carbamate (**2b**):*

Aminoethyl pyridine (**2a**, 1 g, 8.2 mmol) was added to a round-bottom flask and dissolved in methanol (MeOH, 5 mL). The solution was cooled to 0°C on ice while stirred, at which point Boc_2O (1.8 g, 8.2 mmol, 1 eq) was added dropwise. After 1 h, ice was removed, and the solution was stirred overnight at room temperature. Solvent was evaporated and the crude product was suspended between water and ethyl acetate (EtOAc) in a separatory funnel. The organic layer was collected, and the aqueous layer was extracted three times with EtOAc. The combined organic was dried with Na_2SO_4, filtered, and evaporated. The resulting product was a clear oil (**2b**, 1.6 g, 89%). **^{1}H NMR:** (400 MHz, $CDCl_3$) δ 8.49 (d, *J* = 6.1 Hz, 2H), 7.11 (d, *J* = 6.1 Hz, 2H), 4.68 (s, 1H), 3.38 (q, *J* = 6.7 Hz, 2H), 2.79 (t, *J* = 7.0 Hz, 2H), 1.41 (s, 9H). **^{13}C NMR:** (100 MHz, $CDCl_3$) δ 155.79, 149.90, 148.05, 124.20, 79.47, 40.82, 35.62, 28.37.

*Synthesis of 4-{2-[(tert-butoxycarbonyl)amino]ethyl}-1-(3-sulfopropyl)pyridin-1-ium (**2c**):*

2b (1 g, 4.5 mmol) was added to a round-bottom flask and dissolved in dry dimethylformamide (DMF, 5 mL). A solution of DMF (1 mL) containing 1,3 propanesultone (.83 g, 6.8 mmol, 1.5

eq) was added to the starting material and stirred for 48 h. Toluene (15 mL) was added, and both solvents were evaporated. Chilled diethyl ether (0ºC) was added to the crude product and was mixed with a glass rod by hand to form a semi-solid wax. The wax was vacuum filtered with three diethyl ether washes. The wax was resuspended and evaporated in toluene three times and left on a high vacuum overnight. The resulting product was a pale white powder (**2c**, 1.2 g, 76% yield). **^{1}H NMR:** (400 MHz, D_2O) δ 8.74 (d, *J* = 6.1 Hz, 2H), 7.93 (d, *J* = 7.0 Hz, 2H), 4.70 (t, *J* = 7.5 Hz, 2H), 3.46 (t, *J* = 6.1 Hz, 2H), 3.07 (t, *J* = 6.4 Hz, 2H), 2.95 (t, *J* = 7.2 Hz, 2H), 2.42 (p, *J* = 7.2 Hz, 2H), 1.32 (s, 9H). **^{13}C NMR:** (100 MHz, D_2O) δ 160.97, 157.81, 143.53, 128.75, 80.97, 59.13, 46.98, 39.58, 35.76, 27.49, 26.14.

*Synthesis of 4-(2-aminoethyl)-1-(3-sulfopropyl)pyridin-1-ium (**PSB**):*

A solution of 4 M HCl in 1,3 dioxane (10 mL) was added to a round-bottom flask and was cooled to 0ºC on ice under stirring. **2c** (1.2 g, 3.5 mmol) was dissolved in 5 mL of dichloromethane (DCM), added to the round-bottom flask, and stirred for 30 min. Ice was removed, and the solution was heated to 40ºC under stirring for 1 h. The solvent was evaporated, redissolved in water, flash frozen in liquid nitrogen, and freeze-dried overnight to give the resulting product as a tan powder (**PSB**, 0.93 g, quantitative yield). **^{1}H NMR:** (400 MHz, D_2O) δ 8.82 (d, *J* = 7.0 Hz, 2H), 8.00 (d, *J* = 6.9 Hz, 2H), 4.74 (t, *J* = 7.3 Hz, 2H), 3.41 (d, *J* = 7.4 Hz, 2H), 3.33 (t, *J* = 6.9 Hz, 2H), 2.96 (t, *J* = 7.3 Hz, 2H), 2.44 (p, *J* = 7.3 Hz, 2H). **^{13}C NMR:** (100 MHz, D_2O) δ 157.49, 144.27, 128.50, 59.40, 46.93, 38.27, 32.42, 26.01.

General cell culture methods:

MDA-MB-231 cells and RAW 264.7 bone marrow macrophages were grown in supplemented DMEM (10% fetal bovine serum (FBS) and 1% penicillin/streptomycin (P/S)) under cell culture conditions. Cells were grown to 80% confluency and passaged three times

before being seeded into 24-well plates and grown again to 80% confluency prior to any nanoparticle uptake experimentation.

Optimization of nanoparticle concentration for cellular uptake experiments:

Fe@SB and Fe@HCys was dispersed in the supplemented DMEM culture media to a final concentration of either 50, 20, 10, or 5 μg/mL Fe and briefly sonicated. The growth media of plated, confluent MDA-MB-231 cells was replaced with this nanoparticle-containing supplemented media. Cells were incubated for 4 h under cell culture conditions. Following incubation, media was aspirated, and cells were washed three times with warm (37ºC) PBS. Cells were removed the plate by incubation with 0.25% trypsin-EDTA, diluted with supplemented media and centrifuged at 400 xg (5 min, 4ºC). Cell pellets were resuspended in 5 mL of warm PBS and centrifuged at 400 xg (5 min, 4ºC). This was repeated three times to further remove unbound particles from cells. The final cell pellet was resuspended in 100 μl of warm PBS and an aliquot of this solution was diluted 1:1 with trypan blue to be read by a ThermoFisher Countess II cell counter. Cells were diluted further with warm PBS according to the cell count to a concentration 1.25 mil cells/mL. One hundred microliters of this solution was placed in a CytoSep™ funnel connected to a coverslip, placed in a Shandon™ CytoSpin^3, and spun at 1000 RPM for 5 min. Funnels were removed from the coverslips, dried for 1 min by air, then fixed in a 3:1 v/v methanol:acetic acid solution for 10 min. The slide was washed with distilled water then incubated in a modified PPB solution for 20 min (20mL solution containing 20% v/v HCl and 20% w/v potassium ferrocyanide). This was washed with distilled water and counterstained with freshly prepared Nuclear Fast Red (20 mg Nuclear Fast Red, 1 g aluminum sulfate, 20 mL distilled water) for 10 min. After washing with distilled water, slides were dehydrated by 5 min incubations in solutions of distilled water with increasing ethanol

concentrations (70%, 95%, and 99%), followed by clearing with xylenes (5 min and 10 min in fresh xylenes each time). Slides were air dried and sealed with coverslips using Epredia CytoSeal™. Slides were imaged using a Nikon NiU Ratiometric Microscope.

Optimization of nanoparticle incubation time for cellular uptake experiments:

Fe@HCys was dispersed in the supplemented DMEM culture media to a final concentration of either 50 µg/mL Fe and briefly sonicated. The growth media of plated, confluent RAW-264.7 cells was replaced with this nanoparticle-containing supplemented media. Cells were incubated for either 4 h or 24 h under cell culture conditions. Following incubation, media was aspirated, and cells were washed three times with warm (37ºC) PBS. Cells were removed the plate by incubation with 0.25% trypsin-EDTA, diluted with supplemented media and centrifuged at 400 xg (5 min, 4ºC). Cell pellets were resuspended in 5 mL of warm PBS and centrifuged at 400 xg (5 min, 4ºC). This was repeated three times to further remove unbound particles from cells. The final cell pellet was resuspended in 100 µl of warm PBS and an aliquot of this solution was diluted 1:1 with trypan blue to be read by a ThermoFisher Countess II cell counter. Cells were diluted further with warm PBS according to the cell count to a concentration 1.25 mil cells/mL. One hundred microliters of this solution was placed in a CytoSep™ funnel connected to a coverslip, placed in a Shandon™ CytoSpin^3, and spun at 1000 RPM for 5 min. Funnels were removed from the coverslips, dried for 1 min by air, then fixed in a 3:1 v/v methanol:acetic acid solution for 10 min. The slide was washed with distilled water then incubated in a modified PPB solution for 20 min (20mL solution containing 20% v/v HCl and 20% w/v potassium ferrocyanide). This was washed with distilled water and counterstained with freshly prepared Nuclear Fast Red (20 mg Nuclear Fast Red, 1 g aluminum sulfate, 20 mL distilled water) for 10 min. After washing with distilled water, slides were dehydrated by 5 min

incubations in solutions of distilled water with increasing ethanol concentrations (70%, 95%, and 99%), followed by clearing with xylenes (5 min and 10 min in fresh xylenes each time). Slides were air dried and sealed with coverslips using Epredia CytoSeal™. Slides were imaged using a Nikon NiU Ratiometric Microscope.

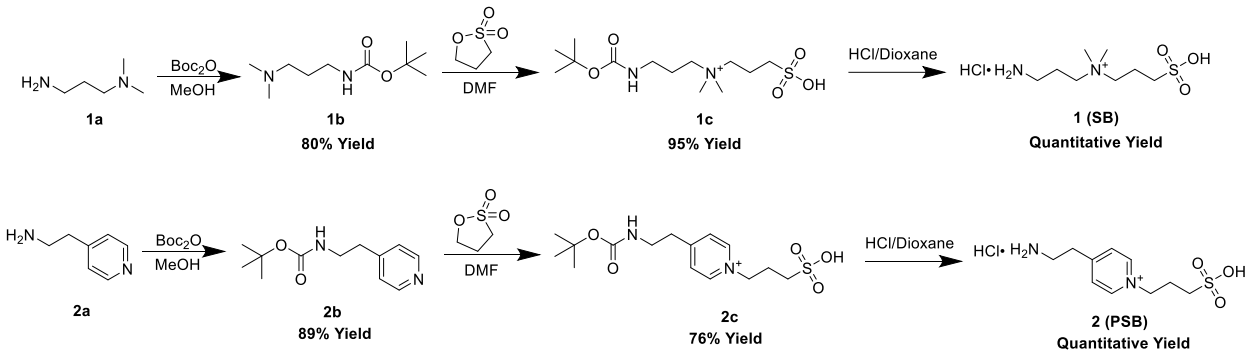

Scheme 1. Synthetic routes for sulfobetaine (SB) and pyridinium sulfobetaine (PSB).

General synthetic scheme for synthesis of the hard zwitterions SB and PSB.

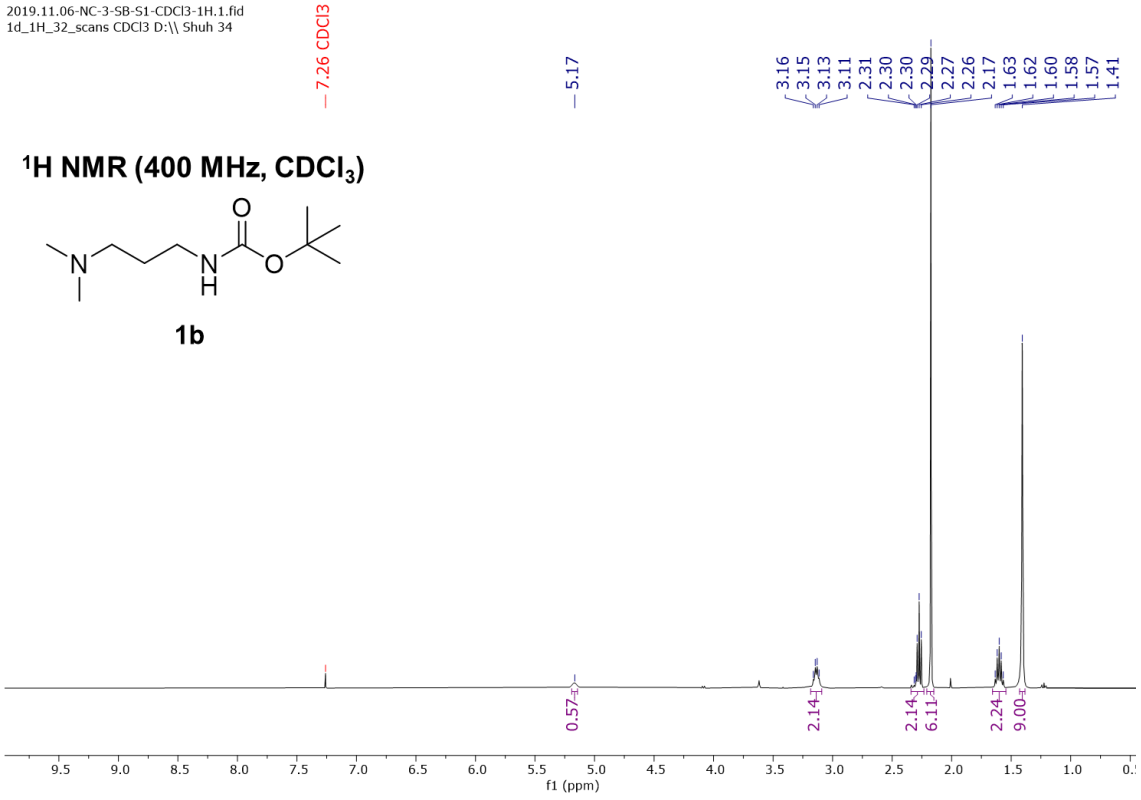

Supplementary Figure 1. ^{1}H NMR spectrum of compound 1b in $CDCl_3$.

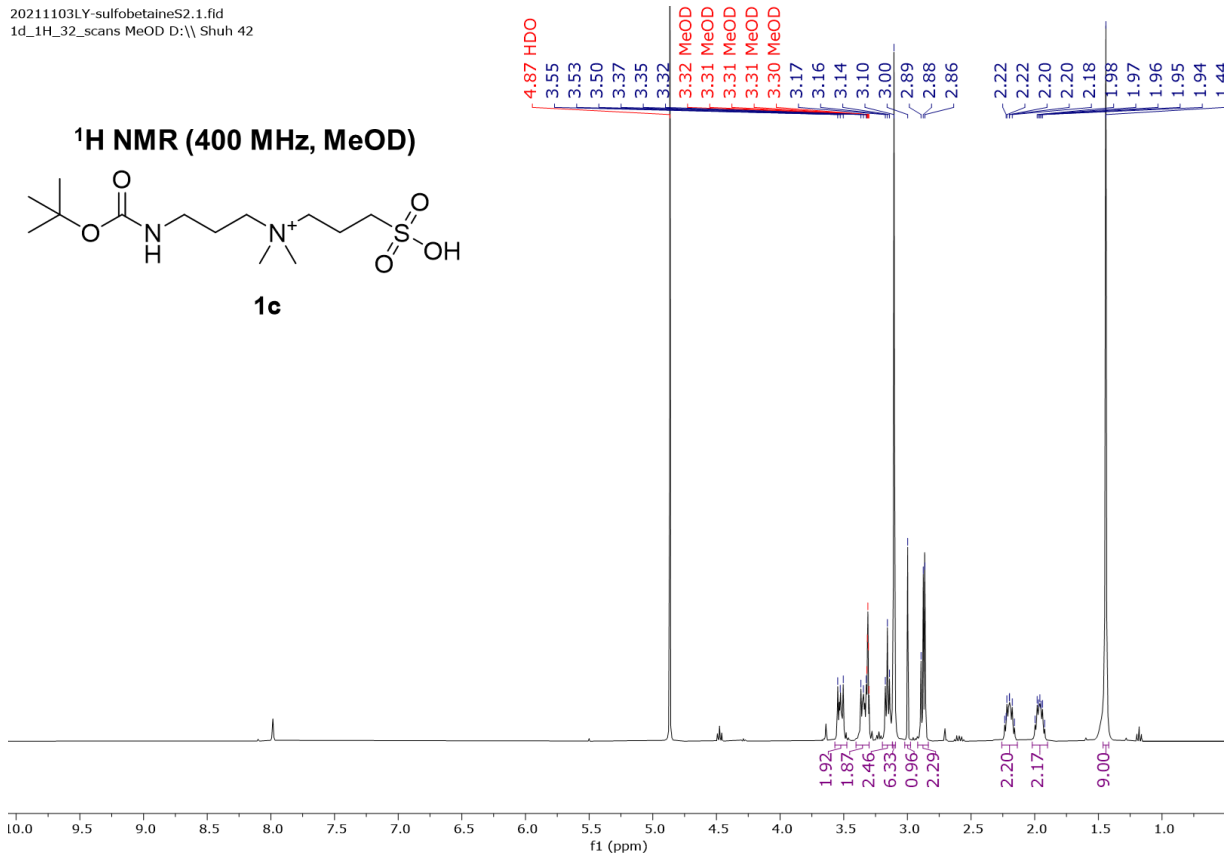

Supplementary Figure 2. ^{1}H NMR spectrum of compound 1c in MeOD.

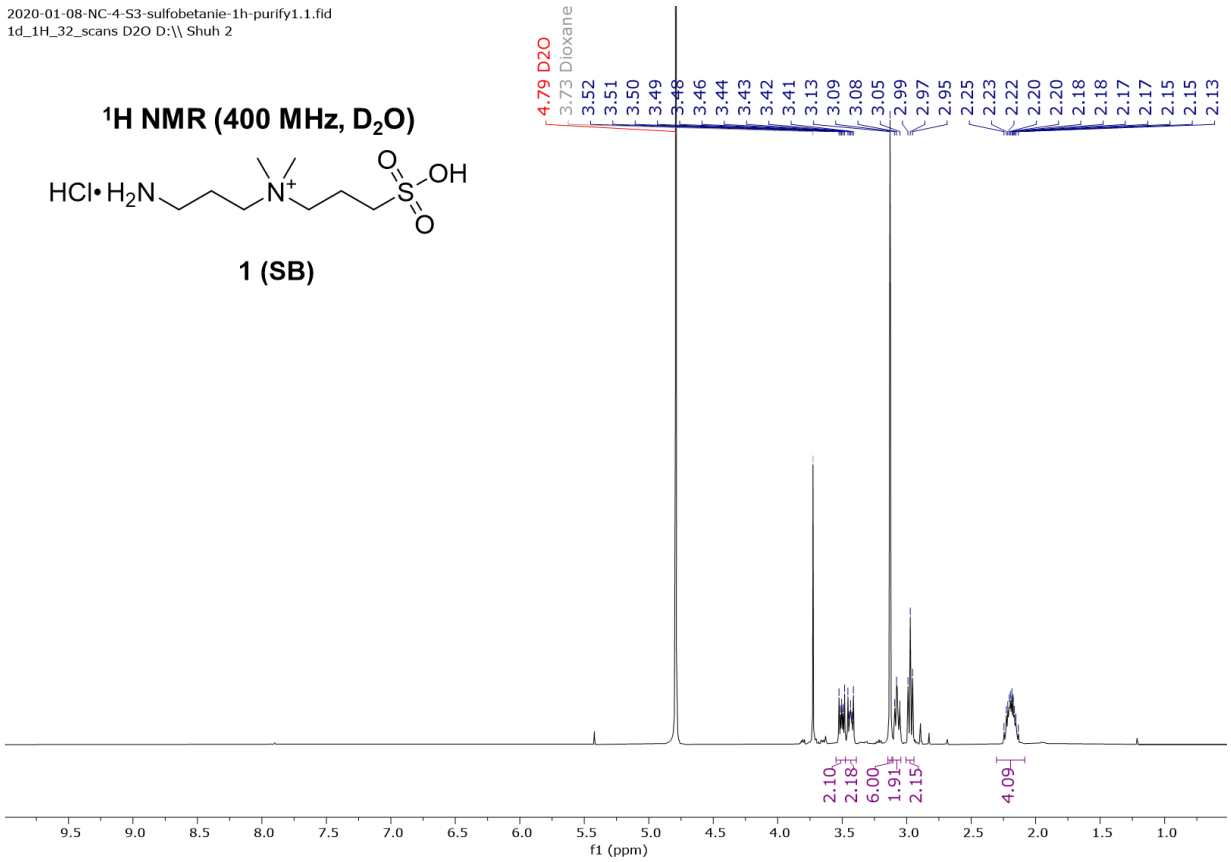

Supplementary Figure 3. ^{1}H NMR spectrum of compound SB in D_2O.

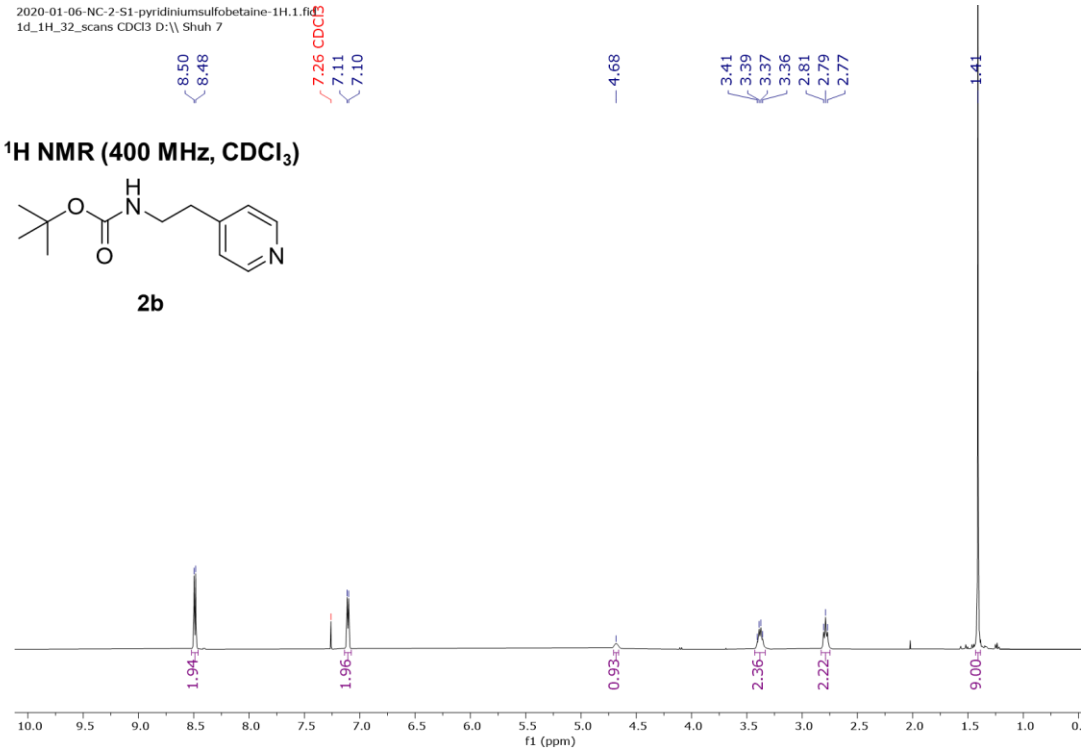

Supplementary Figure 4. ^{1}H NMR spectrum of compound 2b in $CDCl_3$.

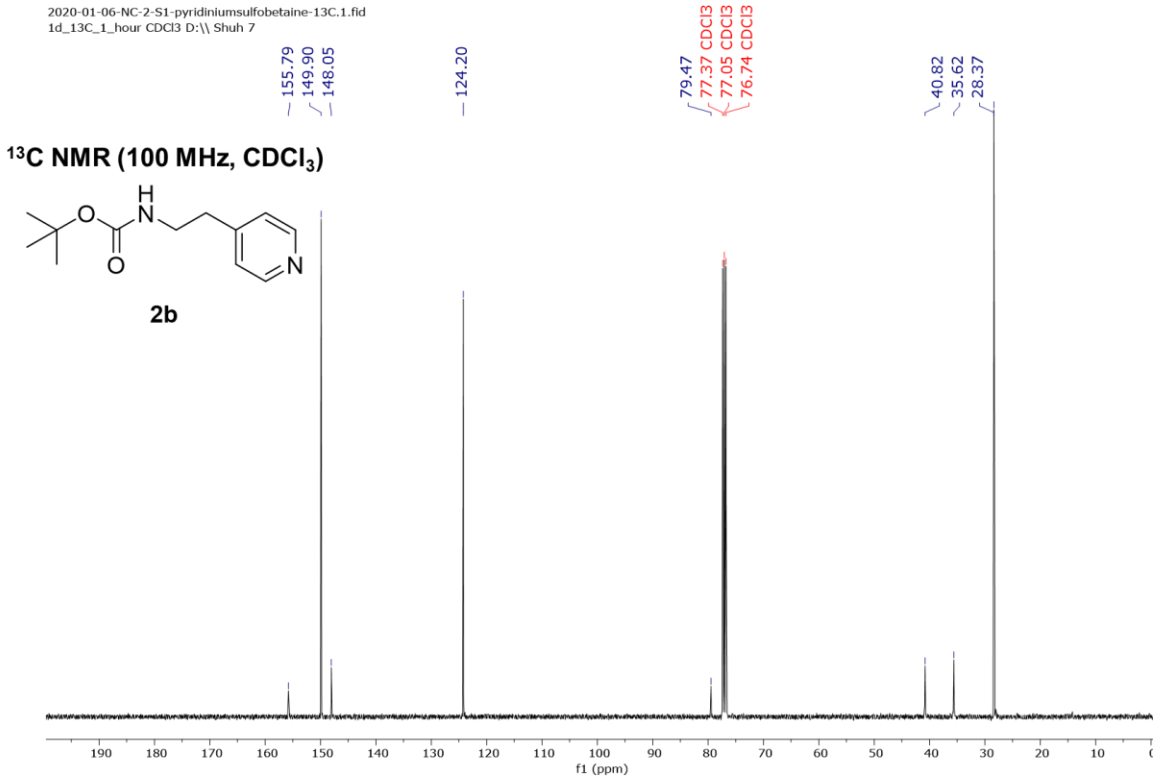

Supplementary Figure 5. ^{13}C NMR spectrum of compound 2b in $CDCl_3$.

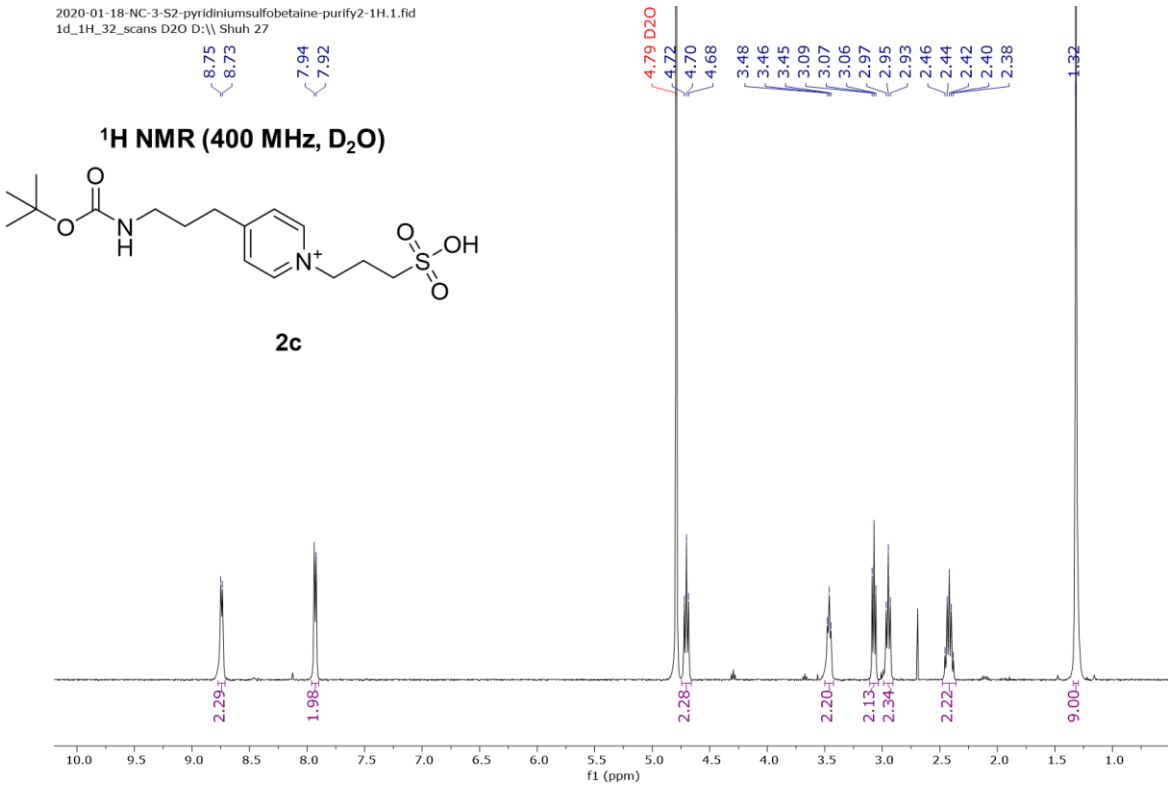

^{1}H NMR (400 MHz, D_2O)

2c

Supplementary Figure 6. ^{1}H NMR spectrum of compound 2c in D_2O.

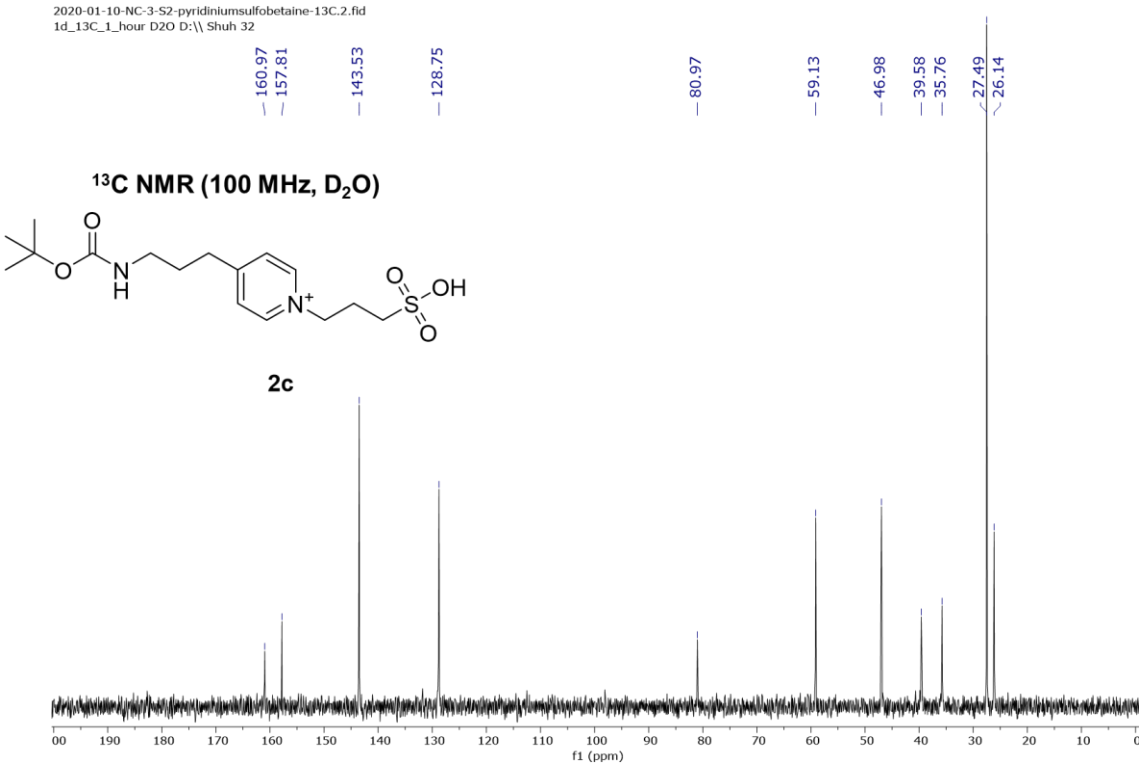

Supplementary Figure 7. ^{13}C NMR spectrum of compound 2c in D_2O.

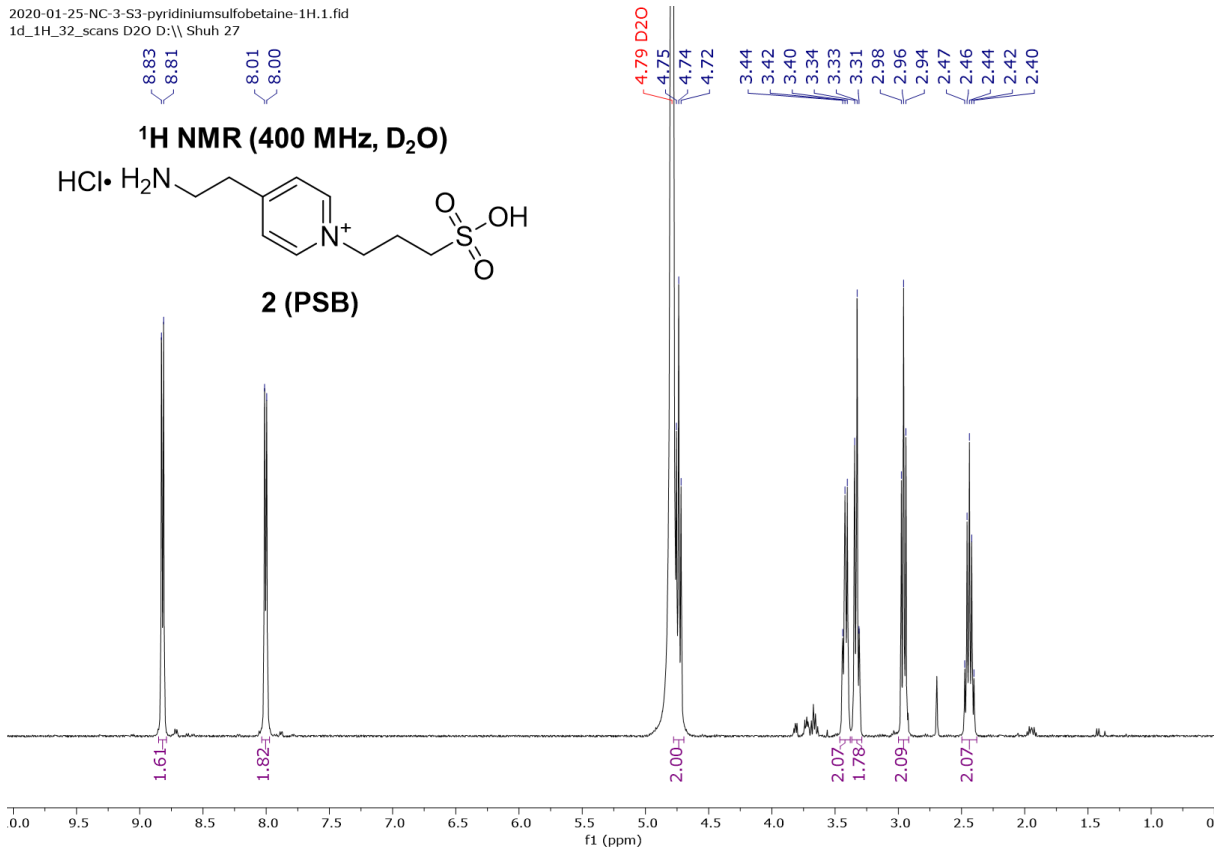

Supplementary Figure 8. ^{1}H NMR spectrum of compound PSB in D_2O.

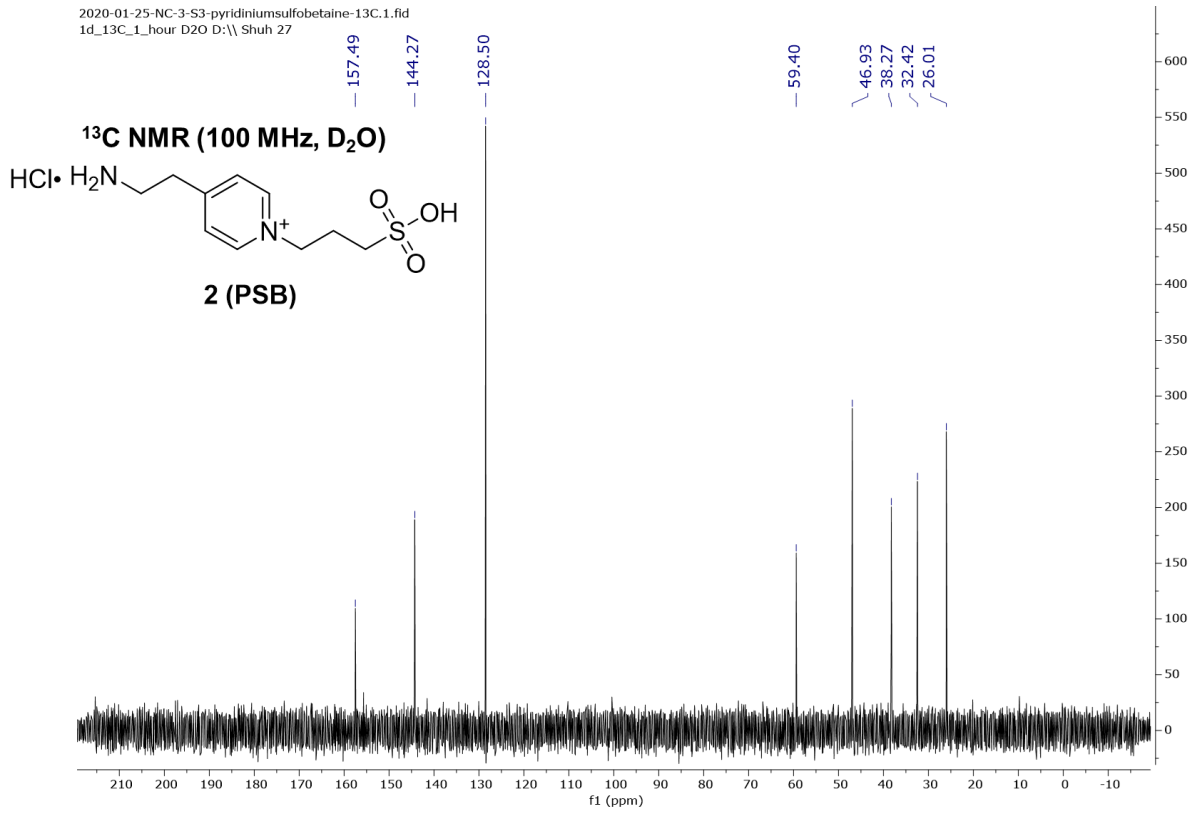

Supplementary Figure 9. ^{13}C NMR spectrum of compound PSB in D_2O.

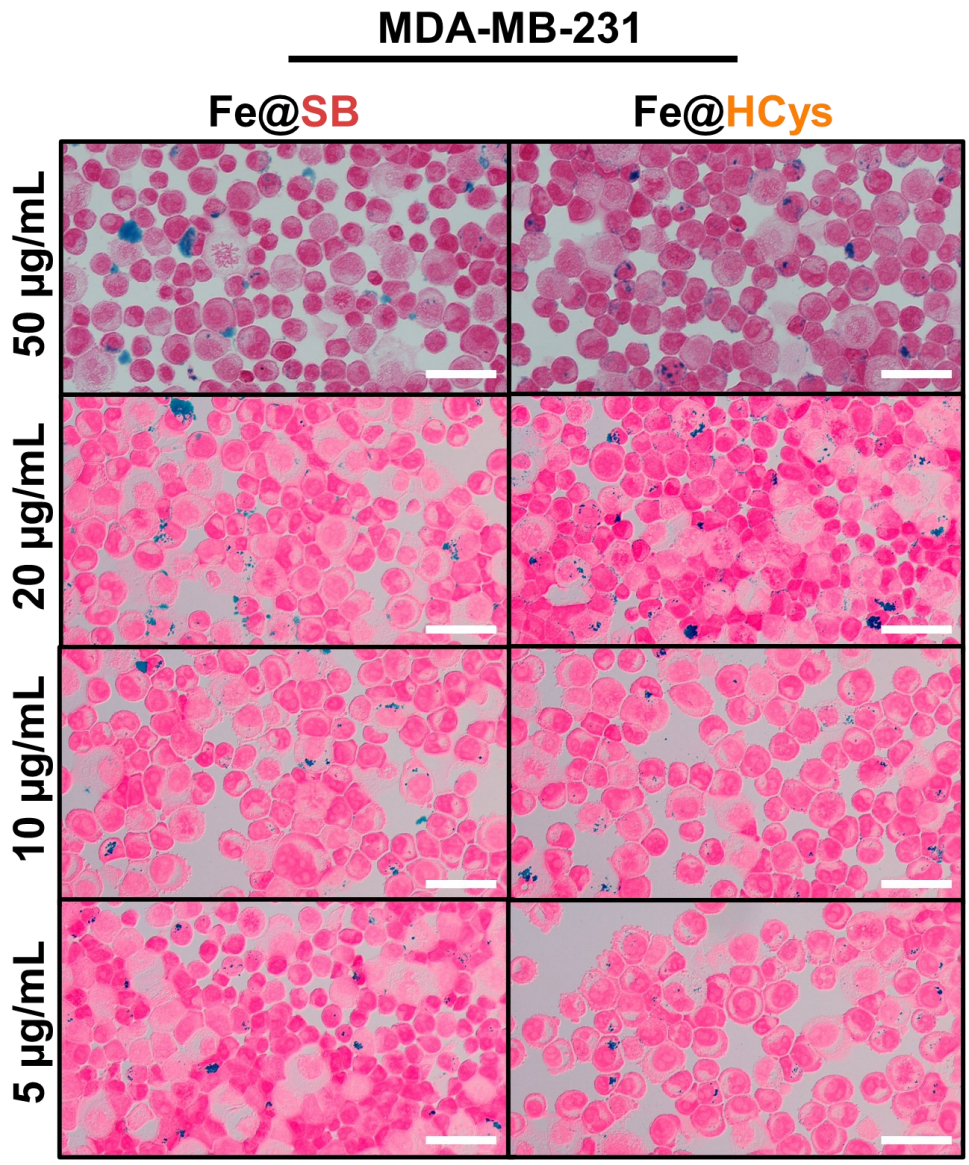

Supplementary Figure 10. Cellular uptake of hard and soft zwitterion functionalized superparamagnetic iron oxide nanoparticles (SPIONs) at different Fe concentrations. SPIONs functionalized with hard or soft zwitterionic functional groups were incubated with MDA-MB-231 cells at different concentrations of total Fe for 4 h. under cell culture conditions (37ºC, 5% CO_2, and humidified environment). Cells were washed, fixed, and stained with Perl's Prussian Blue (blue stain) to detect Fe, and with Nuclear Fast Red (pink stain) to detect cellular components prior to imaging. All scalebars represent 50 µm

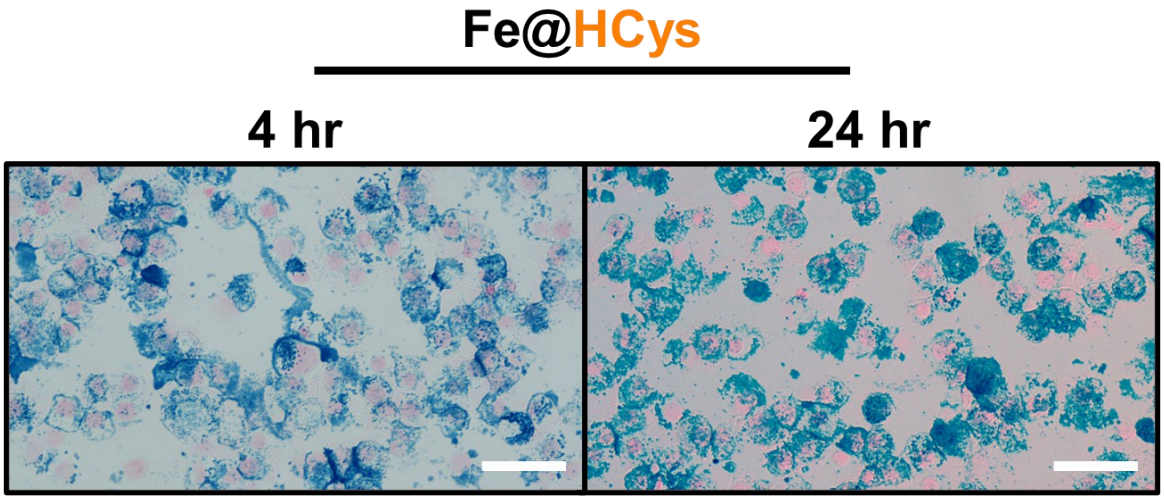

Supplementary Figure 11. Cellular uptake of hard and soft zwitterion functionalized superparamagnetic iron oxide nanoparticles (SPIONs) at different timepoints. SPIONs functionalized soft zwitterion homocysteine (HCys) was incubated with RAW 264.7 bone marrow macrophages (50 µg/mL Fe) for 4 h or 24 h under cell culture conditions (37ºC, 5% CO_2, and humidified environment). Cells were washed, fixed, and stained with Perl's Prussian Blue (blue stain) to detect Fe, and with Nuclear Fast Red to (pink stain) to detect cellular components prior to imaging. All scalebars represent 50 µm

References:

[1] W. Wang, X. Ji, A. Kapur, C. Zhang, H. Mattoussi, *J Am Chem Soc* **2015**, *137*, 14158.

[2] L. Lu, C. Liu, G. Li, L. J. Liu, C. H. Leung, D. L. Ma, *Sens Actuators B Chem* **2018**, *257*, 860.

Chapter 5: Conclusions and Future Directions

5.1. Chapter 2: Direct Mapping of Kidney Function by DCE-MRI Urography Using a Tetrazinanone Organic Radical Contrast Agent

5.1.1. Conclusion to Chapter 2

The work discussed in this chapter was inspired by the absence of alternative ORCAs to the nitroxyl radical, which is unstable to biological reductants. We first found the verdazyl molecule in scientific literature, where it had primarily been used for catalysis, electronics, and magnetics applications. There had been no prior investigations into verdazyl use as an MRI contrast agent, or any type of biological experimentation. We used the available verdazyl literature to create an optimized synthetic route for synthesizing high yield, high purity glucoverdazyl for *in vivo* evaluation. The first MR imaging of a glucoverdazyl solution was performed, with a T_1 relaxivity determined to be 0.30 ± 0.03 $mM^{-1}s^{-1}$, similar to nitroxyl radicals such as TEMPO. Unlike TEMPO, glucoverdazyl showed no loss of paramagnetic activity in a variety of biologically relevant redox environments. *Intravenous* injection of glucoverdazyl when monitored by MRI showed only localization into the kidneys ($184 \pm 21\%$ at t = 2.5 min post injection) and clearance to the bladder ($438 \pm 48\%$ at t = 40 min post injection), with no significant contrast enhancement observed in other tissues. Finally, glucoverdazyl was able to spatially map kidney function in two different models of kidney dysfunction, with the rates of contrast clearance shown to be indicative of GFR. This was the first indication of a new class of ORCAs that could quantitatively and qualitatively evaluate kidney function, while showing no evidence of acute toxicity. This could be a potential solution for using MRI to stratify the kidney disease population as an alternative to GBCAs and other metal-based contrast agents.

5.1.2. Future Directions for Chapter 2

In addition to its use as a kidney functional agent, glucoverdazyl presents as a contrast agent with potential clinical significance in providing contrast-enhanced MRI in patients who are currently ineligible for use of GBCAs. This work has aimed to be an entry point for an entirely new class of ORCAs that could provide an effective, alternative way of performing MRI-MI. Conceptually, the verdazyl scaffold can be segmented into three modular components: the contrast generating radical-bearing tetrazinanone core, solubility arms, and a targeting arm (Figure 5.1). Since verdazyls are small molecules and do not have the same physicochemical drawbacks as GBCAs (high M_w, highly hydrophilic, metal-coordinated), they may allow for a meaningful amount of cellular uptake with the right molecular targeting component. The addition of a targeting group would allow for receptor or transporter interactions, facilitating significant intracellular uptake and generating MRI-MI. The lack of anomeric oxygen afforded to glucoverdazyl prevented GLUT interactions and any meaningful levels of cellular uptake. However, we have nearly completed synthesis on two new verdazyl molecules that will serve as the first verdazyl MRI-MI probes to evaluate alternative diagnostic uses for these ORCAs beyond kidney functional imaging (Figure 5.2). Sestaverdazyl is an ORCA mimic of ^{99m}Tc-sestamibi, a SPECT blood pool agent for blood pool imaging with specific indications in thyroid and breast nodules. Sestamibi requires very high doses of radiation to acquire quality imaging, and sestaverdazyl may be a non-radioactive, non-metal alternative. Galaverdazyl is an attempt at providing cellular uptake to glucoverdazyl. Galactose has more favorable protecting chemistry than glucose, allowing the anomeric oxygen to be conserved and verdazyl linkage to occur at carbon 6 which has very little involvement with GLUT uptake. This should allow galaverdazyl

to be internalized through GLUT transport, potentially having indications in MRI-MI for cancers.

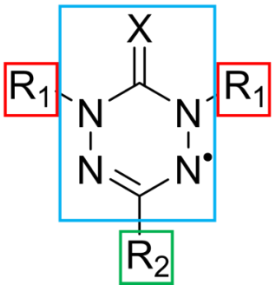

Figure 5.1 An overview of the important molecular components of the general verdazyl molecule. R_1 (red boxes) represents the solubility arms that can bear several chemical groups to help control the degree of aqueous solubility and plasma circulation time. R_2 (green box) represents the targeting arm that can be functionalized with molecular targeting moieties or functional groups to allow for intracellular uptake or receptor binding. The cyan represents the core verdazyl scaffold, where X can be O, S, or N, with the delocalized radical that generates MRI contrast.

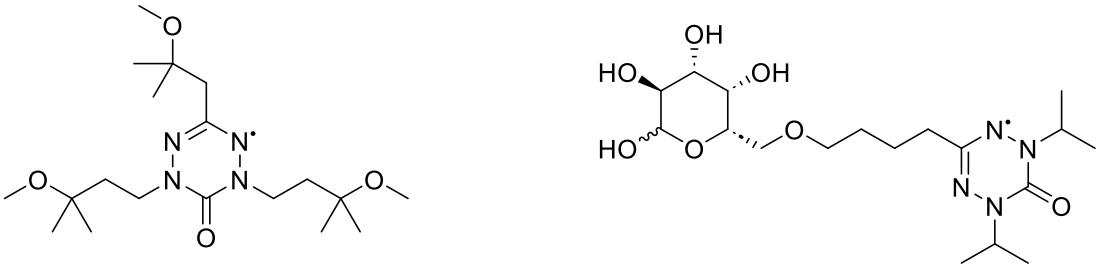

Figure 5.2 New verdazyl molecules for molecular imaging. Sestaverdazyl, an ORCA mimic of ^{99m}Tc-sestamibi is a SPECT blood pool imaging agent used for several different pathologies. Galaverdazyl, a transportable version of glucoverdazyl with the anomeric oxygen retained.

Moving forward, we must consider that the low inherent relaxivity of verdazyls preclude MRI contrast as strong as that of GBCAs. Consideration of a dimer or trimer verdazyl core may lead to higher levels of contrast. There has also been interest in the development of a ^{15}N tetrazinanone verdazyl, which may modulate the molecule's relaxivity due to the reduction in

delocalization around the tetrazinanone ring and reduction in the splitting of the electron paramagnetic peak.

5.2. Chapter 3: Highly NIR-II Scattering Gold Superclusters for Intravascular Optical Coherence Tomography Molecular Imaging

5.2.1. Conclusion to Chapter 3

This work aimed to develop a novel nanomaterial for facilitating IV-OCT MI with two major focuses; 1) generating a new Au-based nanomaterial that was both NIR-II active and water-dispersible, 2) functionalize the Au nanomaterial to be able to bind a molecular target *in vivo* and create IV-OCT MI contrast. We developed and characterized a novel synthetic route to controllably assemble AuNPs to produce a spherical AuSC that was highly dispersible in water due to its stabilization with Myrj52. AuSC possessed a peak LSPR of 1300 nm. AuSC generated three-fold greater contrast enhancement than similarly sized (500 nm) AuNPs (54.2 ± 2.3 arb. units versus 18.4 ± 2.7 arb. units). The Myrj52 coating that facilitated AuSC water dispersion chemically functionalized with a novel targeting group that mimicked SLeX, which demonstrated targeting efficacy for P-selectin protein *in vitro*. Variations in concentrations of the F and S portions of this target moiety showed that the 2:1 ratio of F:S generated a three-fold improvement in preferential binding in comparison to the unfunctionalized AuSC (287.7 ± 70.2% versus 70.2 ± 20.4%), and that increasing the ratio to 3:1 F:S slightly improved binding. Finally, after validating a rat model of arterial inflammation using *intravenous* injections of LPS for increased P-selectin expression, we were able to show the first instance of IV-OCT MI with our P-selectin targeting AuSC@$(13FS)_2$. Targeted AuSC resulted in significantly more ROSEs when imaged using a clinical IV-OCT system (11.2 ± 8.9 ROSEs/cm) than the same clusters in the absence of inflammation (0.2 ± 0.4 ROSEs/cm), as well as the untargeted AuSC@$(Myrj52)_2$

in the presence of inflammation (1.9 ± 1.5 ROSEs/cm). Additionally, we observed a linear correlation between the severity score of inflammation and the number of ROSEs observed. At the time of writing, this work was the first example of an IV-OCT MI agent that provides contrast enhancement to inflammatory marker P-selectin in an *in vivo* system.

5.2.2. Future Directions for Chapter 3

The general synthetic route for AuNP clustering presented can be used for clustering of other plasmonic metals. In fact, we have recently demonstrated a similar effect of clustering and LSPR shift with synthesized AgNPs, forming AgSC@$(Myrj52)_2$ (Figure 5.3). The AgSC show similar grain of AgNPs forming the cluster as was observed in AuSC (Figure 5.3A & B) demonstrated a red-shifted LSPR of ~900 nm in comparison to the original LSPR of AgNPs of ~400 nm (Figure 5.3C). A potential area of interest that this type of synthesis unlocks is the ability to produce metallically heterogeneous clusters (i.e. an AgNP/AuNP hybrid cluster). There have been no reports of the effect of LSPR modulation between two different plasmonic materials locked in proximity. These new materials could have potential uses for AuSC in catalysis or energy uses, given its unique interactions with NIR-II light.

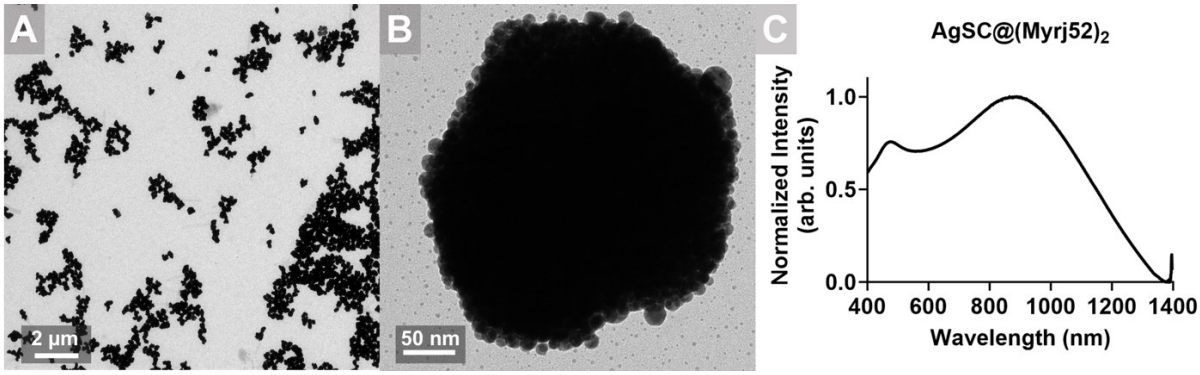

Figure 5.3 Silver superclusters (AgSCs) formed from individual silver nanoparticles AgNPs. The AuSC synthetic procedure was performed identically as previously described, with the exception directly swapping $HauCl_4$ for $AgNO_3$. A) and B) TEM images of AgSC@$(Myrj52)_2$. B) LSPR spectra of AgSC@$(Myrj52)_2$ in water.

Towards furthering IV-OCT MI, this work has developed a biocompatible material that can bind molecular markers of inflammation. The chemistry described in this work for the electrophilic activation of Myrj52 makes it functionally accessible to a wide range of targeting groups with a nucleophilic handle. This allows us to treat the AuSC as a contrast-generating core with modular surface chemistry allowing for a wide variety of potential molecular targets. As was discussed in Chapter 1.4.2, there has yet to be a true consensus target for both unstable plaques and in-stent restenosis. While P-selectin binding capabilities have been demonstrated in this work, AuSC may currently be best served as a research tool for evaluating new targeting moieties to stratify biomarkers of interest in these diseases, allowing it to act as an IV-OCT basic science tool for biomarker characterization, while still providing ideal physicochemical properties to be an IV-OCT contrast agent with clinical potential.

5.3. Chapter 4: The Careful Selection of Zwitterionic Nanoparticle Coating Results in Rapid and Efficient Cell Labelling for Imaging-Based Cell Tracking

5.3.1. Conclusion to Chapter 4

This work aimed to provide an evaluation of the effects on modulating SPION surface chemistry, specifically using biomimetic molecules for optimizing SPION intracellular uptake. Functionalization of Fe@PMAO SPIONs with either hard or soft zwitterionic ligands maintained the high aqueous dispersibility and the excellent magnetic properties necessary for strong MPI contrast. However, the use of either zwitterionic ligand class prevented aggregation in cell culture media, a problem that persisted for Fe@PMAO. In both cell types with clinical relevance to cell therapies, RAW 264.7 and MSC, both hard (Fe@SB) and soft (Fe@HCys) SPIONs had a greater degree of cell labelling efficiency and subsequent MPI signal than Fe@PMAO. Finally, using Fe@HCys and Fe@PMAO to track labelled MSCs injected into the hindlimbs of mice

demonstrated the ability for the soft zwitterion functionalized SPION Fe@HCys to retain a higher degree of labelling and higher overall MPI signal for a longer period than Fe@PMAO. This study will serve as an excellent example of the importance of surface functionalization in optimized cell labelling for cell tracking purposes, without sacrificing the ideal physicochemical properties of anionic SPIONs.

5.3.2. Future Directions for Chapter 4

This work serves as a primer for what should be a much larger scale investigation into the use of different zwitterions for a truly optimal approach to cell labelling. As was introduced in Chapter 1.2.3, the receptor and transporter expression on cells is highly variable, and this effect could be seen in the uptake response of the functionalized SPIONs to different cell types in this work, such as significantly higher uptake of Fe@HCys in RAW 264.7, but similar levels of uptake between Fe@HCys and Fe@SB in MSC. A larger analysis of specific classes of biomimetic zwitterions, in addition to differences between hard and soft, and their overall uptake effects on different cell types would be extremely valuable research to the MPI community. This potential work could serve as a guideline for cell therapies on what SPION surface chemistry to use depending on the type of cell being tracked, perpetually allowing for optimal cell tracking. These types of surface chemistry would also be particularly interesting in a more MI approach to MPI imaging; one could reasonably functionalize SPIONs with glucose or other amino acids to facilitate high levels of uptake in tumors or cells with aberrant uptake processes, utilizing the highly sensitive and specific features of MPI and further its diagnostic capabilities.

5.4. Overall Conclusions

While the body of work within this thesis covers different imaging modalities, chemical approaches to contrast agents, and disease models being evaluated by MI, it is consistent in its approach to contrast agent design. The overarching theme is the necessity of truly multidisciplinary approach to contrast agent design with constant consideration for downstream pre-clinical and clinical utility. This work has taken care at designing chemical probes and targeting moiety that are synthetically scalable, interact with a target of clinical relevance, and will generate meaningful contrast within standard clinical imaging workflows. All three contrast agents presented in this work serve as platform technologies, where we have demonstrated a strong, imaging modality-specific signal generating core, with chemistry designed that molecular targeting groups of interest can be easily swapped without interfering with contrast generation or binding. This multidisciplinary approach is a critical consideration to keep in mind for future work as the need for new MI agents continues to grow both within and outside of the imaging modalities covered in this work.